The influence of clay diagenesis on the petrophysical properties of sandstone reservoirs in the Pletmos Basin Offshore South Africa

By

Nothando Mguni (3340760)

UNIVERSITY *of the*
WESTERN CAPE

Thesis submitted in fulfilment of the requirements for the degree of Masters of Science (MSc.)
In
Applied Geology

Supervisor: Prof. Tapas K Chatterjee

Department of Earth Science
Faculty of Natural Sciences
University of the Western Cape, Bellville
Cape Town, South Africa

December, 2019

Declaration

I declare that the research project titled **"The influence of clay diagenesis on the petrophysical properties of sandstone reservoirs in the Pletmos Basin Offshore South Africa"** is my work, that it has not been submitted before for any degree or examination in any other university, and that all the sources I have used or quoted have been indicated and acknowledged by means of complete references.

Nothando Mguni **December, 2019**

Acknowledgements

I am extremely grateful for my supervisor Prof. Tapas Chatterjee for providing me the opportunity to pursue my masters as well as his guidance throughout my work; along with Doctor Opuwari who helped me to find direction in my research. I would like to thank the Petroleum Agency of South Africa (PASA) for the data used in this work as well as the National Researchers Fund (NRF) for contributing to the financial support which made everything come together.

I would like to extend my gratitude to Doctor Moses Magoba for reviewing my work and providing his input and guidance, it is truly appreciated.

My family members have been the most vital people in the pursuit of my MSC thesis as they have been a source of strength throughout this study. I would like to express my gratitude to my sisters Naledi, Nobukhosi and Nobuhle whose love, guidance and support are with me in all that I pursue. A special thanks goes to my uncle Njabulo and aunt Annah for reminding me of the end goal and encouraging me. For family and friends not mentioned by name (as the list would be endless) who contributed positively to the success of my project, I truly cherish you all.

This work is dedicated to my late father Moffat Mguni who did a splendid job in raising me and laid the foundation to my ambition and success, not forgetting the almighty God whose word is a lamp unto my feet and a light unto my path.

Abstract

Pletmos Basin is a Mesozoic half graben located in the southern part of South Africa and has undergone numerous tectonic changes which involve alteration of structure and reworking of sediments. Clay diagenesis has become a more prominent factor affecting the quality of the tight shaly sandstone reservoirs in the southern Pletmos Basin. The present study focused on Block 11a as a primary area of interest .The tight sandstone reservoirs encountered in the four wells, viz. Ga-Q1, Ga-Q2, Ga-Z1 and Ga- E2 were studied using four different methods to incorporate and infer the overall diagenetic effect on the reservoirs, caused by materials of argillaceous origin. The methods adopted in the present research are formation evaluation using wireline logs and calibration of core data using Interactive Petrophysics software, thin section petrography, X-Ray Diffraction (XRD) and, Scanning Electron Microscope (SEM) along with Energy Dispersive X-Ray Spectroscopy (EDS). The availability of core samples were limited to wells Ga- Q1 and well Ga- Z1. Four reservoirs within the Cretaceous age were identified in each well and the best reservoirs were associated with facies B and D.

The integrated study shows a strong correlation between a decrease in petrophysical parameters, particularly porosity and permeability, with an increase in depth. The porosity ranged from 3.5% to 28.6% and permeability ranged from a negligible value to 3.27mD. The water saturation ranged from 25.28% to 83.7% and the volume of clay ranged from 17.6% to 41.14%. The history of the Pletmos Basin revealed that the source of some of the studied minerals are of detrital origin and were deposited under shallow marine environment. Petrographic studies proved that both processes of neoformation and diagenesis are characteristic of these clays with authigenesis being the more eminent process, as polytypes from XRD further confirm the ambient environment of formation. Although the major identified clays, namely Illite, chlorite flakes and green glauconite pallets were found to have originated and developed in an organic rich, small fractioned micro-organism accommodating matrix, there were anomalous amounts of kaolinite. Transition/alteration of one mineral to another was a result of local chemistry.

The major clay minerals identified were present as both positive and adverse contributors to petrophysical properties. Favourable contributions being porosity and permeability preserving grains particularly illite and chlorite as they hindered the initiation and continuation of overgrowth of underlying grains such as quartz. An additional favourable contributor being the dissolution of minerals which led to secondary porosity. Adverse contributors were minerals forming part of the clay matrix making it compact and reducing primary pore spaces characteristic of the shallower depths and blocking fluid flow pathways. In addition to the quartz which formed a large amount of the samples and thus highly contributed to the cementing material, the presence of glauconite, feldspars and micas

contributed to the permeability destructing clay matrix. The above mentioned minerals were assisted by compaction as it played a vital role in compressing primary pores and thus altering pore geometry.

Keywords: clay, diagenesis/diagenetic, reservoir, petrophysical properties, petrography, porosity, permeability

Table of contents

List of Figures

List of Tables

CHAPTER 1: INTRODUCTION

1.1. Introduction

One of the most substantial factors contributing to the quality of sandstone reservoirs is clay diagenesis (Worden & Morad, 2003; Ohen & Civian, 1993). Diagenesis refers to the sequence of processes such as compaction and lithification that contribute to the change of sediments or sedimentary rocks (Zhao et al., 2018). This involves related changes in terms of the structure, texture, composition and sediments involved (Zhao et al., 2018). The changes take place at pressures and temperatures lower than those present for a metamorphic rock (Milliken, 2003).

Alteration is a major process that takes place concurrently with diagenesis as the latter leads to modification of initial pore spaces along with pore space geometry, making this process extremely influential on various petrophysical properties (Moore & Wade, 2013; Milliken, 2003). This may be seen through the modification and re shaping that the sedimentary rock goes through. Early stage diagenesis portrays a history pertaining to an environment from which it stems from (Morad et al., 2000), therefore even early cementation will reflect the incorporation of fluids associated with the depositional environment (Milliken, 2003). This is contrary to diagenesis occurring much later which portrays broader and more external factors such as regional fluid migration and multiple facies intersecting each other (Stonecipher & May, 1990; Land & Macpherson, 1992; Hanor, 1994). The presence of clay minerals has an impeccable influence on sandstones and shales as they tend to have both a physical and chemical influence on these lithologies (Abedi et al., 2012; Bennion et al.,1998).

The reactions involved during the very early stages of diagenesis serve as a basis for the follow up diagenetic trajectory in relation to depth. The presence of clay minerals tend to increase the surface area of sediments due to their very fine grained particle size; they may also change chemical properties of which cation exchange capacity (CEC) is amongst these properties (Ahmad et al., 2018). Sedimentary rocks have an elementary composition that is a factor of a combination of the following; source rock composition, weathering processes including erosion that took place in the source area, transport as well as the immediate and subsequent depositional environment (Lewis & McConchie, 1994). The subsidence of a basin, as well as its depositional history, varies from basin to basin, and therefore the diagenetic history will also vary accordingly (Fadipe, 2012; Samakinde et al., 2016). Other important factors that vary and play a role are provenance, facies, sedimentation rates, geothermal gradients and pore water chemistry (Bjørlykke, 1997). With varying diagenetic history there has remained a mutual predicament with regards to reservoir quality, this predicament being whether clay diagenesis contributes positively or adversely to the quality of sandstone reservoirs. As

a result of this complication, this research has made use of certain methods which aimed to clearly determine the effects of clay diagenesis on petrophysical properties.

The formation of clay is a very delicate process as it deals with very fine grained particles that are present at depth ranges being representative of particular processes (Kerr, 1952). They are associated with the presence of minerals such as silicates, feldspar and micas that are commonly found and altered under the influence of subsurface temperatures and pressures, as well as through weathering (Barton, 2002). Therefore the methods that were used were aimed at showing the type of mineral phases present and crystal structures to highlight the processes that are most likely to have taken place.

The Pletmos basin is dominated by clastic associations of sandstone where shale is more dominant than sandstone. The first borehole in this basin was drilled in 1986 (McMillan et al., 1997). This borehole had a lithology of synrift shallow marine sandstones as well as quartzite basement of Ordovician to Devonian age that produced gas at rates that were potentially commercial (Roux & Soekor, 1997). Few boreholes have been drilled in the Southern Pletmos Basin in the synrift succession and managed to intersect gas saturated sandstones. It is believed that a relatively huge percentage of this gas in the synrift reservoirs has been acquired through the updip migration from early rift shales that are found within the Outeniqua Basin (Roux & Soekor, 1997).

1.2.Thesis Outline

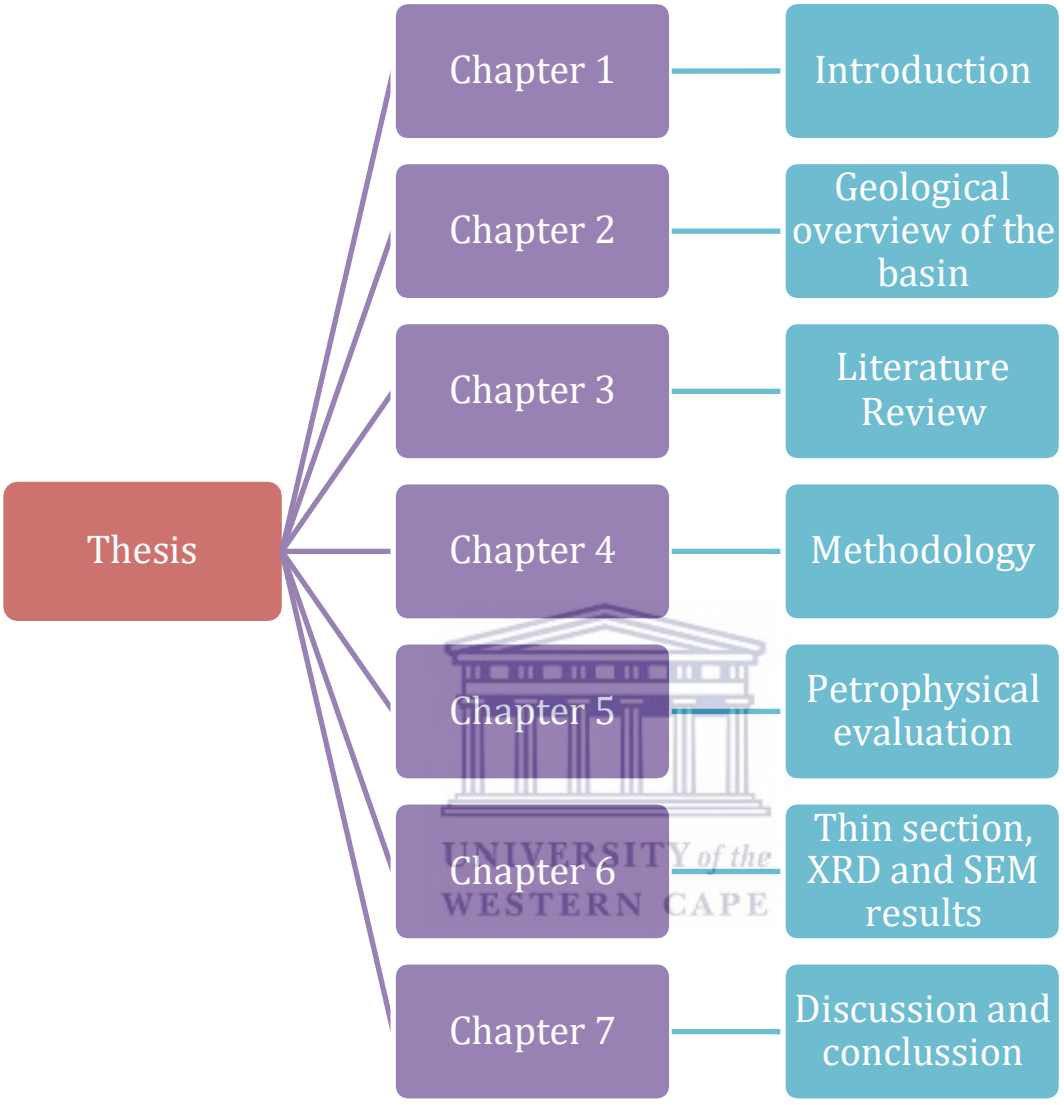

Chapter 1: Comprises the general introduction of the work pertaining to the current study and gives an overall and general synopsis as to what is to be expected from the research. This is where the tone for the research has been set. It is followed by the location of the study area where the country, region, basin, sub- basin and coordinates are stated. Chapter one transcends into the scope of the problem statement, aims and objectives where the bulk significance of the research is routed from. These aims and objectives seek to briefly outline the entire scope of the work that will becovered.

Chapter 2: This chapter covers the geological overview of the basin, basin evolution, tectonic occurrence and sediment deposition of the basin. Within all these four sub- topics, the history of the sedimentary formation is revealed to form a chronological sequence of its evolution all the way to its present form. Therefore, a general synopsis of the structure of the basin, formation tops of the area of interest, the area covered by the basin and the surrounding sub basins are covered in chapter two.

Chapter 3: Literature review of previous work done with regards to the influence of clay diagenesis on petrophysical properties of sandstone reservoirs. In addition to this the chapter covers a break- down of the wireline logs that were used for petrophysical evaluation.

Chapter 4: Covers the methodology flowchart as well as the step to step description used to carry out the method.

Chapter 5: This chapter focused on the petrophysical evaluation of sandstone reservoirs where the primary parameters of interest such as the volume of clay, porosity, permeability and water saturation were calculated. The calculated parameters were also calibrated with available core data.

Chapter 6: This chapter presented the petrography results. Each sample under thin section was analysed for minerals present and properties of those minerals as well as the relationship between 1.) Minerals and petrophysical properties, 2.) Minerals in relation to each other, 3.) Petrophysical properties in relation to each other.

XRD results were presented for quantitative analysis to determine mineral phases present along with the abundance of each mineral

The SEM was accompanied by EDS results and were used concurrently for the contribution to the overall petrographic analysis (chapter 6). Similar to thin section, each sample is analysed for minerals present and properties of those minerals as well as relationship between 1.)Minerals and petrophysical properties, 2.)Minerals in relation to each other, 3.)Petrophysical properties in relation to each other

Chapter 7: The overall discussion and conclusion of the thesis

1.3. Location of the study area

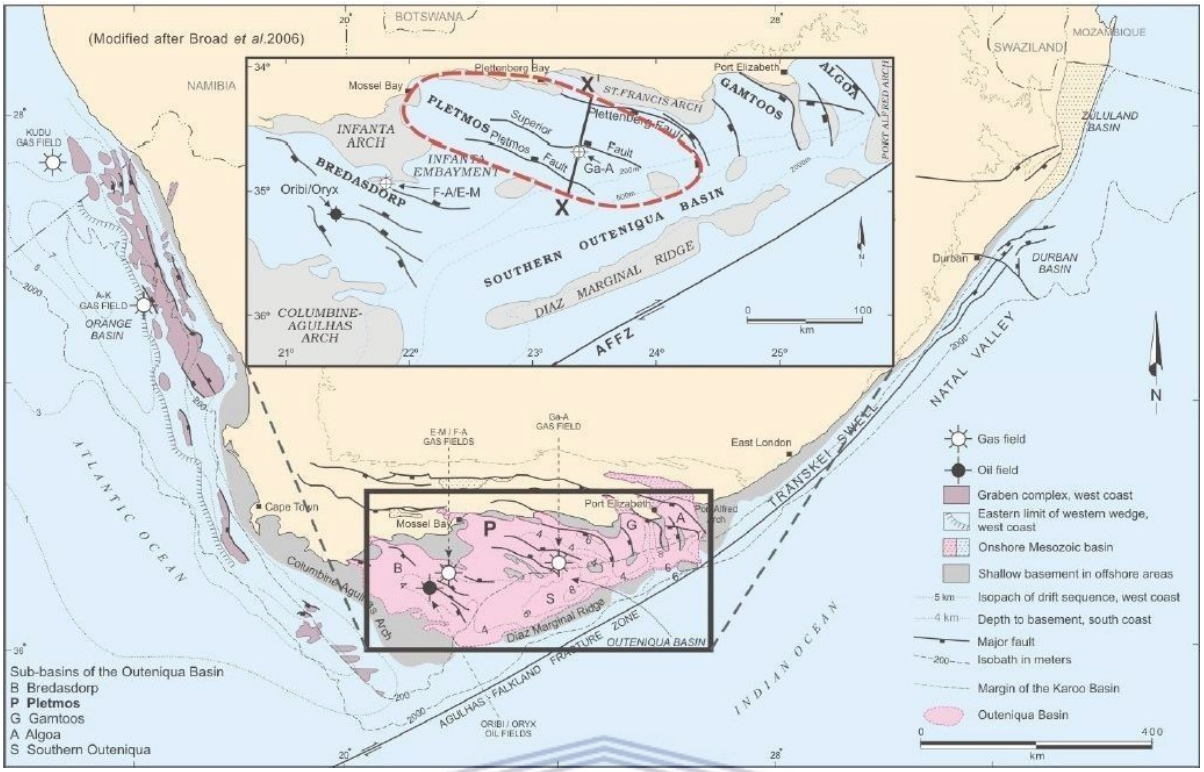

Figure 1. 1: Pletmos Basin within the Southern Outeniqua Basin, modified after (Broad et al., 2006).

Well Ga- Q1, Ga-Q2, Ga-Z1 and Ga-E2 are located in the Southern Pletmos Basin (Figure 1.1) within the Outeniqua Basin, offshore South Africa (Brown et al., 1996). The exact location of these wells accompanied with other well specifics are shown in Table 1.1.

The Outeniqua Basin is located on the southernmost tip of Africa (McMillan et al., 1997). Contained in this basin is a sequence of rift basins which are the Bredasdorp, Pletmos, Gamtoos and Algoa sub-basins (McMillan et al., 1997) in order of location from west to east. These meta-sediment basins are of Ordovician to Devonian age and are part of the Cape Supergroup in the form of divided fault-bounded basement arches. The Cape Fold Belt is most likely to be the cause of formation of the arcuate trend of the basin bounding fault systems (De Swardt & Maclachlan, 1982).

The Pletmos Basin is an offshore extension comprising of a sequence of basins that are small in size extending from Worcester through to Robertson, Swellendam, Heidelberg and Mosselbay (Visser, 1998). Pletmos Basin covers a total area of 18 000 km2 (Brown et al., 1996, Brown et al., 2006).

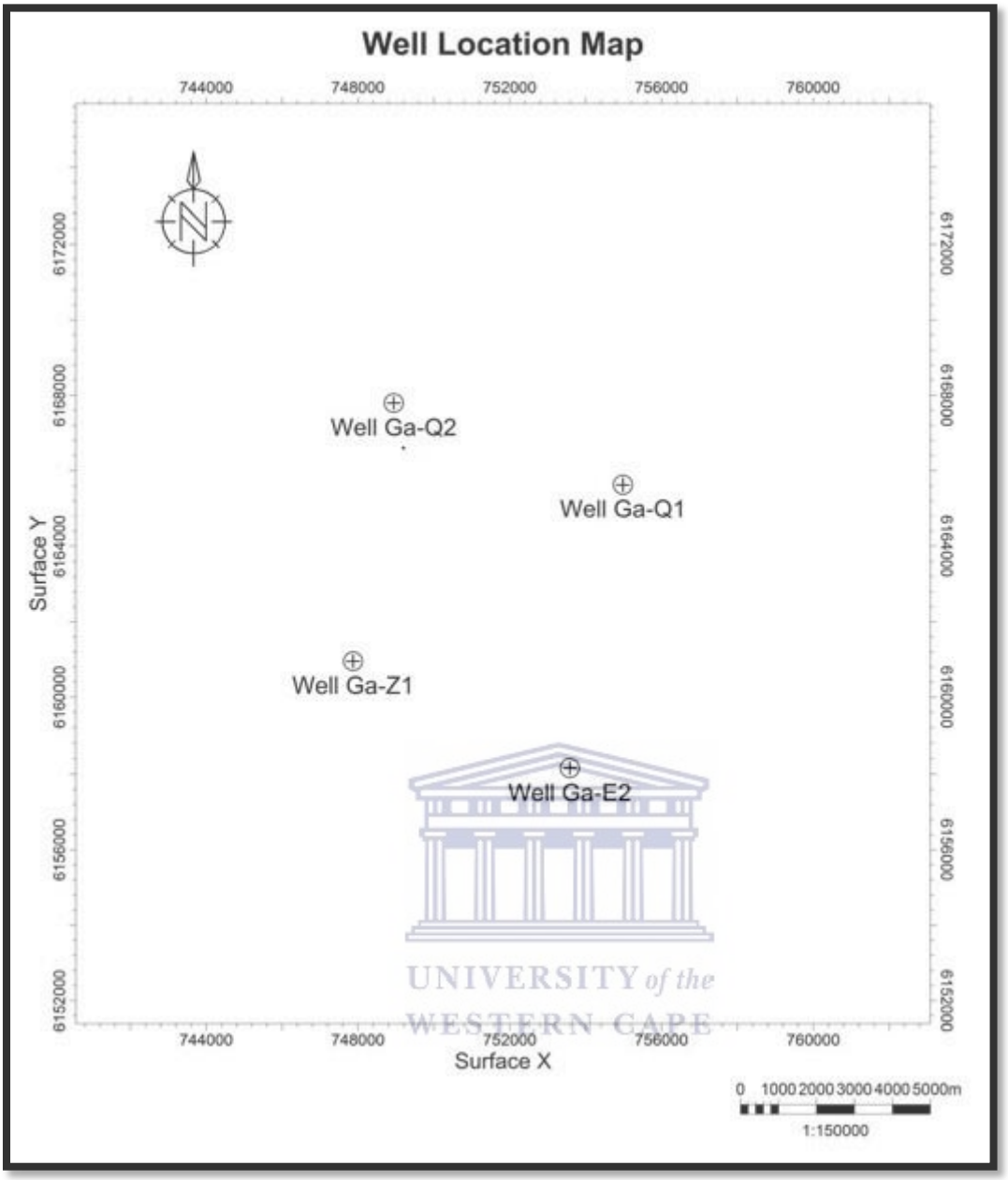

Figure 1. 2: Well location map of 4 wells

Table 1. 1: Well Specifics

	Well Ga-Q1	Well Ga-Q2	Well Ga-Z1	Well Ga-E2
Well Classification	Wildcat	Wildcat	Wildcat	New Filed Exploratory
Trap Classification	Faulted Dome	Faulted Dome	Stratigraphic	Closure against fault
Location	70km SSE of Plettenberg Bay, offshore South Africa	152km SE of Mossel Bay, offshore South Africa	75km SSE of Plettenberg Bay, offshore South Africa	75 km SSW of Plettenberg Bay
Co-ordinates	34° 37' 10,00" S 23° 46' 53,60" E	34° 36' 05,2" S 23° 42' 54" E	34° 39' 45,99" S 23° 42' 19,68" E	23° 46' 06,742"E 34° 41' 13,552" S
Water depth	124m	121m	132m	126,8m
Total depth drilled	3249m (Driller) 3243m (Wireline)	3180m (Driller) 3177m (Wireline)	3200m	4396,43m

1.4. Problem Statement

The lithology of the southern Pletmos Basin varies from dominantly organic rich shales to marine sandstones and claystones. Segments of this formation are found in the form of interbedded calcareous sandstones and marls (PASA, 2018). The basin is considered to be prospective due to its good potential of gas and oil reserves (PASA, 2018).

The mapping and evaluation for this basin was previously done by both Roux & Soekor (1997) and Ranger U.K Limited (2000) and showed that there is sufficient potential in the offshore Pletmos Basin in water depths exceeding 300 metres. Further mapping has been done, known as prospect mapping which indicates the presence of structures that are untested, domal in shape and are large in size (Roux and Soekor, 1997). Oil and gas are expected to be found in the deep marine fans which have been developed in the drift succession. The expectation of these fans is that they contain reservoir sandstones that are of good quality and that are similar to some of the intersected sandstones in the Bredasdorp Basin to the west (Brown et al., 1996). The Pletmos Basin remains a location of much interest in terms of gas and oil exploration, however, because of its high clay content, it proves to be problematic for the commencement of exploration. The effect of the clay present is not well understood, and this study seeks to find the influence that clay minerals have on the promising sandstone reservoirs.

1.5. Aims and Objectives

The aim of this study was to investigate the effect of clay diagenesis on the petrophysical properties of sandstone reservoirs of the selected wells in the Southern Pletmos Basin using core and geophysical wireline log data.

This was achieved by integrating the following methods: Petrography studies (thin section, SEM (Scanning Electron Microscope) accompanied by EDS (Energy Dispersive Spectroscopy) and XRD (X-Ray Diffraction)) and petrophysical evaluation for modelling and interpretation using wireline logs and core data. Interactive petrophysics 4.2 version was used extensively throughout the petrophysical studies. The following objectives were fulfilled to achieve the aim.

- Identify the reservoir zones by making use of the gamma ray and density logs, as well as facies.
- Calculate the clay volume from gamma ray log using linear method.
- Calculate porosity from porosity logs (density, neutron and sonic).
- Calculate water saturation from Indonesia and Simandoux equation.
- Calibration of petrophysical properties (porosity, permeability and water saturation) from wireline logs with core data to validate the logs generated from IP software.
- Evaluate thin section slides of core samples under microscope in order to identify mineralogy, morphology of the minerals and porosity.
- Determine the phases of the minerals present using XRD.
- Determine the exact composition and relative abundance of elements and compounds from EDS in relation to a specific area corresponding to the SEM image.

CHAPTER 2: GEOLOGICAL BACKGROUND OF PLETMOS BASIN

2.1. Geological overview of the basin

A sequence of northwest striking faults such as the Plettenberg, Superior and Pletmos faults led to the sub-division of the Pletmos Basin into half- grabens. Commencement of rifting and half- graben formation was during the Mesozoic Era (Dingle et al., 1983). These half- grabens manifest themselves into different tectonic and sedimentary histories (Bate et al., 1992). The Pletmos Basin Mesozoic half graben covers an area of approximately 12 500km2 (Bate et al., 1992). The local depocentres have a sedimentary thickness reaching 11 000 m, these are located adjacent to the basin boundary faults (McMillan et al., 1997).The late Jurassic period was also characterised by negative inversion, this may be seen along the Late Proterozoic and Palaeozoic thrust zones, as it led to the formation of Port Elizabeth, Gamtoos and Plettenberg faults amongst other basin bounding fault zones (Nicolaysen, 1985; De Wit and Ransome 1991; Gresse et al., 1992).

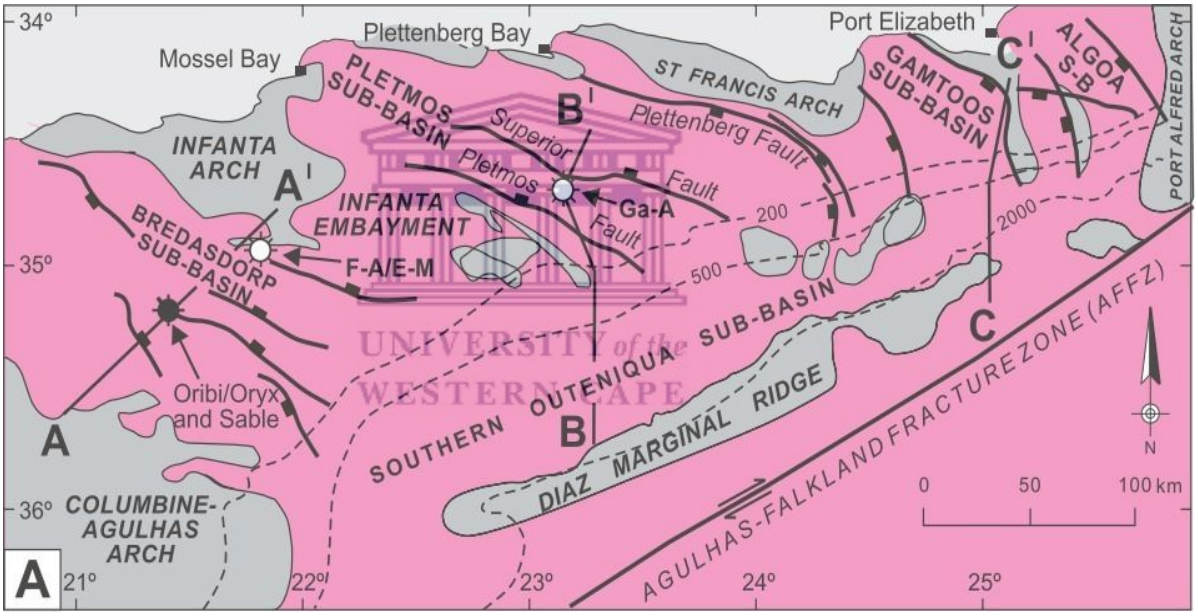

Figure 2. 1: Pletmos Basin in Southern Outeniqua basin (Broad et al., 2006).

The Southern part of the Outeniqua Basin denotes the outer part of the area affected by geological activity below the 300m isobaths. It is connected to the western part of the Columbine- Algulhas Arch, to the eastern part of the Port Alfred Arch and is bounded to the south through the Diaz Marginal Ridge (Ben- Avraham et al., 1993, 1997; Broad et al., 2006) as seen in Figure 2.1. The Mesozoic sediments characteristic of this area have a thickness of approximately 8000m. The Diaz Marginal Ridge (Figure 2.1) is characterised by its non- magnetic, stratified basement feature which is most likely to be of continental origin, trending sub- parallel to, and is truncated by the AFFZ (Ben- Avraham et al., 1993, 1997; Broad et al., 2006)

2.2. Basin evolution

The early graben fill in the Pletmos Basin primarily consists of synrift 1 sediments which date back to the late Jurassic (Kimmeridgian stage) time frame, however in deeper and unexplored sections are areas that date back to a period between 157 and 155 million years ago. In areas where intersected, synrift 1 sediments in the south consists of marginal marine sandstones and in the north consist of thick aggradational fluvial sediments (Broad et al., 2006). The overall formation tops constituting the identified reservoirs in this study are 1At1, 12At1, 17At1, 22At1, O and i. The ages of the reservoirs are enclosed in red polygons in Figure 2.2 where the stratigraphy of Pletmos Basin is displayed. From the image delineating the stratigraphy of Pletmos Basin it is evident that the main depositional environment influences are that of regressive cycles in response to tectonic and eustatic influences. In addition to this were some shelf to deep marine deposits upon formation.

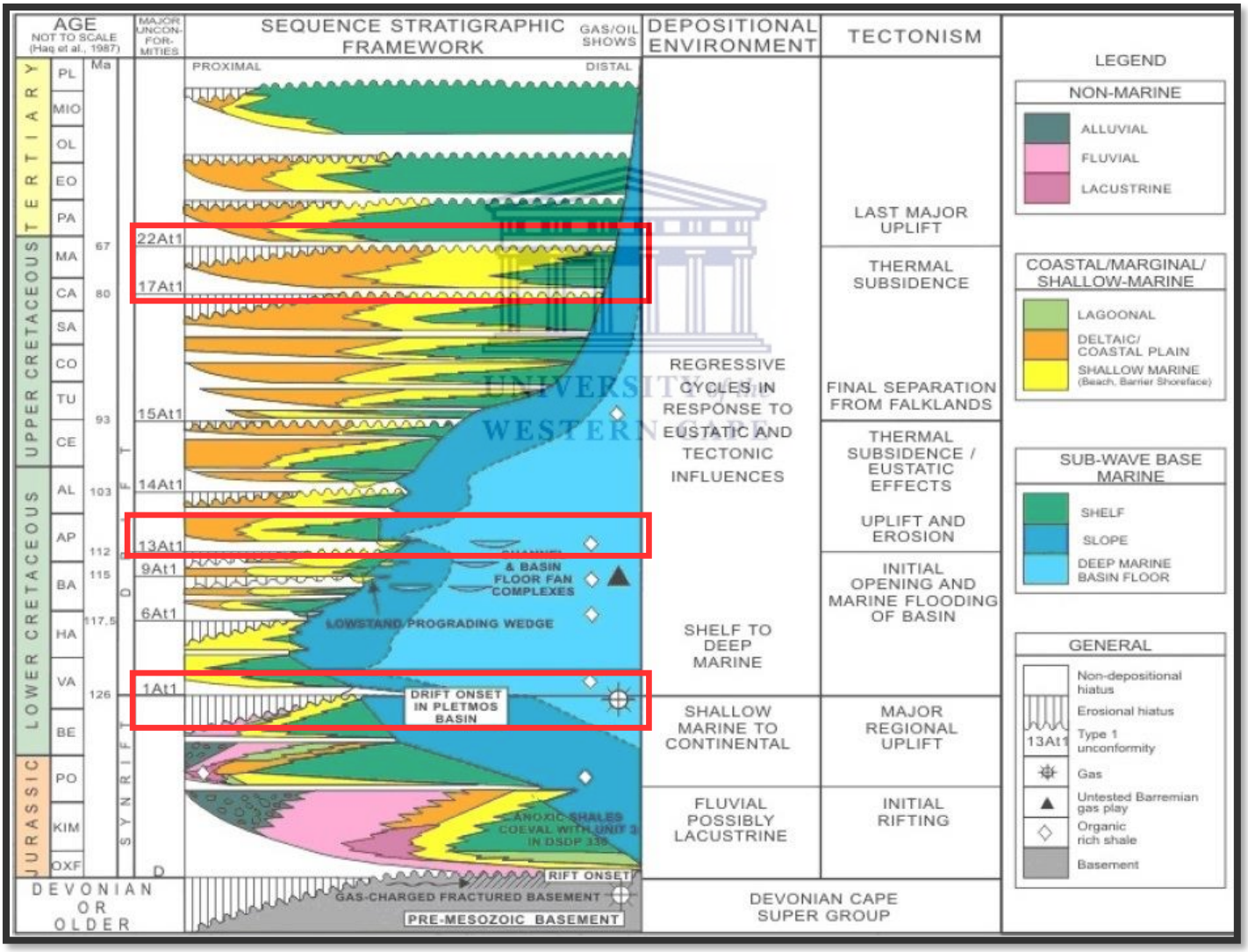

Figure 2. 2: Chronostratigraphy of the Pletmos Basin (after McMillan et al., 1997) with the stratigraphic ages adjusted as per the International Commission on Stratigraphy (Cohen et al., 2013; updated)

The synrift 1 interval in the south (Portlandian to Valanginian) is made up of shallow marine, fluvial and shelf deposits that originally came from the southwest and northwest margins of the basin (Broad et al., 2006). The horizon unconformity which is to be found directly above it was previously known as the drift- onset unconformity. In terms of comparison and analogy with its neighbouring basin viz. Bredasdorp, it indicates that it also marks the beginning of the transform movement of the AFFZ (Agulhas- Falkland Fracture Zone) as well as the beginning of synrift 2; the second phase of rifting. This subsequent rifting phase was similar to the initial one as it was also extensional but to a lesser degree (Bate et al., 1992), this led to the initiation of the separation between South Africa and South America (Norton and Sclater, 1979; Dingle et al., 1983). This separation is marked by the AFFZ, this transform boundary ultimately led to the formation of oceanic crust (Martin et al.,1982).

Deep marine and poorly oxygenated conditions within the Pletmos Basin as well as other nearby basins was a result of major subsidence of the Outeniqua basin which took place after the transform-onset unconformity. Sequences contained within the synrift 2 deposition consists of aggradational deep- marine claystones along with thin turbidites , within them are shales rich in organic matter making them significant petroleum source rocks (Broad et al., 2006)

2.3. Tectonic occurrence and Sedimentation formation of the basin

The beginning of rifting occurrence in the Pletmos Basin was during the middle-late Jurassic period. This rifting occurrence resulted in a dextral transtensional stress exerted on the Aghulas fracture zone towards the north, this led to the initiation of normal faulting along the northwest-southeast striking Plettenberg, Superior, and Pletmos fault systems (McMillan et al., 1997). There was a continuation of normal faulting as well as synrift deposition until approximately 126 million years ago, this was when the majority of the extensional faulting and synrift deposition had come to a halt, of which this halt was accompanied by the initiation of postrift tectonics, erosion as well as deposition (Bate et al., 1992).

The subaerial erosion of a second order drift onset conformity of approximately 126 million years old was enhanced by a widespread upliftment north of the Agulhas-Falkland Fracture Zone. Following this event was the deposition of the first postrift supercycle (taking place between 126 and 115 million years ago) which was localized in the Plettenberg Basin. In the Plettenberg Basin the fault subsidence remained as the main tectonic control on sedimentation. Approximately 117 million years ago transpressional upliftment took place. The geohistory curve resulted in clockwise rotation of the former rift system, enhanced basement anticlines as well as the termination of the second order unconformity (Broad et al., 2006).

Between 117.5 and 112 million years ago a second post rift supercycle was formed as a result of initial rapid subsidence, this subsidence was later accompanied by diminished subsidence rates which are speculated to have been caused by renewed transpressional stress of this time period. This stress is most likely to have been the cause of the Pletmos Basin being locked and thus reduced subsidence for approximately 4 million years (between 116 and 112 million years ago). This led to conditions that allowed the deposition of 33 well-developed fourth-order simple sequences. Approximately 112 million years ago was the marking of the end of this cycle along with the last movement of the Falkland Plateau towards the west past the Agulhas Platform and thus allowing the proto-Indian and proto-South Atlantic Ocean to be combined. This event led to extensive uplift and subaerial erosion of the second order unconformity in the region of the fracture zone towards the north. The southernmost part of Africa was cleared by the Falkland Plateau, this clearance was followed by released external stresses as well as thermally driven subsidence which began to dominate the Pletmos Basin (Broad et al., 2006).

CHAPTER 3: LITERATURE REVIEW

3.1. Literature Review

The Outeniqua Basin has a stratigraphic succession that can be correlated in terms of age to the majority of the basins that are found East of Africa. The correlation between the Outeniqua Basin and the basins of East Africa is quite minimal as it ends with the age of the basins being the common factor. The South Outeniqua compared to East African basins such as those forming part of Kenya, Mozambique, Uganda and Tanzania has more geological features and properties that are more suitable for oil and gas exploration. The South Outeniqua Basin is one of the building blocks that form the intra- cratonic rift basin (Moses, 2000).

Several publications (Adie, 1952; Brown, 1995; Roberts & Bally, 2012) suggest that the South Outeniqua as well as the Falklands Graben, situated offshore of South America, are part of the South Outeniqua Basin; therefore they are coeval to each other and have similar geological structures and lithologies representing a syn- Gondwana and post Gondwana evolution (Stanca et al., 2019; Thomson, 1998; Broad at al., 2012). In addition to this, studies carried out by Curtis & Hyam (1998) suggest that the Falklands were connected to the eastern part of the Cape Fold Belt of South Africa. Southwestern Gondwana was comprised of continental lithosphere of both Southern America as well as Southern Africa, this part of Gondwana was mainly assembled towards the end.

Recent research on the diagenesis of clay minerals has proven to be progressive especially towards reaching a feasible explanation regarding the formation process leading to the exhibition of argillaceous and arenaceous lithologies that show alteration on both small and large scale formations (Jeans, 1989).

Previous work conducted by Fadipe (2012) in the Bredarsdorp Basin which is an adjacent basin and an analog to the study area had a focal section pertaining to diagenetic processes and its influence on porosity and permeability. Fadipe (2012) noticed that diagenetic processes are multi influential as they can contribute to the preservation, creation or destructing of both porosity and permeability. Although multiple minerals were identified, the primary pore and permeability destructing minerals were found to be quartz and kaolinite with accessory mica; this was revealed through multi-mineral analysis. Within the study conducted, the low-porosity was attributed to increased temperature as this led to the formation of kaolinite. The identified kaolinites were of the following nature; 1) inter-grain kaolinite as they neoformed between expanded mica flakes, 2) vermiform kaolinite and 3) kaolinite forming part of the matrix in the form of euhedral kaolinite crystals.

In another study focusing on a different analog i.e. Orange Basin, was conducted by Samakinde et al., (2016), it presents quartz, calcite, montmorillonite, mixed clays and illite as the primary detrimental contributions to porosity and permeability of the wells. The methods incorporated in the study were petrographic and geochemical studies which were carried out on the selected core samples. In addition to the primary minerals mentioned above that had detrimental repercussions, XRD studies show the presence of albite, siderite, calcite and halite as additional cementing minerals. Further studies carried out by Ruhovets & Fertl (1982) and Kamel & Mohamed (2006) also conclude that the presence of clay minerals contributing to the shaly lithology of rock formations lead to severe repercussions that primarily reduce the effective porosity, total porosity as well as the permeability within the identified reservoirs of their study. In addition to this Shedid et al., (1998), Shedid (2001) and Shedid-Elgaghah et al., (2001) have observed that the presence of clay lead to uncertainties in estimating hydrocarbon reserves, reservoir characterisation as well as conventional estimation of hydrocarbon reserves. Studies addressing the topic pertaining to the effect of clay diagenesis have been carried out in both Bredasdorp and Orange Basin amongst other basins which have paved the way for this topics to be studied in the Pletmos Basin.

In some cases where both petrographic and XRD analyses have been conducted in order to further understand diagenetic processes of clay, these analysis' have resulted in a contradiction between the results of the 2 separate analysis. According to Jeans (1989), petrographic studies carried out in sandstones usually exhibit evidence of neoformation and these neoformed clays in sandstones precipitated due to the pore fluids present at the time, this process also applies to the cement which serves as a lining around the pores. On the other hand, XRD analysis that was carried out on the US Gulf Coast on mudstones found deep below the earth's surface implies that the paramount process was that of a transformational hypothesis and implies that the structure of current clay minerals were inherited from pre-existing mineral structures. The hypothesis by Hower et al., (1976) has been recognized and acknowledged throughout the geology community. It was however rejected by some that are accustomed to working with alternating arenaceous/ argillaceous lithology types and their variations. The problem reached with these conclusions is the sole reliance of the results based on a single method applied i.e. neoformation as a result of petrographic studies and transformation as a result of XRD analysis conducted. The results of these separate analysis, therefore, depict a contradiction as they do not lead to the same process clarifying the genesis of the clay minerals. This has led to the question posed on whether it is possible or rather likely that there is more than one process in charge of diagenesis of clay minerals in both lithologies of mudstones and sandstones; even though the clay mineral content of the two lithologies depict resembling patterns of variations (Jeans, 1989).

The proof supplied from a large number of techniques further implies that the transformation hypothesis from XRD analysis is an over-reliance, not because of any faults within the analysis, but as a result of it being done solely and in the absence of other experiments which would increase its reliance. Therefore, it would be beneficial to conduct this analysis in conjunction with other methods that would provide results that are in support of this hypothesis for further validation. It is also speculated that the transformation from smectite to illite that is observed (through XRD) in burial diagenesis in the majority of mudrocks is not necessarily as a result of transformation and that the change could be an outcome of the dissolution of smectite particles as well as neoformation of illite crystals, provided that the composition of the pore fluid is favourable for illite crystals to form (Jeans, 1989).

The investigation of the effect of shale and clay mineral diagenesis on sandstone reservoirs containing hydrocarbons has proven to be partially troublesome because of the obstacles encountered thus far. There is a high possibility of finding these minerals in the structure of clasts, shale laminae as well as dispersed shale matrix. Clay minerals are also commonly present as authigenic/diagenetic clays which have formed within the sandstone. These include pore-filling kaolinite, pore-lining chlorite and pore-bridging illite (Wilson & Pittman 1977).

Studies conducted on the effect of clay diagenesis by Nadeau (1998) through the use of core analysis only faced some challenges such as 1. Being able to identify and precisely quantify the amount of clay content present, 2. Sample heterogeneity, 3. The manner in which they are spread out in the reservoir as well as the types found in the various areas they are spread out in, 4. The contamination caused by the drilling mud that the minerals are highly susceptible to including invasion damage, 5. Hydrocarbon procedures as well as conventional drying methods that lead to wettability, and 6. Clay microstructures that have been altered. The above-mentioned problems encountered contribute to making it almost impossible to segregate the effect of clay diagenesis as a function the clay content without the surrounding factors. This is especially heightened when it comes to minerals formed in sandstone following the deposition period and simultaneously present a huge impact on the rock properties regardless of the very low contents of diagenetic clays. This is particularly true for illite and smectite as they are amongst the most commonly encountered diagenetic clays (Nadeau,1998).

Studies previously conducted by Bill et al., (1988), McHardy et al., (1982) and Pallatt et al., (1984) were primarily focused on the mixed-layered illite-smectite and illite which occurred separately shows that the amount of diagenetic clay present is not a controlling factor because even when there is a limited quantity of the clays present there is still an enormous reduction in the porosity and permeability of

the sandstones. It was also deduced that there is a significant chance of collapse when the core samples are being air dried because of the delicate physical arrangement of the clay; and lastly, consideration needs to be taken towards the fact that the effects tend to be overlooked by conventional core analysis methods (Nadeau, 1998).

It is these factors that inspired (Nadeau, 1998) to produce an experimental solution that was aimed at alienating the problematic factors of the core based studies. Therefore the petrophysical research created with the goal of avoiding any deviation to the topic at present and to directly (without the effects that are of no interest to the study that is difficult to isolate) resolve the diagenetic effect of clays by making use of hydrothermal mineral reactions in sandstone that have been fabricated.

The methods incorporated for the study of the synthetic sands were XRD (x-ray diffraction), EMP (electron microprobe), ED (electron diffraction) and SEM (scanning electron microscope). The findings of the experiment reveal that very small amounts of clay; amounts less than 5wt% of smectite clay have an enormous effect on the permeability as they resulted in a significant decrease in the permeability. This reduction in permeability was found to inevitably be of direct relation to the physical structure of the microporous clay cement; this physical structure also referred to as the clay morphology collapses once exposed to air drying. It was also deduced that the processes involved in conventional sample preparation may contribute to adverse effects such as creating smectite along the lining of the pores in these synthetic sand reservoirs. The core analysis derived from conventional core samples consisting of smectite most likely does not serve as a good example in depicting reservoir properties of the subsurface (Nadeau, 1998). The work of Nadeau (1998) led to the conclusion that experimental petrophysics may serve as one of the most useful methods put in place for resolving the diagenetic clay effects on sandstone reservoirs as this method eliminates a lot of bias and discrepancies that are inevitably found in the sandstone reservoirs.

Diagenetic processes can be classified into two types of diagenesis; namely eodiagenesis and mesodiagenesis, which is also widely known as burial diagenesis. The first being the genesis of the two as it takes place during the very initial stages of the digenetic cycle of burial. Eodiagenesis can be further explained by splitting it up into two categories, the first being one where the burial of the sediments takes place at slightly shallow depths which are less than 2000m, these depths also correlate to temperatures that are less than 70 degrees Celsius (Morad et al., 2000). The second explanation being the processes that take place when oxygenated water is easily accessible to the subsurface sediments (Worden & Burley, 2003). The contrast in definitions of eodiagenesis is not of the utmost importance in this study because significant alteration and cementation are most likely to

take place when diagenesis occurs in temperatures exceeding 70 degrees Celsius which is more likely to occur at deeper depths, during mesodiagenesis.

Work carried out by Bjørlykke (1997) shows that in order for pore water to remain in its stable state that is ideal for the presence of kaolinite, there needs to be a removal of the potassium and silica content, only when this happens can the dissolution of feldspars and the precipitation of kaolinite take place. The pore water is required to have a low ratio of K+: H+. A study (Bjørlykke, 1997) carried out in the North Sea Basin shows the presence of carbonate content, the state of balance between the pore water and calcite, and the great amount of influence that carbon dioxide has on the pH.

The buffering capacity of clay minerals is directly proportional with an increase in depth, especially depths that are => 3km, and reaches its peak buffer capacity between 3 and 4km. Organic acids are characterised by buffering capacities that are less than that of silica and carbonate systems and thus have minimum influence on the PH (Hutcheon et al., 1993). The stability environment for kaolinite is disturbed when there are some potassium feldspars because the ratio of K+: H+ of the pore fluid will be too much. This stability environment is further disturbed upon the dissolution of more potassium feldspars and micas as there is a further increase in the potassium content in the fluid. This process of dissolution continues until there is no more potassium and the reaction ends, as this is usually the only means by which potassium is depleted. The bulk of the mineralogy of the North Sea sandstone reservoirs that have formerly been identified as kaolinite has been misidentified as it is actually dickite. This is because at depths reaching between 2 and 3 km the clay mineral commonly misidentified as kaolinite is dickite (Ehrenberg et al., 1993). The transformation of this kaolinite clay mineral to dickite at these depths is not well understood and thus needs further studies in order to determine the factors involved. Bjørlykke (1997) suggests that the kaolinites found in shales have a high probability of being clastic but knows that it is hard to prove on account of the compaction they have undergone which in turn has destroyed the primary textures that were present before compaction. Mudstones, however, have relatively low porosity and permeability and are therefore not susceptible to the flow of meteoric water.

Authigenic illite is uniquely characterised by its fibrous pore filling structure which explains why its presence leads to an immense reduction in permeability in sandstone reservoirs. When making use of XRD analysis for the quantification of authigenic illite it proves to be a problematic task. This is because of the interference caused by the clastic illite as well as the mica. The northern parts of the North Sea (Giles et al., 1992; Bjørlykke & Aagard 1992) and the Haltenbanken (Bjørlykke et al., 1986; Ehrenberg & Nadeau, 1989) reflect a substantial increment in the illite content relative to that of kaolinite in depths ranging from 3.7 km to 4 km. However, in North Sea Mesozoic reservoir sandstones that are

found at depths less than 3.5 km, it has been observed through SEM and thin section that there is a limited amount of pore filling illite. In these environments it is mostly found that the pore water chemistry coincides with that of the stability required for illite, the problem lies with the precipitation kinetic rate which is low and it occurs at temperatures ranging from less than 120 degrees Celsius to approximately 140 degrees Celsius. When authigenic illites are found in great concentrations they tend to be affiliated with the process whereby unstable aluminous mineral phases go through dissolution, this unstable aluminous mineral being kaolinite. In addition to kaolinite, smectite serves as another example of a good precursor mineral of illite. Smectite is however found in much smaller quantities at low depths less than 2km thus advocating for a low primary smectite content in Mesozoic sandstones. In spite of this low content, tertiary sandstones are more likely to contain higher contents of smectite. The following are good examples of various ways that lead to the formation of illite (Bjørlykke, 1998).

Smectite + K § = illite + silica (via mixed-layer minerals) (1) A12SiOs(OH)4 + KAISi308 = Kaolinite K-feldspar KA13Si3Olo(OH)2 + 2SIO2 + H20 (2a) Illite Quartz

3A12Si2Os(OH)4 + 2KA1Si308 + 2Na + = Kaolinite K-feldspar 2KA13Si301o(OH)2 + 2NaA1Si308 + 2H + 3H20 (2b) Illite Albite

(Bjørlykke, 1998).

A thermodynamic drive is an important factor needed for reactions that are of a diagenetic nature, this ensures the stability of the precipitated minerals to be more than that of the dissolved minerals. Hydrous minerals including kaolinite, gibbsite and smectite tend to form at low temperatures corresponding with low depths, of which meteoric water flow influences the initial phase of diagenesis of the hydrous minerals, and therefore these hydrous minerals may form through weathering or through early diagenetic processes. Another way of viewing these diagenetic processes is to think of them as a continuation to weathering regardless of whether the pore water is reducing or oxidising (Bjørlykke, 1997).

The following is the overall reaction:

Rock (feldspar, mica) + water = clay + cations.

These minerals become unstable at greater burial depth and higher temperatures and this reaction is often referred to as reversed weathering:

clay (kaolinite, smectite) + cations (K +) = aluminosilicate (illite) + quartz + water.

(Modified by Velde, 1995)

The sandstone reservoirs in the North Sea and Haltenbanken of similar age to sandstones of this study Mesozoic has been the fundamental focus in this study conducted by Bjørlykke, 1997. The minerals of fundamental concern being feldspar and micas are found to not be stable in the subsurface where they are close to weathering processes as they have a higher chance of being exposed to meteoric water containing low ionic strength. These minerals are stable in environments that are of much higher temperatures and with lower flow rates which are found during burial diagenesis. It is of common knowledge that the feldspars contained in arkose are initially exposed to greenschist facies or higher grades of metamorphism. Certain clay mineral reactions such as the precipitation of illite are possible at deeper depths and higher temperatures but require the preceding formation of unstable clays at shallower depths, clays such as kaolinite and smectite. When dealing with reservoirs that are very well sorted, there is a great possibility that the bulk clay minerals are authigenic and the diagenetic processes control the distribution of the clays (Bjørlykke, 1997).

3.1.1. Wireline logging

Well logs measure and record data primarily relating to petrophysical properties and do so in correlation to depth. This process is used widely by oil and gas companies and was discovered less than a century ago by Marcel and Conrad Schlumberger in 1927. It was initially referred to as electrical coring. Since its discovery, it has made a booming effect in the industry and has ever since been further developed in order to suit the different needs of companies (Serra,1983).

The logging tools form part of a connected system whereby one end of the wireline attached to an electronic system embarks on its logging journey to the subsurface, this end is located inside a vehicle stationed at the surface where it is both controlled and monitored by a wireline operator. The wireline that is attached to the electronic system in a vehicle on the surface is hauled past the winch which is responsible for manoeuvring the wireline log so that it may be transported back and forth between the surface and subsurface.

One of the tools necessary for this system is the sonde which is attached to the other end of the wireline and is the part that enters the subsurface first. It serves as the tool where outgoing energy stems from it or as a recipient of incoming energy i.e. it serves as the sensor of the system. In addition to this, there is a cartridge which is responsible for the conversion of data as it is recorded state when drilling to a more ideal configuration for transmission of data to the surface.

The force driving the trajectory of the cable downwards is gravity. The smoother the well under operation the easier it is for the cable to make its travel all the way to the bottom (Crain, 2018). However, there are assistive alternatives for wells that are slightly more troublesome and not as

smooth as well as horizontal wells; these include making use of machinery such as a wireline tractor and a well stroker (Kruger, 2007).

As a result of borehole measurements not taking place in the most ideal system as the associations of exploring in the subsurface of nature can only be controlled to a certain extent. The surrounding and involved parameters that cannot be controlled during the time of drilling are measured in their original state and are referred to as “apparent properties”, whereas the processed parameters that exclude surrounding environmental factors are referred to as “true rock properties”. These factors constituting the inhomogeneous environment include the effects of borehole and caliper, invaded zone, layers surrounding the measured section, dip of layers etc. (Schön, 2015)

The principle of wireline logging can be seen in the simplified version in Figure 3.1 as well as the expanded version in Figure 3.2.

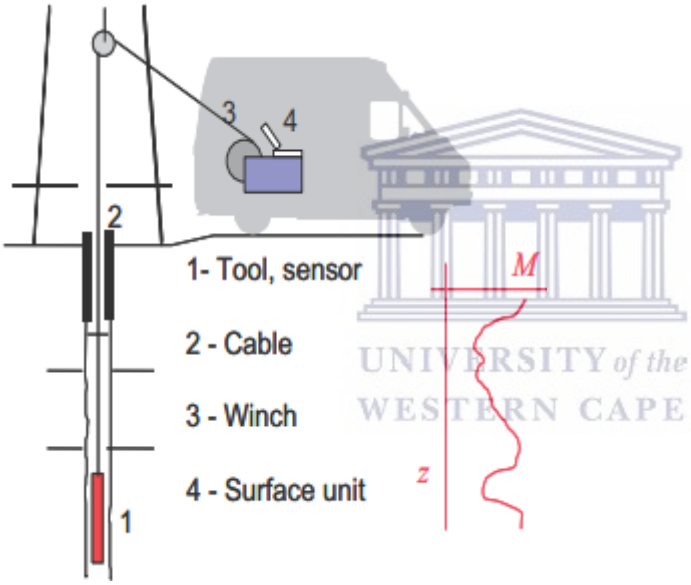

Figure 3. 1: The logging unit principle simplified (Schön, 2015)

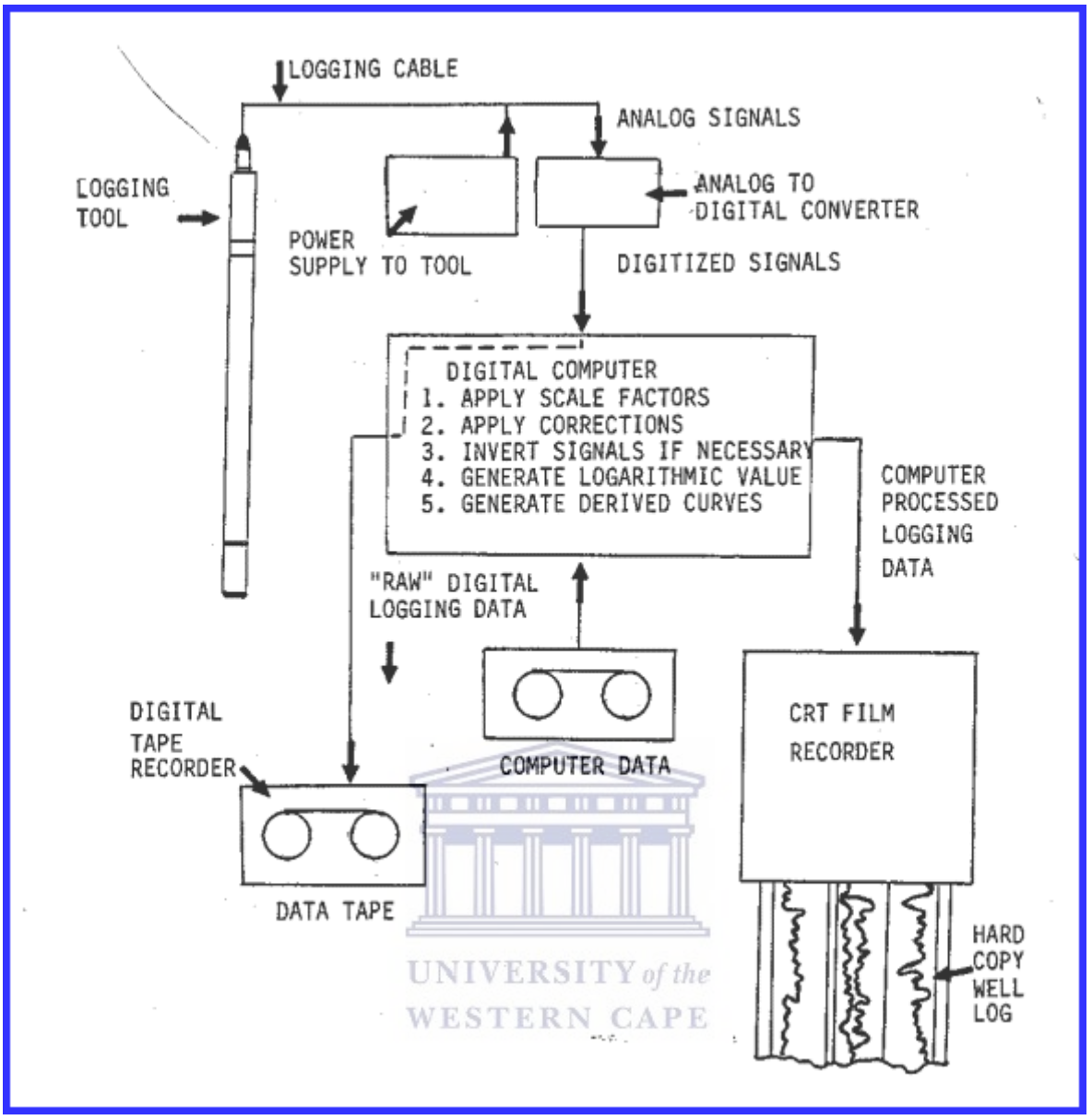

Figure 3. 2: The logging unit principle expanded (Crain, 2018)

Caliper tools

These tools are useful for the measurement of both the shape and size of the hole. The mechanical calliper takes measurements of the variations in borehole diameter with increasing depths. The mechanical calliper has two articulated arms which are pushed against the borehole hole, these arms are linked towards the cursor of the variable resistance. The electrical output is a result of the lateral movement of the arms that are translated into movements of the cursor along the resistance.

Gamma ray logs

The primary application of gamma ray logs is to measure the amount of gamma radiation which is usually detected in naturally occurring uranium, thorium and potassium in various lithologies. The simple version of this log conveys the radioactivity of all three elements combined together. The gamma ray logs are used for characterising the rock or sediment in a borehole by measuring the naturally occurring gamma radiation. Varying rock types emit different gamma radiation spectra. This difference in radioactivity between the different lithologies allows the gamma ray logging tool to distinguish between the lithologies.

The process of acquiring the measurements is carried through the initial lowering of the instrumentation down the hole and recording the gamma ray values within the various depths. This log is smaller in terms of diameter of the borehole as a result of properties such as the borehole being filled by the fluid (Rider & Kennedy, 2002).

Sonic/ Acoustic Log

This log depicts a measurement pertaining to the interval transit time of a formation, i.e. how much the formation is able to transmit sound waves, its capacity to transmit sound waves is influenced by the lithology, rock texture and porosity. This log is a quantitative measurement and is used for the evaluation of porosity in logs filled with liquid. The amount of time it takes the acoustic energy to travel the distance between transmitter and receiver is significantly longer when it is travelling through fluid filled pore spaces; therefore decreased velocity corresponds to high porosity. A combination of the rock matrix, pore lining rock constituents as well as fluid in pore spaces is a good indication of the travel time. There are two factors, namely chemical composition and confining pore pressure that affect the travel time (Δt_{ma}) (Tixier et al, 1959).

Resistivity log

This log measures the resistivity of the formation, the amount of resistivity present when there is an electric current passing through. In most cases the fluids contained within the formations are conductors with the outer covering rock formations being insulators. Hydrocarbons deviate from this likelihood to be conductors and on the contrary are infinitely resistive and are therefore insulators. Porous formations that have salty water content will therefore result in a low resistivity reading whereby formations containing hydrocarbon content will have higher resistivity readings (Rider & Kennedy, 2002). These logs therefore only show significant peaks in conductive muds and not in holes that have oil based muds or freshwater muds.

In addition to this, these logs also give significant information about the clay content as the high resistivity zones represent minimal amounts of diagenetic clays. The low resistivity zones represent an increased amount of clay content such as chlorite, this increased amount of clay corresponds to a decrease in porosity and permeability (Nadeau, 2000).

Density log

This log records the formations continuous rock density. This density incorporates all factors within the formation and it is a function of the density of minerals that form the rock along with the fluids that are found in it (matrix and porosity). This log calculates porosity and consequently the hydrocarbon density.

The technique used for density logging involves the bombardment of medium energy focused gamma ray along with measuring the attenuation within the tool source and detectors. The attenuation refers to the number of electrons that are found in the formation and is thus the electron density which is very similar to the common density (g/m3). The identification of denser formations from less dense is that the Compton scattering attenuation is extreme leaving a few of the detectable gamma rays reaching the tool's detectors, this is characteristic of denser formations. The less dense formations are identified by a higher number of detectable gamma rays reaching the tools' detectors (Glover, 2000).

Neutron log

The neutron log provides a continuous record of formation's reactions to fast neutron bombardment and is indicative of the hydrogen index (hydrogen richness) which in turn is converted to neutron porosity limits. Quantitatively this log provides a measurement of the porosity, while qualitatively it is highly useful in discriminating between gas and oil. It is therefore used for the identification of gross lithology and presence of evaporates, hydrated minerals and volcanic rock fragments. It is optimally used when combined with the density log on computable scales and thus forms as a great subsurface lithology indicator (Rider & Kennedy, 2002).

CHAPTER 4: METHODOLOGY

4.1. Methodology Flowchart

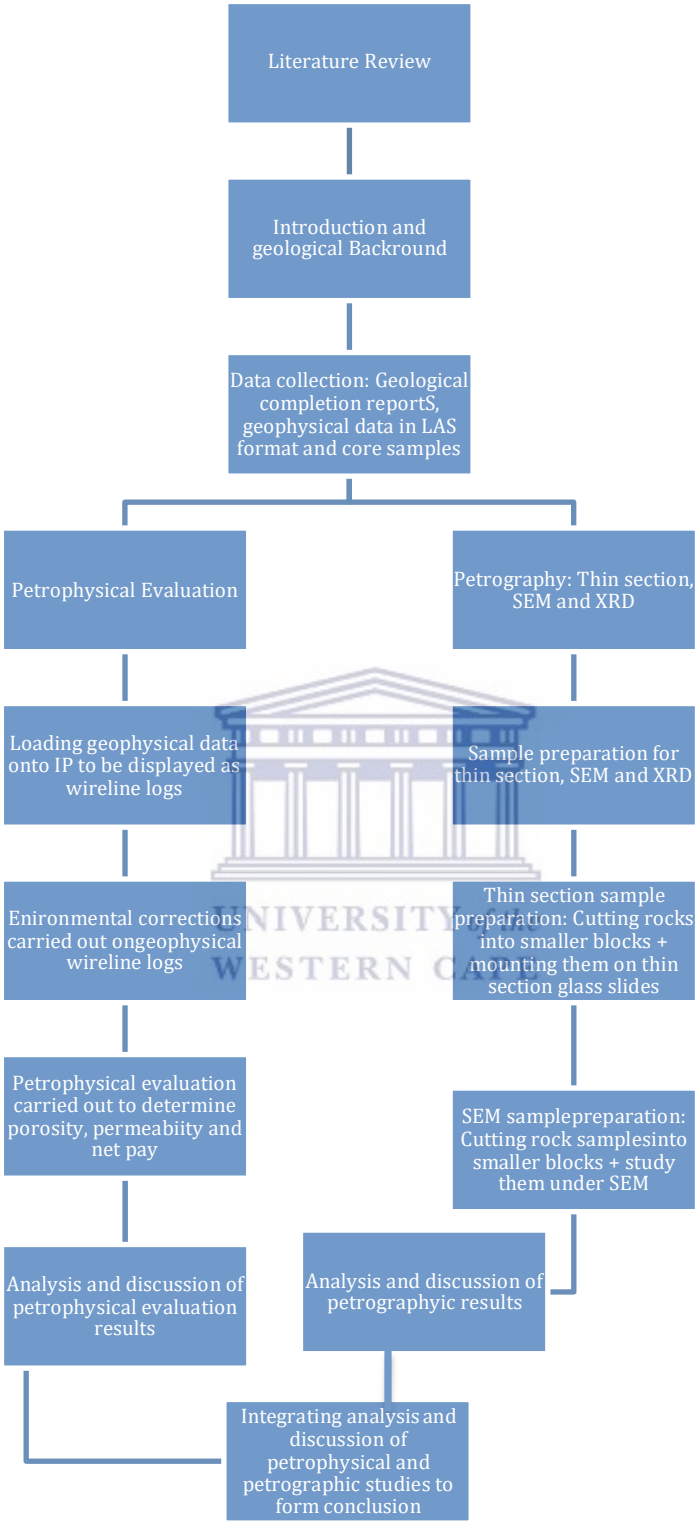

Figure 4. 1: Methodology flowchart of steps taken to carry out the objectives

4.2. Method

The research methods adopted comprises of two analysis, namely, petrophysical evaluation and petrographic analysis (Thin section, XRD and SEM).

4.2.1. Petrophysical evaluation

1. The first step was to acquire all necessary data (geological well completion reports, conventional core analysis report and geophysical wireline logs (LAS)) from the 4 studied wells. The data was provided by PASA (Petroleum Agency of South Africa).
2. The next step was to load the data onto the Interactive Petrophysics 4.2 software to be displayed as log curves.

4.2.1. a. Environmental corrections

Environmental corrections (Figure 4.2), depth corrections and quality control were performed in order to improve the quality of the data and ensure the accuracy of the results. The log splicing (merging logs of a particular curve where there is an identified gap along the curve resulting from different runs) was also applied and presented in Figure 4.3.

In addition to this, the "filling data gaps" function was applied as can be seen in Figure 4.4.

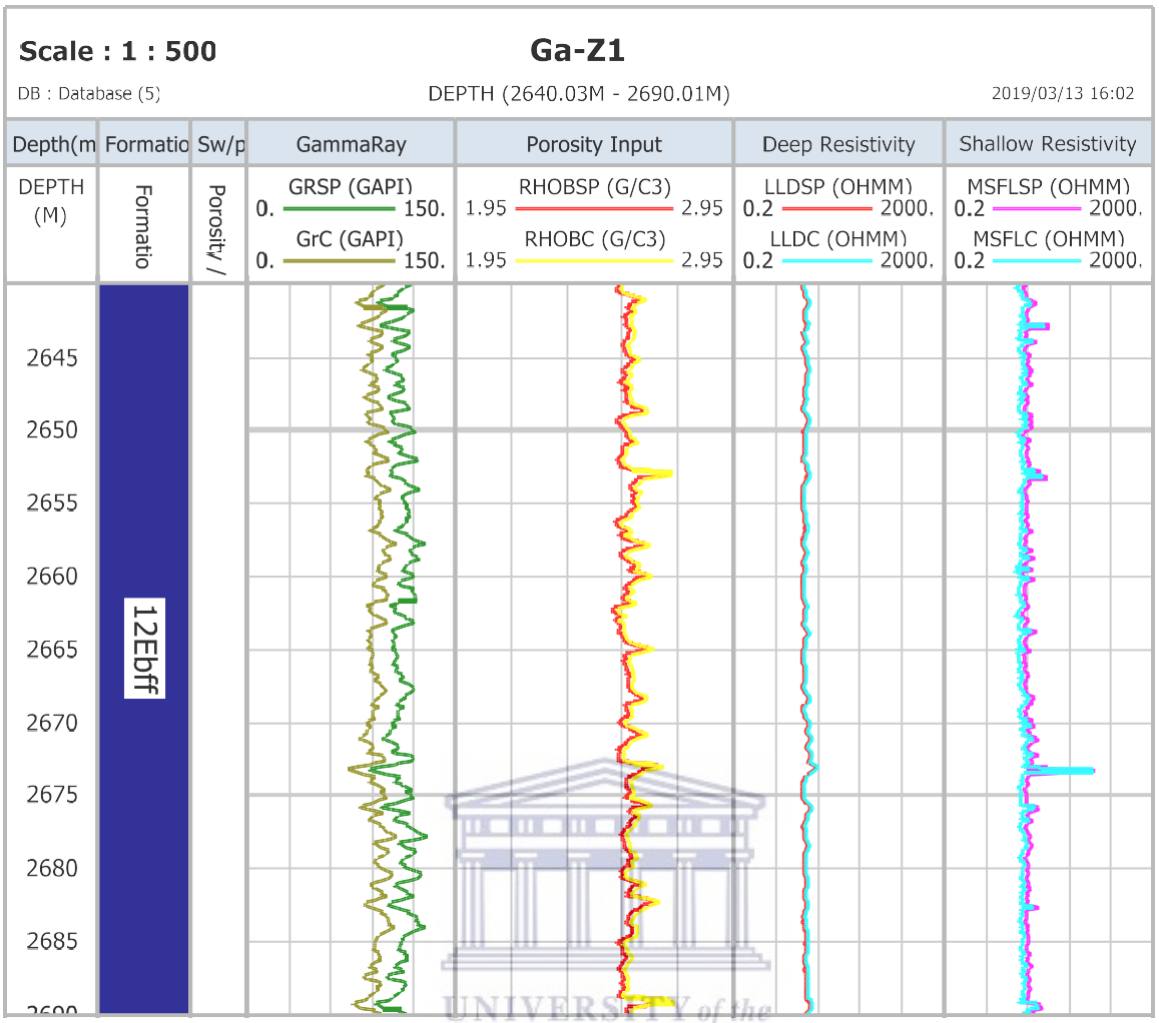

Figure 4. 2: Environmental corrections

Environmental corrections were carried out on gamma ray, density and resistivity curves. Input parameters necessary for these corrections included the mud weight, cement density, mud resistivity, temperature of mud resistivity, mud cake resistivity, the temperature of mud cake resistivity, caliper log and bit size.

Corrections including the effect of mud filtrate invasion were amended as it tends to increase the reading of gamma ray and resistivity logs, as well as to correct the hole size. As seen from Figure 4.2 the uncorrected gamma ray curve has a higher reading and is situated on the right of the corrected gamma ray log.

4.2.1. b. Splicing

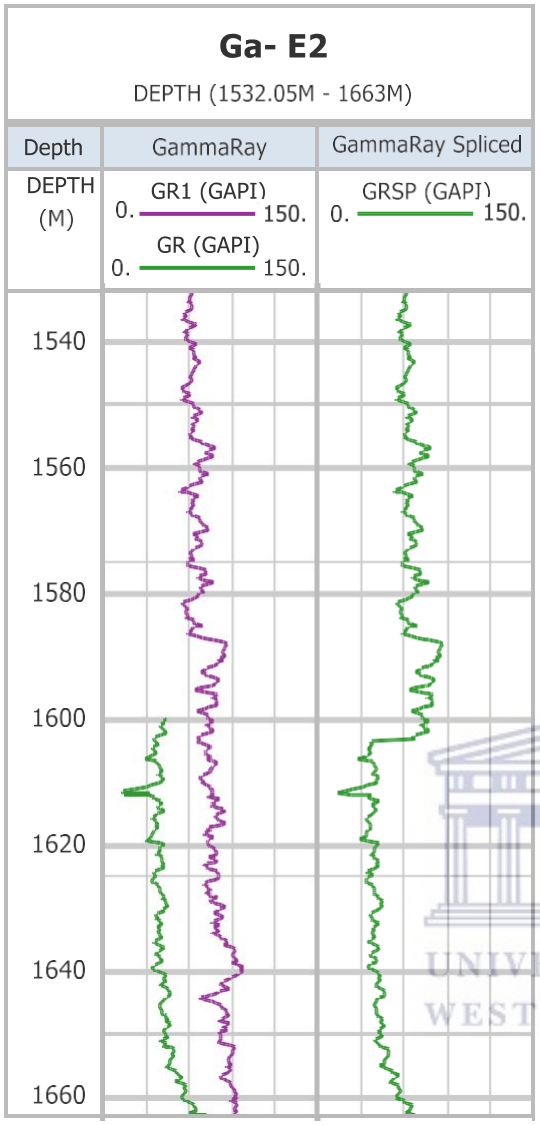

Figure 4. 3: GR logs before and after splicing

Various logs that were of different runs yet representing the same log were spliced together in order to merge the overlap in depth and form a single continuous curve.

4.2.1. c. Data gaps before and after correction

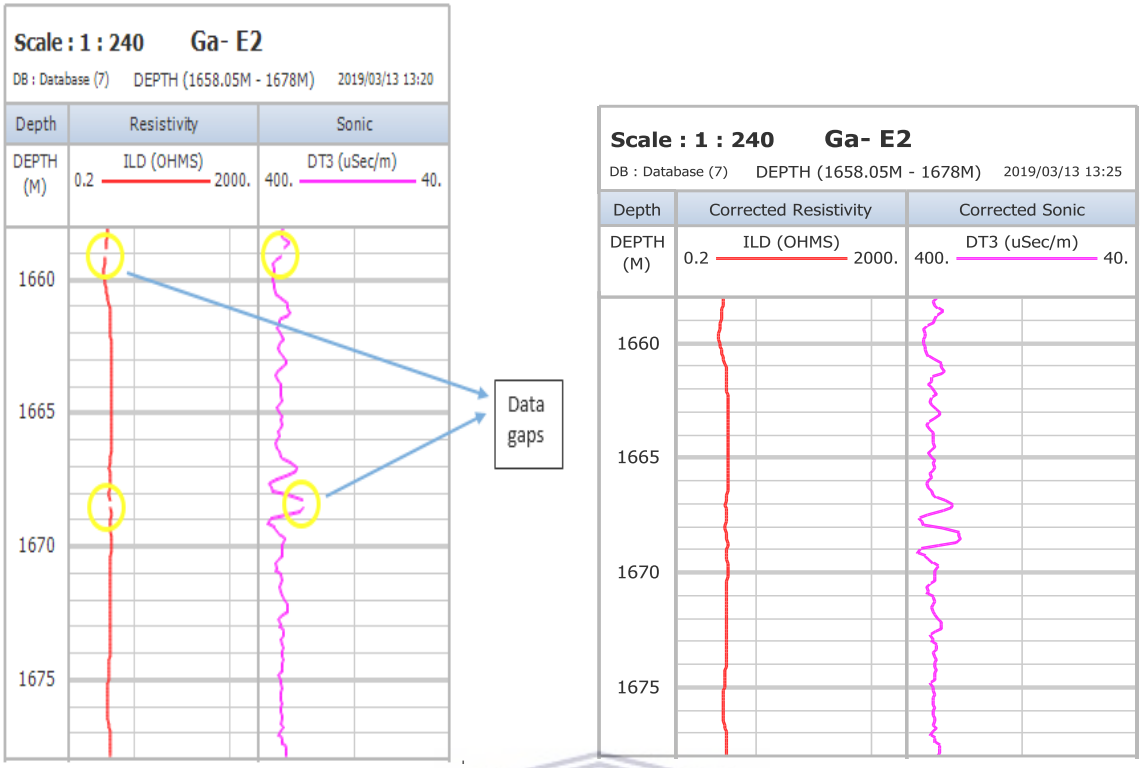

Figure 4. 4: Data gaps before and after correction

Filling minor data gaps was carried out in order to further adhere to quality control. These gaps were filled by values ranging between 2 to 4 and are speculated to be a result of environmental factors such as gas that has infiltrated the mud consistency or as a result of washout.

4.2.1. d. Initial fluid saturations and water saturation determination.

The Pickett Plot was introduced by Pickett (1973), his emphasis upon introducing this plot was for it to be a means of identifying patterns so that the trends and discriminations within the clouds of the cross plot can be related to the pay zone evaluation and reservoir structure. The picket plot, which is a plot of porosity (Phi) versus resistivity in logarithmic scale, was obtained to calculate the initial water saturation parameters (m, n, a and Rw) which are required to calculate water saturation and effective porosity. In order to obtain the accurate initial water saturation parameters for the 4 wells, the 100% water saturation line (red color) in the plot (Figure 4.5) was required to pass through the lowest resistivity point (x axis). The values toward the right hand side of the red line represent lower amounts of water saturation and are less water saturated than the values on the left hand side. These lower values are represented by the 50%, 30% and 20% water saturation lineintercepts.

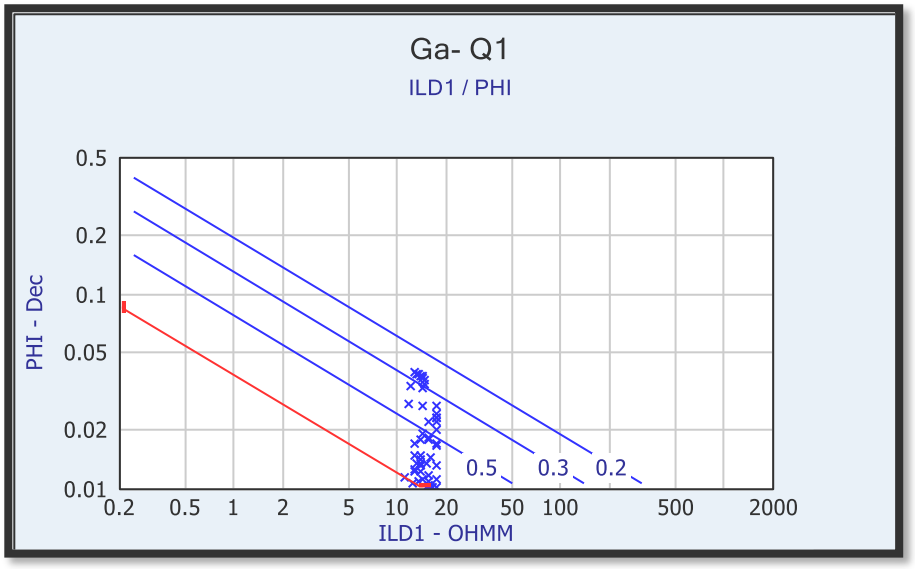

Figure 4. 5: Pickett plot of water interval in well Ga-Q1

Fluid saturation is an important parameter in the petrophysical analysis as it assists in finding the fluid volume of both water and hydrocarbons present. The relationship between fluid saturation and fluid resistivity can be explained by numerous equations that were adopted from Archie's equation.

The Archie equation was one of the earliest water saturation models developed and does not cater for shaly sand formation as can be seen in the absence of the volume of shale (Vsh) in the equation.

$$S_w = \left(\frac{a R_w}{\varphi^m R_t} \right)^n$$

(Archie, 1942)

It assumes the absence of electrical conductivity in the rocks (Doveton, 2001), therefore this model was specifically designed for formation evaluation of clean sandstones. This is also due to clean sands not having other factors affecting water saturation whereas in clay rich sediments the clay content has a direct influence on rock fluid leading to complications that require more dynamic and accommodating models. The shaly sand lithology tends to have significantly higher conductivities compared to pure sandstone lithology provided that even the slightest moisture content is present. The Archie model would have likely discredited the results obtained if it was used for this study due to the conducive properties of clays which are not present in sand (Egbele et al., 2005); as well as the effect of their CEC (Cation Exchange Capacity) properties. These clays would have led to an increased reading of water saturation (Doveton, 2001). When water is in contact with these materials the ions adhering to the surface may disintegrate into the water filled micro pores and thus form connecting conductivities within the water saturated spaces (McNeill, 1980). However these minerals tend to

have a stronger effect on pore waters that are less saline as they are not already conductive (McNeill, 1980).

After Archie's model was created there were numerous water saturation models created that specifically catered for shaly sand formation. These include laminated shale model (Poupon et al., 1954), Simandoux model (Simandoux, 1963), Indonesia model (Poupon & Leveaux, 1971) and total shale model (Schlumberger, 1972) among others.

From the above mentioned models only two, namely Indonesia and Simandoux were incorporated in this study as the models were applied to shaly sand formations. These two models were the best fit as they did not have specific shale distribution requirements, as the shale in the wells investigated comprised of a combination of distributions; hence the laminated and dispersed shale models were avoided. They also take into account the type and size of interstitial structures formed in the presence of clay and shale as well as their effect on the overall resistivity. The total shale model was also excluded because it does not include the cementation factor in its equation which was needed in this study.

Some beneficial factors of the Indonesia model are that it makes use of log analysis parameters meaning that input information may be conveniently accessed. This is seen as a progressive step as the model was initiated through Indonesian field observations where shaly sands contained measurable water. Its origin adds to its reliability in the petroleum industry as it is a theory that was tested in the field as opposed to laboratory experiments (Poupon & Leveaux, 1971).This model is however not limited to this location and can be applied world-wide provided that the lithology is that of shaly sand. The main difference between the incorporated models was that the Indonesia model was developed through field studies and Simandoux was developed through laboratory experiments of which both are credible (Egbele et al., 2005).

The Picket plot assists in determining the water saturation. The water saturation is the parts of the pore spaces that are occupied by water. Therefore the water saturation affects the oil and gas reservoirs as they both occupy the pore spaces. The product of porosity and water saturation is the bulk volume of water, this bulk water volume provides information about the producibility when related to pore character and reservoir type. Water saturation is a vital property of reservoir evaluation as it is used to quantify the hydrocarbon saturation.

The Indonesia model (Poupon & Leveaux, 1971) is based on the following water saturation equation (SwInd):

$$Sw = \left[\frac{\frac{1}{R_t^{0.5}}}{\frac{V_{sh}^{1-Vsh/2}}{R_{sh}^{0.5}} + \frac{\phi^{m/2}}{(a * Rw)^{0.5}}} \right]^{2/n}$$

$$\frac{1}{R_t} = S_w^{n/2} \left(\frac{V_{sh}^{1-V_{sh}/2}}{\sqrt{R_{sh}}} + \left(\frac{\varphi^{m/2}}{\sqrt{a}\, R_w} \right) \right)$$

Where:

Sw= water saturation

V_{sh} = volume of shale (fraction)

R_{sh}= resistivity of shale (ohm)

Rw= water resistivity

Rt= deep resistivities

ø= porosity

(Poupon & Leveaux, 1971)

The Simandoux model is based on the following water saturation equation:

$$S_w = \frac{a R_w}{2 \varphi^m} \left[\left(\frac{-V_{sh}}{R_{sh}} \right) + \sqrt{\left(\frac{V_{sh}}{R_{sh}} \right)^2 + \left(\frac{4 \varphi^m}{a R_w R_t} \right)} \right]$$

(Simandoux, 1963)

The meaning of the parameters in the Simandoux equation are the same as those of Indonesia equation discussed above. These parameters are compulsory for the determination of water saturation.

4.2.1. e. Calculation, calibration and net pay

1. The volume of clay log curve was calculated from the gamma ray log.
2. The porosity log:

3. There are three types of logs that are generally used to calculate the porosity namely, density, neutron and sonic logs. The porosity log curve for this study was calculated from the corrected sonic log and made use of the Wyllie equation which is asfollows:

   PHIS = (DTC - DTCMA) / (DTCW - DTCMA) / KCP

   Where:

   KCP = compaction factor (fractional)

   DTC = sonic log reading in zone of interest (usec/ft or usec/m)

   DTCMA = sonic log reading in l00% matrix rock (usec/ft or usec/m)

   DTCW = sonic log reading in 100% water (usec/ft or usec/m)

   PHIS = porosity from sonic log

   PHIsc = porosity from sonic log by Wyllie method (fractional)

   PHISSH = apparent sonic porosity of 100% shale after compaction correction (fractional)

   Vsh = shale volume (fractional)

   (Crain, 2018)

4. The predicted permeability was calculated from the core porosity and core permeability poro-perm plot (discussed under chapter 5).
5. The next step was to calibrate the wireline logs with core data in order to validate the models produced from the software.
6. In addition, the net-pay cut off values were determined to differentiate between gross reservoir and net pay intervals within the reservoir. Included are the cut off values of porosity, clay volume and water saturation.
7. In order to determine the reservoir zones from the logs it was necessary to analyse the lithology, reservoir flag and pay flag.
8. Once all the analyses were completed a petrophysical result summary report was produced and was of great assistance to the overall interpretation as it pointed out relevant trends.

4.2.2. Thin section

1. Ten rock samples used in this study were collected from PASA (Petroleum Agency of South Africa) core library facility. Core data was only available from two wells (Ga- Q1 and Ga-Z1). The data necessary for petrophysical evaluation for the other two wells were collected from geological well completion reports (WCR) and well logs. Figure 4.6 exhibits the microscope which was utilised to conduct thin section studies, placed alongside it are the 10 thin section slides retrieved from the core samples of the two wells.

2. Five representative rock samples of selected depths were collected from each well, making a total of 10 rock samples
3. A thin sliver of rock was cut from each sample and ground optically flat. It was mounted on a glass slide and then grounded smoothly using finer abrasive grit until the sample was more or less than 30 µm thick (to avoid any fracturing or plucking).
4. Epoxy resin was added to the thin section during the preparation of the sample in order to accentuate any pore spaces and/or fractures present that would under normal circumstances have been burdensome to identify
5. The 10 rock samples were then observed under the microscope through plane and polarised light under the following magnification: 40x, 10x and 4x

Figure 4. 6: Microscope with thin section samples

6. When placed between two polarizing filters set at right angles to each other, the optical properties of the minerals in the thin section result in a change in colour and intensity of the light as seen by the viewer. As different minerals have different optical properties, most rock forming minerals were identified through this method.

4.2.3. XRD (x-ray diffraction):

"X-ray crystallography is a technique for determining the three-dimensional structure of molecules, including complex biological macromolecules such as proteins and nucleic acids. It is a powerful tool in elucidation of the three-dimensional structure of a molecule at atomic resolution. Data is collected by diffracting X-rays from a single crystal, which has an ordered, regularly repeating arrangement of atoms" (Brenner and Picknett, 2001, p. 2154). When a beam of incident x-ray light hits the surface of the crystal atoms/s the phenomenon of diffraction of the light into different angles occurs. The measured angles and intensities of the diffracted beams make it possible to create 3D images depicting the electron density found in the crystal. The value of the electron density allows for the establishment of the average position of the atoms along with their corresponding chemical bonds, a crystallographic disorder etc. As a result of the characteristic many materials possess to form crystals, XRD has played a rudimentary role in the expansion of various scientific disciplines. Even when dating back to the XRD process's early stages of discovery, it proved itself useful as it was able to determine the size of atoms, their lengths, types of chemical bonds present, as well as the atomic-scale differences among various materials, especially minerals and alloys (Warren, 1969).

XRD was incorporated into this study in order to identify the mineral phases present in each sample by their unique polymorphic forms i.e. "finger prints".

XRD is based on the relationship formed by the interference pattern produced as light (x-ray) is reflected off a crystal surface. The cathode ray tube is responsible for creating the incident x-rays which are filtered to create monochromatic radiation, directed towards the sample and have a collimated concentration (XRD Topic 5a, 2018). This relationship was formulated by physicist Sir W.H Bragg and his son Sir W.L Bragg and was named "Bragg's Law" in 1913 of which the formula for this relationship is as follows:

$$\sin\theta = n\lambda / 2d$$

Where:

$\sin\theta$ = x-ray angle of incidence as it comes into contact with crystal surface

n = integer

λ = wavelength of incident x-ray beam

d = distance between atomic layers in a crystal

(W.H. Bragg and W.L. Bragg, 1913)

4.2.3. a. XRD Sample preparation

The following checklist for sample preparation applied by Kleenberg (2018) was adopted in the present work:

1. The sample has to be homogeneous as well as a good representation of the study area for the purpose of determining phases present.
2. The grinding energy is dependent on the most sensitive phase.
3. Priority must be given to the preservation of sensitive phases, therefore, it is more desirable to keep larger grains than to grind them if it will lead to the destruction of phases.
4. Preventing the loss of material through dusting can be done by ensuring that containers are tightly sealed.
5. Preventing phase alteration by working at a speedy pace to avoid contact with exterior agents including air.
6. Keeping a steady temperature as significantly increased temperatures could also alter phases.
7. First crush rock samples that are relatively big to ensure smooth milling process.
8. Mill the crushed samples for a designated amount of time to prevent over milling and thus loss of sample in powder form.

4.2.3. b. XRD steps carried out:

1. The first step involved in sample preparation for XRD is to grind the rock samples into smaller pieces and then to mill them in order to create a powder form.
2. Once all 10 powdered samples were acquired they were sent to iThemba laboratory (Cape Town) for XRD analysis.
3. An XRD machine consisting of the following was used: x-ray source, sample holder and detector. The XRD method incorporated in this study was outlined by Attfield et al., (2018). The sample was mounted on the sample holder (and rotated to prevent any bias reading), the detector was responsible for the conversion of X-ray photons into an electrical signal as it is a two-stage process. The X-ray photon collides with a phosphor screen, or scintillator, which forms the coating of a thallium-doped sodium iodide crystal. The latter produces photons in the blue region of the visible spectrum. These are subsequently converted to voltage pulses by means of a photomultiplier tube attached directly behind the scintillator. The number of electrons ejected by the photocathode is proportional to the number of visible photons which strike it, which in turn is proportional to the energy of the original X-ray photon, this is done in order to obtain the output phases that were recorded.
4. Once results were received, a thorough analysis was then possible.

4.2.4. SEM (Scanning Electron Microscope):

Figure 4. 7: Auriga SEM machine

1. The rock samples were cut into small cubes of rock in order to fit on the SEM stub
2. Each rock sample was mounted onto the stub and silver liquid was lightly brushed onto the sides of the samples as well as very slightly on the top and bottom edges. This was done to assist and ensure the flow of electrons, i.e. ensuring that conduction of electrons will take place.
3. The rock samples were then ready to be coated with carbon and were put in the Auriga machine where the SEM process took place as shown in Figure 4.7.
4. For each sample SEM pictures of 2-3 locations on the surface of the rock were selected in order to prevent any bias when it comes to analysing, interpreting and making a conclusion.

CHAPTER 5: PETROPHYSICAL EVALUATION AND RESULTS

5.1. Introduction: Petrophysical models

The petrophysical evaluation of the four wells was carried out to determine the volume of clay, porosity, water saturation and permeability in order to assess the quality of the reservoirs.

The calculated results from the software were calibrated with the available routine core analysis data from 3 wells (Ga-Q1, Ga- E2 and Ga- Z1) to validate and increase the reliability of the results. The core data includes porosity, permeability, water saturation and grain density. It is important to perform the calibration due to the differences between the 2 methods of acquiring roughly the same information i.e. well logs usually produce dynamic measurements which tend to exceed that of core samples. The core samples usually depict static measurements due to strain amplitude differences between the two methods.

The petrophysical analysis is focused on the shaly sandstone reservoirs belonging to the early and late Cretaceous age. The formation tops assist in further classifying the ages of these formations so as to acquire a better understanding of certain influential factors that contributed to formation and characteristics such as structure, lithofacies and mineral constituents of the current lithology. Four reservoirs were identified from each of the four wells considered under the present investigation.

The overall formation tops constituting the identified reservoirs of the wells in the study area are 1At1, 12At1, 13At1, 17At1, 22At1, BC V, BC V1 and i.

5.1.1. Core data

Detailed examination of core samples is important as it aids in carrying out stratigraphic and wireline log correlation, understanding deposition environment, fluid flow and mechanical properties. It breaks down the interpretation of various sub-surface layers which would have otherwise been left to assumption.

The most ideal process for optimal core interpretation is that core sample properties are measured and recorded within original reservoir conditions i.e. straight after retrieval. It is therefore vital that the samples be handled cautiously from the time of retrieval to transportation and ultimately thorough study in a laboratory in order to maximise the accuracy of measurements.

Core samples are taken from both reservoir and non-reservoir intervals with the latter directly assisting in revealing deposition environment and processes that directly influenced this environment. The deposition environment, in turn, is of great assistance in understanding the morphology and size of hydrocarbon (gas) reservoir zones (Soeder and Randolph, 1987).

Tables 5.1 -5.4 below were used for the classification of grain density and petrophysical parameters of the core data as well as other analysis carried out in this study.

Table 5. 1: Grain density of different rocks

Rock name	Grain density (g/cm3)
Clay	1.63-2.6
Silt	1.80-2.20
Sandstone	1.61-2.76
Shale	1.77-3.30
Limestone	1.93-2.90
Dolomite	2.28-2.90

(Densities of sedimentary rocks, 2018)

Table 5. 2: Grain density of different minerals

Mineral name	Grain density(g/cm3)
Chlorite	2.80
Glauconite	2.30
Kaolinite	2.59
Illite	2.66
Smectite/montmorillonite	2.1-2.6
Clinoperthite A/B	2.54/2.57
Dolomite A/B	2.85/2.87
Calcite	2.71
Orthoclase	2.57
Plagioclase	2.64

(Pettijohn, 1975)

Table 5. 3: Porosity classification

Porosity (%)	Classification
0 – 5	Negligible
5 – 10	Poor
10 – 15	Fair
15 – 20	Good
20 – 25	Very good

(Toro, 2016)

Table 5. 4: Permeability classification

Permeability values (mD)	Classification
Less than 1	Poor
Between 1 and 10	Fair
Between 10 and 50	Moderate
Between 50 and 250	High
Between 250 and 1000	Very high
Above 1000	Exceptional

(Modified after Tiab and Donaldson, 2015)

Well Ga-Q1

The measurements for porosity, water saturation, gas saturation and grain density were retrieved from 2329.22m – 2334.95m and permeability was retrieved from 2329.22 m – 2347.14 m.

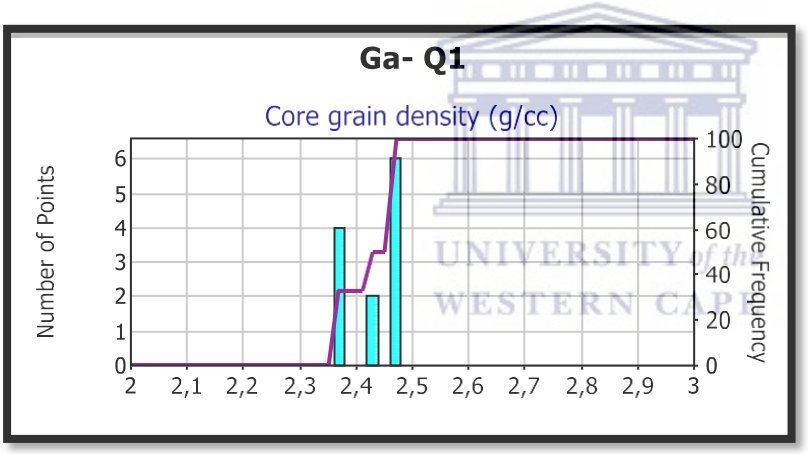

Figure 5. 1: Core grain density of well Ga-Q1

Figure 5.1 shows that the core grain density ranges from 2.37g/cc to 2.56 g/cc with the mean value of 2.43 g/cc. The standard deviation is 0.04206 meaning that there is a minimal deviation from the mean value and that the values of the grain density samples are very similar to each other. The range of these samples show that all of the core samples lie within the sandstone and clay mineralogy range as seen in Table 5.1.

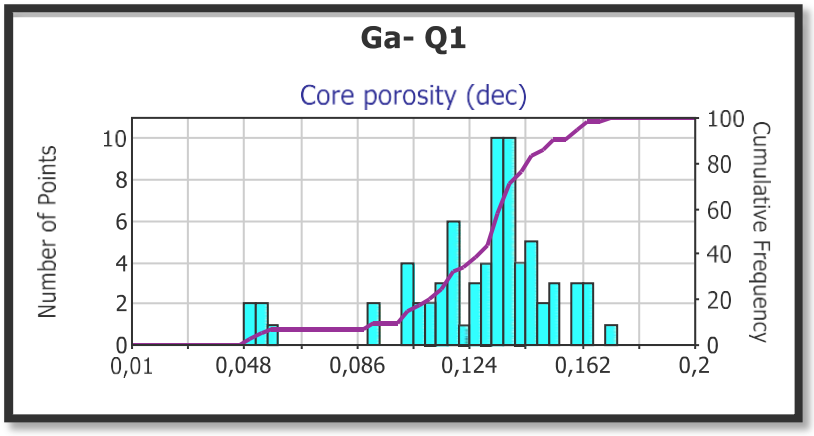

Figure 5. 2: Core porosity of well Ga-Q1

The core porosity values ranged from 0.048 to 0.171 with a mean value of 0.12679. Therefore, the mean value depicts an overall fair porosity according to Table 5.3. The standard deviation is 0.02647, meaning that the variation in porosity values is very minimal i.e. porosity values of this batch are very similar to each other and the mean value.

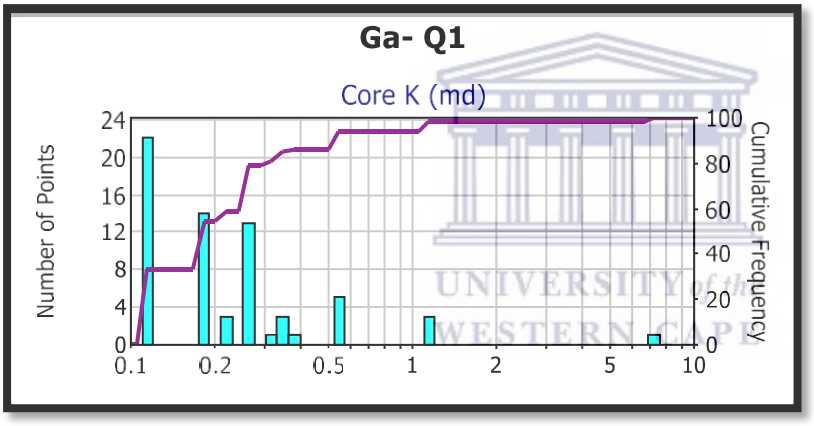

Figure 5. 3: Core k of well Ga-Q1

The core permeability ranges from a minimum of 0.12 mD to 7.4 mD with a mean value of 0.23mD. The standard deviation of 2.084 means that there is a noticeable difference within this group of core samples, therefore, the permeability values are spread out across a wider range of values that deviate from the mean value. The average permeability of this interval can be classified as poor as it falls below 1mD.

Well Ga- Z1

The measurements for porosity, permeability, water saturation, gas saturation and grain density were retrieved from 3023.39 m – 3029.15 m.

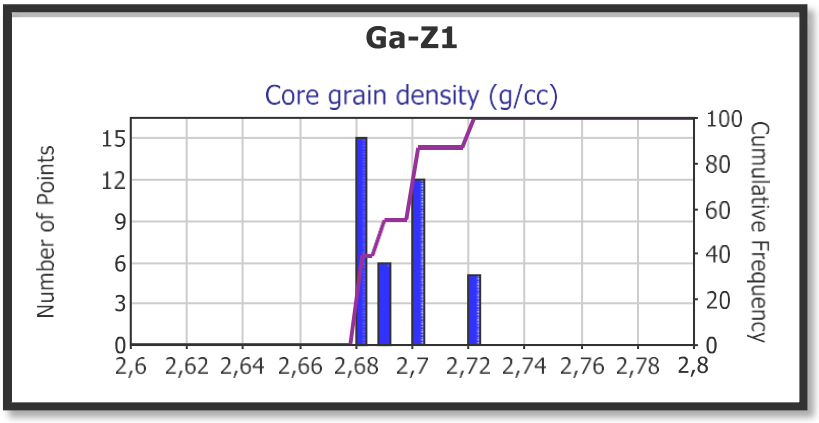

Figure 5. 4: Core grain density of well Ga-Z1

The core grain density of well Ga-Z1 from Figure 5.4 ranges from 2.68 g/cc to 2.72 g/cc with a mean value of 2.7g/cc and the standard deviation of 0.01357 meaning that the samples are very similar to each other and the mean. The core grain density ranges within a very short range which leaves no room for a wide variety of minerals or lithology type to be present. These values all point to core samples that were retrieved from sandstone lithology as seen in Figure 5.1, this lithology is further supported through wireline logging reservoir lithology identification in Figure 5.16. It is also possible that this lithology contains some limestone and or dolomite stringers, as well as some shale. The minerals most likely to be present are calcite (2.71 g/cc) and some mica such as plagioclase (2.69 g/cc) of which the plagioclase shows some consistency with thin section, SEM and XRD results (explained further in chapter 6).

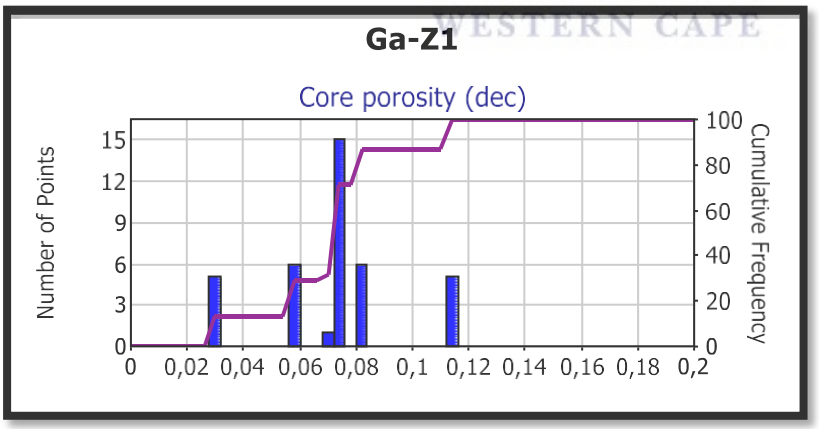

Figure 5. 5: Core porosity of well Ga-Z1

Well Ga-Z1 has a minimum of 3% and a maximum of 11.4% porosity. The low standard deviation of 0.02309 (dec) shows that the porosity values do not vary significantly from each other within this interval. The average porosity is 7.3%, making it a poor reservoir according to Table 5.3.

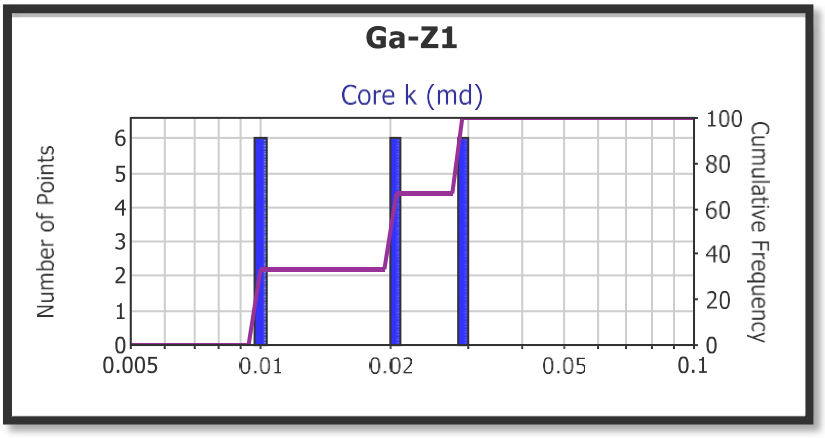

Figure 5. 6: Core k of well Ga-Z1

Core permeability for well Ga-Z1 has a minimum of 0.01mD, a maximum of 0.03mD and a mean of 0.01817mD. The standard deviation of 1.59 shows that there is a noticeable difference within the samples from each other, as well as from the mean value. This interval displays extremely poor permeability.

Well Ga-E2

The parameters for porosity, permeability, water saturation, gas saturation and grain density were retrieved from 3075.5 m – 3084.14 m.

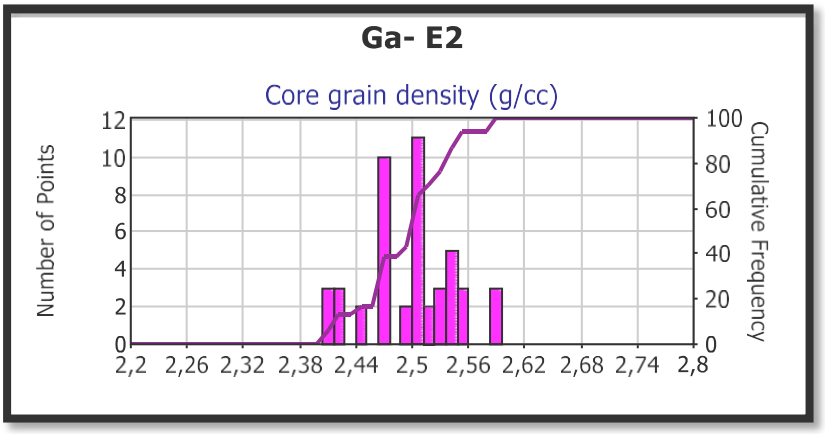

Figure 5. 7: Core grain density of well Ga-E2

Well Ga-E2 had the most core grain density samples which lie between the range of 2.41 g/cc and 2.59 g/cc with a mean value of 2.5 g/cc. The interval representing these core samples lies a few metres below reservoir 1 and is a mixture of shale and sandstone formation. The density range corresponds with the presence of clay minerals i.e. kaolinite, montmorillonite, clinoperthite, and orthoclase. The clay minerals represented by these depths particularly kaolinite are considered to be anomalous as these minerals are not characteristic of deep- sea sediments but rather of continental and nearshore sediments (Weaver, 1956).

The low deviation value of 0.04692 shows that there is not much difference between the samples' mineralogy from each other and the mean in this range.

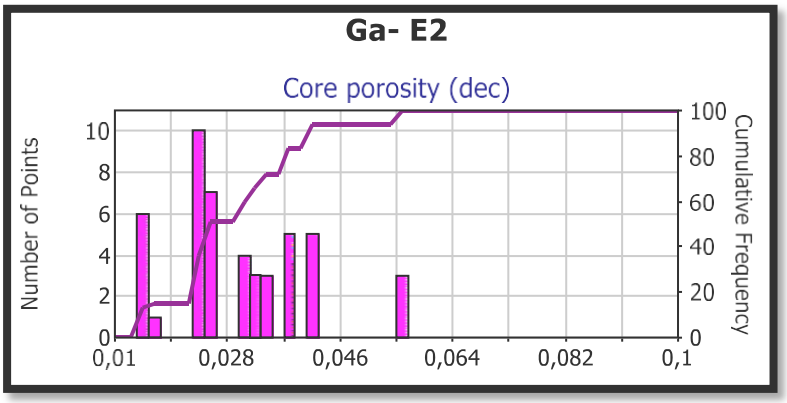

Figure 5. 8: Core porosity of well Ga-E2

The core porosity ranges from 0.0143 - 0.056 with a mean value of 0.02976 and the standard deviation of 0.01076. The 2.97 % porosity average means that this section of the well is classified as negligible

as it falls within 1%-5% porosity. The reservoir negligible porosity does not have the potential to become a conventional reservoir regardless of the lithology or permeability values present. This is because storage is just as important (if not of greater importance) as the other parameters necessary for a petroleum system.

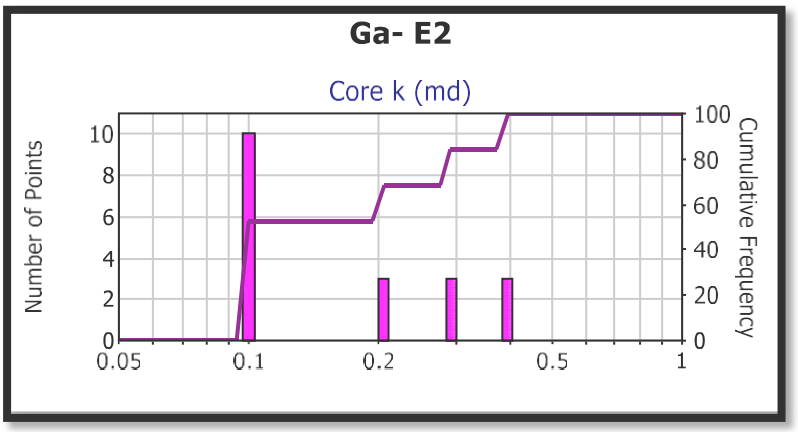

Figure 5. 9: Core porosity of well Ga-E2

The core permeability ranges from 0.1 mD - 0.4 mD with the mean value of 0.17 mD and the standard deviation of 1.79. Although the range from the minimum to the maximum values is greater than those presented by well Ga-Z1, this interval is also classified as having poor permeability according to Figure 5.4.

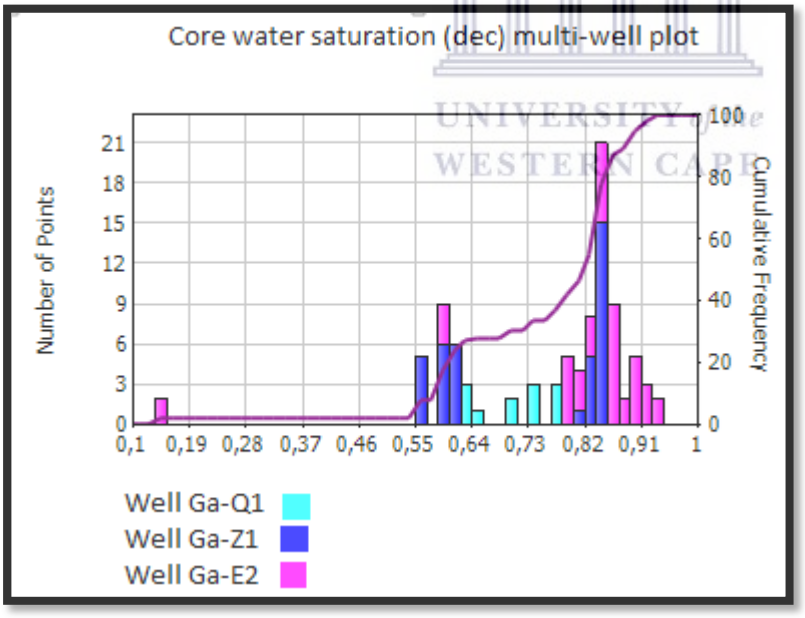

Figure 5. 10: Core water saturation multi-well plot

Core water saturation for well Ga- Q1 ranges from 63% - 77% with the mean value of 70%. Well Ga-Z1 ranges from 55% - 85% with the mean of 72.9%. Well Ga-E2 has a much wider range than the 2 previous wells with a range from 13.9% - 94% and a mean value of 80%. The standard deviation values

of well Ga-Q1, Ga-Z1 and Ga-E2 are 0.056, 0.1272 and 0.168 respectively. All 3 wells have relatively low standard deviations particularly well Ga-Q1, showing that the different water saturation values representative of that depth do not veer too far from the 70% average. Ga-Z1 and Ga-E2 do not poses standard deviation values that are significantly high, however they are slightly high, indicating some variations within the water saturation.

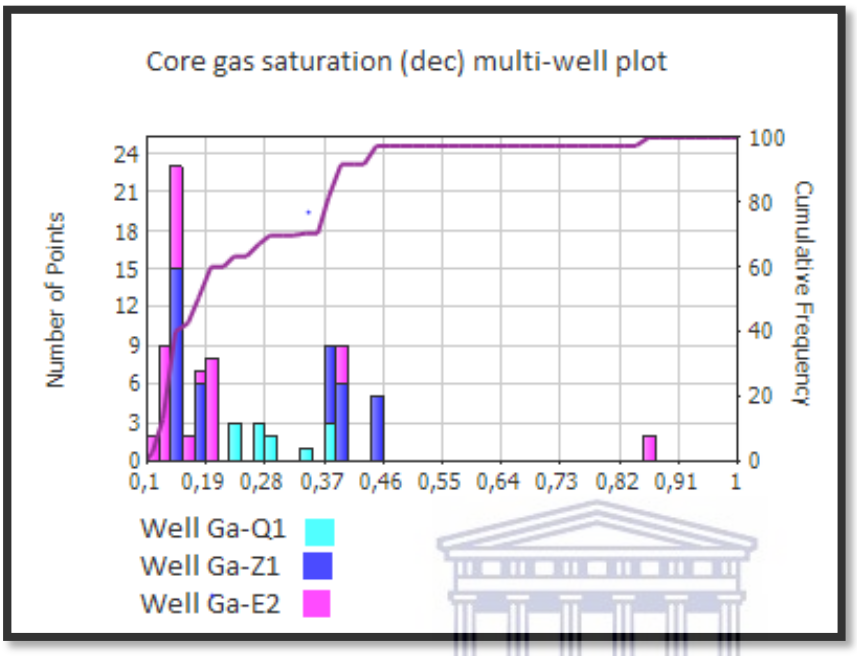

Figure 5. 11: Core gas saturation multi-well plot

Well Ga-Q1 has core gas saturation ranging from 23% - 37% with a mean value of 29.5%. Ga-Z1 has values ranging from 15% - 45% with a mean of 27% followed by Ga-E2 with a minimum of 10.38%, a maximum of 86% and a mean of 22% gas saturation. The standard deviations for Ga-Q1, Ga-1 and Ga-E2 are 0.056, 0.13 and 0.22 respectively. The standard deviation values are all very low with well Ga-Q1 having the lowest value therefore the least variety of values, and slightly more variety is found in deviation from the mean value are found in Ga-Z1 and Ga-E2. The overall highest gas saturation based on mean value is Ga-Q1, the overall highest gas saturation based on maximum value isGa-E2.

5.1.2. Volume of clay/shale determination

The volume of shale refers to the ratio of the volume of clay, silt as well as other fine grained particles to the entire rock volume (Szabó, 2011).

There are three classifications that best describe the distribution of this parameter, namely laminated distribution, which is the layered structural arrangement of clay between sand lithology; structured distribution describes the clay particles that are found within the grains and thus form part of the makeup of these grains; and dispersed distribution where the clay particles are found in pore spaces between the grain constituents of the rock (Shedid & Saad, 2017) .The gamma ray log is used

as the basis for calculating the volume of shale and clay in reservoirs of varying porosity by incorporating the minimum and maximum values from the histogram. This value of shale volume is represented as a decimal fraction and is expressed as Vsh (Asquith & Krygowski,2004).

There are various linear and non-linear equations for the gamma ray log. The equations with the non-linear relationships are as a result of the location or age of the particular formation. These relationships are characterised by their optimistic values as their shale volume values are lower than those produced from the linear equation (Asquith & Krygowski, 2004). Therefore in this research the linear equation was used in order to prevent over optimistic results and interpretation.

Figure 5.12 is a gamma ray multi well histogram for all four wells showing the values that were used to calculate the volume of shale.

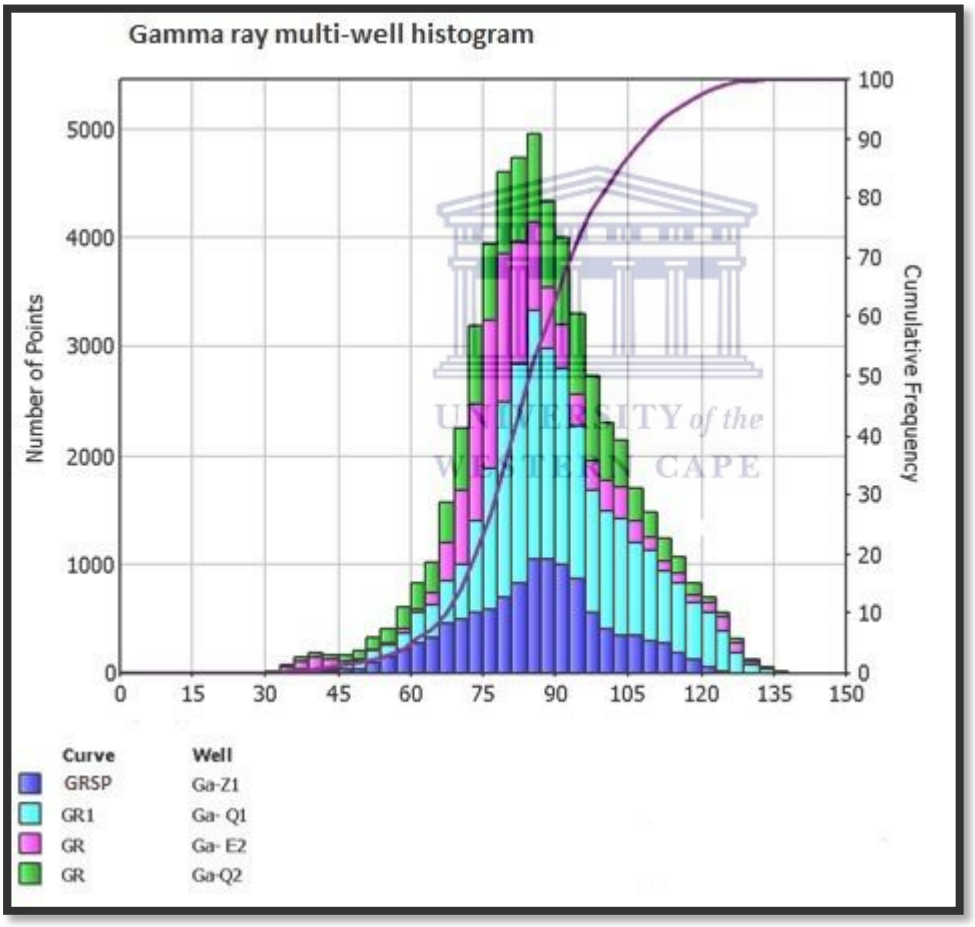

Figure 5. 12: GR Multi-well histogram

The following equation was used to calculate the volume of shale:

Linear response (Vsh = IGR):

$$V_{sh} = I_{GR} = \frac{GR_{\log} - GR_{\min}}{GR_{\max} - GR_{\min}}$$

Where:

V_{sh} = volume of shale

I_{GR} = gamma ray index

GR_{log} = gamma ray reading of formation

GR_{min} = minimum gamma ray (clean sand or carbonate)

GR_{max} = maximum gamma ray (shale)

(Schlumberger, 1974)

5.2. Wireline log evaluation of well Ga-Q1, Ga-Q2, Ga-Z1 and Ga-E2

This section focuses on the interpretation of wireline logs within the selected reservoir intervals. Track 1 within the log plots represents the depths of the reservoir zones, track 2 the formation tops and track 3 numbers the identified reservoir zones using gamma ray log. Track 3 is followed by the gamma ray log which was the input parameter for identification and delineation between clay and sandstone, this is because clay is known to react more radioactively than other lithologies such as sand and carbonates. In track 4 the gamma ray log was used for the identification of the reservoir zones. The depositional environment was inferred through gamma ray log pattern in correspondence with the classification depicting depositional environment from gamma ray shape, which may be seen in Figure 5.13.

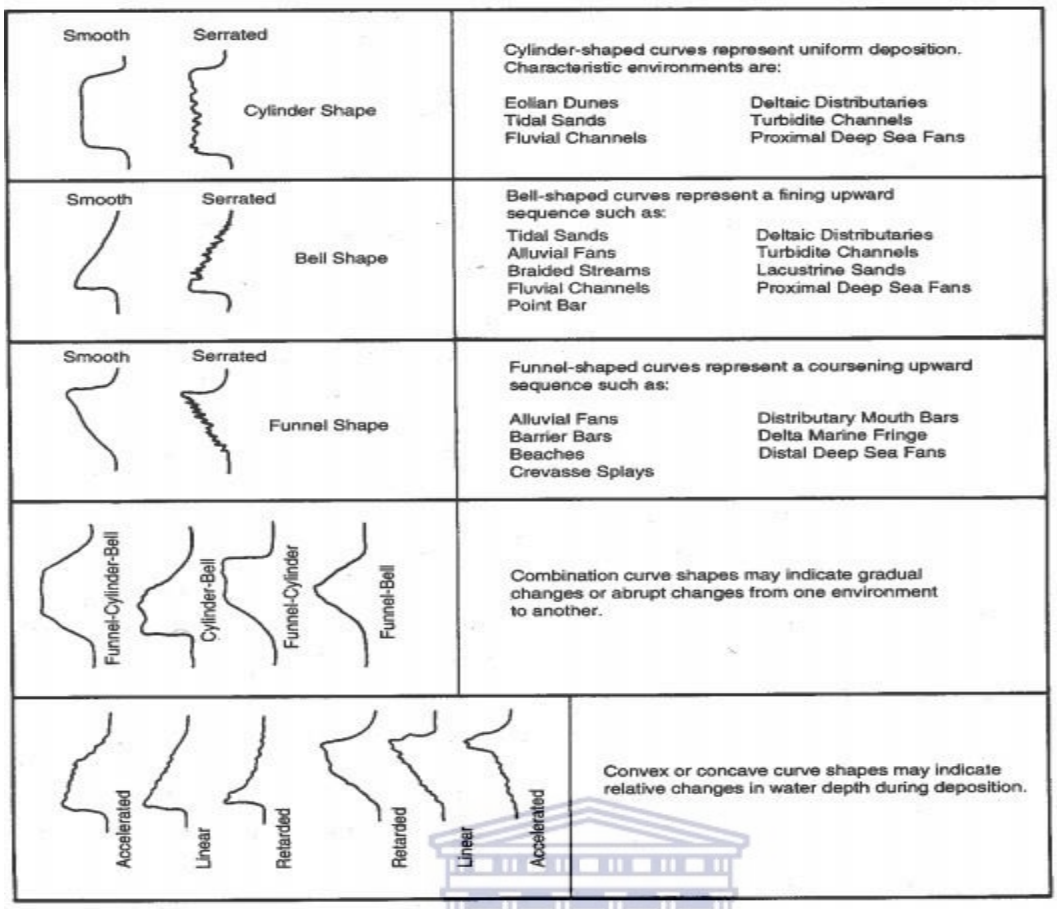

Figure 5. 13: Depositional environments from gamma ray shape (Atlas, 1995)

Neutron porosity and density logs are represented in track 5, deep and shallow resistivity logs in track 6, sonic log in track 7. The lithology in track 8 represents the lithofacies which are grouped as follows:

Table 5. 5: Facies description

Facies	Facies description
Facies A	interbedded claystone and siltstone with well-developed quartz sand at the base as well as occasional sandstone and limestone and minor dolomite stringers
Facies B	Sandstone sequence capped upwards, upward coarsening units
Facies C	Sequence of interbedded sandstone, siltstone and claystone with traces of pyrite
Facies D	argillaceous sandstone
Facies E	Tight sandstone with traces of glauconite, pyrite and dolomite

The caliper log which assists in representing the physical shape of the well by showing the variations in borehole diameter with depth (Rider & Kennedy, 2002) is shown in track 9 and temperature log in track 10.

In order for gamma ray curve to make accurate delineation between sand and shale lithology, a baseline had to be determined specified to GR log used in each well. Therefore the mean value of each gamma ray log (derived from histogram) was utilised as the baseline. The following baselines 90, 85, 85 and 83 were used for wells Ga-Q1, Ga-Q2, Ga-Z1 and Ga-E2 accordingly, and are therefore listed in order of shaliest to cleanest wells.

In order to derive a temperature log for all 4 wells, an IP calculator was used to calculate the log using the "gradient" input method. This involved the use of temperature geothermal gradient with equivalent depth provided in the geological well completion reports. In wells where multiple depths and temperatures were recorded, the deepest depth was used.

5.2.1. Petrophysical Evaluation of Well Ga-Q1

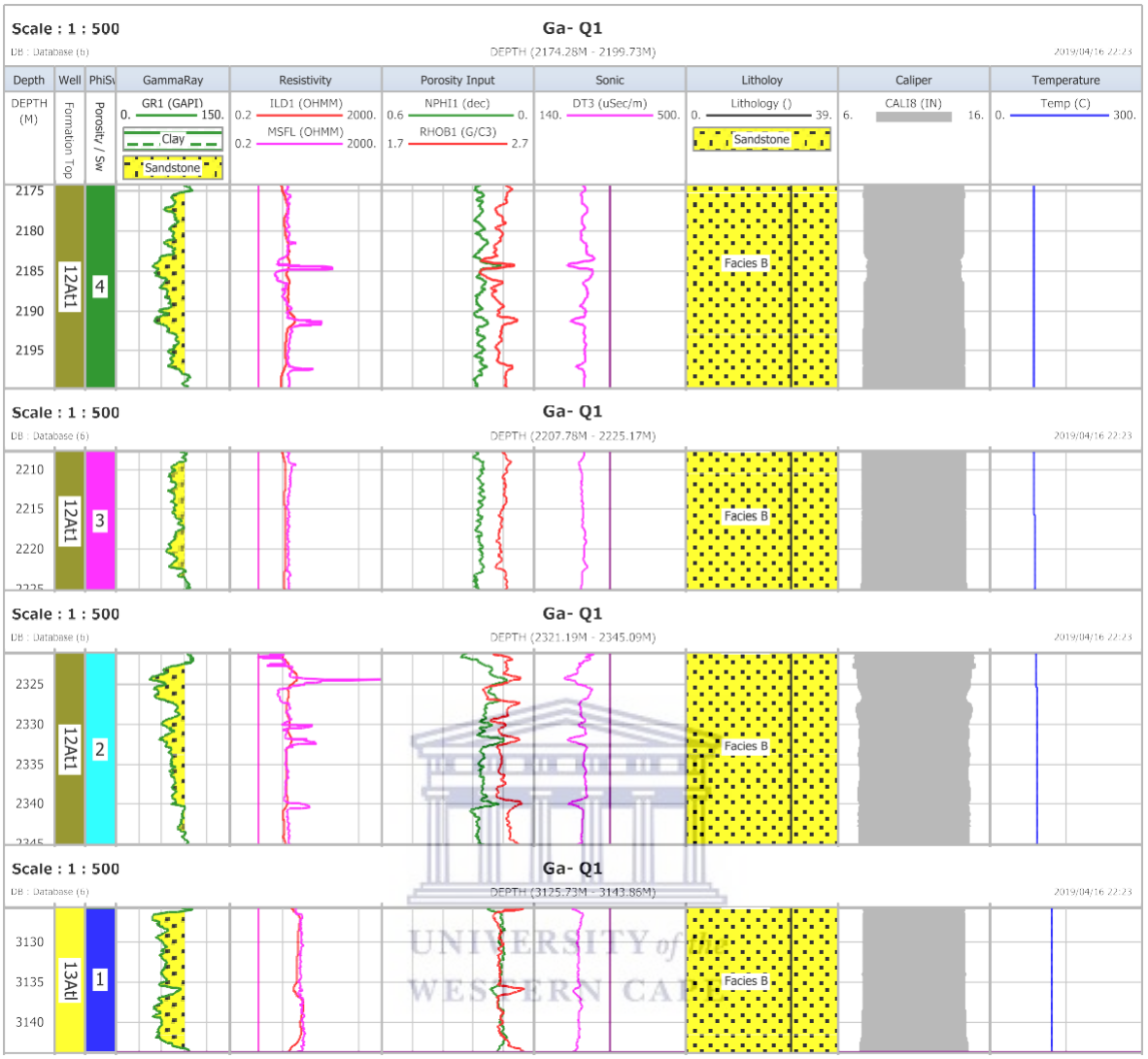

Figure 5. 14: Well logs representing well Ga-Q1

The identified reservoirs numbered 1-4 are of the following depths; 1. 3125.7m -3143.9 m, 2. 2321.1 m- 2345.1m, 3. 2207.8 m – 2225.8m and 4.2174.3 m- 2199.7 m. In well Ga-Q1, reservoir 1 is identified by well formation top 13At1, and reservoir 2-4 is identified by 12Atl1, therefore reservoir 1-4 are of Aptian age.

Well Ga-Q1 was mainly characterised by serrated gamma ray log (GR1) in track 4. The shape of the gamma ray log was used to further identify depositional environment as depositional environments varied throughout the depth of the well and subsequently the basin.

The majority of well Ga-Q1 zone 1-4 do not display specific shapes but rather a combination of serrated and cylindrical GR shapes. The majority being serrated represents fluvial floodplain as well as sediment deposition under the influence of a deep marine slope.

Zone 1 displays a dominating cylindrical shape which displays uniform deposition without any breaks in between. This is typical of a depositional environment influenced by aeolian action in combination with braided fluvial channel and submarine canyon fill which was potentially assisted by deposition of evaporites in the basin which is further supported through well completion reports.

In zone 2 and 4 the resistivity (purple curve) in track 5 shows patterns that are significantly deflecting towards the right hand side indicating high resistivity values. These high resistivity values indicate low water saturation, the presence of hydrocarbons, as well as a limited distribution of diagenetic clay such as chlorite (Nadeau, 2000). In zones 1 and 3 the resistivity is relatively low, meaning that there is presence of water in the pore spaces which accounts for decreased resistivity levels. In addition to this, the low resistivity is indicative of an increased distribution of diagenetic clay minerals and consequently decreased permeability (Nadeau, 2000).

Track 6 represents the density and neutron curve. In places where the density curve is towards the left, this curve was not in contact with the neutron curve thus forming a plume. The density curve moving towards the left with the lower densities indicates the presence of sandstones, where the reservoirs have been identified. In reservoir 1 the neutron and density curves show an overlay indicating the presence of limestone. The neutron curve is seen to be trending towards the lower values, this is particularly seen in reservoir 2-4. In the identified reservoirs where the neutron and density logs cross each other forming plumes, it indicates the presence of gas and/or light hydrocarbon and are known as gas plumes. Gas contains considerably lower amounts of hydrogen per unit mass leading to a relatively low neutron response (Fens, 2000). In track 7 the decrease in the sonic curve also assisted in identifying reservoir zones, this is because a decrease in sonic log values is accompanied by an increase in effective porosity. Lithofacies represented by track 8 are grouped as facies B which is argillaceous sandstone, meaning that these are poor and tight reservoirs as the argillaceous formation highly decreases the porosity to form an overall compact formation. The irregularities in depths 2182m- 2187m and 2325m- 2328m indicate the presence of possibly washed out zones and fracturing as a result of a collapse which can be identified through caliper log in track 9. This is caused by drilling mud filtrate situated at a proximal distance to the drilled area being rearranged, as a result these areas tend to be a mixture of mud filtrate and collapsed sedimentary rock. Track 10 represents the increase in temperature with increasing depth.

5.2.2. Petrophysical Evaluation of Well Ga-Q2

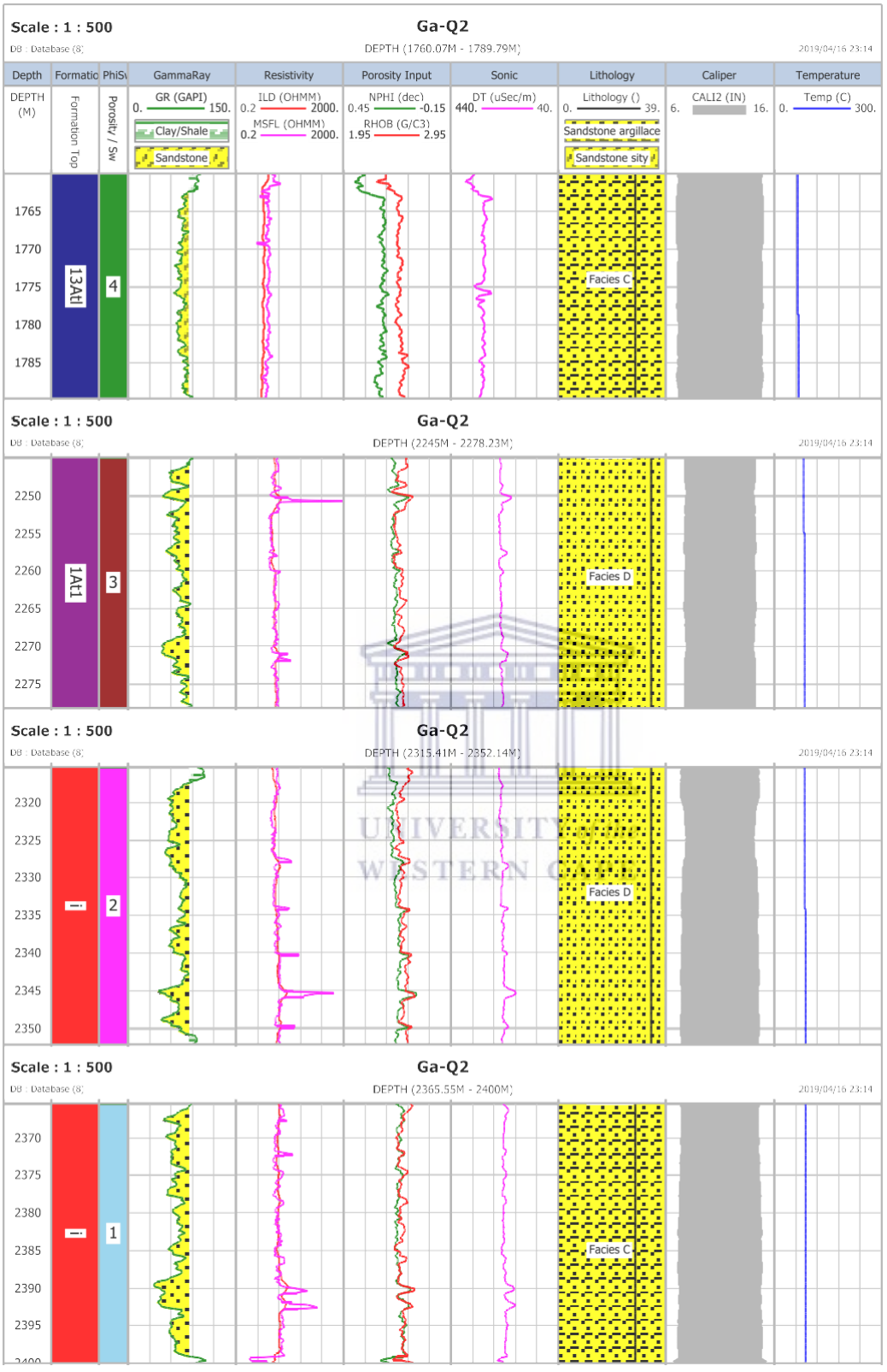

Figure 5. 15: Well logs of well Ga-Q2

The identified reservoirs numbered 1- 4 are of the following depth intervals; 1. 2365.5 m -2400 m, 2. 2315.4 m- 2352.1m, 3. 2245 m – 2278.2m, 4.1760 m- 1789.8 m.
Track 2 shows that reservoir 1 and 2 fall under formation top i, reservoir 3 under 1At1 and reservoir 4 under 13At1. These formation tops correspond to the lower and middle Cretaceous age (Valanginian and Aptian).

From zone 1 -4 the overall lithology is characterised either by serration shape or serration combined with another shape. In zone 3 track 4 at approximately 2270 m, a funnel shape can be seen indicating that the lithology is prograding upwards. The formation of the top part of zone 2 resembles that of a cylindrical shape with slight serration. The majority of the lithology with saw teeth or serration represents fluvial floodplain and deep marine slope depositional environment.

The resistivity logs namely deep and shallow resistivity represented in track 5 provide significant information about the fluids within the pore spaces. Zone 4 is characterised solely by low resistivities. From zone 1- 3 there is a combination of low resistivity with some high peaks. The low peaks represent areas of water in pore spaces and wide distribution of diagenetic clay. The high peaks particularly in zone 2 is a good hydrocarbon indicator and show a limited distribution of diagenetic clay.

The density and neutron curves represented by track 6 do not have significant cross over between curve NPHI and RHOB which was seen in previous well inferring the presence of gas. Although various depths are marked with density neutron cross over the space in between is quite small and at some places, it resembles an overlay of the 2 logs. This overlay in the neutron and density curve is indicative of limestone. In reservoir 4 the NPHI curve is on the right of the RHOB, whereas in the proceeding 3 reservoirs it is to the left of the RHOB curve indicating the presence of gas. It is evident that minor amounts of gas/light hydrocarbon are more likely to be present at deeper depths with reservoir 1 having the greatest chance of gas presence, according to readings deduced from track 5. This is because gas is being represented by lower hydrogen per unit and thus low NPHI reading. The NPHI curve shows higher values at shallower depths in reservoir 4 and gradually decreases towards reservoir 1.

The RHOB curve simply represents slight density differences within the same sandstone lithology, where the lower values may be a result of minor pore spaces and the higher values represent the actual rock occupying space.

The sonic curve has an inverse proportionality to porosity, therefore a decrease in the sonic curve in track 7 is accompanied by an increase in effective porosity. The sonic log has higher values at the

shallower depths of zone 4 which slightly decreased from zone 3 where they became more constant throughout to zone 1, and therefore remain consistent in these bottom 3 zones.

Lithofacies represented by track 8 are grouped into facies D in zone 1 and 4, and facies C in zone 2 and 3. Facies C indicating a sequence of interbedded sandstone, siltstone and claystone with traces of pyrite and facies D indicating an argillaceous sandstone sequence.

Unlike the previous well, the caliper log in track 9 indicates a good well throughout the reservoirs as there are no discrepancies in a caliper log shape. With regards to the temperature in the last track, it shows a slight increase from top to bottom.

5.2.3. Petrophysical Evaluation of Well Ga-Z1

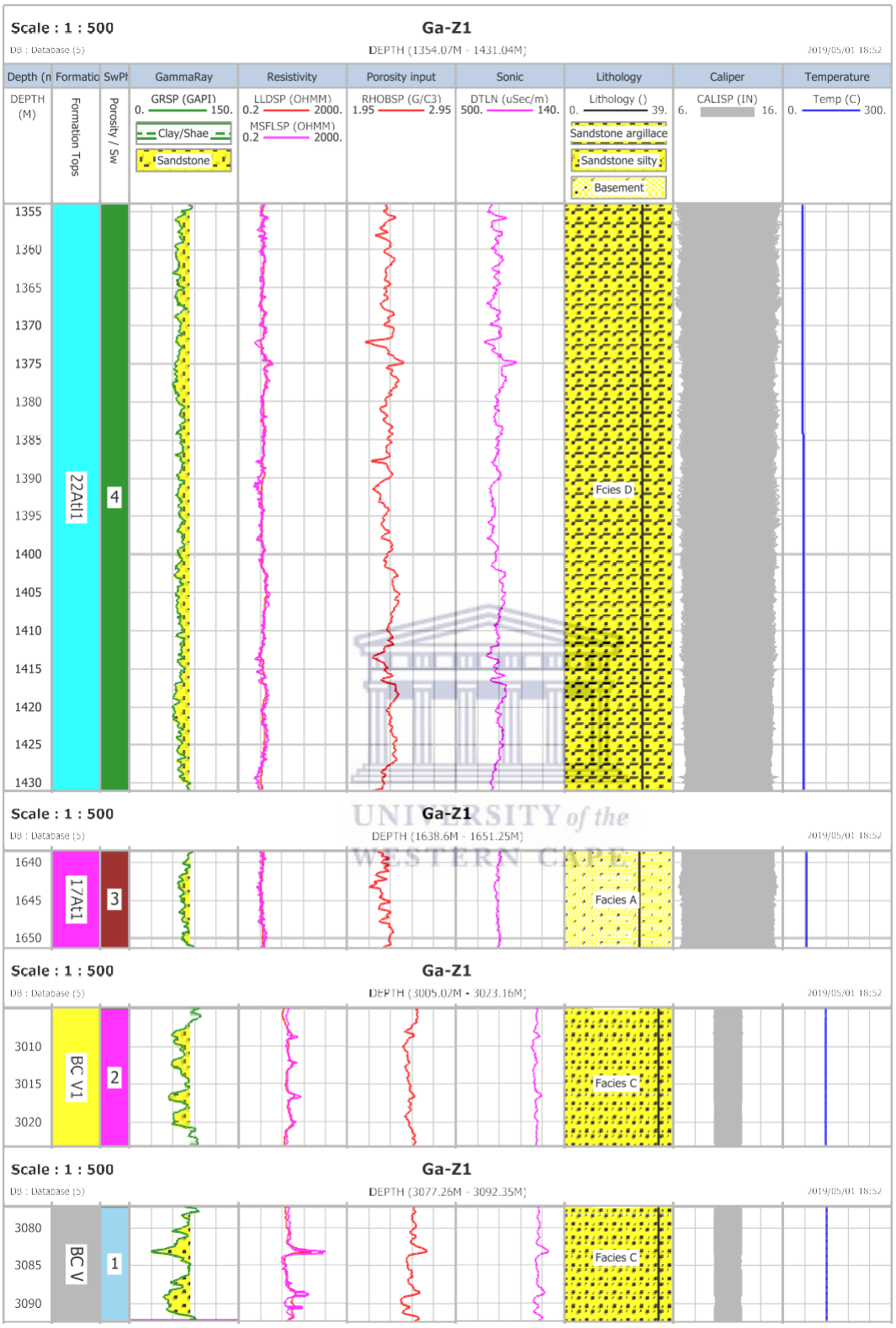

Figure 5. 16: Well logs of well Ga-Z1

The identified reservoirs numbered 1- 4 are from the following depth intervals; 1. 3056.8m -3096.5 m, 2. 3003.8m- 3047.5 m, 3. 1638.6 m- 1651.3 m, 4. 1354 m- 1432.2 m. In track 2 reservoir 1 and 2 are

represented by formation tops 17At1, reservoir 3 is a combination of 22At1 and 17At1 with 22At1 making up the majority of the reservoir, and reservoir 4 in 22At1 formation. Both these tops belongs to the late Cretaceous age with 22At1 corresponding to Maastrichtian stage and 17At1 corresponding to Campanian stage.

Well Ga-Z1 reservoirs are dominated by a cylindrical shape which is most eminent in zone 4 which corresponds to depths 1354m – 1432.2m. From zone 1- 3 in track 4 this well is dominated by combination of cylindrical and serrated gamma ray curve. The cylindrical shape implies depositional environment under influence of aeolian forces, braided fluvial channel fill and submarine canyon fill with partial evaporate fill of the basin.

Well Ga-Z1 is the only well without a neutron curve therefore track 5 is solely occupied by a density curve and therefore the gas effect cannot be determined for this well. The density curve moving towards the left with the lower densities indicates the presence of sandstones, where the reservoirs are located. All these cases with the lower densities corresponded to a fall in the gamma ray log, and the zones with higher densities corresponded to an increase in gamma ray indicating a shaly lithology. As these reservoirs were selected on their basis of them being sandstone, the lower densities within the sandstones could be areas with slightly dispersed clay particles thus holding slightly higher amounts of radiation, however the overall lithology is sandstone.

The resistivity logs of track 5 do not show much variation between shallow and deep resistivity and they are both rather constant from the first reservoir all the way to the fourth reservoir. This means that there is not much variation of fluids within the pore spaces. Both resistivity's do however remain on the lower values therefore there is a great chance that these reservoirs are occupied by saline waters as well as a significant distribution of diagenetic clay.

The decrease in sonic log curve suggests an increase in porosity, it is evident that there has been no significant changes in porosity as comparison is made from the first to the last reservoir. The curve remains constant as it lies towards the left of the reference line (dark purple straight line) in track 7, with a very short peak at approximately 1375m just crossing the reference line towards the right.

Lithofacies in track 8 are grouped into facies C in zone 1 and 2, D in zone 4, and A in zone 3. Facies A comprises of interbedded claystone and siltstone with well-developed quartz sand at the base as well as occasional sandstone and limestone and minor dolomite stringers. Facies C indicating a sequence of interbedded sandstone, siltstone and claystone with traces of pyrite and facies D indicating an argillaceous sandstone sequence. Out of the 4 zones zone 1 and 2 are the most likely to be the more conducive reservoir as they consist of interlayers of pure sandstone which is the more suitable

lithology for an optimal reservoir as it makes room for porosity. These two zones are followed by zone 3 which to a lesser extent only has a few stringers of sandstones and limestone. The well-developed quartz sand found at the base of this facies has a constructive contribution to the reservoir as it is not tightly compacted and allows room for fluids. Lastly zone 4 being of argillaceous sandstone is the poorest reservoir out of the 4 reservoirs.

Well Ga-Z1 is similar to Ga-Q2 in terms of caliper log as it does not show any signs of a bad hole, as the entire depth runs through the borehole unaltered by for example borehole fluids and physical force applied upon drilling. Therefore track 9 resembles nothing but a perfectly mirrored caliper log shape. Lastly in track 10 is a constant temperature curve which is also unaltered without the slightest increase or decrease with depth. Although temperature is generally expected to increase with depth, the constant temperature curve is most likely due to the reservoirs not occurring in a wide depth range and therefore an increase in temperature would have been noticeable at deeper depths.

5.2.4. Petrophysical Evaluation of Well Ga-E2

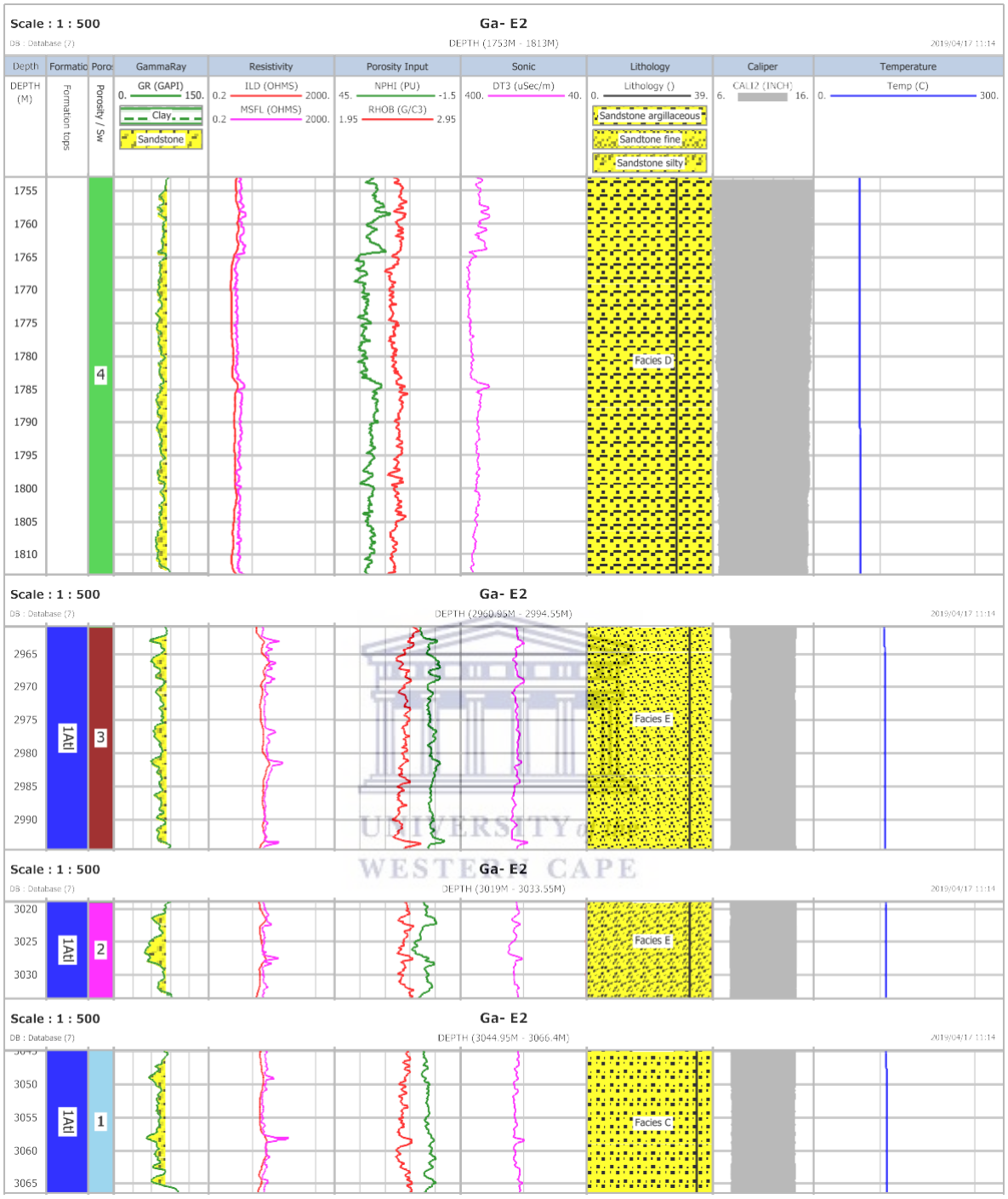

Figure 5. 17: Well logs of well Ga-E2

The identified reservoir numbers 1- 4 are of the following depth intervals; 1. 3045 m-3066.4, 2. 3019 m- 3033.6 m, 3. 2961m- 2994.5 m, 4. 1753 m- 1813 m. In well Ga-E2 reservoir 1- 3 all share a common formation top, being 1At1, just like well Ga-Q2 reservoir 3, meaning that these reservoirs also represent the Valanginian age.

Well Ga-E2 is also dominated by a combination of cylindrical shape with slight serration, particularly in reservoir 4. This implies that these sediments were deposited under the influence of fluvial floodplain, deep marine slope, as well as braided fluvial channel and submarine canyon fill. Reservoir 4 shows deposition that is almost uniform and irregularities in deposition begin to be more eminent from reservoir 1- 3 as the serrated shape becomes more defined. Zone 2 represents a proximal of 5 metres of hour glass shape at depths around 3025 m deep. Therefore these sediments are a result of reworked offshore bar along with regressive to transgressive shore face delta. Reservoir 1 and 3 are that of a typical serrated shape as they are mostly influence by deep sea fan deposition.

The density and neutron curve in track 6 are located with quite some distance between each other throughout the depth of the log, but are in brief contact at depths reaching 2961m. In reservoir 4 the neutron curve is trending towards the left of the density curve making it more likely for this interval to possess light hydrocarbons within its interstitial and larger pore spaces. There is a significant increase in neutron values form reservoir 1- 3 where it thereafter has a relatively constant reading and is situated to the right of the density curve. Unlike the neutron curve, the density curve maintains a relatively constant range throughout the identified reservoirs which further supports that the lithology of the identified reservoirs are indeed sandstones.

The following track representing resistivity curves is that of low resistivity in reservoir 4 (1755m-1810m). It is followed by an increase in overall resistivity from reservoir 1- 3, within these 3 deeper reservoirs are some high peaks in both deep and shallow resistivity curves, forming good hydrocarbon indicators and limited distribution of diagenetic clay. The lower resistivities present in reservoir 4 is most likely to be that of water in the rocks and a higher distribution of diagenetic clay compared to zones of higher resistivities.

The sonic log in track 7 is positioned to the left of the baseline (dark purple straight line) in reservoir 4, thereafter from reservoir 1- 3 it is positioned to the right of the baseline. Although reservoir 4 lies in the shallow most part of the well, the overall lower values in neutron, density, deep and shallow resistivity, and sonic logs in reservoir 4 make it the most likely to possess hydrocarbon content. The only factor working against it from being a completely ideal reservoir is that good reservoirs tend to be positioned at deeper depths.

Lithofacies represented by track 8 are grouped into facies C in zone 1, E in zone 2 and 3, and D in zone 4. Facies C indicating a sequence of interbedded sandstone, siltstone and claystone with traces of pyrite, facies D is that of argillaceous sandstone sequence and facies E of tight sandstone with traces of glauconite, pyrite and dolomite. Out of the 4 zones zone 1 is most likely to be the best reservoirs as a result of the interlayers of pure sandstone which is the more suitable lithology for an optimal reservoir. It is followed by zones 2 and 1, and lastly zone 4 of facies D.

With regards to the caliper log, it shows that the formation does not occupy the entire borehole space. There are some irregularities from reservoir 2- 4 with prominent irregularities at depths 1963m-1815m in reservoir 3 and reaching the uppermost of reservoir 2 at approximately 2960m. The deeper irregularity is seen in reservoir 2 at approximately 3025m. These irregularities in caliper shape are most likely due to washed out zones and fracturing as a result of a collapse. The temperature curve in the last track has an abrupt increase from reservoir 4 and thereafter has a very gradual increase all the way till reservoir 1.

5.3. Initial fluid saturation parameters interpretation

The intervals selected for the Pickett plots were chosen according to those best representing water zone intervals. The picket plots may be seen in Appendix A and the results of the electrical parameters of the reservoir zones are displayed in Figure 5.7; these parameters are briefly outlined below:

Rw = Formation water resistivity at formation temperature. The majority of methods that compute water saturation make use of knowledge of formation water resistivity at the formation temperature. The majority of the dissolved solids in hydrocarbon reservoirs are made up of sodium chloride with various other compounds. Salts break down into various ions when they dissolve, it is these ions that make the water conductive. An increase in salinity leads to a decrease in water resistivity, but for a given salinity water resistivity also decreases with an increase in temperature. Therefore saline waters are represented by lower water resistivity whereas fresh waters are represented by higher resistivity.

m exponent = Cementation exponent, is a function of the shape and distribution of pores (Luca and Jean-Claude, 2001). The cementation exponent is inversely proportional to the degree of connectivity of the pore, therefore, an increase in cementation exponent is accompanied by a decrease in pore network (Glover, 2009). A path that is more complex is accompanied by an increase in the cementation exponent. The process of dissolving mineral components in the interstices of sediments which ultimately leads to the combining of sediment to form new rock is a more accurate definition of exponent m (Boggs, 2006). A higher value of m is associated with a higher tutosity value (Ellis and Singer, 2007) (to be discussed further below). The cementation exponent (m) of the four wells ranges

from 1.98- 1.99 meaning that they are all moderately cemented with clay type that is either detrital, diagenetic or a mixture of the two.

Table 5. 6: Classification of rock cementation

Classification	**Cementation (-m) values**
Highly cemented	2.0- 2.2
Moderately cemented	1.8- 1.9
Slightly cemented	1.6- 1.7
Very slightly cemented	1.4- 1.5
Not cemented	1.30

(Pirson, 1958)

n exponent = Saturation exponent; a parameter that depends on the type of rock as well as the connection of the pores. The following affect the value of n; wettability, type and amount of clay, overburden pressure and reservoir fluid distribution (Tiab & Donaldson, 2015). The measured water saturation exponent for all of the wells was 2.

a factor = value of tutosity (constant), it is determined from the slope of the formation resistivity factor versus porosity plot. This value reflects the tutosity of the interconnected pore space (Luca & Jean-Claude, 2001). The value for all of the 16 identified reservoirs is 1 which depicts a well compacted formation throughout. Values lower than 1 depict poor consolidation and values greater than 1 depict extremely tight compaction, i.e. lower connectivity (Bennion et al., 1996).

Table 5. 7: Water saturation parameters

Zones	Well name	Zone	m exponent	N Exponent	a factor	Rw	Gr min	Gr max	Temp (degrees Celsius)
1	Ga-Q1	1	1.99	2	1	0.00213	49	100.87	87.45
2	Ga-Q1	2	1.99	2	1	0.00213	66	99.187	88.582
3	Ga-Q1	3	1.99	2	1	0.00213	43.781	103.43	93.001
4	Ga-Q1	4	1.99	2	1	0.00213	47.937	101.18	123.46
5	Ga-Q2	1	1.98	2	1	0.0165	64	101.87	67.927
6	Ga-Q2	2	1.98	2	1	0.0165	47.093	89.875	84.961
7	Ga-Q2	3	1.98	2	1	0.0165	42.281	107.31	87.487
8	Ga-Q2	4	1.98	2	1	0.0165	36.343	108.18	89.202
9	Ga-Z1	1	1.99	2	1	0.0124	59.625	87.062	57.264
10	Ga-Z1	2	1.99	2	1	0.0124	51.437	138.62	59.945
11	Ga-Z1	3	1.99	2	1	0.0124	36.187	100.81	62.27
12	Ga-Z1	4	1.99	2	1	0.0124	29.687	104	66.851
13	Ga-E2	1	1.99	2	1	0.014	64.788	88.328	73.705
14	Ga-E2	2	1.99	2	1	0.014	56.428	90.145	113.13
15	Ga-E2	3	1.99	2	1	0.014	49.071	91.371	114.73
16	Ga-E2	4	1.99	2	1	0.014	51.932	102.81	115.34

5.4. Poroperm plot

Porosity is a void fraction and a property that determines the empty spaces in a material and forms a fraction of the volume of voids over the total volume, either between 0 and 1 or as a percentage (0-100). Porosity is controlled by various factors such as the rock type, pore distribution, cementation, diagenetic history as well as composition. It is not controlled by grain size, because the volume between the grain spaces is only related to the method of grain packing. Porosity can be determined from the following equation:

$$\text{Porosity} = \frac{\text{Volume of voids}}{\text{Total volume of rock}}$$

Permeability is the property of rocks that indicate whether or not fluids in the form of gas or liquid can flow through the rocks. The higher the permeability the more favorable it is for the fluids to flow at a faster rate through the rocks. It is influenced by the pressure present in the rocks. The unit used to measure permeability is Darcy which received its name from Darcy (Klinkenberg,1941).

"Darcy's law is an equation that describes the flow of a fluid through a porous medium, for example sandstone. The law was formulated by Henry Darcy and it is based on the results of experiments" (Darcy, 1856).

Darcy's Law equation:

$$Q = -\frac{(Pin - Pout)}{\mu L}$$

Where:

Q= Flow rate

k = A constant of proportionality characteristic of the sand/shale pack (permeability)

A= Cross sectional are of sand/shale pack

P_{in}- P_{out}= Fluid pressure gradient

μ= Viscosity of the fluid

L= Length of sand/ shale pack

(Darcy, 1856)

Although porosity plays a huge role in the influence of permeability, both the permeability and porosity have to be relatively high in order to yield significant flow. For example, a rock containing a very high porosity accompanied by a low permeability will not yield a significant flow and is referred to as a "tight rock" and usually needs to be fractured in order to yield a flow.

A poroperm plot is one whereby the permeability (on logarithmic scale) is plotted against the porosity for a particular litho- unit and a correlation coefficient is obtained. The purpose of the correlation coefficient is to determine a linear relationship between the permeability and porosity from the plot. If porosity is not fully correlated to and influential on the permeability it means that there are other factors influencing the permeability such as connectivity to the flow paths of the rock, pore geometry of the rock; permeability is also a directional quantity which can be affected by heterogeneous or directional properties of the pore geometry (Glover, 2000).

The general cut off value for the permeability for a gas reservoir is 0.1 miliDarcy therefore the corresponding porosity should be cross lined and identified accordingly on the y axis which may allow determination of porosity percentage.

The permeability logs in the present work were calculated using the regression equation obtained from the poroperm plot. The principle behind this method was to obtain a correlation coefficient between porosity and permeability that is close to the value of 1. The closer the value is to 1 the more reliable the calculated logs of permeability are. The equations used to calculate the permeability are presented in Table 5.8- 5.10.

5.4.1. Well Ga-Q1

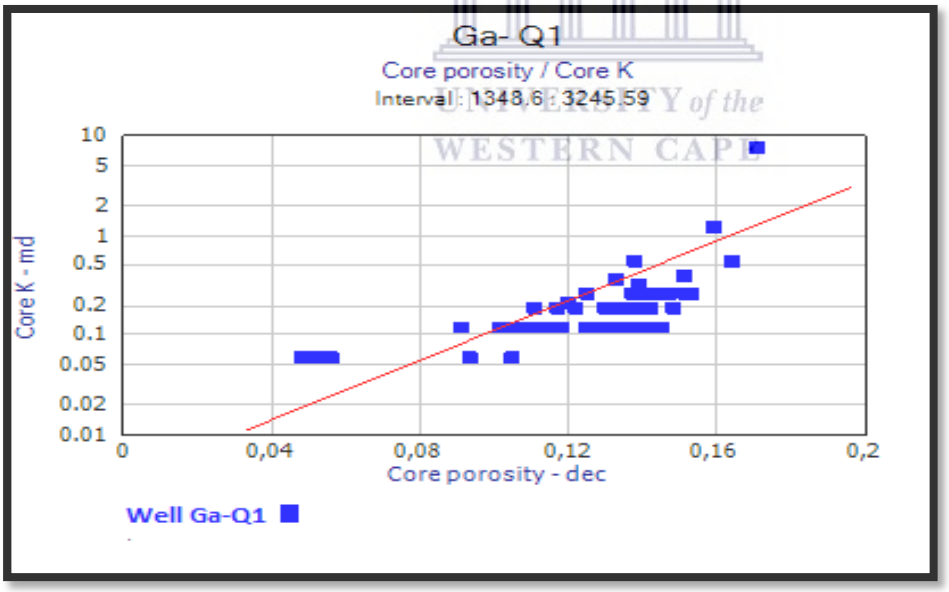

Figure 5. 18: Ga-Q1 poroperm plot

In Figure 5.18, it is evident that the core porosity and core permeability have a directly proportional relationship to each other. However, there are a few outliers which deviate from the line of best fit. The correlation coefficient (R2) is 0.60 showing a relatively fair correlation between the two parameters represented in the plot. The correlation coefficient of this well shows that the lithology

within the interval is clay cemented sandstones as classified in Figure 5.19. If porosity is not fully correlated to and influential on the permeability it means that there are other factors influencing the permeability such as connectivity to the flow paths of the rock and pore geometry of the rock. Permeability is also a directional quantity which can be affected by heterogeneous or directional properties of the pore geometry (Glover, 2000).

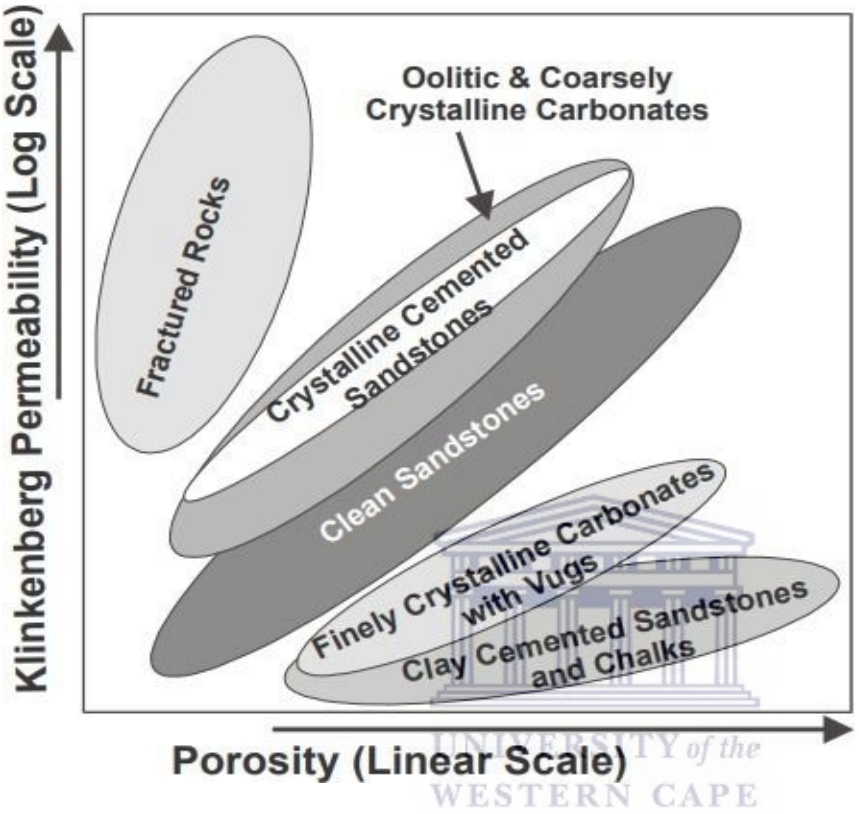

Figure 5. 19: Porosity vs permeability poroperm crossplot (Glover, 2000)

Table 5. 8: Porosity- permeability function

Well name	Porosity- permeability function/ equation	correlation coefficient (R^2)
Ga- Q1	y= 10^(-2.78009+ 17.7201 * PhiSon)	0.60

5.4.2. Well Ga-Z1

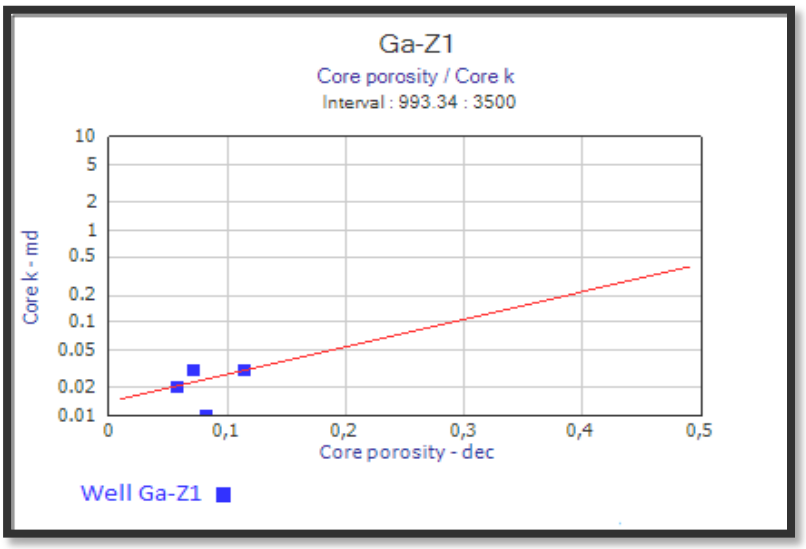

Figure 5. 20: Ga-Z1 poroperm plot

Well Ga-Z1 had very few data available for the plot. As a result, there were not a lot of anomalies that could have possibly discredited the output plot.

This reliance of interpretation based on a little data has slightly reduced confidence in the results for this particular well, but was used as they are still an indication of the porosity and permeability of the well. A linear relationship between the core porosity and core permeability has been established as the line of best fit goes through 50% of the points. With this having been accomplished the correlation coeficient was reached at 0.85, meaning that there is a good relationship between the two parameters.

Table 5. 9: Porosity- permeability function

Well name	Porosity- permeability function/ equation	correlation coefficient (R^2)
Ga- Z1	y= 10^(-1.8554+ 2.96695 * PhiSon)	0.85

5.4.3. Well Ga-E2

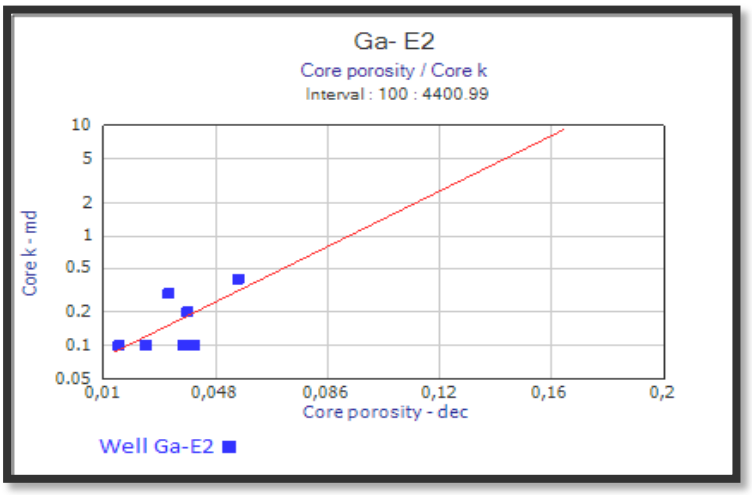

Figure 5. 21: Ga-E2 poroperm plot

In Figure 5.21 a correlation between the core porosity and core permeability indicates that they are directly proportional to each other, however, it is not a very convincing correlation as the correlation coefficient value is 0.45. The line of best fit partially goes through some of the points leaving a few at a short distance from the line of best fit. This is an indication that there are other factors affecting permeability apart from porosity such as the diagenetic factors.

Well Ga-Q1, Ga-Z1 and Ga-E2 have similar factors affecting the linear relationship between porosity and permeability, these external factors have a greater influence particularly on well Ga-E2 and by Ga-Z1.

The poroperm plot (Figure 5.21) reveals 0.1 mD as the trend constituting the majority of the permeability values and 0.03 (dec) makes up the majority of the porosity values.

Table 5. 10: Porosity- permeability function

Well name	Porosity- permeability function/ equation	correlation coefficient (R^2)
Ga- E2	y= 10^(-1.23821+ 13.2397 * PhiSon)	0.45

5.5. Calibration of core data with log curves

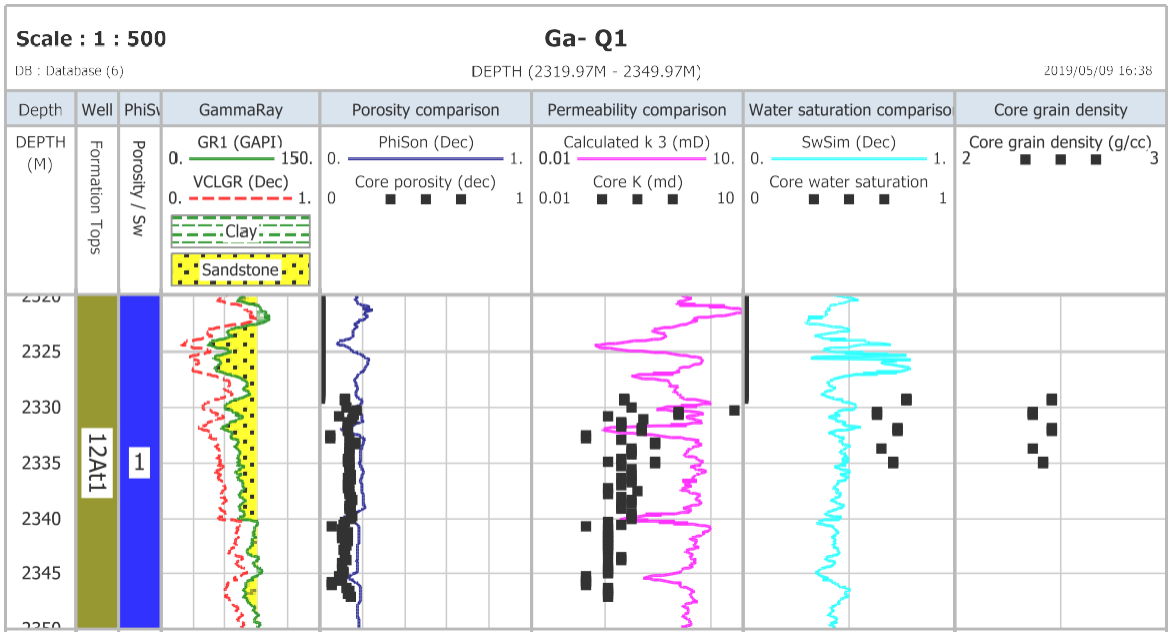

Figure 5.22: wireline logging of calibrated logs

The calculated effective porosity (PhiSon), permeability and water saturation logs were calibrated with core porosity, core permeability and core water saturation to validate the results. A good match was found between log analysis and core data at depths of 2321.05 m to 2349 m for porosity in well Ga-Q1. The core and calculated permeability showed a poor calibration between the two with a few core data points aligned with the curve. The core water saturation showed a noticeable deviation from the calculated water saturation indicating minimal correlation between the core and calculated water saturation. The poor relationship exhibited by the correlation between core and calculated water saturation is most likely a result of diagenetic factors. This is supported through the core grain density as it represents the presence of clay and mica mineralogy.

Previously, the difference between high core and low log water saturation readings were postulated to be the result of water-based drilling mud which was unaccounted for (Thomas et al., 2003). However, it has been recently shown that the presence of glauconite causes high saturation values in rock samples where the mineral is prevalent. Glauconites, especially in the form of pellets (discussed further in thin section and SEM) have a tendency to retain water in their pore spaces, especially in core samples regardless of their distribution within the matrix (Thomas et al., 2003). This leads to core samples having higher water saturations and explains the poor correlation of water saturation in Figure 5.22. Another effect of glauconite in petrophysical properties is the reduced variation in porosity that is accompanied by an increase variation in permeability (Thomas et al., 2003), as seen in well Ga-Q1. The average grain density is 2.416 g/cm3 and is a good indication of shale lithology which

is derived from a mixture of clay and siltstone.

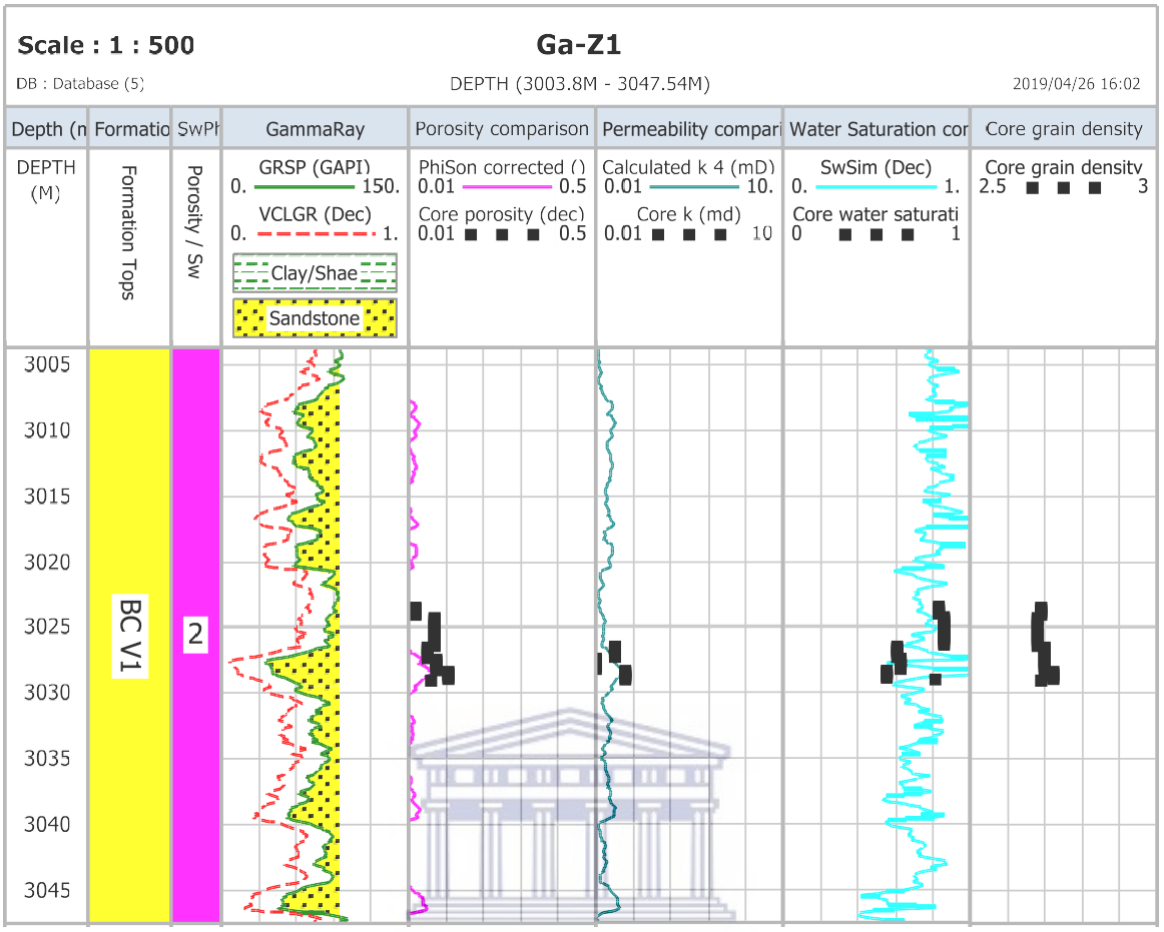

Figure 5.23: Core and log calibration for well Ga-Z1

There is a great match between log curve and core data at depths of 3023 m to 3030 m in all three petrophysical parameters. The results of the correlation are considered to be consistent with the correlation coefficient for the permeability wireline log. Therefore, external factors did not highly affect these three parameters meaning there was not a lot of diagenetic factors affecting this zone. This also means that there were no ambiguous readings with logs as log measurements are not static.

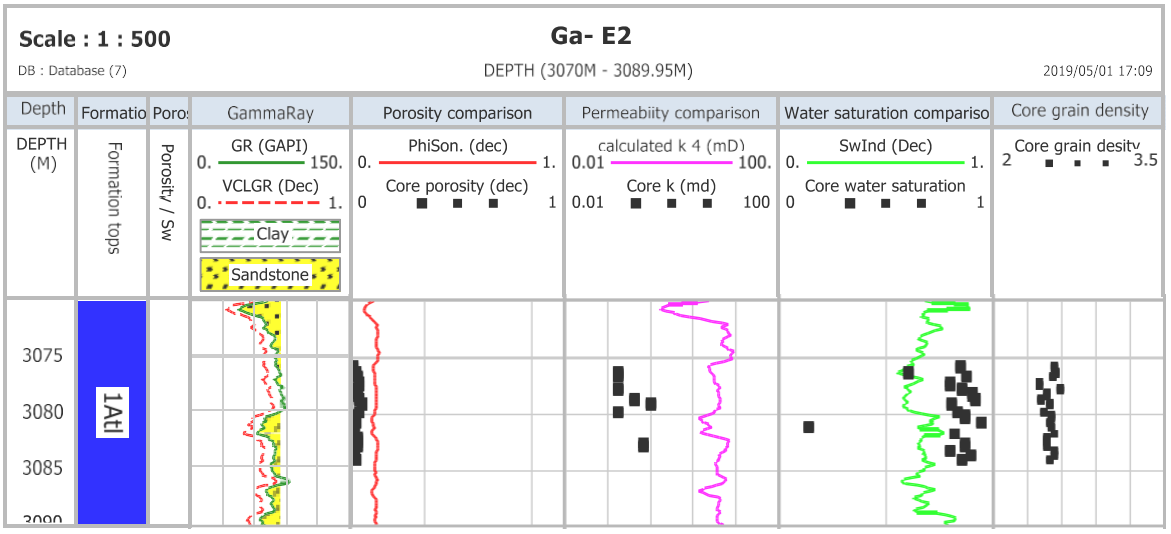

Figure 5. 24: Core and log calibration for well Ga-E2

These core results were retrieved between depths 3075m- 3085m. Well Ga-E2 did not show a satisfactory calibration. The porosity comparison is not too far from each other, however, the core porosity is noticeably lower than the calculated log. The permeability comparison log shows the poorest correlation as the core samples are located at a noticeably far distance to that of the calculated permeability. The water saturation comparison shows that there is only one point which lies on the curve, with the majority of the core data readings at the higher end values of the curve but still relatively close to the curve.

The poor correlation exhibited by the permeability was expected as the correlation coefficient determined from the poroperm plot was 0.45. The core grain density is representative of clay mineralogy which seems to be the leading cause for the poor correlation, as the absence of these diagenetic effects would lead to a strong calibration for all three parameters. The same trend seen in well Ga-Q1 is identified in this well, as the varying permeabilities are accompanied by little porosity variation.

5.6. Cut off determination of petrophysical properties

The cut off values serve as the input parameters for the elimination of reservoir intervals that will not be economically viable for production (Crain, 2018). Furthermore, cut-offs are usually applied to calculated results in order to exclude poor quality and unproductive zones. They are made for the purpose of removing the parts of the formation that are of negligible value to the petrophysical evaluation of the hydrocarbon zone (Worthington & Cosentino, 2005). The physical characteristics of a reservoir are used as a basis for the cut-off determination. The 4 parameters presented below, namely; water saturation, volume of clay, porosity and permeability cut off were based on the typical cut off values as illustrated by Crain (2018).

Volume of clay/shale= 0.25-0.45

Phie= 0.03-0.16

Sw= 0.3-0.7

K= 0.1-1

A standard cut off value was applied in all four wells within the studied reservoir units because they are of similar age i.e. Cretaceous age. The standard cut offs would aid in elimination of bias when comparing petrophysical properties and diagenesis effects of one reservoir to the next. Therefore the applied permeability cut off was 0.1mD (this value is usually applied to gas reservoir), porosity was =>6%, water saturation was =<50% and volume of clay was =< 40%. This is to say for an interval to be classified as net pay the permeability must be equal to or greater than 0.1 mD, porosity equal to or greater than 6%, water saturation equal to or less than 50% and volume of clay equal to or less than 40%. These cut offs can be seen in Appendix B and C.

Some of the reservoir intervals may have hydrocarbons, however, there are other factors hindering their classification into the cut off range for economic viability such as diagenetic influences as these are primarily shaly sandstone reservoirs.

5.6.1. Water saturation cut off

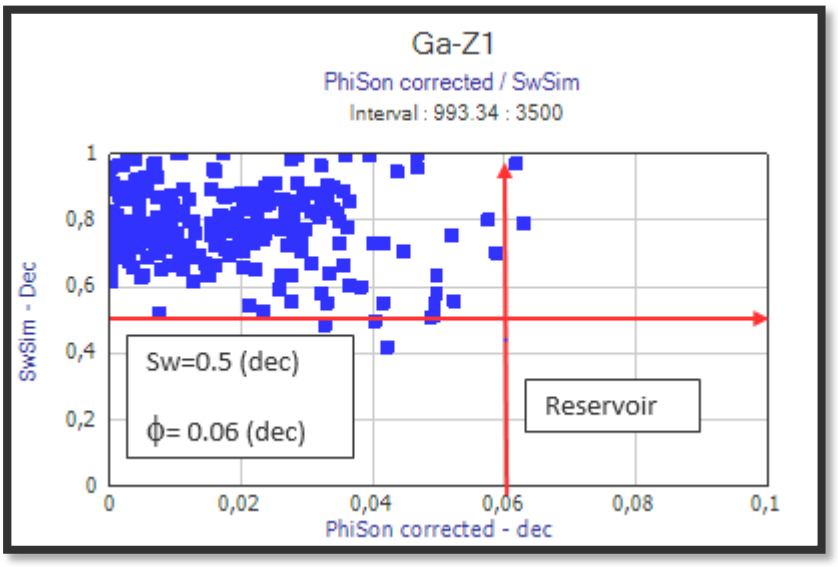

Figure 5. 25: Water saturation cut off for well Ga-Z1

The cut-off cross plots (Figure 5.25 and Appendix B) representing a delineation of the reservoir was annotated in order to produce a visual representation of the amount of values that fall within both the water saturation and porosity cut-off. The other 3 quadrants represent parts of the formation that have potential to be good reservoirs as some of them meet 50% of the criteria i.e. falling within the cut off zone for SW and not effective porosity and vice versa. In addition to this, there are also some parts that do not possess any potential as they do not meet either the water saturation or porosity cut off, these are found at the top left quadrant. For well Ga-Z1 the top left quadrant constitutes the majority of the values.

The order of viable reservoir potential starts with well Ga-Q1, followed by Ga-Q2, Ga-Z1 and then Ga-E2. Well Ga-Z1 has the least potential of having a viable reservoir as none of the values lie within the reservoir quadrant, meaning that it will result in extremely poor net pay and net reservoir outcomes.

5.6.2. Clay cut off

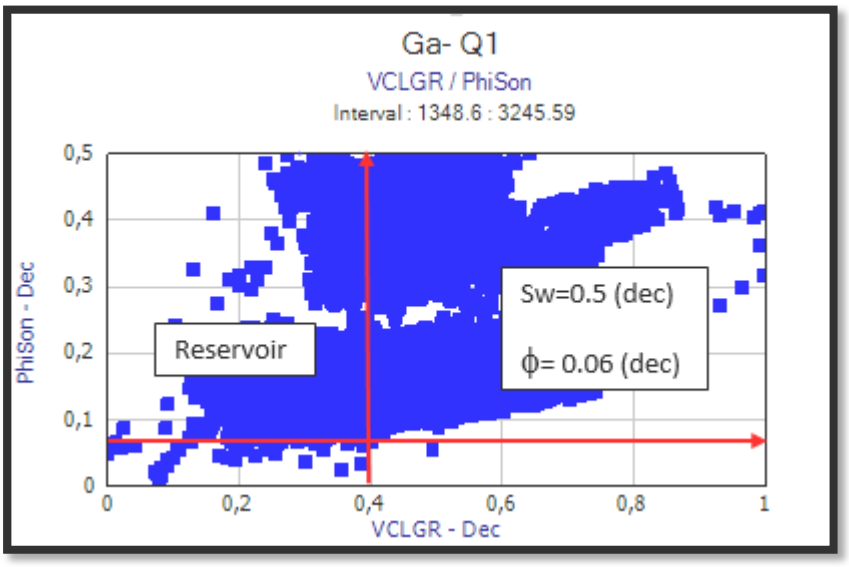

Figure 5. 26: VCLGR cut off for well Ga-Q1

Figure 5.26 is a cross plot of the volume of clay against effective porosity. It is a visual representation of the volume of clay and porosity cut off in order to assist in identifying reservoir flag and net pay. The data points within the top left polygon represent an area that qualifies as a net reservoir. For wells Ga-Q1, Ga-Z1 and Ga-E2 the majority of the points lie outside of the reservoir zones, with the majority of the points in well Ga-Q2 lying within the reservoir as shown in AppendixC.

The areas that do not possess any potential as they do not meet either the water saturation or porosity cut off are to be found in the bottom right quadrant. Very similar to SW cut off plots, well Ga-Q1 shows the most promising net reservoir.

5.7. Net pay and reservoir flags

Very similar to cut offs, there is no standard definition for net pay. Net pay can be described as the depth intervals of the well which contain economically viable hydrocarbons for production. “It defines the effective thickness pertinent to the identification of hydrocarbon flow units, that identifies target intervals for well completions and stimulation programs, and that is needed to estimate permeability through the analysis of well test data” (Worthington and Cosentino, 2005,p.276).

The net pay is an important factor as it essentially refers to the lithology that is of direct economic value, that when drilled, hydrocarbons are almost a guarantee. The flag tracks are a vital part of the evaluation of petrophysics because they improve the reservoir parameter determination. The reservoir flag refers to the thickness of the part of the rock that is able to contribute to economically viable production with today's technology, prices, and costs (Crain, 2018). It is an interval that

represents the part of the reservoir containing high storage space, mobility and significant hydrocarbon saturation.

N/G is the ratio between the net pay and gross reservoir (the entire reservoir column within the evaluation interval) and therefore is a reflection of how much of the total gross reservoir is economically viable. The N/G may be used for different scenarios that aim to serve different purposes. When incorporating this ratio to aid in interpretation, its particular purpose should guide the manner it is incorporated and used (Egbele et al., 2005). Through previous studies conducted there have been varying classifications that aim to best define this ratio of which some classifications tend to overlap, this is caused by petrophysical cut-offs being applied at different phases of investigations (Egbele et al., 2005). Various N/G examples may refer to “net to gross reservoir”, “net to gross pay”, “net reservoir to gross thickness” or “net reservoir to gross reservoir” etc., in this research the ratio refers to “net reservoir to gross reservoir”.

In order for the layer to be identified as net pay it need not fail any one of the cut- offs. Therefore, the net accounts for reservoir zones that comply with both the volume of shale and porosity cut-offs whereas the pay flag is established upon meeting requirements of the volume of shale, porosity as well as water saturation cut-off. As a result of the daily variation in technology, prices and costs; net pay is therefore a moving target. Previously ignored environments characterised by tight reservoirs or shaly zones have become prospective pay zones as a result of technology and further demand for hydrocarbons (Crain, 2018).

Through the cut-offs that were established, it is evident that some zones do not possess any viable hydrocarbons as both reservoir flag and pay flag are not displayed as output logs in the various porosity, water saturation and volume clay tracks. Therefore these were excluded from the log plot (reservoir and pay flag) results and only the zones including reservoir and pay flag were displayed. Well Ga-Q2 and Ga-Z1 are the only two wells where all four zones did not meet cut-offs and were therefore not included in the gross reservoir and net pay plots, however, Table 5.12 and Table 5.13 show the reservoir summary results for these two wells.

From well Ga-Z1 water saturation plot (Figure 5.25) there are no points present within the quadrant of the graph identified as the reservoir, this means that the 4 zones have failed one of the cut-offs and therefore no pay interval flag would be present.

The reservoir intervals that qualified as net pay were from Ga-Q1 zone 1-4 and Ga-E2 zone 1-3. The zones that did not meet the minimum requirements for net pay were not included in the pay flag

plots, but may be seen in Appendix D. Net pay and gross reservoir zones were presented in areas where the reservoir flag was green and the pay flag was red.

Figure 5. 27: Gross reservoir and net pay for well Ga-Q1

Table 5. 11: Well Ga-Q1 reservoir summary results

Zone name	Top depth(m)	Bottom depth (m)	Gross (m)	Net (m)	N/G	Av Phi (dec)	Av K (mD)	Av Sw (dec)	Av Vcl (dec)
Zone 1	3125.7	3143.7	18	16.26	0.903	0.135	0.722	0.322	0.262
Zone 2	2321.1	2345.1	24	10.89	0.454	0.159	1.46	0.452	0.342
Zone 3	2207.8	2225.8	18	3.09	0.172	0.163	2.17	0.486	0.389
Zone 4	2174.3	2199.7	25.4	9.19	0.362	0.221	2.45	0.460	0.353
All Zones	2174.3	3143.7	85.4	39.43	0.472	0.17	1.7	0.43	0.3365

The gross and net in the row “All zones” in Table 5.11 is a summation of the values of the 4 reservoirs and represents the total gross and total net that can be expected from the well. The total gross covers a thickness of 85.4 m and the total net is 39.43 m. From the N/G ratio it is evident that 47.2% of the well is able to produce hydrocarbons and the remaining 52.8% of the well does not have the same potential. Columns N/G, Av Phi, Av Sw, Av Vcl in the row “All Zones” represent the average values of the parameters represented by the 4 zones.

The porosity ranges from 13.5% in zone 1 to 22.1% in zone 4 and is classified as “fair to very good porosity” according to Table 5.3. The permeability ranges from 0.722mD in zone 1 to 2.45mD in zone 4 and is classified as “poor to fair permeability” according to Table 5.4. The porosity and permeability values decrease with increasing depths. This is an indication that the diagenetic processes are more prominent at deeper depths. The water saturation ranges from 32.2% in zone 1 to 46% in zone 4. The overall average water saturation form the 4 zones is just below the 50% limit at 43%. The volume of clay ranges from 26.2% in zone 1 to 35.3% in zone 4. The average volume of clay is just within the cut off value at 33.65%.

Table 5. 12: Well Ga-Q2 reservoir summary results

Zone name	Top depth (m)	Bottom depth (m)	Gross (m)	Net (m)	N/G	Av Phi	Av K (mD)	Av Sw (dec)	Av Vcl (dec)
Zone 1	2365.5	2400	34.5	0	0	0.094	n/a	0.748	0.176
Zone 2	2315.4	2352.1	36.7	0	0	0.0956	n/a	0.735	0.208
Zone 3	2245	2278.2	33.2	0	0	0.0966	n/a	0.776	0.205
Zone 4	1760	1789.8	29.8	0	0	0.1651	n/a	0.837	0.258
All Zones	1760	2400	134.2	0	0	0.1128	n/a	0.7735	0.21175

Well Ga-Q2 was the first well out of the 4 wells that did not have net pay reservoir as none of the zones met the cut-off requirements.

The porosity in Table 5.12 ranges from 9.4% in zone 1 to 16.51% in zone 4 and is classified as "poor to good porosity" according to Table 5.3. The permeability for this well could not be calculated due to the lack of conventional or special core analysis data. Similar to Ga-Q1 the porosity decreases with increasing depths of which the most significant decrease may be seen between the porosity transition in zone 4 at 16.51% to zone 3 at 9.66%. The water saturation ranges from 74.8% in zone 1 to 77.6% in zone 4. The overall average water saturation was well above the 50% limit at 77.35%. The volume of clay ranges from 17.6% in zone 1 to 25.8% in zone 4. The average volume of clay is just within the cut off value at 21.17%. The petrophysical properties of this well are generally poor.

Table 5. 13: Well Ga-Z1 reservoir summary results

Zone name	Top depth (m)	Bottom depth (m)	Gross	Net	N/G	Av Phi	Av K (mD)	Av Sw (dec)	Av Vcl (dec)
Zone 1	3077.3	3092.28	14.98	0	0	0.035	n/a	0.746	0.29645
Zone 2	3005	3023.2	18.2	0	0	0.071	n/a	0.708	0.33591
Zone 3	1638.6	1651.3	12.7	0	0	0.162	0.0162	0.786	0.35296
Zone 4	1354	1431	77	0	0	0.181	0.0173	0.804	0.30007
All Zones	3077.3	1431	122.88	0	0	0.1120	0.01675	0.761	0.3208

Well Ga-Z1 was the second well that did not have net pay reservoir as none of the zones met the cut-offs.

The porosity ranges from 3.5% in zone 1 to 18.1% in zone 4 and is classified as "negligible to good porosity". The permeability ranges from 0.0162mD in zone 3 to 0.0173 mD in zone 4 and is classified as "negligible permeability", zone 1 and 2 do not possess any permeability in the selected reservoirs. The porosity and permeability trend resembles that of Ga-Q1 as they decrease with increasing depths. The water saturation ranges from 74.6% in zone 1 to 80.4% in zone 4. The average volume of clay is just within the cut off value at 32.08%. The overall average water saturation is well above the 50% limit at 76.1%. The volume of clay ranges from 29.6% in zone 1 to 30% in zone 4. The total gross covers a thickness of 122.8 m and the total net is 0 m and the N/G ratio is also 0. Very similar to Ga-Q2, the petrophysical properties of this well are of poor quality.

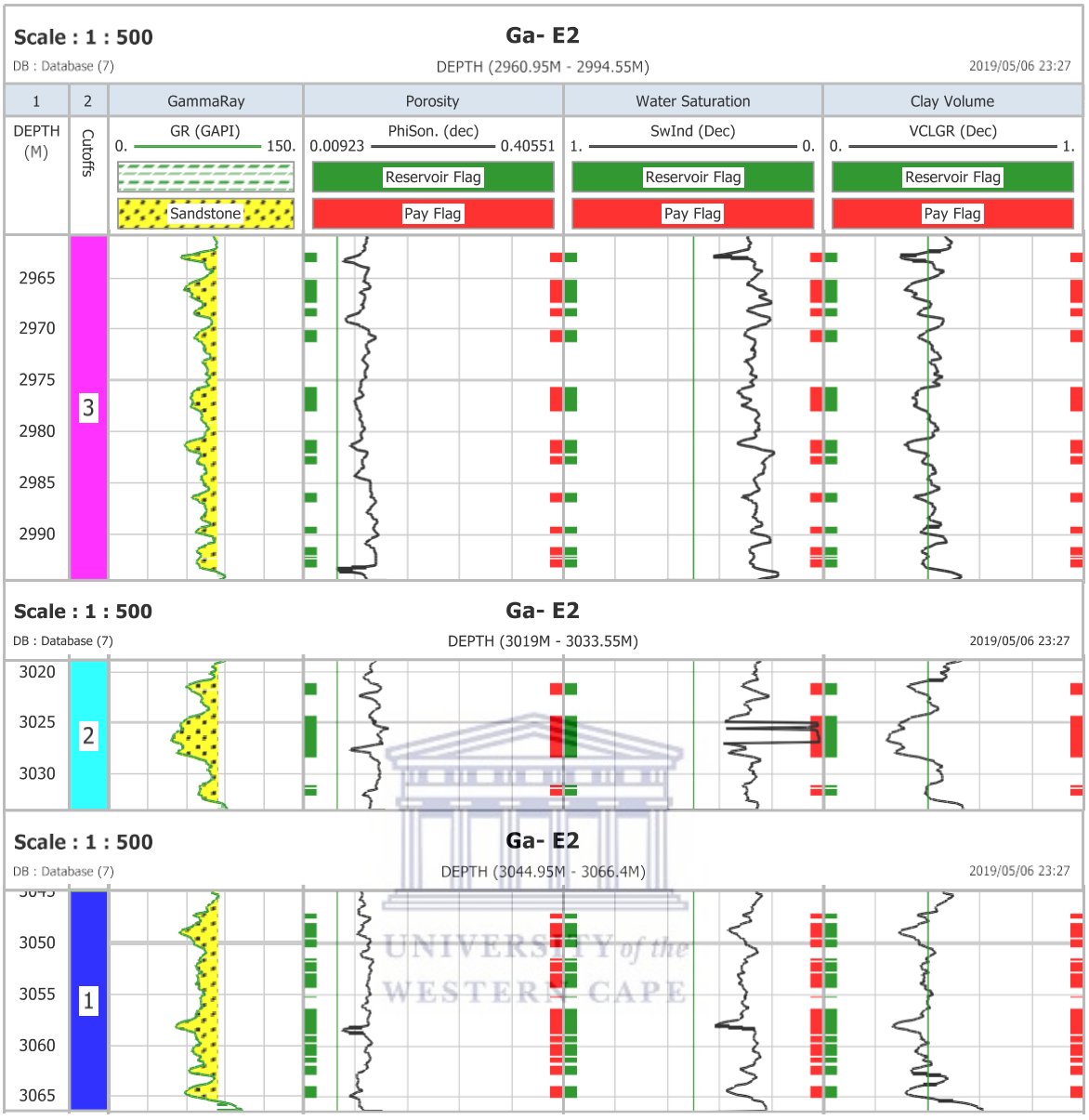

Figure 5. 28: Gross reservoir and net pay for well Ga- E2

Table 5. 14: Well Ga-E2 reservoir summary results

Zone name	Top depth (m)	Bottom depth (m)	Gross	Net	N/G	Av Phi	Av K (mD)	Av Sw (dec)	Av Vcl (dec)
Zone 1	3045	3066.4	21.4	33.3	0.208	0.1028	n/a	0.291	0.396
Zone 2	3019	3033.6	14.6	12.45	0.372	0.1167	1.404	0.2528	0.393
Zone 3	2961	2994.5	33.5	6.45	0.442	0.1031	2.211	0.263	0.399
Zone 4	1753	1813	60	0	0	0.286	3.27	0.721	0.4114
All Zones	3045	1813	229.5	52.2	0.34	0.152	2.295	0.381	0.399

The total gross covers a thickness of 229.5 m and the total net is 52.2m and the N/G ratio is also 0.34 meaning that only 34% of the entire well qualifies as conducive for production.

The porosity ranges from 10.28% in zone 1 to 28.6% in zone 4 and is classified as “fair to very good porosity”. The porosity shows a drastic increase particularly in zone 3 from 10.31% to 28.6 zone in 4. The permeability ranges from 1.404mD in zone 2 to 3.27mD in zone 4 and is classified as “fair permeability”. These permeability values show an overall decrease with an increase in depth as zone 1 shows a lack of interconnecting pores. The water saturation ranges from 29.1% in zone 1 to 72.1% in zone 4. The overall average water saturation is 38.1%. The volume of clay ranges from 39.6% in zone 1 to 41.14% in zone 4. The average volume of clay is just within the cut off value at 39.9%. Zone 1-3 qualify as net pay with zone 4 having values that do not meet the limit.

5.7.1. The 3D parameter viewer

The simulation of petrophysical parameters of a reservoir through 3D visualization serves as a significant contribution to the development of reservoir flow patterns (Nezhad & Tabatabaei, 2017) and multi-well trends.

The 3D parameter viewer was incorporated into this study in order to display the average calculated reservoir parameters for each well, namely porosity, permeability, water saturation and volume of clay. The calculated parameters only accounted for the reservoir intervals (the parameters are derived from the pay plot, however as a result of some reservoirs not meeting the cut off values, the calculated parameters constitute the average results of the identified reservoirs per well) and thus provided more insight on the spatial effect of diagenesis on reservoir properties. As a result of well Ga-Q2 not having calculated permeability, the permeability of the four reservoirs of this well was inferred through the surrounding wells as they share similar age and are of close proximity to each other.

The reservoir parameters were plotted on the 3D plot against True Vertical Depth (TVD). The legend bar located on the right-hand side of the plot was used to differentiate between the ranges of values, which was represented by the different shades of colours displayed within the scale in correspondence to the plot.

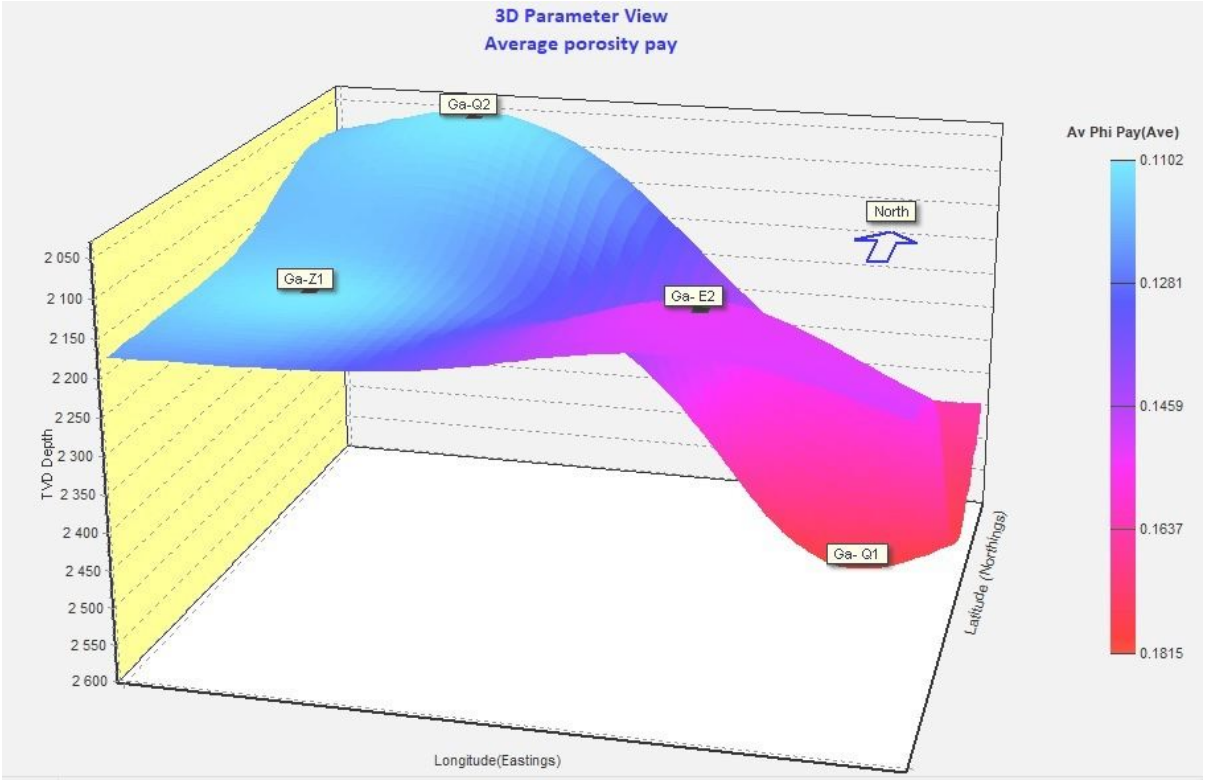

Figure 5. 29: 3D parameter view showing average porosity

Figure 5.29 shows the distribution of porosity across the studied wells. The striking trend exhibited by the model is an increase in porosity from the north west/west direction to the east. Well Ga-Q2 with an average porosity of 11.28% is situated towards the north west direction and well Ga-Z1 with an average porosity of 11.20% is situated towards the west of the plot; these two wells are comprised of low porosity values and are classified as “fair” porosity. Well Ga-E2 is characterised by higher average porosity of 15.2% and Ga-Q1 comprise the highest average porosity of 17% within this field; both the higher end porosity wells are classified as “good” porosity. The overall trend for this parameter reveals an increase in porosity as navigation trends more eastward.

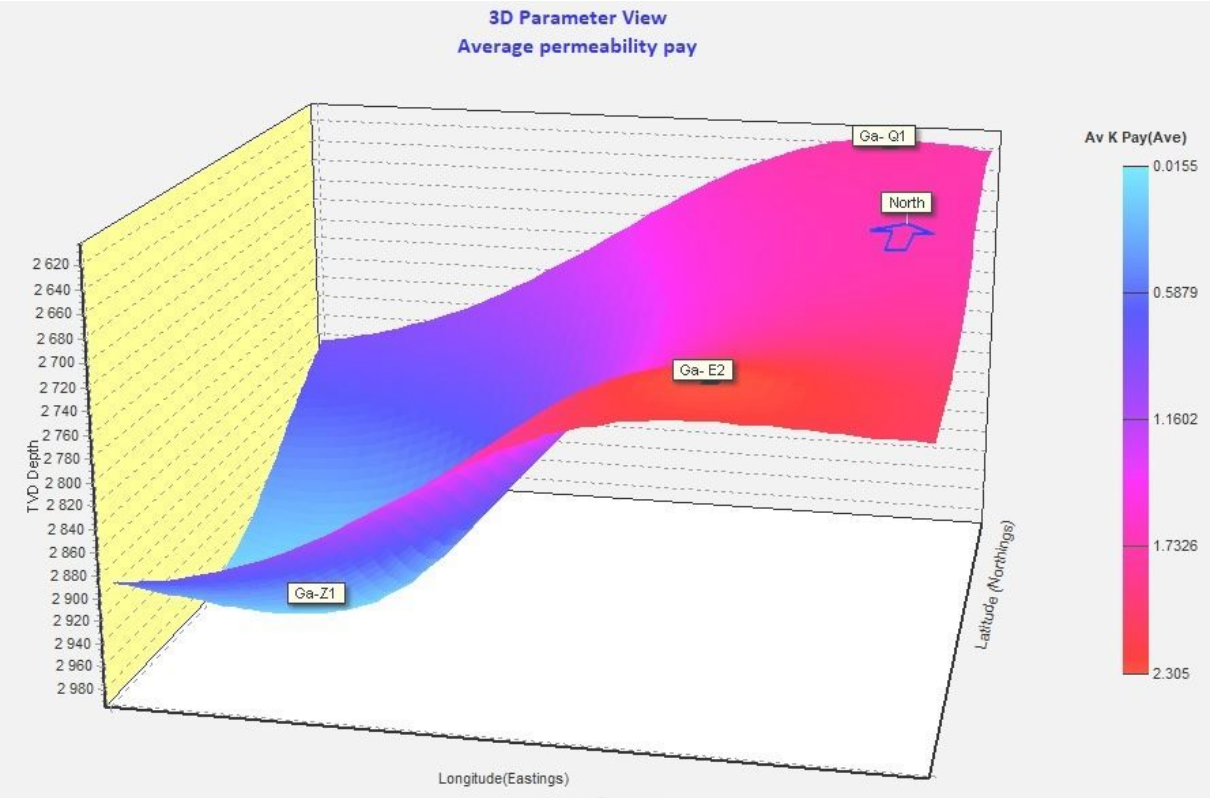

Figure 5. 30: 3D parameter view showing average permeability

The 3D parameter view of permeability shows a different spatial configuration to the other parameters (porosity, volume of clay and water saturation) due to the absence of well Ga-Q2. The calculated permeabilities of the three wells range from 0.0155mD - 2.305mD and can be classified as as “poor to fair”. Well Ga-E2 has the highest permeability of 2.295mD, followed by well Ga-Q1 with 1.7mD and lastly well Ga-Z1 with 0.01675mD. This trend depicts an overall increase in permeability towards the east of the field and an overall decrease in permeability towards the west of the field. Although well Ga-Q2 does not have a calculated permeability, its permeability may be inferred through the assistance of the other three wells, as they have similar rock formations and also because of its close proximity to well Ga-Q1. Well Ga-Q2 would have been located towards the north west of the field and is inferred to have an average permeability of approximately 0.5mD through its proximal location.

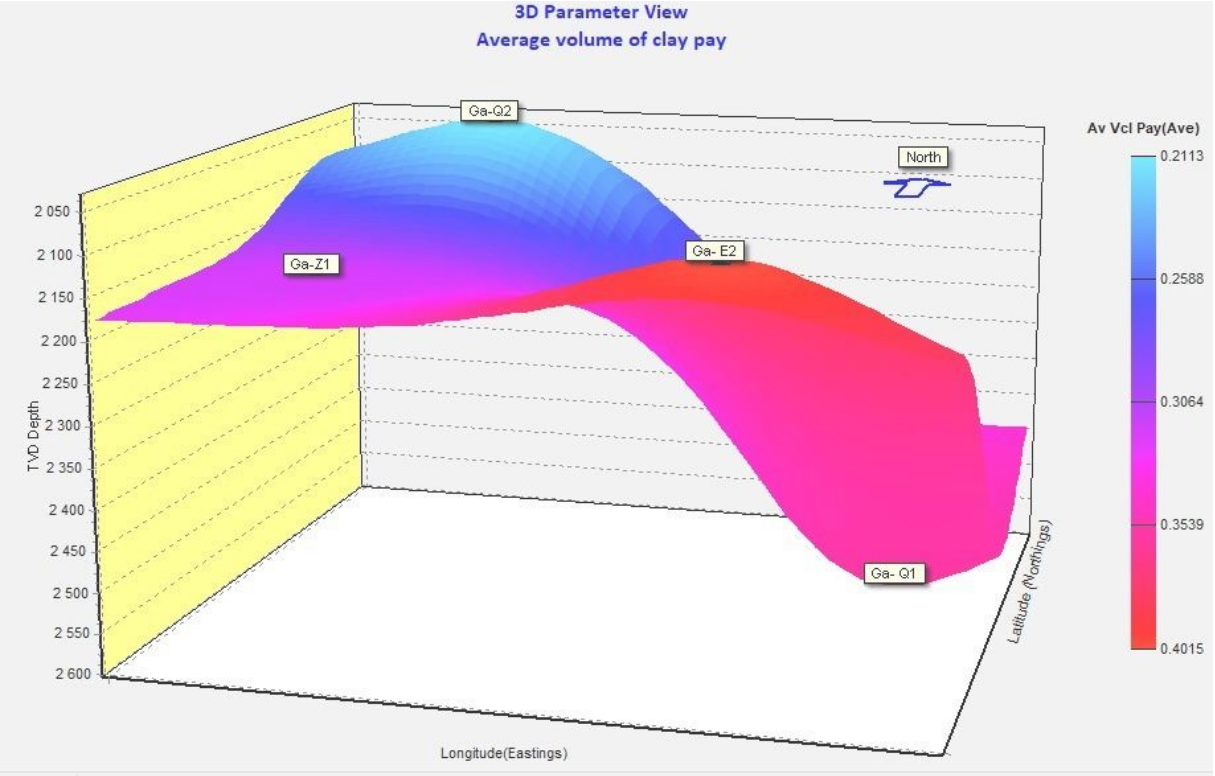

Figure 5. 31: 3D parameter view showing average volume of clay

The volume of clay was distributed within a range of 0.2113- 0.4015. The volume of clay trend for the four wells was not clearly discernible as there seemed to be more than one trend in play. Well Ga-Q2 consisted of the lowest average volume of clay with 21%, whereas well Ga-E2 has the largest amount of clay with 39.9%. Although well Ga-Q2 is located north west of the field and well Ga-E2 is located towards the south of the field it would not be entirely accurate to identify the overall trend as increasing towards the south, however, this is one of the identified trends. The second trend is an increase in volume of clay from the west to the east of the field.

Although the ascending order of the average volume of clay is well Ga-Q2, Ga-Z1, Ga-Q1 and Ga-E2, this does not correspond to a decrease in average porosity and permeability values for those wells respectively. This provides a broader perception of the effect of clay diagenesis on the petrophysical properties. As a result of there not being a single trend of either increase or decrease in petrophysical properties in conjunction with an increase in the volume of clay, this leads to the belief that diagenetic factors are of a detrital and positive contribution to petrophysical properties.

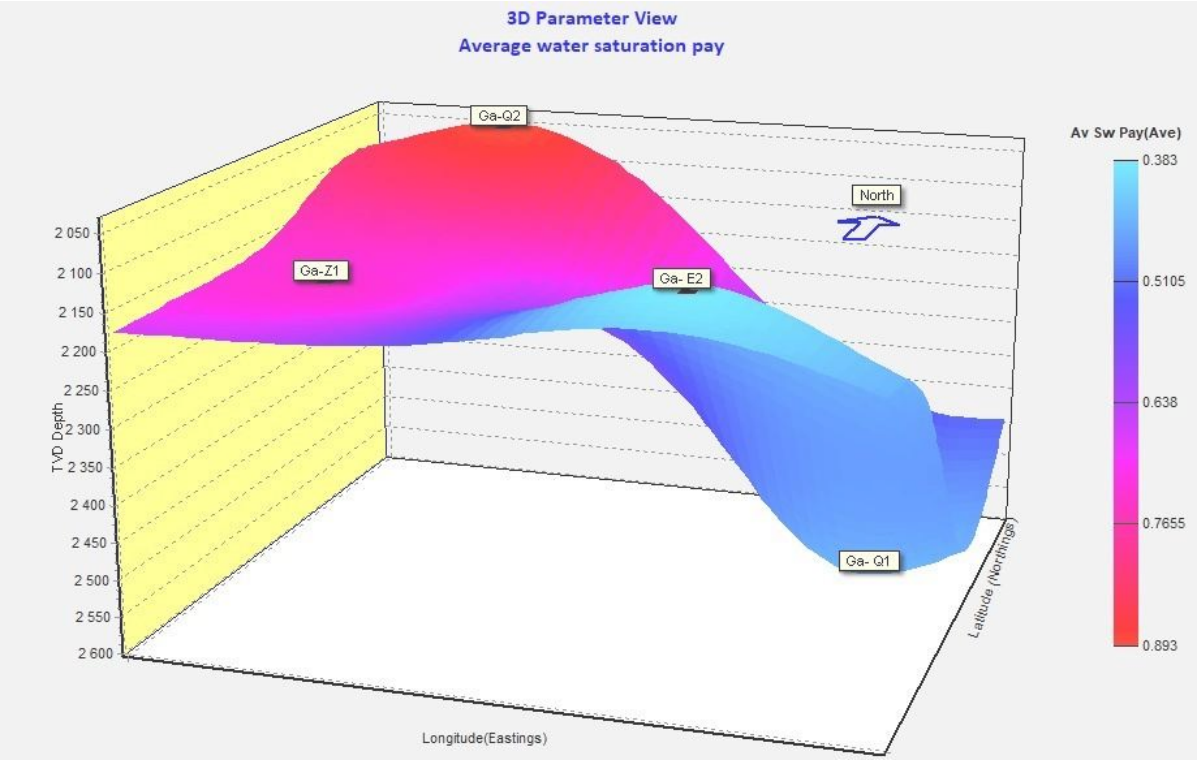

Figure 5. 32: 3D parameter view showing average water saturation

The distribution of water saturation for the four wells were found within a wide range of values, although the scale ranges between 0.383 - 0.893, the values of this parameter lie within the scale and are not represented by the outer limits of the scale. Well Ga-Q2 in the north west direction contains the highest water saturation with an average water saturation of 77.35% and the well Ga-E2 in the south contains the lowest water saturation with an average of 38.5%. The intermediate water saturation of the field was found in well Ga-Q1 with water saturation of 43% and well Ga-Z1 with water saturation of 76.1%. From the information provided by the spatial distribution of the plot, there is no particular overall trend, however, observation of an increase towards both the north and west directions may be seen.

CHAPTER 6: PETROGRAPHY

6.1. Core samples

The core intersected an upward coarsening shallow marine unit consisting of claystone and siltstone at the base, grading to a very fine-grained glauconitic sandstone at the top. The sediments are heavily bioturbated with crossbedding and ripple lamination preserved as seen in Figure 6.2 and is more pronounced in Figure 6.3 well Ga-Z1.

Organic matter has been identified as the majority constituent contributing to the interlaminated well preserved pattern in the rock in some samples, which is consistent with the thin section results as seen in sample 7. These interlaminations range from < 0.5 mm- 2mm in hand specimen.

The samples are a range of pale grey to dark grey colour with the majority of them being a medium grey, as well as a mix of medium grey and light or dark grey. There are a few samples with clast inclusions ranging from < 0.5 mm- 2mm in size, these inclusions are sub-rounded as seen in Figure 6.1.

As a result of the short intervals of some core samples, the characteristics defining the lithology are almost identical, the main difference being the lack of preserved lamination on a few samples. The same may be said for core samples retrieved for well Ga-Z1.

Figure 6. 1: Core sample 4 of shaly sandstone representing facies B retrieved at 2344.07 m.

Well Ga-Z1

The lithology of the core is interlaminated sandstone, siltstone and claystone beds with intervals 3021.25m comprising of large sandstone. They range from pale grey to dark grey in color with most of them being a mix of the 3 shades grading into each other. The core samples show very tightly packed lithology due to the presence of argillaceous material. Just like core samples in Ga-Q2, sediments are bioturbated with cross bedding and ripple laminations are preserved. In some places the ripple lamination resembles sinuous ripples (having curves or turns, lenticular in shape), as observed at 1642

m in Figure 6.2. Places where this characteristic has been identified depicts the ripple height influencing its formation and deposition.

Figure 6. 2: Photomicrograph of sample 7at 1642 m showing lamination with horizontally orientated organic matter under magnification of 4x 0.10 in the thin section on the left. This corresponds to the shaly sandstone core sample representing facies A on the right.

In some samples viz. samples 3, 4, 7 and 8 the brown pigmented matrix composed of organic matter and clay represents a specific orientation which favours horizontal alignment. Figure 6.2 further adds to evidence of slight deformation as the horizontal streaks of the matrix are not 180 degrees straight but have a slight curve which is caused by overburden pressure. In addition to this, when compaction occurs the grain comprised of softer material is the one that will be more susceptible to bending. This feature is also particularly evident in Figure 6.4 in sample 4A.

Figure 6. 3: Core sample 8 of shaly sandstone representing facies C retrieved at 3017 m.

The cementing matrix holding the extremely small clasts and overall rock together disintegrates easily as noted when handling the rock samples for preparation for thin section, XRD and SEM, particularly core sample 10 in Appendix E11. No pore spaces were identified from the hand specimen, however, thin section analysis showed the presence of pore spaces under the microscope.

6.2. Thin Section

Well Ga-Q1

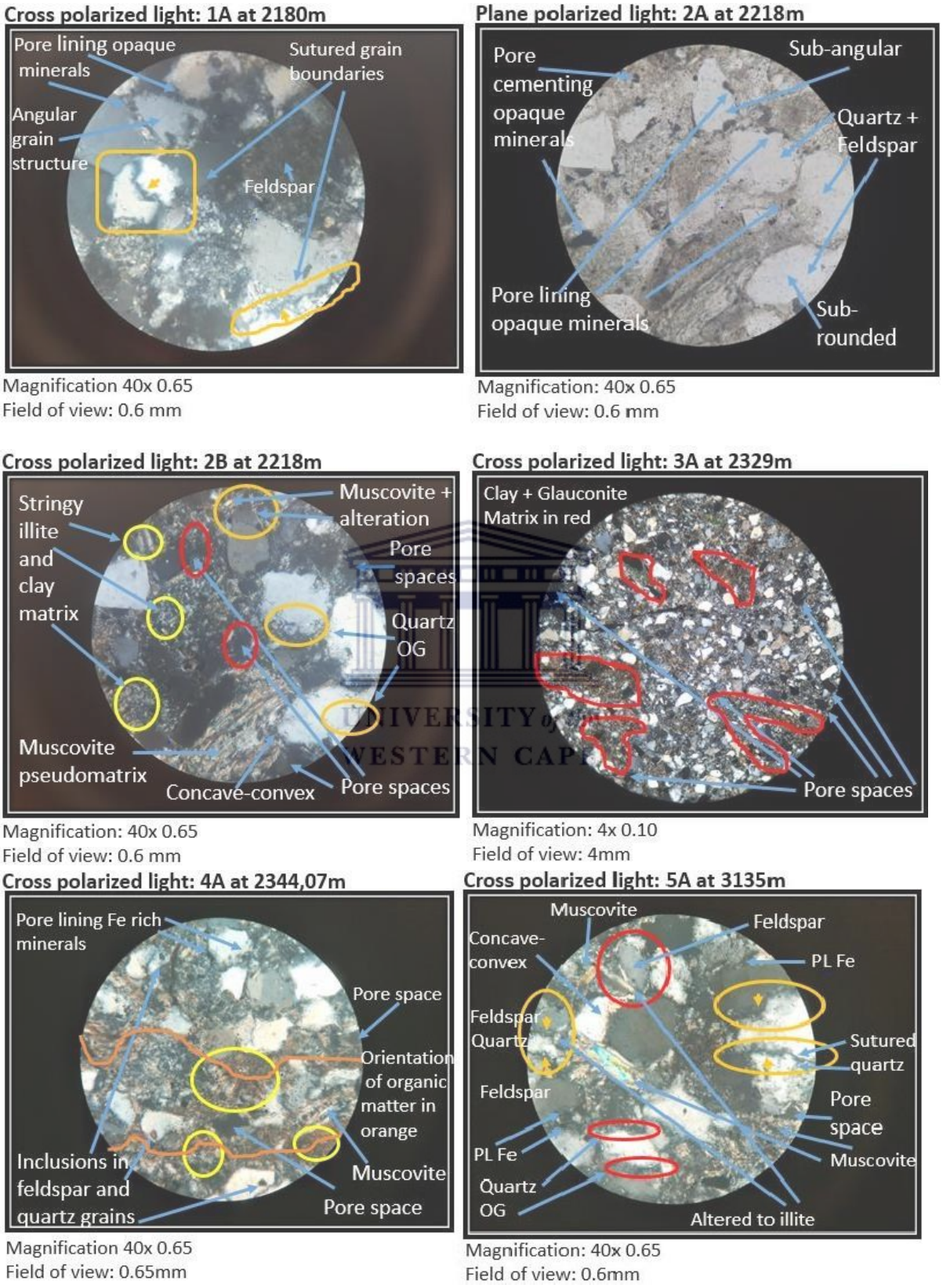

Figure 6. 4: Sub- section photomicrograph of well Ga-Q1 showing mineral aggregates and structure of aggregates in shaly sandsone reservoirs. PL Fe= Pore lining Fe rich minerals

The angularity of grains for Figure 6.4 from 1A at 2180 m to 5A at 3135m ranges from sub- angular to sub- rounded grains. These aggregates are moderately sorted indicating a short travelling distance between the original location and location of deposition from where the samples were retrieved. Upon varying magnifications (4 x 0.1 and 10 x 0.25) of sample 1A in Appendix E the mineral aggregates appear to be similar in size and are relatively evenly distributed and wellsorted.

Mica grains as seen in Figure 6.4, 2B in the form of grain coating platy muscovite as well as in the form of muscovite pseudomatrix as a result of its ductile and elastic properties. These are the properties that led to the concave- convex grain boundary in Figure 6.4, 2B where the pseudomatrix is bent to surround the more rigid grain. Where the mica is grain coating it is gradually altered to illite which contributes to the pore filling clay minerals, this alteration is further confirmed through SEM (discussed in section 6.4). The presence of fully developed illite is visible in 2B, however, it is not well magnified and will be discussed further in SEM analysis. Matrix of organic matter in the blue enclosed shape in Appendix E5 under plane polarised light appears to only be comprised of organic matter, but a closer look at the same sample under cross polarised light exhibits a combination of organic matter intertwined with small traces of illite. In 4A there are quartz grains with accessory zircon inclusions as products of primary crystallization, they were crystallised well before any diagenetic process took place and now form part of the detrital constituents of the sedimentary rock. This is due to zircon properties of being hard, durable and chemically inert and allowed it to prevail through the sedimentary rock. Between the spaces of distinguishable grains is the dominantly brown organic matter showing a preferred horizontal orientation in 4A thus exhibiting direction of deformation as the horizontal orientation of organic matter is accompanied by crests and troughs of this malleable part of the rock. Within the red circle in 5A under cross polarised light, a grain boundary alteration of feldspar (with a small opaque inclusion) to illite (on the outer boundary of the grain) is displayed, which is most likely due to dissolution.

In Appendix E2 representing sample 1A, there is a well-defined fracture which is presumably caused due to deformation either through transportation or deposition. This fracture led to the large pore space i.e. secondary porosity, which is accompanied by many other small pores which were identified in Appendix E. The large pore space formed by the fracture is not merely a secluded pore but is structured in a continuous pore connecting arrangement as it stretches from one end of the thin section to the other. This is an indication of a good flow pathway i.e. permeability. The porosity of 1A is supported by the porosity of the petrophysical results in the previous chapter which was classified as very good. Although there are other pore spaces in 1A identified in Appendix E2, they are not connected to each other. This photomicrograph therefore represents a combination of connecting

porosity as well as non-connecting porosity which supports the “fair permeability” classification reached in the petrophysical results for this zone in the previous chapter.

The brown clay matrix in 3A has infiltrated the pore spaces and is located where the interstitial pore spaces would have been. This clay forming matrix has either one of two roles, the first being that it completely impedes the infiltration of any fluid, or that incoming fluid co-exists with the matrix depending on the various clay properties. With the assistance of processes such as compaction that lead to an increase in pressure, fluids such as oil and gas may coexist with the clay matrix and fully saturate the clay grain interstitial spaces provided that the clay on its own is not too compact. This accommodation, however, can only be made for small quantities of fluid. Water may have the same effect of either co-existing with the clay matrix or being absorbed by it depending on the expansion properties of clays present. Although the brown clay matrix is spread out in 3A, it does not completely override pore spaces which are identified in 3A. The pore spaces of 4A are at a relatively close distance to each other with very few connecting pores, this is better identified in Appendix E6. The grains in between comprise a mixture of quartz, feldspars and clay matrix which are represented in 4A. In-between these grains is a brown clay matrix delineated by the yellow circles in 4A which surrounds the grains in a way that void spaces would have. Both 4A and 5A have minimal porosity and the distance between the pores is quite significant. This is supported through permeability results in petrophysical results in the previous section; the permeability of this sample was found to be 0.289mD for 5A. Therefore thin section supports petrophysical results concluding that an increase in depth has led to a decrease in porosity and permeability.

When sample 1A- 5A were rotated around the microscope stage 90% of the minerals showed pleochroism, out of which approximately 70% were identified as quartz. There are small opaque minerals lining the quartz grain boundary as well as lining the grain boundary of a few other minerals which may be seen in 1A, 2A, 4A and 5A. These grain coating opaque minerals were identified as iron sulphide/ iron oxide which suggests the presence of hematite or goethite. This is later confirmed through SEM analysis where traces of iron were identified corresponding to the amount of opaque minerals found in numerous thin section slides. Some of these opaque Fe rich minerals were randomly distributed thus contributing to cementing material, but the majority of these minerals were grain coating.

One of the major commonly known overgrowth indicators is discernible by the outer edge of the grain containing these smaller materials in the form of iron oxides accompanied by clay minerals. These iron oxides and clay minerals form an irregular and discontinuous pattern on the original surface and the discontinuous patterns form an optimal platform for overgrowth (i.e. quartz and feldspar overgrowth).

The samples retrieved from 2A represent precipitation and nucleation of quartz as overgrowth on quartz substrate which is encouraged by the absence of consistent opaque grain coating minerals. The two red circles in Figure 2B show parts of the grain boundary adjacent to pore space where opaque minerals do not coat the grain; therefore these red circles represent pore spaces optimal for grain overgrowth. The feldspar and mica overgrowth seen in the two red circles on the outer boundary of the interstitial space initially infiltrates the vicinity nearest to the original grain, and thus alters the pore geometry and decreases the adjacent interstitial micro-pores and restricts possible future permeability (Diagenesis, 2018).

The effect of the grain coating minerals varies depending on the mineral forming on the rim of the grain as well as the extent of formation. In the case of 2A, the opaque grain coating minerals which have been identified as iron-rich minerals are the product of ferrihydrite which has undergone diagenesis (Cudennec & Lecerf, 2006) and the lighter amorphous minerals as clay. The opaque iron-rich grains are also known as insoluble residues which are usually accompanied by clay and other minor grains and are characteristic of stylolites which form through the closure of gaps in rocks. Preservation of porosity and subsequently permeability would have been possible provided that these grain coating minerals covered the entire rim of the substrate, and ultimately impeding quartz overgrowth as the original quartz surface would already be occupied and therefore insufficient/non-existent adjacent area for nucleation and precipitation of quartz.

The presence of iron is considered to be of some importance in sandstone diagenesis because of its general widespread presence in this lithology with its presence being attributed to being directly proportional to an increase in both solubility and dissolution of quartz (O'Kane et al., 2007). Hematite has an extensive history of formation as it initially formed in sedimentary environments as accumulations on the ocean floor more than a million years ago. Its genesis began with dissolved iron-rich oceans which were later integrated with oxygen converted CO_2 from photosynthesising ocean bacteria (Hematite, 2018). This was then integrated with more studies such as SEM where bacteria, organic matter were identified insinuating that this is an ongoing process that contributes to the formation of the iron-rich minerals found on the ocean floor which in this study appear merely as minor and trace elements.

An outline of the grain to grain contact within the yellow shapes is visible in 1A. This is evidence of pressure solution represented by the sutured grain boundaries. This characteristic is not solely at local points of contact joining two adjacent grains, therefore it represents the second phase of pressure solution as it shows an increase in surface area of the adjacent grains in contact, and is welded together (as shown 1A and 5A).

Quartz grains in 5B indicated by the 2 yellow circles on the right are proof of dissolution which has taken place as a result of the sutured boundaries. This process is also represented by the yellow circle on the left of 5A showing sutured grain boundary on the top and bottom of the quartz mineral linking 2 feldspars. The sutured grains represented by the two yellow circles led to quartz dissolution and thus the formation of authigenic quartz adding to original quartz grain and thus increasing grain size. Additional quartz overgrowth is represented by the two red circles on the bottom left of 5A. The sutured grain boundary represented by the left yellow circle also led to the dissolution of both silica from quartz and what is believed to be potassium from the feldspar as the formation of illite has been initiated on the feldspar partial grain boundary. This forms part of the initial stage of pressure solution as it is represented solely at local points of contact. The alteration represented by the red circle, however, represents both initial and final pressure solution stages as it also extends the surface area occupied by illite adjacent to altering grain. Concave convex boundaries resulting from compaction may be seen in 5A.

This phenomenon of pressure solution may be explained on the basis of the increase of solubility of quartz and feldspars being directly proportional to an increase in depth and pressure. This increase in the two parameters lead to local pressure exerted on grain to grain boundaries which are caused by a combination of overburden rock. The exerted pressure then triggered small amounts of quartz and feldspar dissolution along the grain boundaries. This has led to some quartz grains infiltrating the surrounding matrix and making it more silicate-rich with a greater silica concentration towards the source. The surface of the minerals adjacent to these grains undergoing pressure dissolution are characterised by less pressure thus giving way for the quartz and feldspar precipitation on their surfaces. This can be a repetitive cycle of simultaneous dissolution and precipitation which leads to adjacent grain surfaces to be larger in size (Diagenesis, 2018). This process of pressure dissolution can ultimately lead to a decrease in porosity.

Well Ga-Z1

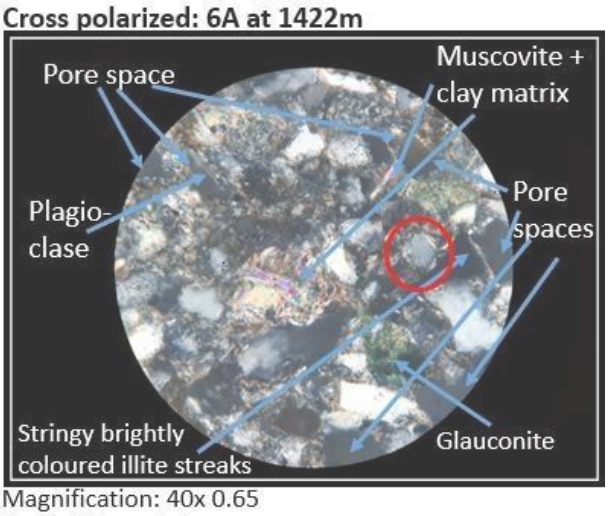

Magnification: 40x 0.65
Field of view: 0.6mm

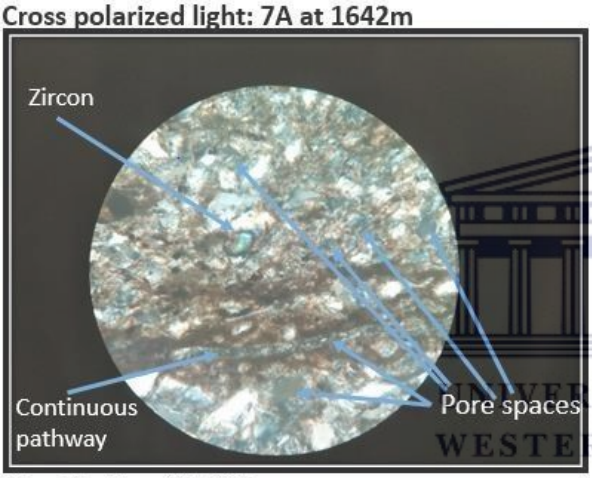

Magnification: 40x 0.65
Field of view: 0.65mm

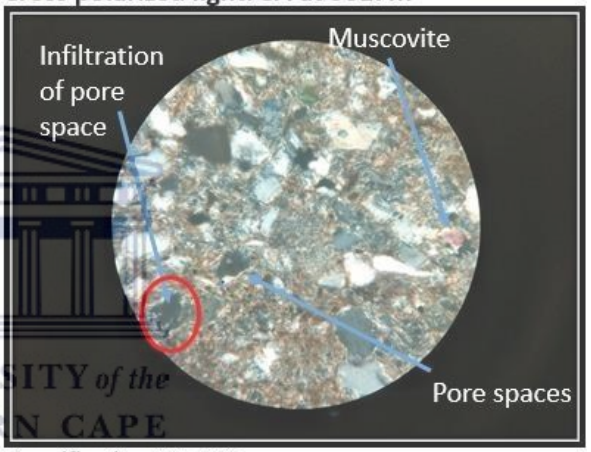

Magnification 40x 0.65
Field of view: 0.65mm

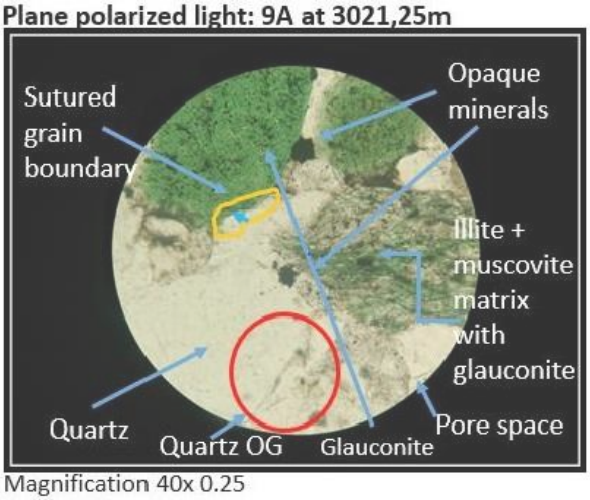

Magnification 40x 0.25
Field of view: 4mm

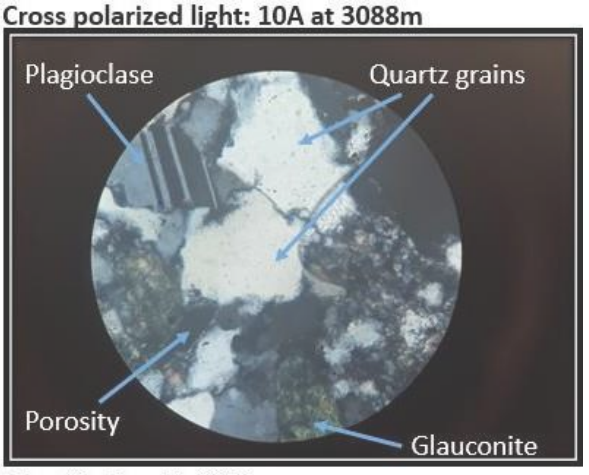

Magnification 40x 0.65
Field of view: 0.65mm

Figure 6. 5: Sub- section photomicrograph of well Ga-Z1 showing mineral aggregates and structure of aggregates in shaly sandsone reservoirs.

The angularity of grains for Figure 6.5 sample 6A at 1422 m to sample 10A at 3088m ranges from sub-angular to sub- rounded grains and are similar to that of well Ga-Q1. These aggregates range from poorly to moderately sorted indicating a short travelling distance between the original location and location of deposition where the samples were retrieved. The varying grain sizes in 7A show that different layers of the sedimentary rock were compacted against each other and over time formed one sedimentary unit as the top layer generally has smaller grain sizes compared to the bottom layer. The mineral aggregates in 6A, 8A, 9A and 10A do not show uniformity in size unlike the size distribution in 7A where the smaller grains are found at the top of the sample and the larger ones at the bottom, the grain size distribution in Figure 6A, 8A, 9A and 10A is random. At places where there is an increased amount of smaller grain sizes, there is an increase in the brown clay matrix cementing these smaller grains together.

As observed in sample 5A of well Ga-Q1, grain boundary alteration of grey coloured feldspar to illite is displayed in the red circle of 6A. This neoformation of illite on the grain boundary has taken up the small adjacent pore spaces. It has done so by almost completely surrounding the grain leaving a few corners exposed. By covering most of the grain, it prevents further neoformation of any new grains. Feldspar and mica minerals such as muscovite contribute to the potassium needed for the formation of illite, these feldspars and micas contributing to the formation of illite were broken down by the surrounding organic acids derived from the organic matter.

The zircon in 7A is characterised by high relief and high interference colours and is adjacent to a quartz crystal and is further surrounded by the clay matrix. In certain samples viz. samples 4 (4A), 7(7A) and 8 (Appendix E9) the brown pigmented matrix composed of organic matter and clay represents a specific orientation which favours horizontal alignment. Figure 6.2 further adds to evidence of slight deformation as the horizontal streaks of the matrix are not 180 degrees straight but have a slight curve which is caused by overburden pressure. In addition to this, when compaction occurs the grain comprised of softer material is the one that will be more susceptible to bending. This feature is also particularly evident in 4A.

A deformed shale matrix with traces of microcrystalline feldspars can be seen in 8A. The deformation is due to sub surficial compaction which readily takes place as a result of shale being mechanically soft. Although the identified muscovite in 8A is unaltered muscovite, most of the muscovite has been altered to feldspars and illite which now form part of the detrital brown matrix surrounding most of the mineral aggregates. Appendix E10 of sample 9 shows a clast supported matrix and has a good representation of the darker hues of glauconite thus indicating a more micaceous composition. This is accompanied by an illite and muscovite matrix in 9A where muscovite was being altered to illite

(may also be seen in Appendix E10). Glauconite was more clearly distinguishable and became more abundant at deeper depths as seen in 9A and in Appendix E10.

Plagioclase identified in 10A is more likely to be the Na-rich end member albite as the counterpart Ca-rich end member is less resistant to weathering, therefore, making it less likely to survive weathering conditions undergone by these sandstones and shales. The plagioclase identified in 10A displays almost perfect twinning and cleavage accompanied by minimal deformation thus suggesting authigenic origin although the lower edges of this mineral aggregate are jagged. The minimal deformation on the edges of the mineral has been identified as structural grain boundary deformation as seen from the rugged edges, this deformation being due to compaction. The identified glauconite in 10A is slightly iron-rich with small opaque blotches of hematite which create an optimal platform for boundary overgrowth, this phenomenon is clearer under plane polarised light in Appendix E12.

Sample 6A which was retrieved from depth 1422m and possess the highest porosity and permeability out of the 4 identified zones in Ga-Z1. The pore spaces are located at close proximity to each other with a few interconnecting spaces which are seen through the dark shadows in Figure 6A. The presence of stringy brightly coloured illite situated on the grain boundary of some grains and pore bridging streaks thus contributed to the obstruction of fluid flow may be seen in 6A. Although the presence of glauconite and mica related minerals such as muscovite accompanied by clay matrix may be identified in the photomicrography of 6A, these minerals have not yet undergone extensive compaction and consequent deformation at this depth hence the presence of some void spaces which reach an average of 18.1% porosity for this zone.

The porosity for this sample can be seen in 7A where there is minimal connectivity between these void spaces, except for the one continuous pathway which is better identified in 7A. Although this pathway is beneficial for permeability it is soon brought to a halt by a brown clay-rich matrix towards the left. The mix of the sub-angular and sub-rounded grains accompanied by varying grain sizes play a role in prohibiting permeability. As a result of this matrix cementing the grains together in 8A, there is not much space left for porosity as demonstrated by the 6.3% porosity attained from the petrophysical results. Enclosed in the red circle are clay minerals extending into the pore space and thus reducing the volume of the pore space.

Thin section analysis of 9A showed the presence of pore spaces under microscope. The pore spaces of this sample are identified in 9A and Appendix E9 with no visible pathways between the various pore spaces, this is supported through the “null/non-existent” permeability results obtained for this interval in petrophysics results; as well as the tightly packed grains and matrix seen with the naked

eye in the hand specimen. A significant contributor to the diminished interstitial spaces of 9A is the quartz overgrowth delineated b the red circle, as a result the average porosity within this depth was 6.3%. The extremely compact hand specimen in Appendix E11 at depth 3088m is supported by the thin section in Figure 6.26 B as the two display an absolute minimal presence of pore spaces with what seems to be an absence of interconnecting pathways for fluid flow. This is supported by the petrophysical results established in the previous chapter comprising this very interval (deepest zone for Ga-Z1). The porosity for this zone was 2.26% and thus classified as negligible, it was accompanied by "null" permeability meaning that the permeability is non- existent. The porosity was very difficult to identify under thin section even with the assistance of epoxy, however, one pore space was identified in 10A.

6.3. XRD

The following were characteristics of the samples before preparation for XRD analysis:

1. Samples comprise of some visible crystals of quartz accompanied by finer grained clay.
2. Differences in density within the materials that made up the sample, a mixture of hard and soft phases directly in contact with each other.
3. Mechanically and/or thermally sensitive phases (especially clays and sulphates (sulfates in sample 7, image 7.1 and 7.3)).

The following mineral phases were identified in order of increasing abundance:

1. Quartz (SiO_2)
2. Albite ($NaAlSi_3O_8$)
3. Illite (2M1)($(K, H_3O)Al_2Si_3AlO_{10}(OH)_2$)
4. Muscovite (2M2); ($(K,Na)Al_2(Si,Al)_4O_{10}(OH)$)
5. Chlinchlore (1Mlb-2)($(Mg,Al,Fe)_6(Si,Al)_4O_{10}(OH)$)
6. Muscovite (1M); ($KAl_2Si_3AlO_{10}(OH)$)
7. Orthoclase ($KAlSi_3O_8$)

Quartz formed the bulk composition in each sample followed by albite. This is because the temperatures and pressures present under subsurface conditions provide the most conducive environment for the existence of quartz in sandstones. Being the most abundant in sandstones it is subsequently the second most abundant in mudrocks. In addition to this, it also forms from a precipitation process as a result of chemical weathering. Within the subsurface and various depths below the subsurface where igneous and metamorphic lithologies are concerned, feldspars reign as the most common minerals (Nelson, 2013).

The minerals identified from the different samples have a significant resemblance to each other, this is due to 1. Some samples' positions not being too far from each other or 2. The lithology in most parts is characterised by the same type of feldspars and clays or 3. The depths and temperature that samples are extracted from are characteristic of elements being in equilibrium/being stable under those conditions. Due to the great resemblance of results, only sample 1 from well Ga-Q1 and sample 6 from well Ga-Z1 are presented in the results with the rest of the XRD results in Appendix F.

As a result of the knowledge of the general abundance of quartz towards the earth's surface as well as in the samples, the results were averaged after removing the quartz present. This was done in order to highlight the significance of other minerals such as feldspars and micas on clay diagenesis. This does not mean any exclusion of quartz when putting into consideration processes that led and contributed to the current state of the samples as well as diagenetic processes involved.

From the XRD results, the addition of the percentages of all the minerals were not equivalent to 100%. Some percentages were exaggerated particularly when it came to quartz making the sample reach a total exceeding the standard 100% needed for averaging, analysing and interpretation. The data were normalised in order to proceed with analysis and avoid bias values that were most likely a result of different scales, anomalies, etc. The normalisation did not have any effect on the quality of the results as its purpose was to decrease redundancy and improve the integrity of the data set of which this concept was initially introduced by Edgar F. Codd as a fundamental part of his relational model (Database normalization [DN], 2018). The following equation was used for normalisation of each mineral assemblage: (Mineral percentage/total mineral percentage of all minerals*100). The normalised results are presented in Table 6.1.

Table 6. 1: XRD Normalised mineral percentages

Sample no.	%Albite normalized	%Illite normalised	%Muscovite (2M2) Normalized	%Chlinochlore normalised	%Muscovite(1M) normalised	%Orthoclase normalised	TOTAL
1	63,277693	5,3110773	7,89074355	4,24886191	7,43550835	11,8361153	100
2	47,185741	6,3789868	18,7617261	4,69043152	8,91181989	14,0712946	100
3	52,094972	6,9832402	10,4050279	5,16759777	9,77653631	15,5726257	100
4	52,104499	6,9666182	10,3773585	5,22496372	9,79680697	15,5297533	100
5	52,085354	6,9835111	10,3782735	5,23763337	9,79631426	15,5189137	100
6	52,048417	6,9832402	10,4283054	5,2141527	9,77653631	15,5493482	100
7	52,130553	6,9809610	10,4261106	5,16772439	9,79147779	15,5031732	100
8	52,086137	6,9986541	10,3633917	5,18169583	9,82503365	15,5450875	100
9	52,130044	6,9506726	10,426009	5,15695067	9,75336323	15,5829596	100
10	52,042007	7,0011668	10,3850642	5,25087515	9,80163361	15,5192532	100

XRD Results of well Ga-Q1:

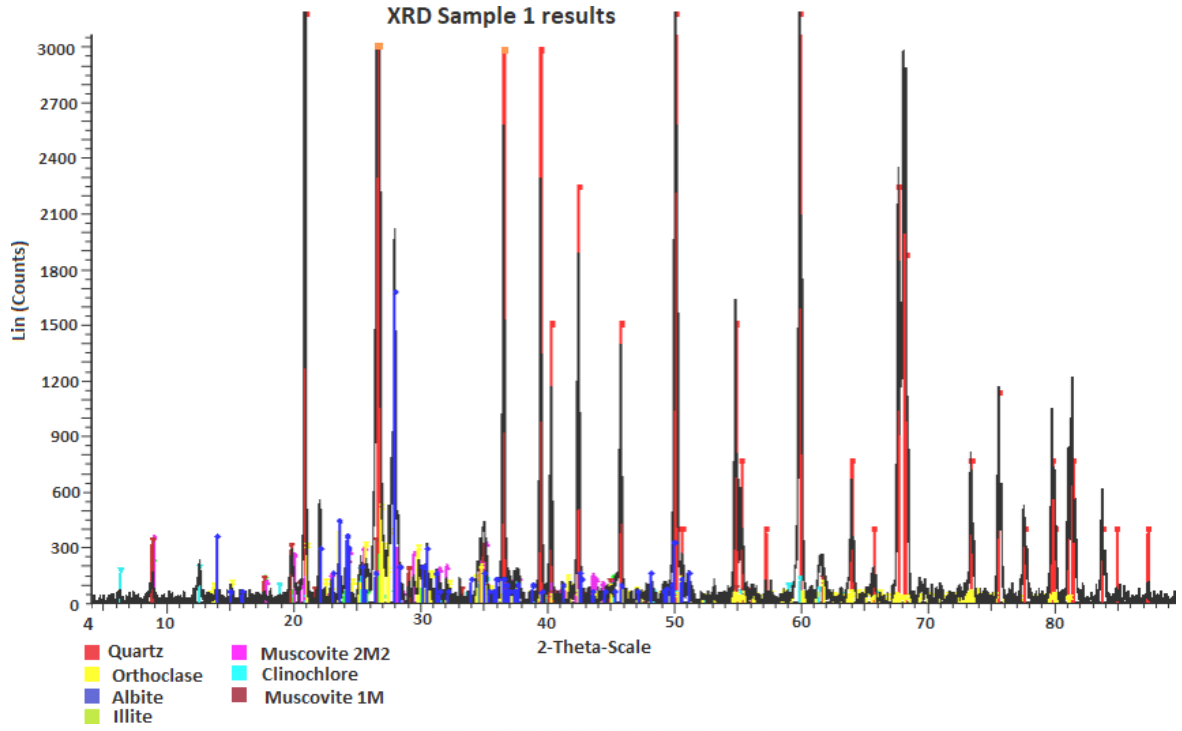

Figure 6. 6: XRD qualitative plot for well Ga-Q1, sample 1 at 2180 m.

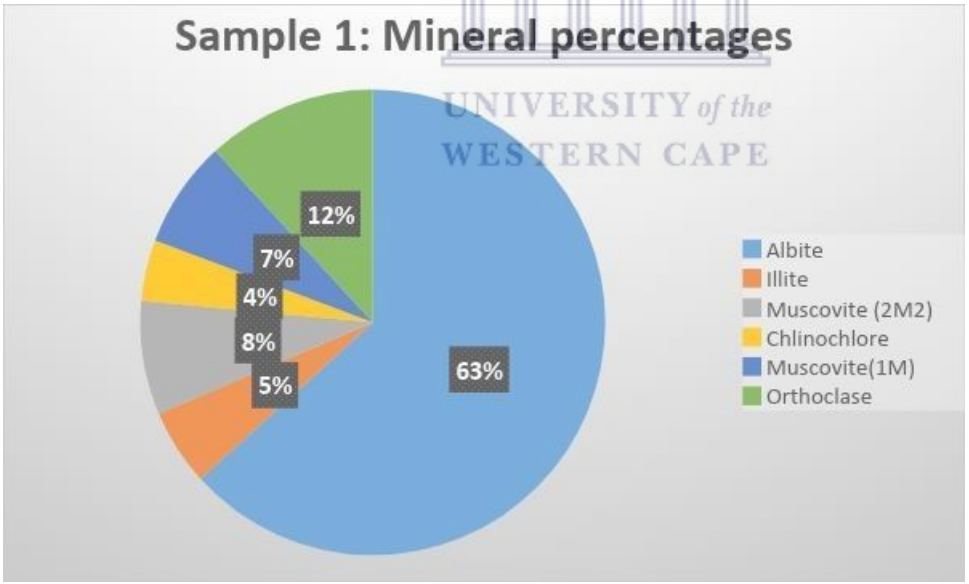

Figure 6. 7: Pie chart of mineral aggregates of sample 1 at 2180 m.

XRD Results of well Ga-Z1:

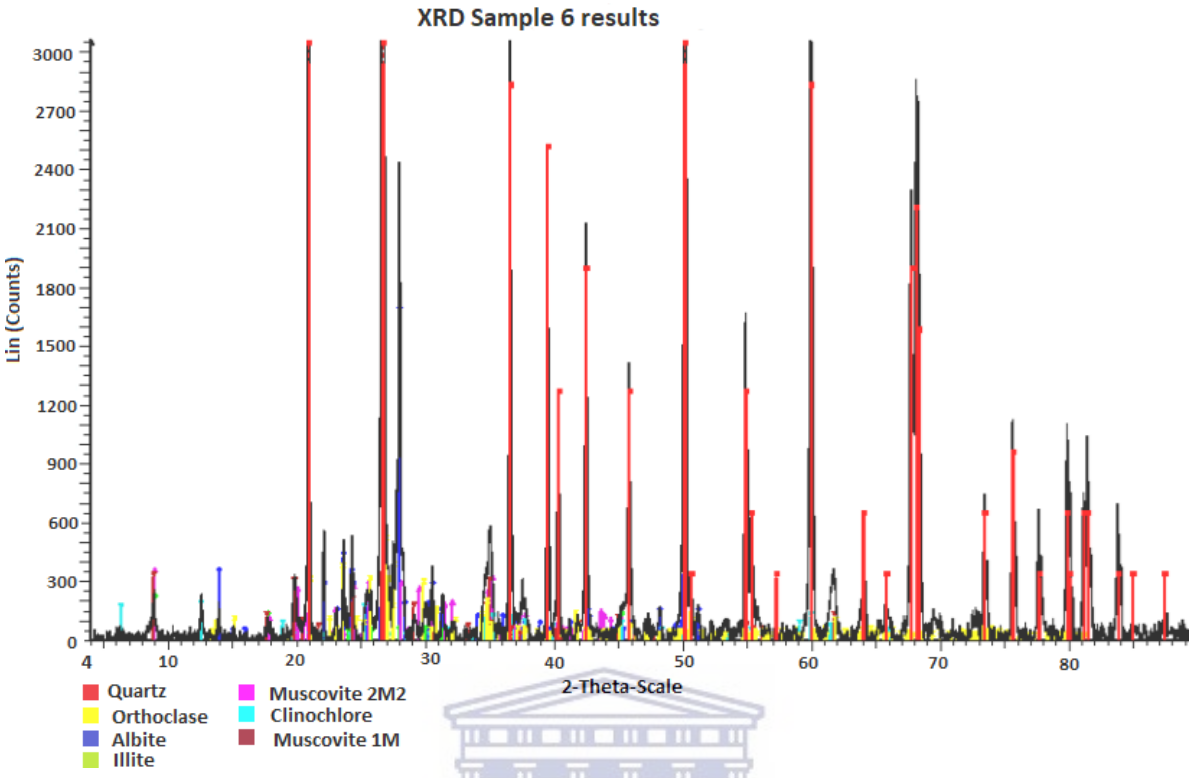

Figure 6. 8: XRD qualitative plot for well Ga-Z1, sample 6 at 1422 m.

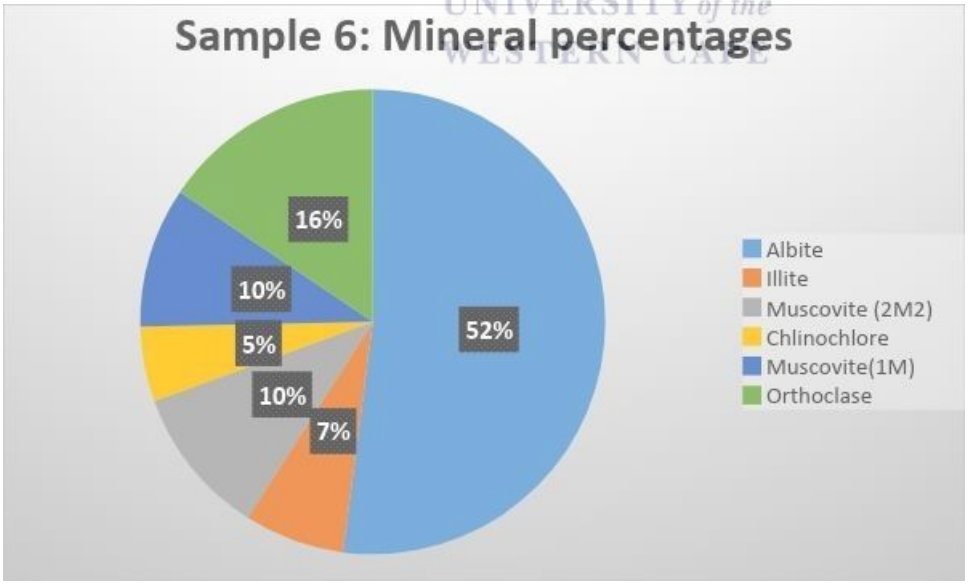

Figure 6. 9: Pie chart of mineral aggregates of sample 6 at 1422 m.

Clastic sedimentary rocks are dominantly of detrital origin as they form through the deposition of the remains of pre- existing rocks, it is possible to identify the origin of certain minerals in these rocks through XRD.

Weaver (1956) examined clays from numerous rock samples of which the overall origin is that of a detrital source and thus strongly reflect the source area more than the depositional environment (Weaver, 1956). The following is a concise description of mineral phases identified in XRD.

1. Quartz (SiO_2): The quartz identified is low temperature quartz that is hexagonal in crystal lattice and mainly white in colour. As a result of it being stable under low temperature it is highly susceptible to alteration upon further diagenetic process that involve deposition. This is due to deposition taking place concurrently with exposure to higher temperatures and pressures leading this type of quartz with XRD pattern 00-046-1045 being unstable with an increase in depth. This mineral phase underwent weathering in the form of erosion, followed by transportation, deposition and compaction. Through this entire process under relatively low temperature conditions it resulted in the silicate rich minerals being soft in texture.

2. Albite ($NaAlSi_3O_8$): Albite represented by XRD pattern 00-009-0466 ranges from colourless to grey to white in colour, it occasionally has specimens that are bluish. It has a lattice structure that is identified as anorthic (triclinic). Although it is a low temperature structure it is characterised by a melting point of 1118 degrees Celsius. A contributing factor owing to this is its composition which is not purely albite (owing to 98.2% of the weight) but has minor orthoclase contributing 1.8% weight to its composition.

3. Illite (2M1) ($(K,H_3O)Al_2Si_3AlO_{10}(OH)_2$): Illite is characterised by the base centered monoclinic crystals with the following chemical composition weight percentage: Si O_2 45.67, Al_2 O_3 36.88, MnO 0.82, K_2 O 8.90, H_2O 6.78, F 0.64, minor Na_2O, Fe O, Fe_2O_3. The conclusion of petrographic analysis conducted show that some of the illite present is of detrital origin. This can be further seen in SEM analysis where illite is extremely deformed (Appendix G5.1). As XRD confirms that the major illite polytype present is 2M1, previous analysis conducted by Yoder & Eugster (1955) show that the 2M polytype is indeed typical of detrital minerals and 1M and 1Md is typical of diagenetic origin in sedimentary basins.

4. Muscovite (2M2); $((K,Na)Al_2(Si,Al)_4O_{10}(OH))$: Just like illite, 2M2 muscovite is characterised by a base-centered monoclinic crystal lattice, along with its chemical composition weight percentage: Si O_2 85.81, Al_2 O_3 7.89, Fe_2 O_3 1.60, CaO 0.96, K_2O 2.11, H_2 O+ 1.10, minor Ti O2, FeO, Na_2 O: (K0.68 Na0.09) Al1.93 Si3.5 Al0.5 O10.6 (O H)1.94.

5. Muscovite (2M2); ((K,Na)$Al_2(Si,Al)_4O_{10}(OH)$) and Muscovite (1M); $KAl_2Si_3AlO_{10}(OH)_2$: Previous research by Pevear (1999) supports the notion that detrital micas characterised by big grain sizes have undergone erosion from their precursor metamorphic rock type such as slates, schists, and phyllites, particularly the 2M1 polytype. The 1M polytype is associated with much finer grain sizes and shows association with minerals such as kaolinite as it is made up of extremely small grain sizes. The polytypes contain the exact same layers but differ in repeating stacking arrangements/patterns (Jackson, 1997) with the 1M being the one layer monoclinic type. Transition of 1M polytypes to 2M polytypes usually transpires at conditions reaching 200-300 degrees Celsius and at pressures reaching 15 000 psi water pressure (Yoder & Eugster, 1955).

   Within the samples the presence of muscovite 1M and muscovite 2M2 depicts the ambient environment of stability where type 1M represents muscovite that is stable in low temperature environments; whereas type 2M represents muscovite that shows stability in high temperature environments.

   Type 1M minerals occur as glauconites amongst other illites through altered feldspars and mixed layer illite-montmorillonites (Yoder & Eugster, 1955). Within this research this is evident through thin section i.e. Figure 6.5 where muscovite is depicted as being in the process of being altered to glauconite where approximately 50% of this muscovite had already been altered. Through XRD studies it is evident that the muscovite undergoing alteration is type 1M as type 1M is more readily altered as opposed to type 2M2.

6. Chlinochlore (1Mlb-2); ((Mg,Al,Fe)$_6$(Si,Al)$_4O_{10}$(OH)): Clinochlore has the following chemical composition weight percentage: Al_2O_3= 22.23, SiO_2= 25.50, Cr_2O_3= 0.03, MgO =18.58, FeO =20.41, H_2O+ =12.25: (Mg1.64 Fe0.96 Al0.40) (Si2.64 Al1.36) O_{10} (OH)$_2$ · (Mg0.69 Fe0.31 Al) (O H)$_6$. This chemical formula is accompanied by a base-centered monoclinic crystal lattice. The polytype identified (1Mlb-2) is of diagenetic origin. Clinochlore is the Mg rich end member of chlorite and was identified as chlorite in previous analysis carried out; namely thin section.

7. Muscovite (1M); $KAl_2Si_3AlO_{10}(OH)_2$: Muscovite (1M) in the samples is characterized by a base centered monoclinic crystal lattice and is represented by a variety of colours namely light green, pink, light brown and colourless.

8. Orthoclase ($KAlSi_3O_8$): Orthoclase is represented by XRD pattern 01-075-1592 and is monoclinic in crystal lattice

The 2M polytypes identified such as illite and muscovite, but namely the former, are most likely to have been degraded micas as they are of detrital origin and are situated at quite a distance from their source. Their degradation routing from partial leaching processes and weathering which possibly occurred prior to reaching their location of deposition. The partially leached constituents did not lead to complete alteration due to their stability and slightly high resistance to alteration. Instead it led to these degraded polytypes adsorbing surrounding cations that are alkalies and thus regaining their complete substrate structure during diagenesis in order to become the identified polytypes.

6.4. SEM

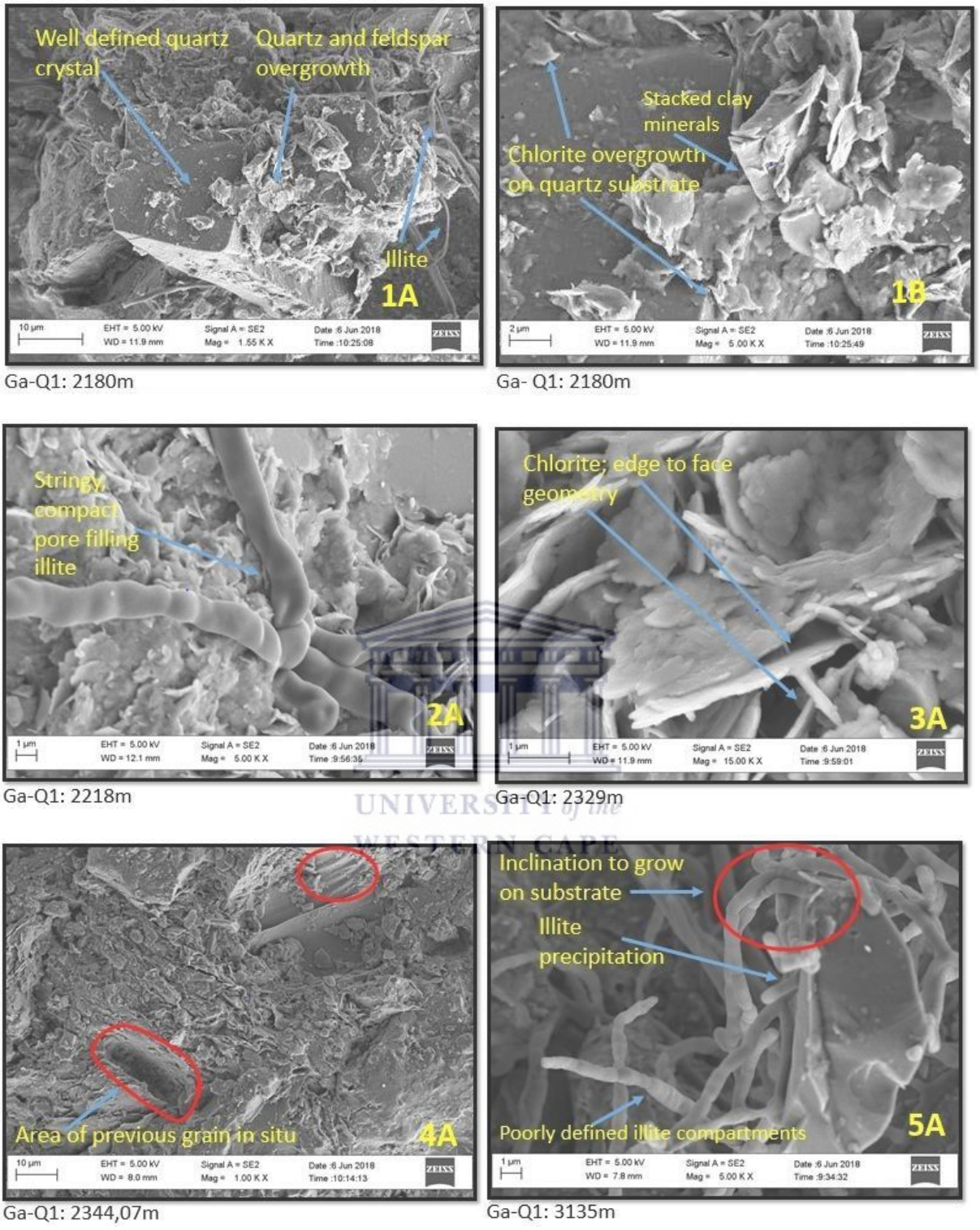

Figure 6. 10: SEM sub- images showing mineralogy and depicting relationship between clay mineralogy and petrophysical properties for sample 1-5 in well Ga-Q1

Figure 6.10 reveals a complicated network of interconnected minerals centred by a large euhedral and well intact quartz crystal in 1A. A large portion of this image exhibits feldspar and clay overgrowth which is more prominent and visible towards the right of 1A. To a lesser degree there are illite strings that manifest themselves as mineral bridging (bottom right of 1A), surface hovering and covering illite.

Sample 1B exhibits what is commonly known as stacked kaolinite despite the fact that EDS (Appendix G1.2 and G1.4) chemical analysis shows the presence of potassium. The potassium is present in small amounts and is likely to be detected from parts of the sample where kaolinite is not present. The precipitation on this stacked clay resembles that of chlorite which points to alteration. The general crystallisation of chlorite from solution in interstitial spaces is noted by Humphreys et al., (1989), this is accompanied by its formation to the detriment of the kaolinite grains (Burton et al., 1987) as can be seen in 1B. It should also be taken into consideration that the transformation of smectite to illite leads to chlorite formation as a by-product of this reaction (Hower et al., 1976; Ahn & Peacor, 1985). Although smectite has not been identified in SEM, its presence may be inferred through the EDS results as all the elements constituting its formula are present in EDS. The smectite general chemical formula is as follows: (Na,Ca)0,3(Al,Mg)2Si4O10(OH)2•n(H2O). Another reason why it was not identified in SEM is due to alteration. As these clay minerals are surrounded by a marine environment, some saline fluids may have seeped in and contributed (regardless of their quantity) to an alteration of kaolinite to chlorite through the addition of Mg cations dissipating from surrounding phyllosilicates. This is further supported in 1B where authigenic chlorite flakes dominate the overgrowth material present, these chlorite flakes are also well presented in 3A. In addition to image 1B implying the formation of chlorite from a kaolinite precursor, the process was a slow undertaking, provided that the kaolinite managed to persist into deeper routed marine sediments that are not in favour of its formation. If this was not the case and alteration was a speedy process, there would be no evidence of the precursor.

Furthermore, EDS (Appendix G) results signify the presence of Ca and Cl which has previously been shown by Millot (1942), to be detrimental for Kaolinite formation. Kaolinite may only form in the complete absence of Ca which may be seen throughout the acquired samples and is accompanied by the absence of kaolinite except for 1B, proving that the minor amounts of kaolinite are in the process of being altered. The two elements encourage the formation of illite andchlorites.

The equation for the transformation of kaolinite to illite is presented as follows:

$$K\,[AlSi_3O_8] + 2Al_2\,[Si_2O_5]\,(OH)_4 \rightarrow KAl_3Si_3O_{10}(OH)_2 + 2SiO_2 + H_2O$$

(K-feldspar) + (Kaolinite) → (Illite) + (Quartz)

This reaction is concomitant to the precipitation of quartz which may be seen as overgrowth (Lima & De Ross, 2002) as shown in 1B and throughout the depth of well Ga-Q1 (supported by Appendix G). The calcium (contributing to calcite formation) which is present in minor proportions and is sourced from biogenic carbonate found in various segments of the lithology, contributes to the smooth cementing clay which is largely quartz dominated (as confirmed through XRD in Appendix F) and is seen in Appendix G1.1. This cementing clay primarily connects the larger and more defined grains to each other and simultaneously diminishes the interstitial spaces between these grains.

Sample 2A shows a detailed magnification of authigenic illite sprouting from a pore space. Some of the illite in 2A was identified to have formed as a result of a reaction that incorporated pore fluids as the illite stems directly out of the pore spaces where its authigenesis was initiated. This further correlates with some previous research by Pevear (1999) where he observes that as diagenesis takes place, the reaction between pore fluids and mineral constituents such as feldspars result in the precipitation of illite. The material concretions delineating the pore space in 2A probably contributed to its precipitation. The stringy, compact pore filling illite represented by the image shows complete destruction of porosity within that area which indicates that any fluid (hydrocarbons, marine waters or fluid consisting of ions) previously occupying the pore space has 1) been evacuated due to illite invasion, or 2) has been incorporated in the formation of the clay mineral through transported pore water (possibly derived from a combination of meteoric and shallow marine water). This illite grows outward where it spreads across a clayey mica matrix.

The pore bridging illite in Appendix G2.1 indicates slight authigenesis as it is partially wrapped around centered accumulations of feldspar, some of the wrapped parts are in their position of authigenesis whereby others have grown in length and as growth progressed it continually wraps itself on the large grains. This stringy illite is sufficient in quantity to obstruct fluid flow in this region. In Appendix G2.1 the authigenic illite overgrowth spreads across the rock matrix and adheres closely to the substrate which is covered by quartz, feldspar and clay overgrowth. It, therefore, forms a surface wrapping network that covers this overgrowth and thus hinders its further progression. Deformed illite through mechanical processes which was on the verge of forming fully compartmentalised stringy illite as seen in Appendix G2.1.

The Chlorite flakes forming matrix which eventually protrudes from the matrix (Appendix G3.1) in the form of flakes is shown in 3A. The geometry of the chlorite is not of uniform alignment as there are various parts representing face to edge geometry. This type of arrangement leads to chlorite occupying a larger volume than what it would have occupied provided that it was for example closely stacked on top of each other. Therefore if any fluids were to be transported to these spaces provided

by the edge to face geometry, they would be stored in isolation to each other thus forming unconventional storage for hydrocarbon accumulation if face to edge geometry is formed well and fully in contact with edges. If the passing fluid/hydrocarbons were to be transported to a favourable reservoir through migration, this type of packing arrangement would only permit small quantities (if there are gaps between face to edge geometry i.e. the “faces” are not in full contact with the “edges” or the “edges” are not in full contact with the “faces”) which would invariably be negligible amounts of fluid flow at a time. Although unfavourable, the previous example would be more ideal than the reality which is most likely to proceed, being that this type of geometry will probably trap fluids (in the form of secondary porosity) that it encompasses as the “face” part of the chlorites are transpired as “many small traps ”. This phenomenon may be compared to sandstone reservoirs containing many pore spaces that are not connected. The presence of these fluids in the chlorite micro-pores is only applicable provided that chlorite formation was not chemically influenced by these fluids as this may lead to a reaction of either further precipitation or alteration of current minerals, therefore these fluids should be hydrocarbons for storage to be accommodated for.

Sample 3 shows some dents which were indicative of glauconite imprints (which were also identified via thin section slides throughout well Ga-Q1), and can be seen in Appendix G3.2. Not too far from their missing counterparts are some glauconite palettes in situ with some of these minerals protruding as if part of the matrix. The smaller one in Appendix G3.2 appears to be placed in position instead of having precipitated and developed from underlying matrix. This shows that the glauconite palettes are readily disintegrated from the ground matrix in this section. Appendix 3.3 shows planes/areas most affected by strain as rock samples were retrieved from location characterised by folding and faulting. These areas of weakness that gave in through stress and strain incurred show that clay minerals are malleable so as to crack and bend irregularly to form their resultant shapes and planes of weakness where cracking and bending occurred.

The outlined area in 4A A depicts a gauge caused by previous euhedral grain in situ either as detrital grain or overgrowth which was most likely to be a dismantled quartz grain. It was dismantled through friction processes undergone during transportation and deposition of sediments. Another likely occurrence leading to this could have taken place during sample preparation as samples were cut into sizes applicable for SEM analysis. Towards the right of 4A, the red circle outlines conchoidal fracture of quartz crystal. This mechanical feature was also observed through previous studies conducted by Margolis and Krinsley (1974) showing that collision through uniform compression involving two sand grains or between a single sand grain and a rough surface lead to the repercussion of varying conchoidal breakage patterns. Furthermore, these features are representative of a fluvial

environment as opposed to an aeolian environment of origin (Margolis and Krinsley, 1971). Grouped chlorite minerals mainly positioned on top of each other with some depicting a slight curve in geometry are seen in Appendix G4.1. These chlorites are the Fe rich end member chamosite and are relatively close to each other in a stacked manner rather than a face to edge geometry, and thus contributing to the ground matrix.

Tabular deformed plagioclase grains which indicate previous euhedral shape are outlined in Appendix G4.2. The red marker shows a borderline plane segregating plagioclase outgrowth towards the left (protruding in area of weakness) and adjacent to it are some flaky chlorites protruding from a chlorite matrix. In addition to this, when observing the lower part that is closer to the clay matrix the plagioclase is still very well in tact thus forming its own pure plagioclase matrix of which the surrounding grains have been partially chipped away exposing cleavage planes and the inner structure. The readily deformed feldspars are the results of diagenetic processes undergone in the marine environment. The main reason as to why it does not occupy the entirety of the void space it protrudes into is due to the deformed edges which have been chipped away reducing the entire volume occupied by the plagioclase.

Sample 5A shows authigenic illite directly in contact with mica (muscovite) substrate as illite grows through precipitation and partially wraps itself around muscovite (this is also supported through thin section studies as seen in Figure 6.4 sample 5A (in the red circle)). Illite is known to form consequently from the degradation and sometimes alteration of muscovite (Howie et al., 1992) which may be seen in 5C, in addition to this, formation of illite is further favoured by alkaline conditions and the presence of Al and K which is confirmed through EDS in Appendix G5.3 and G5.4. The rest of the illite grows outward occupying adjacent space in random orientation. This initial overgrowth is due to alteration of mica to illite. The poorly defined compartments on the stringy illite which are more clearly identified in Appendix G5.1 represent the segments of periodical precipitation of the authigenic illite through the precipitation of mica, therefore the indents show precipitation breaks or pauses with some at closer distances to each other than others. These poorly defined compartments also indicate that dissolution took place from time to time and that it was not an instantaneous process which would have otherwise yielded perfectly straight stringy illite. Sample 5 shows an overall larger amount of the clay grains within the interstitial spaces (Appendix G5.1) as opposed to sample 1-4 whereby the clay grains are more eminently incorporated in the matrix. Appendix G5.1 also shows a lot of quartz matrix with a few eminent quartz crystals exhibiting sub- euhedral crystal faces along with randomly orientated illite and platy muscovite.

There are some feldspar and quartz overgrowth which are further accentuated by a centralised heap of overgrowth accumulation as seen in Appendix G5.2. This overgrowth mainly occurs as post compaction features as they are not intergranular contacts.

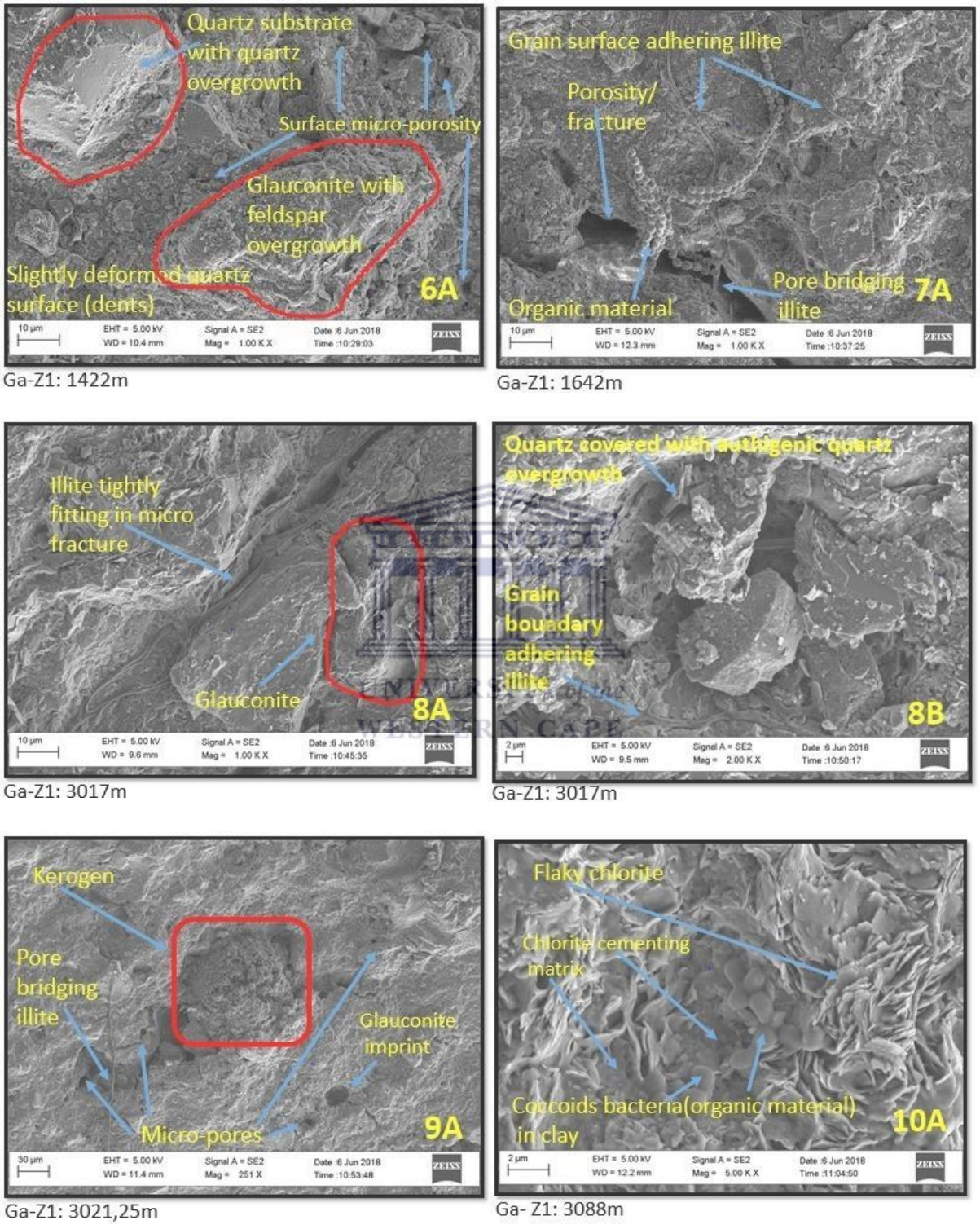

Figure 6. 11: SEM sub- images showing mineralogy and depicting relationship between clay mineralogy and petrophysical properties for sample 6-10 in well Ga-Z1.

Many micro-pores (secondary porosity) formed through dissolution were identified in Figure 6.11 sample 6A, but chances of permeability seem very unlikely here due to a lack of connectivity between the micro-pores. This is seen throughout in well Ga-Z1 as 9A has similar pore structures. On the left of 6A, smooth crystalline quartz covered with small fragments of quartz overgrowth may be seen. A polygonal glauconite pellete substrate protruding from the matrix and thus contributing to the silicate rich cementing material, however not to a large extent.

The geological conditions presented in 6A encompass leached feldspars in coalition with cementing quartz and clay minerals. Surdam & Crossey (1987), van Berk et al., (2013), Yuan et al., (2015) & Yuan et al., (2017) have noted that the disintegration of feldspar through dissolution involves the leaching of CO_2 accompanied by organic acids derived from maturing kerogen (kerogen more explicitly identified in 9A) and the degradation of hydrocarbon, particularly in the subsurface. According to Yuan et al., (2019), chemical processes such as dissolution tend to lead to the enhancement of secondary porosity and permeability provided that this process takes place in an open geochemical system under the influence of moderately deep faults. In terms of closed geochemical systems at similar depths, leached feldpsars trigger the decrease in permeability accompanied with the formation of secondary distributional interstitial spaces. The latter is identified in this throughout the well. The leaching of feldspars contributes to the authigenesis of clay minerals through dissolved solutes that are transferred to the neoformed clays. This highly contributes to the tightening of the rock structure as seen from 6A to 10A and more explicitly in Appendix G6.1, and ultimately contributes to the detriment of porosity and permeability.

Sub- euhedral polycrystalline quartz grains with overgrowth may be seen in Appendix G6. A closer look at some of the micro pores in both 6A and Appendix G6 shows a combination of pores formed through dissolution as well as physical dismantling of the grains that were previously in those micro-pores, thus leading to secondary micro-porosity. Through thin section study it was evident that the majority of the morphology of the interstitial pores comprised of closed pores. A more comprehensive morphological visual in 6A and Appendix G6 outlines the spatial details which exhibits a cul-de-sac morphology. This analysis however does not confirm whether some of these cul-de-sac morphologies are also catenary. The bulk of sample 6 is a representation of polycrystalline quartz which is supported by Appendix G.

Sample 7A displays the presence of a microscopic organism which is partially located on the surface of the rock with its remainder partially hanging in the fracture. By so doing it inflicts porosity and permeability, but it can also contribute to the organic matter needed for production of kerogen and ultimately hydrocarbons under the relevant and conducive conditions. The organic material is

accompanied by surface adhering and pore bridging illite of which the latter is of detriment particularly to permeability. Micro-fractures having good porosity and continuous pathways within sample 7 are also identified in Appendix G7.

Grain boundary adhering illite plays two roles in 8A, 8B and Appendix G8 which result in both a negative and positive outcome with regards to porosity. In 8A the illite is present as a pore lining mineral in the fracture. As a result of the pore lining illite is in direct contact with the flaky chlorite and small feldspar overgrowth. It is then partially and fully wrapped around some of these overgrowth grains which restrains them from growing any further and ultimately infiltrating the available space in the fracture. Sample 8B presents pore lining illite which also inhibits further developments of chlorite and quartz overgrowth. The illite identified in 8B is partially pore bridging (also seen in Appendix G8.2) in the background behind the larger euhedral quartz crystals. These quartz crystals are almost fully covered by quartz overgrowth and clay sized minerals, particularly the quartz grain on the top left of 8B.

Sample 9A depicts the accumulation of kerogen conveniently located in a semi fracture. As time goes on and suitable conditions such as temperature, pressure and deposition depths are reached, hydrocarbon formation will take place in this location of convenient storage. A glauconite imprint representing a glauconite that was previously in situ is seen in 9A, a close up of this is shown in Appendix G9.2. The imprint is a sign of deformation through abrasion that led to the removal of that grain. This surface is associated with glauconite grains situated nearby and are more eminent in Appendix G9.1 along with EDS analysis in Appendix G9. In Appendix G9.1 they partially cover some of the micro-pores with the majority of them located on the dense matrix. Appendix G9.2 also encompasses both feldspar and quartz overgrowth forming a heap of overgrowth.

Sample 10 A represents a centralised chlorite cementing matrix which gradually progresses outward to the bottom left corner of 10A. This image also shows some organic matter in the form of coccoid bacteria which was identified accordingly due to its circular shape and configuration. Flaky chlorite stacked together surrounds the chlorite matrix with coccoid bacteria. The overall cementing material and chlorite leave no room for interstitial spaces, this may also be seen in Appendix G10.1. Sample 10 also has some. Appendix G10.2 and G10.3 show detrital plagioclase where deformation has taken place and seems to be due to abrasion contact undergone from place of detrital origin to location of deposition. The deformation is more prominent on the outermost protruding end of plagioclase as the rest of the mineral shows only slight deformation as it does not have as much exposure as the outermost protruding edge.

CHAPTER 7: CONCLUSIONS

7.1. Discussion

Clays form part of sedimentary rocks that form in terrestrial environments and are at a later stage transported to shallow and deep marine environments through rivers with the assistance of the wind. Upon their transportation, some of these clays encountered reworking processes as a result of agitated waves. Gamma ray shape and pattern in log interpretation served as an indicator of the depositional environment. The most eminent and most recurring patterns were identified as cylindrical, serrated and a combination of the two. The former inferring the influence of eolian, braided fluvial channel fill and submarine channel fill as well as tidal sands. The later inferring fluvial floodplain, strom-dominated shelf and deep-marine slope influence upon formation. Therefore the above formed the depositional environments at different times within the lifespan of the basin as the patterns inferring these environments were found at different depths within the well. These processes were the primary influential factors contributing to the transportation, deposition and thus alteration and compaction of the minerals as a result of the mechanical and chemical process.

The poor correlation coefficients from the poroperm plots implied that porosity was not the only factor affecting the permeability within the studied reservoirs. It was through the petrographic studies that these external factors were isolated for thorough study, of which the prevailing trends were identified. This analysis provided a much clearer understanding as to how external factors interact with the physical, chemical and biological structures that they have infiltrated as they reveal the following clay mineral characteristics; structure, formation, location in relation to each other and the way they occupy pores within the formation. Through the calibration of core and log plots, the core results particularly of well Ga-Q1 and Ga-E2 showed high core water saturation. Petrographic studies show that glauconite was one of the prevailing minerals. Glauconite is known to have a tendency to retain water in its pore spaces, especially core samples extracted offshore; and regardless of its distribution in the matrix (Thomas et al., 2003). This led to core samples having higher water saturations which explains the poor correlation of water saturation. The effect of glauconite on petrophysical properties is not only to occupy pore spaces but to also increase the water saturation retained in these pore spaces.

The cementation exponent (m) from well log calculations of the four wells ranging from 1.98- 1.99 indicates moderate cementation. The clay type present is both of detrital and authigenic origin as seen from petrographic studies.

The approximate composition of the samples deduced from petrographic studies indicates the presence of 53% quartz, 22% feldspar, 20% matrix (including clay and organic material) and 5% accessory minerals. In addition to quartz occurring in the bulk of the samples, they are mostly associated with feldspars and as epimatrix (streaks and blotches of clay that have replaced feldspars). These quartz grains were found in both crystal forms, namely monocrystalline and polycrystalline. The overall quartz, feldspars, micas and clays exhibited good crystallinity with some clays being amorphous.

The poor to moderate sorting of grains was accompanied by sub-angular grains with some edges showing evidence of slight modification. The variation in sorting includes sub-rounded grains where corners are more rounded and native edges and faces have been considerably reduced. The sub-rounded to sub-angular sorting not only infers the distance from the original location to the location of deposition, but it also shows the simultaneous accumulation of some grains during transportation and deposition. The variation in sorting, angularity and sphericity which may be seen in Figure 6.5A and Appendix E10 suggests the overall influence of differential diagenesis. Uniformity in grain size leads to an increase in interstitial space whereas a mixture of varying grain size leads to the counter effect. Thin section study reveals that the grain size alone cannot affect the porosity and permeability, however the relationship between the grain size, shapes and sorting influences the two parameters. Areas that are characterised by increasing sphericity are most likely to be accompanied by reduced interstitial space and areas of high angularity are accompanied by higher interstitial pores. This may be seen in Figure 6.5 (6A) which is characterised by sub-angular grains that are mixed with randomly dispersed platy and needle-like muscovite grains and is supported by higher porosity. This example has greater porosity compared to areas that have either high sphericity or a combination of sub-angular and sub-rounded grains as seen in Figure 6.4 (4A). Within Figure 6.4 (4A), the uniformity would have been increased if it were not for the random distribution of organic matter and clay matrix between the grains. The lack of uniformity in samples was also influenced by grain rotation and mechanical breakage as burial progressed thus contributing to decreased porosity, this may be seen in Figure 6.5 (7A) and 6.5 (8A).

The majority of the retrieved samples were a clast supported rock with a very few being both clast and partially matrix-supported for example Figure 6.4 (4A) and Appendix E5. The thin section slides clearly show that these rocks fall under the clastic and organic classification.

One of the biggest hindrances to the potential of porosity and permeability to thrive in these formations was the horizontal alignment of the fine grained brown clay matrix which was mainly identifiable in representative core specimens and the thin section as seen in Appendix E9. Majority of the samples are characterised by a compact clastic clay matrix and shows the presence of quartz and feldspars. It is above this matrix that detrital, diagenetic and authigenic process is more clearly inferred as opposed to the smooth uniform matrix. This is because the visible grains above the compact clastic matrix provide direct information with regards to the morphology, mineral association, orientation, size, alignment etc. of which these combined aspects allow for the interpretation of the processes that took place as well as the effect of these grains and minerals on petrophysical properties. Compaction eliminated the void spaces and forced the clay matrix to infiltrate the previously unoccupied spaces and thus reduced the volume occupied by the lithology and led to the impediment of permeability. In addition to the above, this led to the subsequent expulsion of mineralised water which migrated throughout the formation of the wells. This migrated water formed a vital contribution to the overall diagenetic processes as it relocated to various parts of the formation while simultaneously transporting dissolved ions which were primarily involved in mineral alteration and neoformation processes.

The porosity values presented in the reservoir summary result tables (Table 5.11- Table 5.14) are relatively good considering the litho-unit in which they are found. These values may be slightly influenced by the shale effect/ bound water effect (surface bound water of the clays constituting the shales leading to higher porosity readings). The petrophysical results show that clay mineralogy has a much higher impact on the permeability than the porosity as the porosity managed to reach a “good porosity” classification whereby the permeability only reached a “fair permeability”. This is supported particularly through the thin section where the pore spaces were easily identifiable, with more difficulty experienced in identifying interconnecting pathways. In between these pathways was a clay matrix which isolated the pore spaces from each other.

As some of the void spaces were eliminated, the pore associated structure was subsequently altered. According to Ishimwe (2014), the classification of porosity through rock morphology may be sub-divided into three separate morphologies accounting for each pore associated structure. The first one is catenary which refers to a pore having more than one throat for fluid flow, the second is cul-de-sac where the pore is characterised by a single throat passage, and the third is a closed pore which has a complete absence of inter-pore connection. Although a more extensive view of the structure is achieved through SEM, the thin section revealed the closed pore morphology as the most prevalent in the samples. The increase in the retrieval depths of samples was concomitant to an increase in

separation between the closed pores, which ultimately led to reduced permeability as seen in Appendix G6.1 and G9.1. This is likely a result of the orientation of clay mineral packing due to pre-diagenetic weathering and lithification upon deposition. Another possibility could be as a result of dissolution from chemical reactions through the interaction of concretions with meteoric water, leading to secondary porosity. This is supported by work conducted by Emery et al., (1990) and França et al., (2003) where they observe that inorganic-original feldspar dissolution is a result of leaching by meteoric freshwater where sedimentary basins are concerned. The destroyed void spaces were mainly primary porosity as the cement was formed around the detrital grains.

Clay distribution is a good indicator of the origin of the grains, it helps to distinguish whether the grains are detrital or authigenic. Structural and laminated distribution is indicative of detrital clay presence (Schmidt & McDonald, 1979), this is due to the clays being confined between grains as the detrital clays are deposited simultaneously to the sandstone grains. Structural distribution may be seen in Figure 6.5 (9A). Laminated distribution may be seen in Appendix E6 and Figure 6.4 (4A) as well as in Figure 6.5 (7A) in sample 7 and a few other samples. The dispersed distribution is indicative of authigenesis (Schmidt & McDonald, 1979) as the clays are precipitated into the void spaces in no specific order or location, as long as conditions for precipitation are met. As a result of clays having significantly larger surface area compared to sand grains, this leads to a property of chemical sensitivity depending on the type of clay present as well as affecting the petrophysical properties (i.e. pore spaces it infiltrates). The dispersed distribution may be seen in Appendix E8. A combination of structural and dispersed distribution may be seen in Figure 6.4(2A).

The Illites are typically formed as a result of weathering and alteration of rocks which are rich in potassium and aluminium and are highly exposed to alkaline environments (Anderson, 2018). Contrary to kaolinite, illite does not require any form of potassium leaching to take place as a prerequisite for its formation. Just as Bjørlykke (1997) observed, it is in the presence of sufficient amounts of potassium which were identified through XRD and SEM (EDS) that led the pore water to be stable enough to accommodate the formation of illite. Some of the authigenic illite was formed through a reaction process that involved the interaction between pore fluids and surrounding mica and feldspars during burial/deposition which was accompanied by an increase in temperatures and pressures. Thin section and XRD show the alteration of feldspars and mica such as muscovite, biotite etc. into clay minerals particularly chlorite and illites including the iron-rich illite end member i.e. glauconite. The alteration of feldspars in subsurface reservoirs of sedimentary basins is one of the indicators leading to the completion of CO_2 sequestration which may promote the formation of illite in mudstone-sandstone formations (Bertier et al., 2006; van Berk et al., 2013).

The clay mineral illite is mainly present as pore filling and pore bridging with some amounts of grain adhering illite. This prevented 1) fluid flow within the reservoir as the pore bridging illite occurred in both isolated pore spaces as well as connecting pore spaces and 2) hydrocarbons from being successfully stored for accumulation to take place.

It is clear that the illite mainly contributes to pore preservation when it is spread across the ground matrix or is micro-fracture lining preventing overgrowth of minerals it spreads across; this is not to be mistaken with authigenic pore filling illite as in Figure 6.10 (2A) characterised by minimal deformation. The pore preservation is seen in Figure 6.11 (8A), Appendix G2.1B and Appendix G8.1C, where in Figure 6.11 (8A) for example it does not fill all the void spaces as it does in Figure 6.10 (2A), but rather covers underlying overgrowth. It is evident that authigenic illite has greater potential to be pore preserving than detrital illite. A good example of micro-fracture lining illite is shown in Figure 6.11 (8A) where the authigenic illite encompasses the mineral substrate of which it mainly precipitated from. The mineral was most likely muscovite as collaborated with thin section and XRD results. This is due to the former having a tendency to adhere to the substrate grain which it forms from and continues to grow while simultaneously adhering to the grain, provided that the grain surface is large enough. This shows diagenetic origin as it is also un-altered.

When illite forms without any surrounding constraints and the attachment strings grow longer they tend to occupy the surrounding area in random orientation. When the orientation becomes too randomised (i.e. lack of preferential orientation/not adhering to substrate) such as in sample 5 as seen in Appendix G it is evidence of detrital illite as it has undergone some degree of deformation. This sample shows that not all of the illite is a result of precipitation from the single muscovite, some of the surrounding illites have been deformed through the diagenetic process are of detrital origin. A closer look at the randomly orientated illite shows a lot of deformation around its structure (Figure 6.10 (5A) and appendix G5.1), whereas the grain adhering illite represents smoother and continuous precipitation (Appendix G2.1B), therefore anything in between shows the mineral is not too far from the location of precipitation. SEM results show that the structure of illite is highly influenced by both the environment of formation and deposition. Stringy Illite is found to be of authigenic origin in various locations and in other locations to be of detrital origin. The detrital illite in SEM was significantly less than its counterpart authigenic illite.

The alteration of feldspars such as biotite to glauconite is a common process that takes place under marine conditions (Hendricks & Ross, 1941), which was observed in the SEM results. The presence of glauconite was easily identified particularly from sample 3 -10, with corresponding depths ranging from 2329m -3088m.

The widespread presence of glauconite and overall micaceous composition as seen in petrographic studies indicate a slow deposition environment and the slow accumulation of sediments. The presence of these minerals particularly glauconite also indicate formation under conditions of perturbed waters which is characteristic of shallow waters (Hadding, 1932). Through the reworking of sediments and over long periods of time sediments were transported to slightly deeper marine environments. The primary conditions favourable for glauconite formation are reducing marine environments, although its formation is not only restricted to this environment. This was accompanied by sufficient concentrations of alkalies such as Mg, Na, k, Ca etc. as identified in XRD and EDS, hence the alteration of certain illites and glauconites from feldspars as they hold a high concentration in these elements, these alterations can be seen in both thin section and SEM.

The dark grey colour in some glauconite minerals is indicative of increased contents of hematite/ iron oxide within the grain composition and these minerals mainly occurred as glauconite pallets. These pallets had an overall larger effect on porosity than permeability as the pore spaces that were being closed off were micro-pores that were separated by clay matrix. In various samples, the glauconite imprints show that these grains were occupying (Appendix G8.1C) and closing pore spaces (Appendix G9.1B). The pore spaces which clearly represent grains that were previously in situ further support that these samples have undergone numerous deformation processes. Deformation in the form of mechanical processes that involve the rearrangement of mineral structure and thus the removal of grains from their positions. The majority of grains were characterised by fractured grain surfaces as well as protrusions and depressions covering up entire surfaces, these are indicative of detrital origin as they have been slightly reworked. The grain surfaces varying from smooth crystalline to slightly crystalline texture are indicative of authigenesis for example Appendix G1.1.

Time was another vital factor playing a role in the alteration of minerals to glauconite, the longer the environment prevailed in being unaltered, the more complete the alteration process was. If not, however, and alteration does not reach completion, the results can be seen in the prevalence of minerals that are not stable in marine environments being present, such as kaolinite. With minor amounts of kaolinite identified it is deduced that these samples experienced a period of rapid deposition possibly accompanied by a source area where kaolinite was a common mineral. If the latter is true this points to alteration of kaolinite to the vast amounts of chlorite present, hence the minor occurrence of kaolinite, due to its alteration and therefore depletion.

There was some difficulty encountered in identifying chlorite through thin section because it formed part of the intergranular very fine grained clay matrix, therefore making it harder to distinguish from other fine grained material. The intergranular feature signifies formation under pre-compaction processes. Chlorite that was identified through its morphology in SEM as well as from corresponding EDS results was later confirmed to be the Mg rich end member termed clinochlore through XRD analysis. Thin section studies show the presence of some iron oxides of which the iron oxides could have interacted with the alumina silicates to form the less occurring Fe rich end member, chamosite. The overall chlorite identified was a flaky texture and occurred as part of the ground matrix. In addition to chlorite being present as a flaky texture, it was also present as a face to edge geometry which led to an increased disruption of permeability pathways. It was possible to identify the areas of transition between the matrix and the chlorite flakes as the flakes appeared to be rising from the matrix (Figure 6.11 (10A) and Appendix G10.1), meaning that in those areas conditions were highly favourable for chlorite formation as this mineral formed in abundance in certain areas as seen in Appendix G4.1. The matrix where these chlorite flakes protrude and therefore precipitated from contributed to the micro-inter-porosity filling matrix thus reducing porosity and permeability. The observation of alteration into chlorite is supported by De Ros et al., (1994) as they have observed that transformation is highly common when Fe and Mg are present in pore waters, therefore preferential ferromagnesian concretions such as biotite and amphibole react with these pore waters and transform to chlorite.

This study shows a very close correlation between the presence of clay minerals and organic matter. The morphology and orientation between the two were best represented through the thin section where the widely spread organic matter surrounding the minerals persist throughout most of the samples. Further on in SEM is the presence of what seems to resemble micro-organisms as well as organic matter and kerogen. It is therefore postulated that the formation of the major clays identified namely illite and glauconite somehow incorporate the presence of these bacteria into their formation either through bacteria action or the actual components playing a role.

The crystallisation of most minerals from solution was assisted by silica and oxygen ions that were available when the ubiquitous quartz grains were disintegrated and resultant ions formed part of interstitial fluid. The quartz overgrowth in the thin section which signified a post compaction diagenetic process was seen in Figure 6.4 (2B and 5A) and 6.5 (9A), this was supported by SEM particularly in Figure 6.11 (6A and 8B), Appendix G5.2 and G9.2. The overgrowth was also characterised by syntaxial quartz overgrowth which was more visible in Figure 6.4 (2B) and 6.5 (9A).

Through the thin section, the main identified mechanisms were deformation, compaction, recrystallization, cementation and dissolution. XRD studies show that the majority of the illites are of

detrital origin and other clay minerals occur as both detrital and authigenic. SEM further supports mineral overgrowth and neoformation i.e. the overall identification of authigenic minerals particularly fine grained quartz, followed by clays and then feldspars. Petrography and SEM show a stronger affinity towards an authigenic origin and XRD show a stronger affinity towards a detrital origin although both types were identified in all analysis.

7.2. Conclusion

This study was set out to determine the effect of clay diagenesis on the petrophysical properties of sandstone reservoirs in block 11a in the Pletmos Basin where four reservoirs were identified in each of the four wells (Ga-Q1, Ga-Q2, Ga-Z1 and Ga-E2). These corresponded to facies analysis A- E where the best reservoirs were dominated by facies B and D. In well Ga-Q1, the porosity decreased from 22.1% in zone 4 (2174.3 m- 2199.7 m) to 13.5% in zone 1 (3125.7 m- 3143.7 m) and permeability decreased from 2.45 mD in zone 4 to 0.722 mD in zone 1. This well had average water saturation of 43% and an average volume of clay of 33.65%. From well Ga-Q2, the porosity decreased from 16.51% in zone 4 (1760 m- 1789.8 m) to 9.4% in zone 1 (2365.5 m- 2400 m), this well had average water saturation of 77.35% and an average volume of clay of 21.17%. From well Ga-Z1, the porosity decreased from 18.1% in zone 4 (1354 m- 1431 m) to 3.5% in zone 1 (3077.3 m- 3092.28 m) and permeability decreased from 1.73 mD in zone 4 to n/a in zone 1. This well had average water saturation of 76.1% and an average volume of clay of 32.08%. From well Ga-E2, the porosity decreased from 28.6% in zone 4 (1753 m- 1813 m) to 10.28% in zone 1 (3045 m- 3066 m) and permeability decreased from 3.27 mD in zone 1 to n/a in zone 4. This well had average water saturation of 38.1% and an average volume of clay of 39.9%. The calibration of core data with wireline logs in order to validate the logs generated form IP show an overall poor calibration for well Ga-Q1 and Ga-E2, whereas well Ga-Z1 shows an overall good calibration. This means that external factors namely diagenetic factors had a larger influence on the intervals of wells Ga-Q1 and Ga-E2 as opposed to well Ga-Z1.

The porosity in the most shallow depth intervals (as revealed in petrophyhsics and petrography results) represents the primary porosity. The initial decrease in porosity represents the destruction of primary porosity as the pore geometry is altered with an increase in depth leading to either secondary porosity or a complete destruction of it. In addition to this, the collected core samples used for petrography showed limited amounts of lithic fragments which accounted for the reduced porosity as the depths increased. This was accompanied by sub-rounded to sub- angular grains as determined through thin section. Petrographic studies show that illite, chlorite and green glauconite pallets were the major identified clay minerals along with very fine grain ubiquitous quartz. These were

accompanied by the presence of very minor kaolinite minerals. Similar to the observations made by Worden & Burley (2003), this study shows that when sequential dissolution and precipitation occur simultaneously it leads to another process of diagenetic environments which is known as alteration which can take place on both minerals and detrital grains. Along the trajectory leading to the poorer petrophysical properties in increased depths, the alteration of micas and feldspars to illites and chlorites compromised the quality of the reservoirs in certain areas as they contributed to the dense inter-grain matrix. The presence of glauconite, feldspars and micas contributed to the permeability destructing clay matrix, this led to permeability being affected to a larger extent than porosity, as a trend of the decrease in porosity was accompanied by the complete destruction of permeability. Through thin section and SEM, more so the latter, a greater understanding of the pore type and evolution was reached. The majority of the illite occurred as pore bridging illite thus interfering with the pore geometry as it also acted as a pore throat.

Through petrographic studies, it is evident that the diagenetic and authigenic clay minerals influenced the creation of the secondary porosity that resulted through dissolution preceded by compaction. The adverse effects of the major clay minerals were accompanied by porosity and permeability preserving illite and chlorite in places where they hindered the initiation and continuation of overgrowth of underlying clay minerals protruding from the highly siliceous ground matrix.

The ambient environment of formation and deposition, precursor material composition, depositional environment, surrounding chemical conditions, pre-diagenetic weathering, mineral composition and sorting, physical conditions including tidal currents and topography of deposition environment etc. were all taken into consideration upon the study of the trajectory leading to and affecting clay diagenesis. In summary, the final principal diagenetic process affecting the petrophysical properties of the reservoirs were dissolution, precipitation, alteration, compaction and deformation, of which these processes were partially assisted by meteoric water.

7.3. Recommendations

A systematic study incorporating core samples from the identified reservoirs of wells Ga-Q2 and Ga-E2 should be acquired in order to carry out petrographic studies. Once the petrographic studies are carried out from these two wells an improved analysis and more accurate trends for the effect of clay diagenesis on petrophysical properties will be acquired. The core permeability for well Ga-Q2 should also be acquired as it was not available during the course of the present study. This will assist in producing a poroperm plot for this well and it will add to the permeability trend identified in Figure 5.30.

From the 3D parameter viewer, the petrohysical properties of porosity and permeability show an increase as navigation trends more eastward, and a decrease in these parameters towards the west. The results of this research should instigate appraisal towards the eastern parts of block 11a in the Pletmos Basin.

With regards to potential exploration in the area, the diagenesis is partially conducive to the petrophysical properties. As observed in the study, the porosity is classified as fair to good, however, there are insufficient flow pathways and this affects the flow and thus the accumulation of hydrocarbons in significant amounts, therefore fracking should be considered.

REFERENCES

Abedi, L., Vafaie, S., Baghban, S., M.A, M., & Naderi, H. (2012). Gelation time of hexamethylenetetramine polymer gels used in water shutoff treatment. *Journal of Petroleum Science and Technology, 2*(2), pp. 3-11.

Adie, R. J. (1952). The position of the Falkland Islands in a reconstruction of Gondwanaland. *Geological Magazine, 89*(6), pp. 401-410.

Ahmad, K. M., Kristály, F., Turzo, Z., & Dócs, R. (2018). Effects of clay mineral and physico-chemical variables on sandstone rock permeability. *Journal of Oil, Gas and Petrochemical Sciences, 1*(1), pp. 18-26.

Ahn, J. H., & Peacor, D. R. (1985). Transmission electron microscopic study of diagenetic chlorite in Gulf Coast argillaceous sediments. *Clays and Clay Minerals, 33*(3), pp. 228-236.

Anderson. (2018). Retrieved August 2018, from https://web.viu.ca/earle/geol312/USC-anderson-clays.pdf

Archie, G. (1942). The Electrical Resistivity Log as an Aid in Determining Some Reservoir Characteristics. *Transaction of AIME, 146*(1), pp. 54- 62. doi:https://doi.org/10.2118/942054-G

Asquith, G., & Krygowski, D. (2004). Basic Well Log Analysis. *AAPG Methods in Exploration*, pp. 31-35.

Atlas, W. (1995). Introduction to wireline log analysis. *Western Atlas International Inc.*

Attfield, M., Barnes, P., Karl Cockroft, J., & Huub, D. (2018). X-ray detectors. Retrieved October 2018, from http://pd.chem.ucl.ac.uk/pdnn/inst1/detects.htm

Barton, C. D. (2002). Clay minerals. In c. Rattan Lal (Ed.), *Encyclopedia of Soil Science* (pp. 187-192). New York: Marcel Dekker.

Bate, K., Malan, J., De Wit, M. J., & Ransome, I. (1992). Tectonostratigraphic evolution of the Algoa, Gamtoos and Pletmos basins, offshore South Africa. *Inversion tectonics of the Cape Fold Belt, Karoo and cretaceous basins of Southern Africa*, pp. 61-73.

Ben- Avraham, Z., Hartnady, C., & Kitchin. (1997). Structure and tectonics of the Agulhas-Falkland Fracture zone8. *Tectonophysics*, pp. 83-98.

Ben- Avraham, Z., Hartnady, C., & Malan, J. (1993). Early tectonic extension between the Agulhas Band and the Falkland Plateau due to the rotation of the Lafonia microplate. *Earth Planet*, pp. 43-58.

Bennion, D. B., Bennion, D. W., Thomas, F. B., & Bietz, R. F. (1998). Injection water quality-a key factor to successful waterflooding. *Journal of Canadian Petroleum Technology, 37*(6).

Bennion, D., Thomas, F., & Bietz, R. (1996). Determination of initial fluid saturations- A key factor in By-passed pay determination. *Hycal Energy Research Laboratories Ltd*, pp. 1-9.

Bertier, P., Swennen, R., Laenen, B., Lagrou, D., & Dreesen, R. (2006). Experimental identification of CO2–water–rock interactions caused by sequestration of CO2 in Westphalian and Buntsandstein sandstones of the Campine Basin (NE-Belgium). *Journal of Geochemical Exploration, 89*(1-3), pp. 10-14.

Bill, K., De Waal, J., Dicker, A., & Kantorowicz, J. (1988). Petrophysical core analysis of sandstones containing delicate illite. *The Log Analyst, 29*(5).

Bjørlykke, K. (1997). Lithological control on fluid flow in sedimentary basins. In Fluid flow and transport in rocks . *Springer, Dordrecht*, pp. 15-34.

Bjørlykke, K. (1998). Clay mineral diagenesis in sedimentary basins, a key to the prediction of rock properties. Examples from the North Sea Basin. *Clay Minerals, 33*, pp. 15-34.

Bjørlykke, K., & Aagaard, P. (1992). Clay minerals in North Sea sandstones. W: Origin, diagenesis and petrophysics of clay minerals in sandstones. (D. Houseknecht, & E. Pittrnan, Eds.) *Society of Economic Paleontologists and Mineralogists*, 65-80.

Bjørlykke, K., Aagaard, P., Dypvik, H., Hastings, D. S., Harper, A. S., & Spencer, A. M. (1986). Diagenesis and reservoir properties of Jurassic sandstones from the Haltenbanken area, offshore mid-Norway. *Habitat of hydrocarbons on the Norwegian continental shelf*, 175-286.

Boggs, S. (2006). *Principles of sedimentation and Stratigraphy.* Upper Saddle River, New Jersey: Prentice Hall.

Bragg, W. H., & Bragg, W. L. (1913). The reflection of X-rays by crystals. *Proceedings of the Royal Society of London. Series A, Containing Papers of a Mathematical and Physical Character, 88*(605), pp. 428-438.

Brenner, S., & Picknett, T. (2001). Encyclopeadia of Genetics: X-ray crystallography. 2154. doi:https://doi.org/10.1006/rwgn.2001.1396

Broad, D. S., Jungslager, E. H., McLachlan, I. R., & Roux, J. (2006). Offshore mesozoic basins. *The Geology of South Africa. Geological Society of South Africa, Johannesburg/Council for Geoscience*, pp. 553-571.

Broad, D. S., Jungslager, E. H., McLachlan, I. R., Roux, J., & Van der Spuy, D. (2012). South Africa's offshore Mesozoic basins. *Regional Geology and Tectonics: Phanerozoic Passive Margins, Cratonic Basins and Global Tectonic Maps*, pp. 534-564.

Brown, L. (1995). Sequence Stratigraphy in Offshore South African Divergent Basins. *An Atlas on Exploration for Cretaceous Lowstand Traps by Soekor (Pty) Ltd, AAPG Studies in Geology 41*.

Brown, L., Benson, J., Brink, G., Doherty, S., Jollands, A., Jungslager, E., Koenan, J., Muntingh, A., Van Wyk, N. (1996). Sequence stratigraphy in offshore South African divergent basins. *An atlas on exploration for Cretaceous Lowland Traps*(184).

Burton, J. H., Krinsley, D. H., & Pye, K. (1987). Authigenesis of kaolinite and chlorite in Texas Gulf Coast sediments. *Clays and Clay Minerals, 35*(4), pp. 291-296.

Cohen, K., Finney, S., Gibbard, P., & Fan, J. (2013). The ICS international chronostratigraphic chart. *Episodes, 36*(3), pp. 199-204.

Crain, E. (2018). *Crain's Petrophysical Handbook*. Retrieved July 2018, from www.spec2000.net

Cudennec, Y., & Lecerf, A. (2006). The transformation of ferrihydrite into goethite or hematite. *Journal of Solid State Chemistry*(179), 716-722. Retrieved from https://etd.ohiolink.edu/rws_etd/document/get/bgsu1355966847/inline

Curtis, M. L., & Hyam, D. M. (1998). Late Palaeozoic to Mesozoic structural evolution of the Falkland Islands: a displaced segment of the Cape Fold Belt. *Journal of the Geological Society, 155*(1), pp. 115-129.

Darcy, H. P. (1856). Les Fontaines publiques de la ville de Dijon. Exposition et application des principes à suivre et des formules à employer dans les questions de distribution d'eau, etc. . *V. Dalamont.*

Database normalization. (2018). Retrieved from https://en.wikipedia.org/wiki/Database_normalization

De Ros, L. F., Anjos, S. M., & Morad, S. (1994). Authigenesis of amphibole and its relationship to the diagenetic evolution of Lower Cretaceous sandstones of the Potiguar rift basin, northeastern Brazil. *Sedimentary Geology, 88*(3-4), 253-266.

De Swardt, A., & McLachlan, I. (1982). The geological framework and hydrocarbon potential. (H. Glen, Ed.) *Petroleum exploration in the South African offshore*, 147-161.

De Wit, M. J., & Ransome, J. G. (1991). Inversion Tectonics along the Southern Margin of Gondwana: A brief overview. *Inversion tectonics of the Cape Fold Belt, Karoo and Cretaceous Basins of Southern Africa*, pp. 15-21.

Densities of sedimentary rocks. (2018). Retrieved October 2018, from https://gpg.geosci.xyz/content/physical_properties/tables/density_sedimentary_rocks.html

Diagenesis. (2018). Retrieved August 2018, from https://ocw.mit.edu/courses/earth-atmospheric-and-planetary-sciences/12-110-sedimentary-geology-spring-2007/lecture-notes/ch7.pdf.

Dingle, R., Siesser, W., & Newton, A. (1983). *Mesozoic and Tertiary Geology of Southern Africa.* Rotterdam: Balkema.

Doveton, J. H. (2001). All models are wrong, but some models are useful:'solving'the Simandoux equation. In *J. of the International Association for Mathematical Geology Conference, Cancun, Mexico*.

Egbele, E., Ezuka, I., & Onyekonwu, M. (2005). Net-to-gross ratios: Implications in integrated reservoir management studies. *In Nigeria Annual International Conference and Exhibition.* Society of Petroleum Engineers.

Ehrenberg, S. N., & Nadeau, P. H. (1989). Formation of diagenetic illite in sandstones of the Garn Formation, Haltenbanken area, mid-Norwegian continental shelf. *Clay Minerals, 24*(2), 233-253.

Ehrenberg, S., Aagaard, P., Wilson, M., Fraser, A., & D.M.L, D. (1993). Depth-dependent transformation of kaolinite to dickite in sandstones of the Norwegian Continental Shelf. Clay Miner. *Clay Minerals*(28), 325-352.

Ellis, D. V., & Singer, J. M. (2007). Well logging for earth scientists. *Dordrecht: Springer., 692*.

Emery, D., Myers, K. J., & Young, R. (1990). Ancient subaerial exposure and freshwater leaching in sandstones. *Geology, 18*(12), pp. 1178-1181.

Fadipe, O. A. (2012). Reservoir quality, structural architecture, fluid evolution and their controls on reservoir performance in block 9, FO gas field, Bredasdorp Basin, offshore South Africa. *Doctoral dissertation, University of the Western Cape*.

Fens, T. W. (2000). Petrophysical properties from small rock samples using image analysis techniques.

França, A. B., Araújo, L. M., Maynard, J. B., & Potter, P. E. (2003). Secondary porosity formed by deep meteoric leaching: Botucatu eolianite, southern South America. *AAPG bulletin, 87*(7), pp. 1073-1082.

Giles, M., Stevenson, S., Martin, S., & Cannon, S. (1992). The reservoir properties and diagenesis of the Brent Group: a regional perspective. (A. Morton, R. Haszeldine, M. Giles, & S. Brown, Eds.) *Geological Society of London Special Paper*(61), 289-327.

Glover, P. (2000). *MSc Petroleum Geology.* University of Aberdeen, Department of Geology and Petroleum Geology, UK.

Glover, P. (2009). What is the cementation exponent? A new interpretation. *The Leading Edge, 28*(1), pp. 82-85.

Gresse, P. G., Theron, J. N., Fitch, F. J., Miller, J. A., De Wit, M. J., & Ransome, I. G. (1992). Tectonic inversion and radiometric resetting of the basement in the Cape Fold Belt. *Inversion tectonics of the Cape Fold Belt, Karoo and Cretaceous Basin*.

Hadding, A. (1932). The Pre-quaternary Sedimentary Rocks of Sweden: Glauconite and Glauconitic Rocks. *Gleerup*.

Hanor, J. S. (1994). Physical and chemical controls on the composition of waters in sedimentary basins. *Marine and petroleum geology, 11*(1), pp. 31-45.

Hematite. (2018, October). Retrieved August 2018, from Gems Element Finest Jewellery: https://www.gemselement.com/history-of-hematite.

Hendricks, S. B., & Ross, C. S. (1941). Chemical composition and genesis of glauconite and celadonite. *American Mineralogist: Journal of Earth and Planetary Materials, 26*(12), 683-703.

Hower, J., Eslinger, E. V., Hower, M. E., & Perry, E. A. (1976). Mechanism of burial metamorphism of argillaceous sediment: 1. Mineralogical and chemical evidence. *Geological Society of America Bulletin, 87*(5), 725-737.

Howie, R., Zussman, J., & Deer, W. (1992). An introduction to rock-forming minerals. *Longman*.

Humphreys, B., Smith, S. A., & Strong, G. E. (1989). Authigenic chlorite in late Triassic sandstones from the Central Graben, North Sea. *Clay Minerals, 24*(2), pp. 427-444.

Hutcheon, I., Shevalier, M., & Abercrombie, H. J. (1993). pH buffering by metastable mineral-fluid equilibria and evolution of carbon dioxide fugacity during burial diagenesis. *Geochimica et Cosmochimica Acta, 57*(5), 1017-1027.

Ishimwe, D. (2014). Reservoir rock properties. Retrieved from https://connect.spe.org/blogs/donatien-ishimwe/2014/09/29/reservoir-rock-properties

Jackson, J. (1997). Glossary of Geology. *American Geological Institute*.

Jeans, C. (1989). Clay diagenesis in sandstones and in shales: An introduction. *Clay Minerals, 24*(2), 127-136.

Kamel, M., & Mohamed, M. (2006). Effective porosity determination in clean/shaly formations from acoustic logs with applications. *Journal of Petroleum Science and Engineering, 51*(3-4), pp. 267-274.

Kerr, P. F. (1952). Formation and occurrence of clay minerals. *Clays and clay minerals, 1*(1), pp. 19-32.

Kleenberg, R. (2018). *Preparation of powder specimen for quantitative XRD*. Retrieved August 2018, from https://www.google.co.za/search?q=Preparation+of+powder+specimen+for+quantitative+XRD+Reinhard+Kleeberg+TU+Bergakademie+Freiberg&rlz=1C1NDCM_enZA798ZA798&oq=Prep

Klinkenberg, L. J. (1941). The permeability of Porous media to liquids and gases. *American Petroleum Institute*, 200-213.

Kruger, C. (2007). The challenges of deviated wells. In SPE/IADC Middle East Drilling and Technology Conference. *Society of Petroleum Engineers*.

Land, L. S., & Macpherson, G. L. (1992). Origin of saline formation waters, cenozoic section, Gulf of Mexico Sedimentary Basin. *AAPG Bulletin, 76*(9), pp. 1344-1366.

Lewis, D. W., & McConchie, D. (1994). Processes in Sedimentation. *Practical Sedimentology*, pp. 57-88.

Lima, R. D., & De Ros, L. F. (2002). The role of depositional setting and diagenesis on the reservoir quality of Devonian sandstones from the Solimoes Basin, Brazilian Amazonia. *Marine and Petroleum Geology, 19*(9), pp. 1047-1071.

Luca, C., & Jean-Claude, S. (2001). Integrated réservoir Studies. 120.

Margolis, S., & Krinsley, D. (1971). Submicroscopic frosting on eolian and subaqueous quartz sand grains. *Geological Society of America Bulletin, 82*(12), pp. 3395-3406.

Margolis, S., & Krinsley, D. (1974). Processes of formation and environmental occurrence of microfeatures on detrital quartz grains. *American Journal of Science, 274*(5), pp. 449-464.

Martin, A. K., Goodlad, S. W., Hartnady, C. J., & Plessis, A. D. (1982). Cretaceous palaeopositions of the Falkland Plateau relative to southern Africa using Mesozoic seafloor spreading anomalies. *Geophysical Journal International, 71*(3), pp. 567-579.

McHardy, W., Wilson, M., & Tait, M. (1982). Electron microscope and X-ray diffraction studies of filamentous illitic clay from sandstones of the Magnus Field. *Clay Minerals, 17*(1), pp. 23-41.

McMillan, I., Brink, G. I., Broad, D. S., & Maier, J. (1997). Late Mesozoic sedimentary basins off the south coast of South Africa. *Sedimentary Basins of the World. Elsevier, 3*, pp. 319-376.

McNeill, J. D. (1980). Electrical conductivity of soils and rocks. *Geonics Limited*.

Milliken, K. L. (2003). Late diagenesis and mass transfer in sandstone shale sequences. . *Treatise on geochemistry, 7*(407).

Millot, G. (1942). Relations entre la constitution et la genese des roches sediment aires argileuses. *2*.

Moore, C. H., & Wade, W. J. (2013). Porosity and diagenesis in a sequence stratigraphic framework . *Carbonate reservoirs, 67*.

Morad, S., Ketzer, J., & DeRos, L. (2000). Spatial and temporal distribution of diagenetic alterations in siliclastic rocks; implications for mass transfer in sedimentary basins. *Sedimentology, 47*, 95-120.

Moses, A. (2000). Risks and prospects of South Africa's South Outeniqua Basin. Retrieved from https://www.oilandgasonline.com/doc/risks-and-prospects-of-south-africas-south-ou-0001

Nadeau, P. (1998). An experimental study of the effects of diagenc clay minerals on reservoir sands . *Exxon Production Research Company*.

Nadeau, P. (2000). The Sleipner Effect: a subtle relationship between the distribution of diagenetic clay, reservoir porosity, permeability, and water saturation. *Clay Minerals, 35*(1).

Nelson, S. (2013). *Geology 212: Occurrence, Mineralogy, Textures, and Structures of Sedimentary Rocks.* Retrieved from http://www.tulane.edu/~sanelson/eens212/sedrxintro.htm

Nezhad, H., & Tabatabaei, H. (2017). Simulation of Petrophysical Parameters of Asmari Reservoir Using SGS Method in Mansuri Oil Field, Southwest of Iran. *Open Journal of Geology, 7*(8), p. 1188.

Nicolaysen, L. O. (1985). On the physical basis for the extended Wilson cycle, in which most continents coalesce and then disperse again. *Trans. Geol. Soc. S. Africa, 88*, pp. 562-580.

Norton, I., & Sclater, J. (1979). A model for the evolution of the Indian Ocean and the breakup of Gondwanaland. *Journal of Geophysical Research: Solid Earth 84, no. B12*,pp. 6803-2830.

Ohen, H. A., & Civan, F. (1993). Simulation of formation damage in petroleum reservoirs. *SPE Advanced Technology Series, 1*(1), pp. 27-35.

O'Kane, A., Onasch, C. M., & Farver, J. R. (2007). The role of fluids in low temperature, fault-related deformation of quartz arenite. *Journal of Structural Geology, 29*(5), 819-836.

Pallatt, N., Wilson, J., & McHardy, B. (1984). The relationship between permeability and the morphology of diagenetic illite in reservoir rocks. *Journal of Petroleum Technology, 36*(12), pp. 2-225.

PASA. (2018). Barremian Prospects of the Northern Pletmos Basin. *Petroleum Agency of South Africa*. Retrieved November 2018, from http://info.matchdeck.com/hubfs/PASA_-_Northern_Pletmos_Basin.pdf

Pettijohn, F. (1975). Sedimentary Rocks. *New York: Harper and Row*.

Pevear, D. R. (1999). Illite and hydrocarbon exploration. *Proceedings of the National Academy of Sciences, 96*(7), 3440-3446.

Pickett, G. R. (1973). Pattern recognition as a means of formation evaluation. *The Log Analyst, 14*(4). Pirson, S. (1958). Oil Reservoir Engineering. *Mcgraw Hillbook company, 2*, 735.

Poupon, A., & Leveaux, J. (1971). Evaluation of water saturation in shaly formations. *Society of Petrophysicists and Well-Log Analysts*.

Poupon, A., Loy, M., & Tixier, M. (1954). A contribution to electrical log interpretation in shaly sands. *Journal of petroleum Technology, 6*(6), pp. 27-34.

Ranger U. K. Limited. (2000). Ranger U. K. Limited: Leads and Prospects in South Outeniqua Basin, offshore South Africa. Abidjan, Cote d'Ivoire.

Rider, M., & Kennedy, M. (2002). The geological interpretation of well logs. *Sutherland. Scotland, Rider-French Consulting Ltd.*

Roberts, D., & Bally, A. (2012). Regional geology and tectonics: Phanerozoic passive margins, cratonic basins and global tectonic maps. *Elsevier., 1*.

Roux, J., & Soeker, E. (1997, July 21). Potential outlined in southern Outeniqua Basin off Shore Africa. *Oil and Gas Journal, 95*(29).

Ruhovets, N., & Fertl, W. (1982). Digital shaly sand analysis based on Waxman-Smits model and log-derived clay typing. *The Log Analyst, 23*(3).

Samakinde, C., Opuwari, M., & van Bever Donker, J. M. (2016). The effects of clay diagenesis on petrophysical properties of the lower Cretaceous sandstone reservoirs, Orange Basin, South Africa. *South African Journal of Geology, 119*(1), pp. 187-202.

Schlumberger. (1972). Log Interpretation. *Principles Chapter 16, 1*.

Schlumberger Limited. (1974). Log interpretation. *Schlumberger, 1*.

Schmidt, V., & McDonald, D. (1979). The role of secondary porosity in the course of sandstone diagenesis. (P. Scholle, & P. Schluger, Eds.) *Aspect of Diagenesis, 26*, pp. 175-207.

Schön, J. H. (2015). Physical properties of rocks: Fundamentals and principles of petrophysics. *Elsevier, 65*.

Serra, O. E. (1983). *Fundamentals of well-log interpretation.*

Shedid, S. (2001). A Multi-Purpose Reservoir Characterization Model. In SPE Middle East Oil Show. *Society of Petroleum Engineers*.

Shedid, S. A., & Saad, M. A. (2017). Analysis and field applications of water saturation models in shaly reservoirs. *Journal of Petroleum and Gas Engineering, 8*(10), pp. 111-122.

Shedid, S. A., Tiab, D., & Osisanya, S. O. (1998). Improved reservoir description of shaly sands using conventional well log-derived data for flow units identification. *Permian Basin oil & gas recovery conference* , pp. 427- 440.

Shedid-Elgaghah, S. A., Tiab, D., & Osisanya, S. O. (2001). A new approach for obtaining J-function in clean and shaly reservoir using in situ measurements. *Journal of Canadian Petroleum Technology, 40*(7).

Simandoux, P. (1963). Mesures diélectriques en milieu poreux-Application à la mesure des saturation en eau= Etude du comportement des massifs argileux. *Revue de l'Institut Français du Pétrole, n Hors-Série*, pp. 193-215.

Soeder, D., & Randolph, P. (1987). Porosity, Permeability, and Pore Structure of the Tight Mesaverde Sandstone, Piceance Basin, Colorado. *SPE Form Eval 2 (2)*. Retrieved from http://dx.doi.org/10.2118/13134-PA

Stanca, R. M., Paton, D. A., Hodgson, D. M., McCarthy, D. J., & Mortimer, E. J. (2019). A revised position for the rotated Falkland Islands microplate. *Journal of the Geological Society*.

Stonecipher, S., & May, J. (1990). Facies controls on early diagenesis. (D. Meshri, & P. Ortoleva, Eds.) *AAPG Memoir, 49*, 25-44.

Surdam, R. C., & Crossey, L. J. (1987). Integrated diagenetic modeling: a process-oriented approach for clastic systems. *Annual Review of Earth and Planetary Sciences, 15*(1), pp. 141-170.

Szabó, N. P. (2011). Shale volume estimation based on the factor analysis of well-logging data. *Acta Geophysica, 59*(5), p. 935.

Thomas, W., Ringen, J., & Rash, S. O. (2003). Effect of glauconite on petrophysical properties as revealed by core analysis. *In Estudio presentado en el Symposium de la sociedad de analistas de cores*.

Thomson, K. (1998). When did the Falklands rotate. *Marine and Petroleum Geology, 15*(8), pp. 723-736.

Tiab, D., & Donaldson, E. (2015). *Petrophysics: theory and practice of measuring reservoir rock and fluid transport properties.* Gulf Professional Pubishing.

Tixier, M., Alger, R., & Doh, C. (1959). Sonic Logging. *J Pet Technol Trans., AIME, 216*(106).

Toro. (2016). 13_Reservoirs1. *Geology 493, powerpoint*. Retrieved November 2018, from https://www.scribd.com/document/367962013/13-Reservoirs1#

Tucker, M. (1991). *Sedimentary Petrology* (2nd ed.). Blackwell. Retrieved from http://www.virtual-geology.info/sedimentology/sst-diag-lect.html

van Berk, W., Schulz, H. M., & Fu, Y. (2013). Controls on CO2 fate and behavior in the Gullfaks oil field (Norway): How hydrogeochemical modeling can help decipher organic-inorganic interactions. *AAPG Bulletin, 97*.

Velde, B. (1995). Origin and Mineralogy of Clays. *Springer Verlag*.

Visser, D. (1998). The geotectonic evolution of South Africa and offshore areas (explanation of structure map, scale 1: 1000000).

Warren, B. (1969). X-ray Diffraction. Retrieved from https://en.wikipedia.org/wiki/X-ray_crystallography

Weaver, C. (1956). A Discussion on the origin of clay minerals in sedimentary rocks. *Clays and Clay Minerals, 5*(1), 159-173.

Wilson, M. D., & Pittman, E. D. (1977). Authigenic clays in sandstones; recognition and influence on reservoir properties and paleoenvironmental analysis. *Journal of Sedimentary Research, 47*(1), 3-31.

Worden, R. H., & Burley, S. D. (2003). Sandstone diagenesis: the evolution of sand to stone. *Sandstone Diagenesis: Recent and Ancient, 4*, 3-44.

Worden, R. H., & Morad, S. (2003). Clay mineral cements in sandstones. *(Special Publication 34 of the IAS) , 10*, pp. 1-41.

Worthington, P. F., & Cosentino, L. (2005). The role of cut-offs in integrated reservoir studies. *SPE Reservoir Evaluation & Engineering, 8*(4), 276- 290.

XRD Topic 5a. (2018). Retrieved October 2018, from http://web.pdx.edu/~pmoeck/phy381/Topic5a-XRD.pdf

Yoder, H. S., & Eugster, H. P. (1955). Synthetic and natural muscovites. *Geochimica et Cosmochimica Acta, 8*(5-6), 225-280.

Yuan, G., Cao, Y., Gluyas, J., & Jia, Z. (2017). Reactive transport modeling of coupled feldspar dissolution and secondary mineral precipitation and its implication for diagenetic interaction in sandstones. *Geochimica et Cosmochimica Acta, 207*, pp. 232-255.

Yuan, G., Cao, Y., Jia, Z., Gluyas, J., Yang, T., Wang, Y., & Xi, K. (2015). Selective dissolution of feldspars in the presence of carbonates: The way to generate secondary pores in buried sandstones by organic CO2. *Marine and Petroleum Geology, 60*, pp. 105-119.

Yuan, G., Cao, Y., Schulz, H. M., Hao, F., Gluyas, J., Liu, K., & Li, F. (2019). A review of feldspar alteration and its geological significance in sedimentary basins: From shallow aquifers to deep hydrocarbon reservoirs. *Earth-science reviews*.

Zhao, X., Jin, F., Zhou, L., Wang, Q., & Pu, X. (2018). Re-exploration Programs for Petroleum-rich Sags in Rift Basins.

APPENDICES

Appendix A: Pickett plots

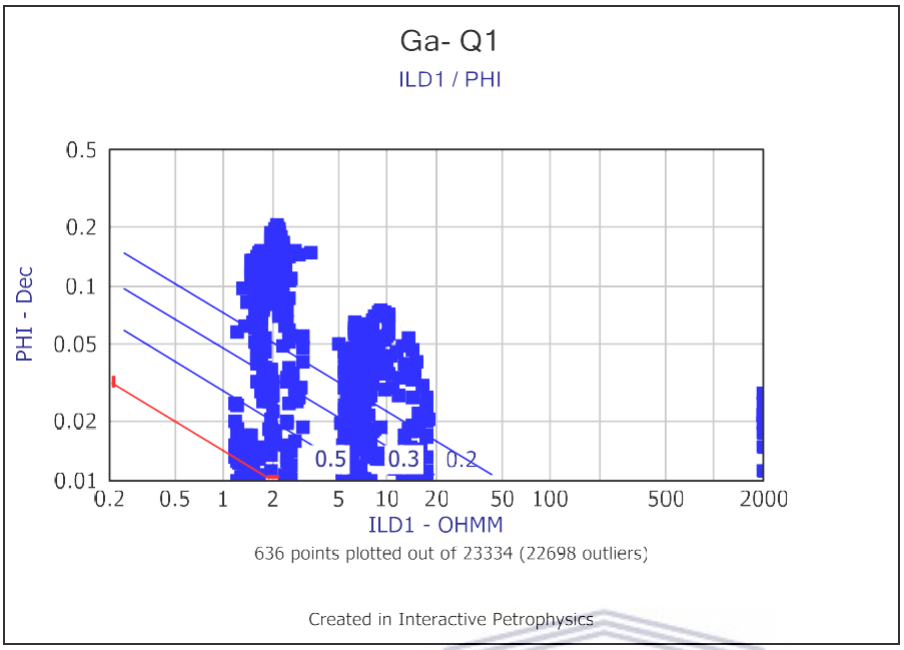

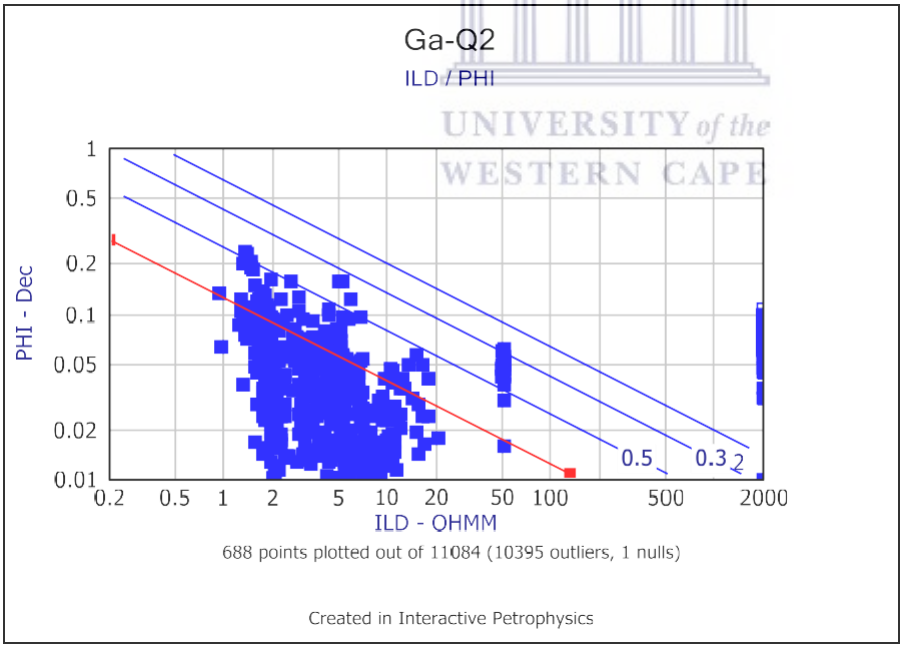

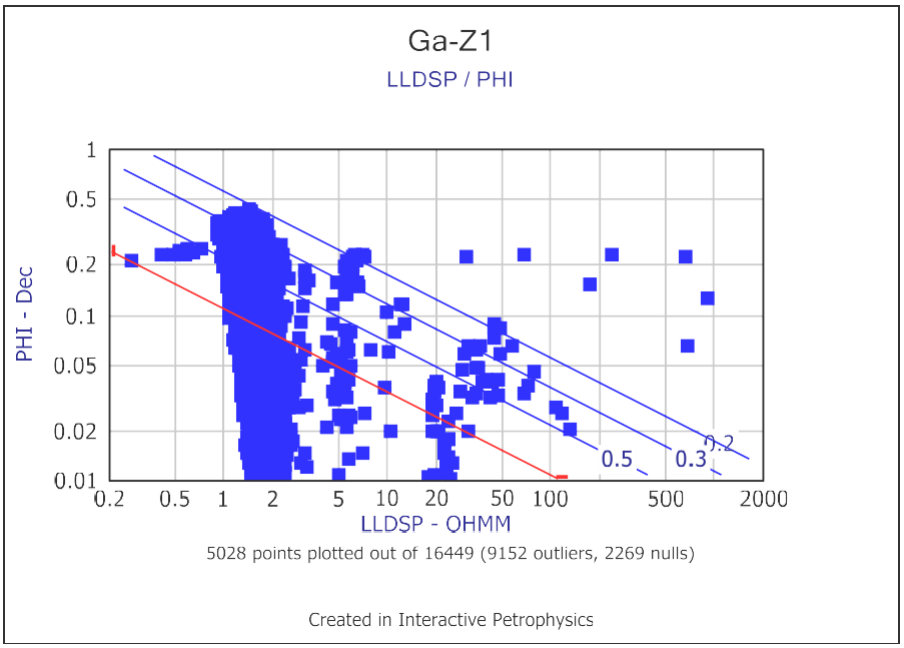

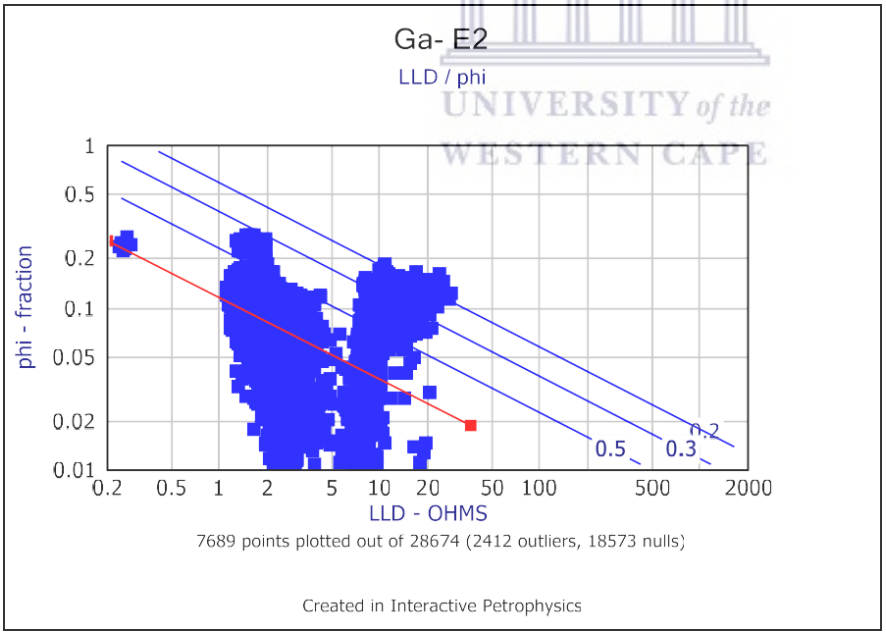

Appendix B: Sw cut offs

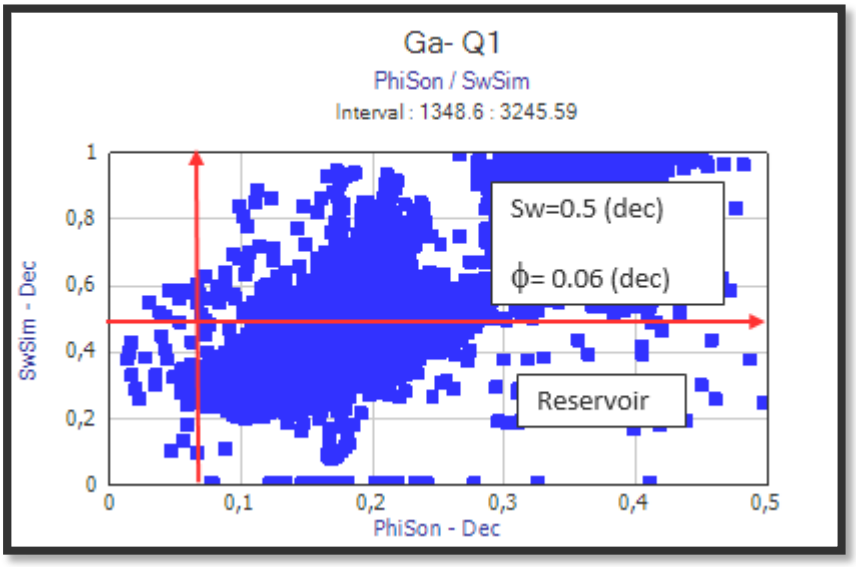

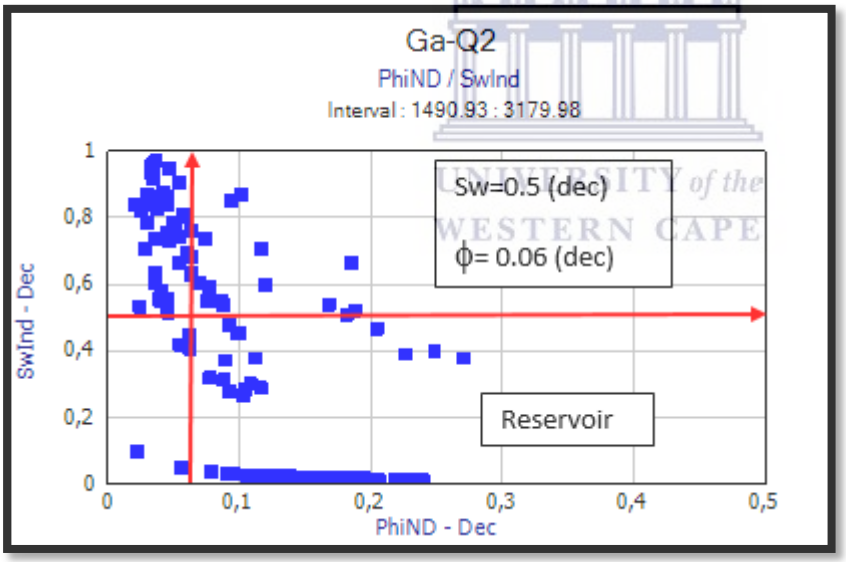

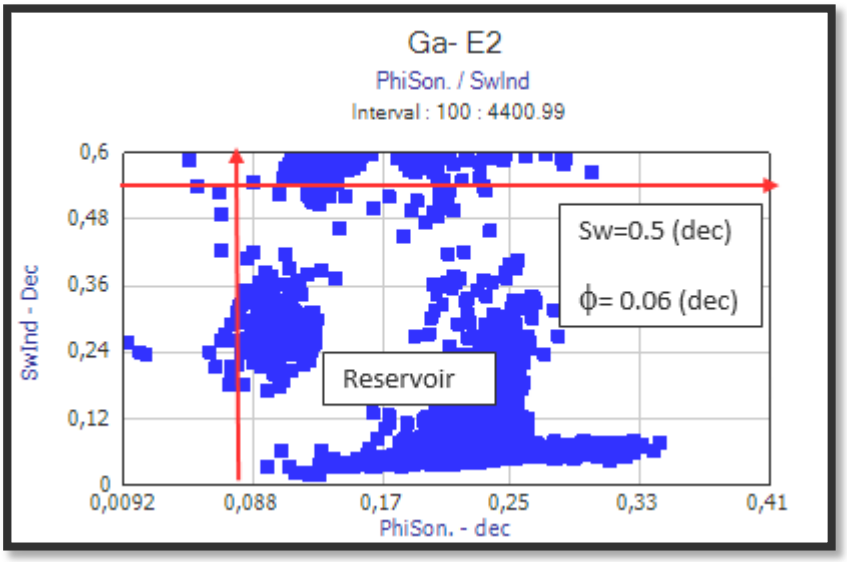

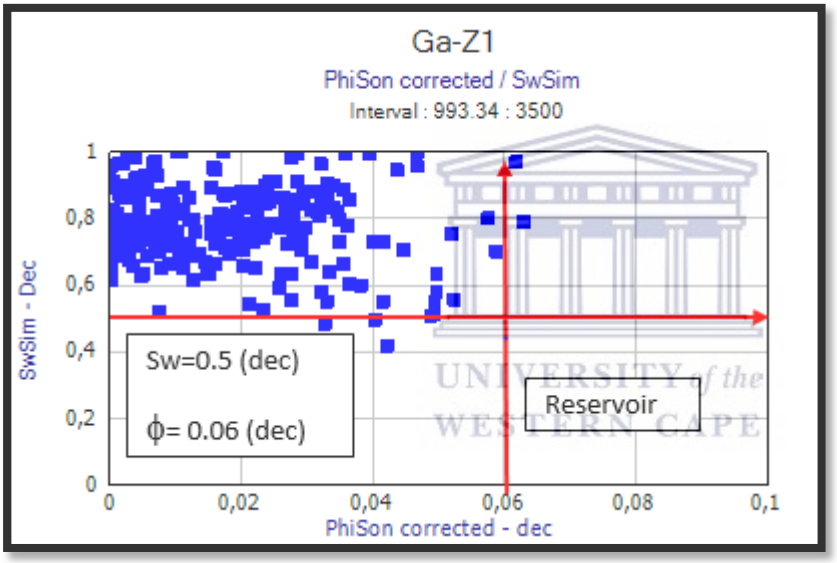

Appendix C: Clay cut offs

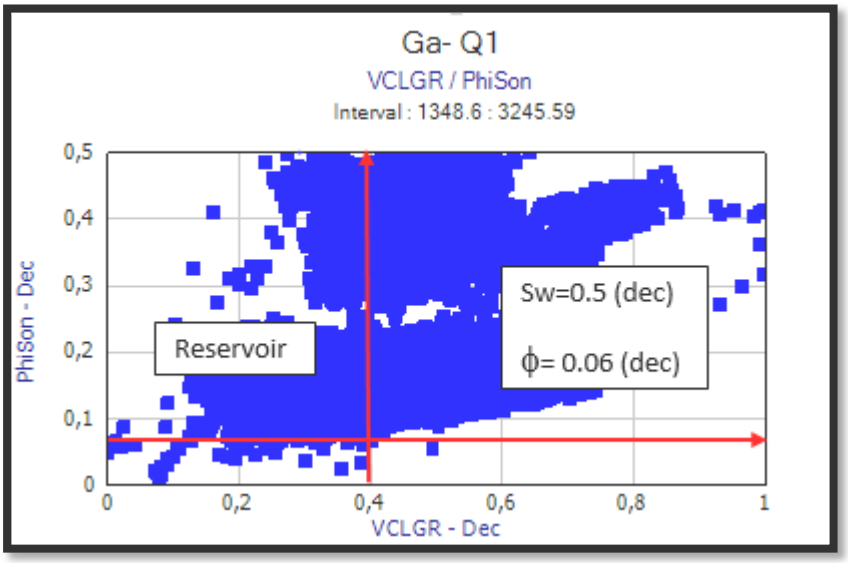

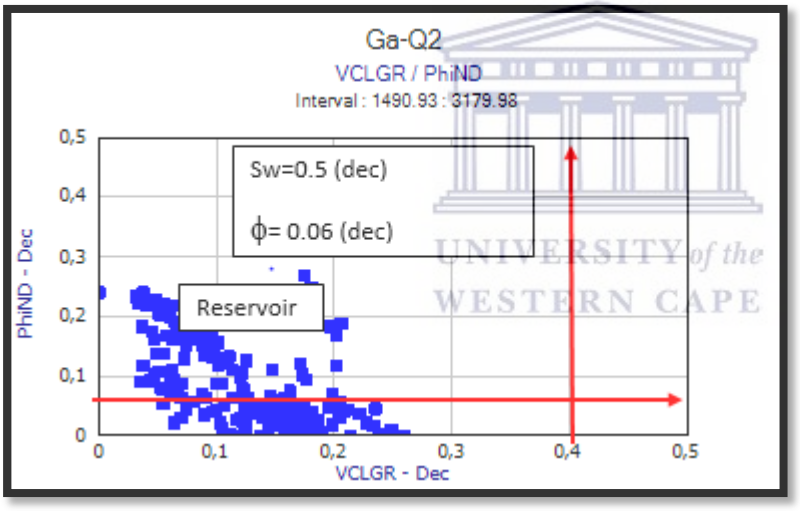

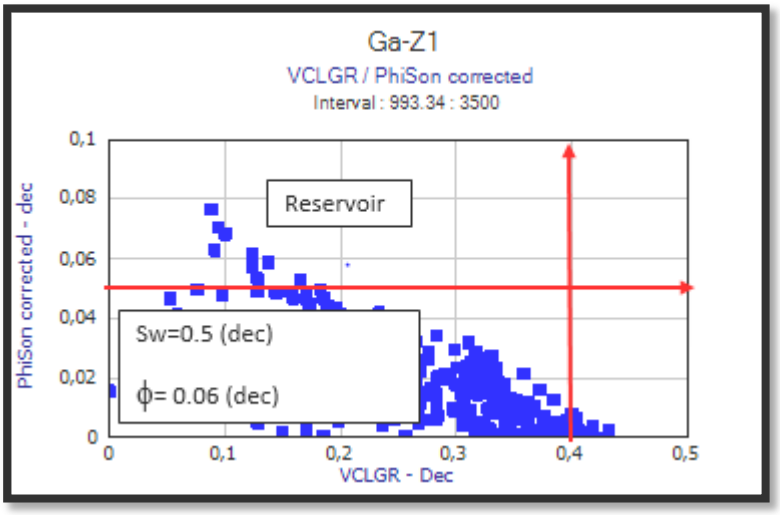

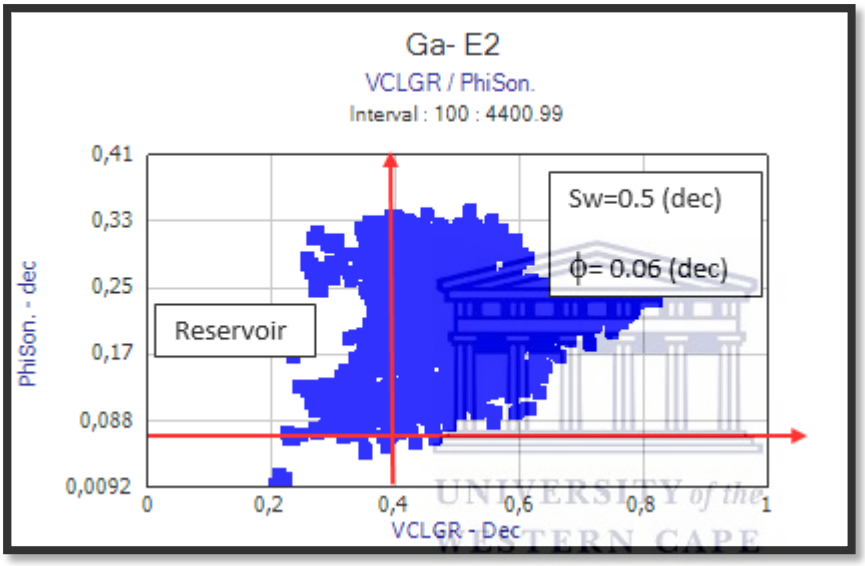

Appendix D: Net pay

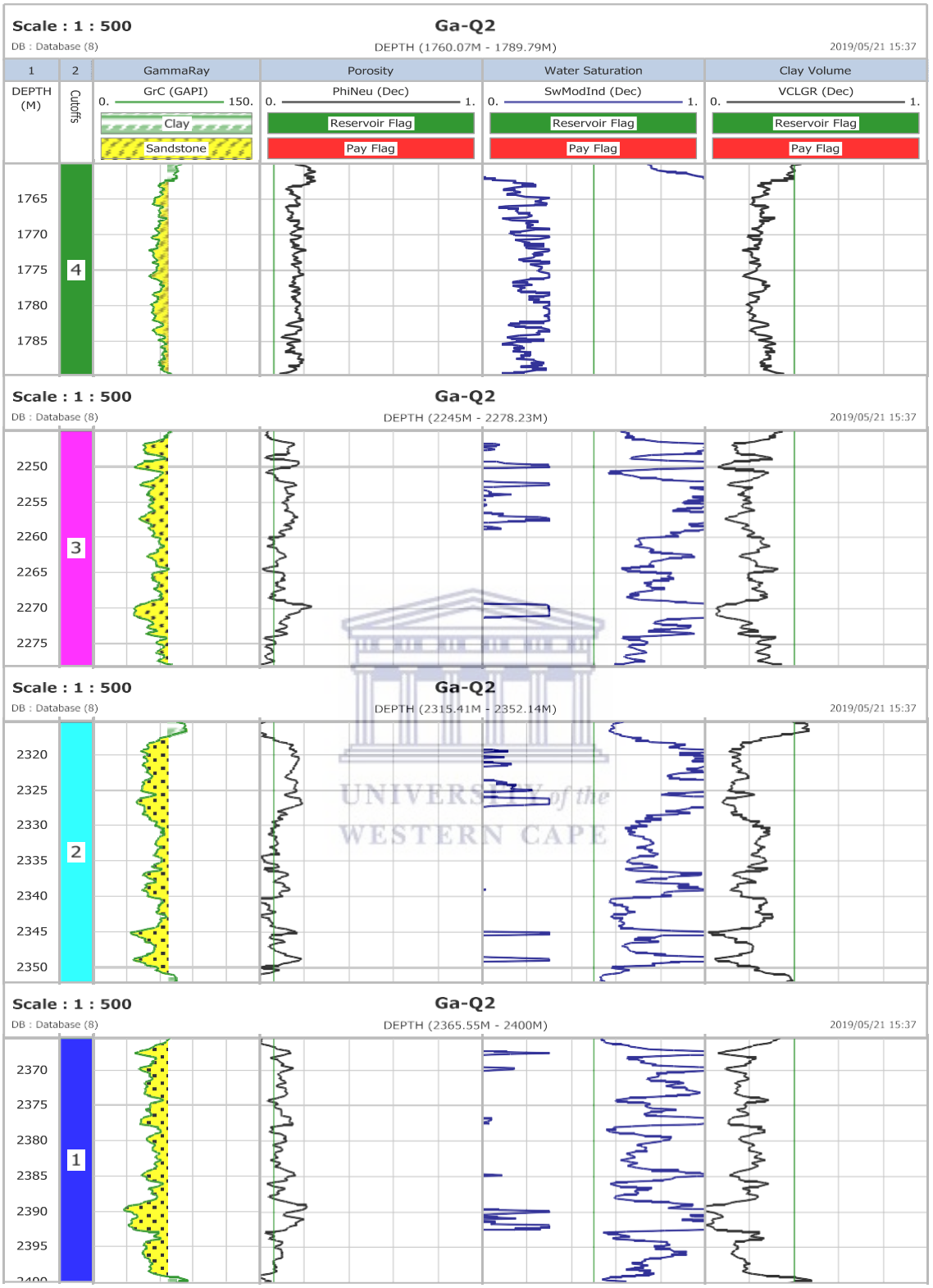

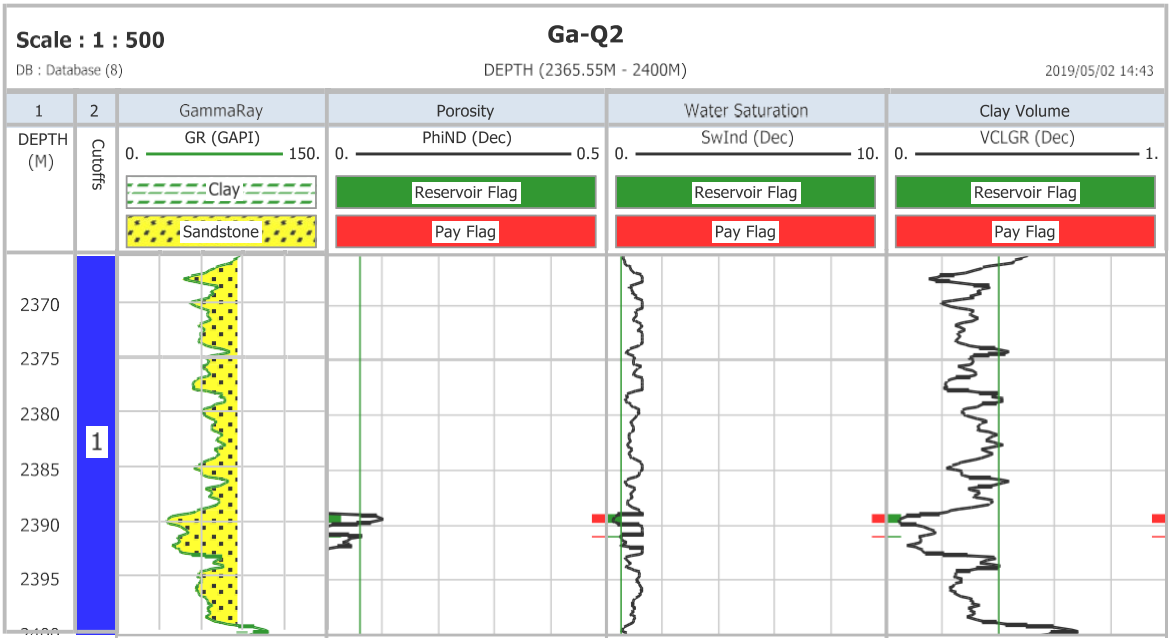

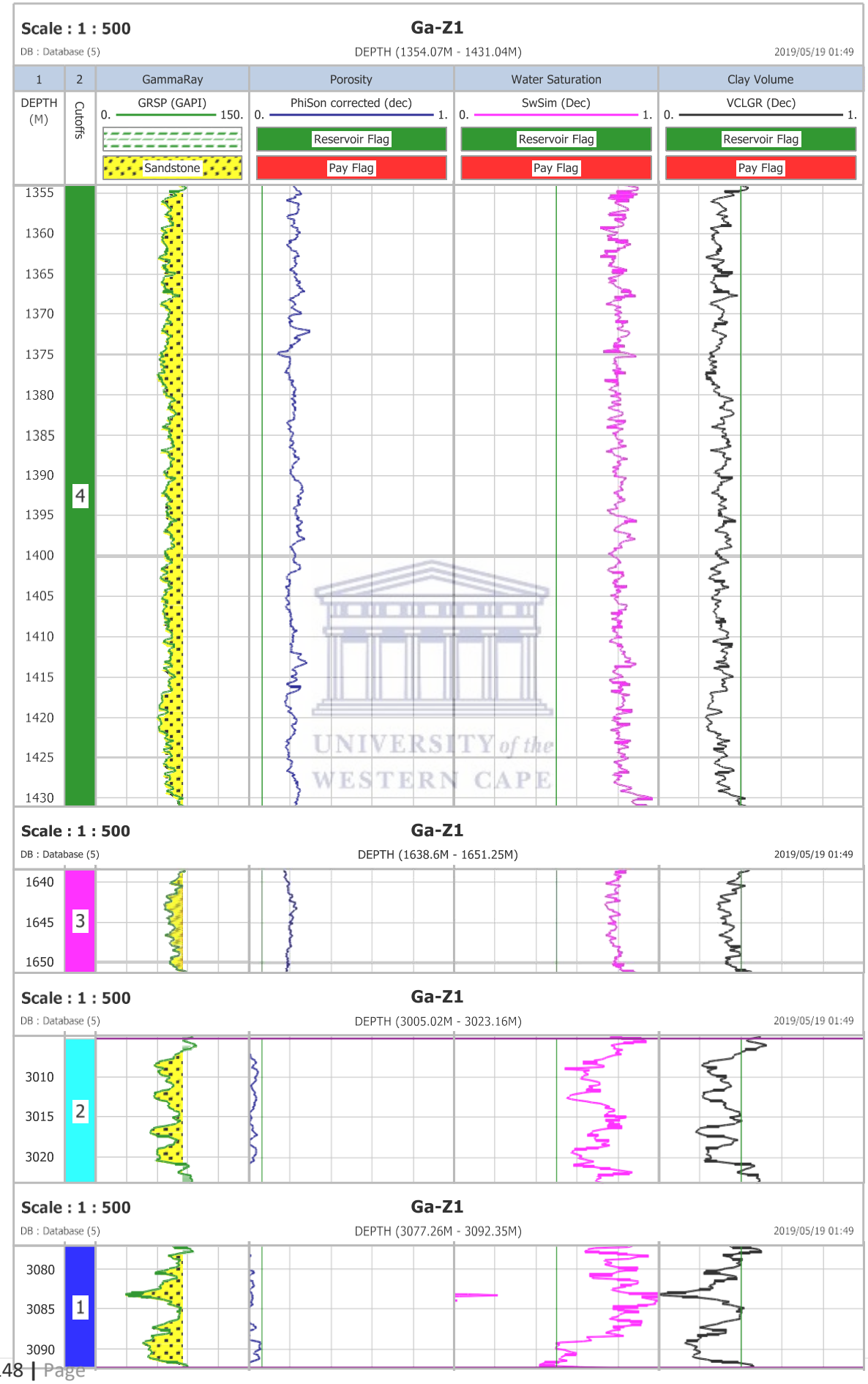

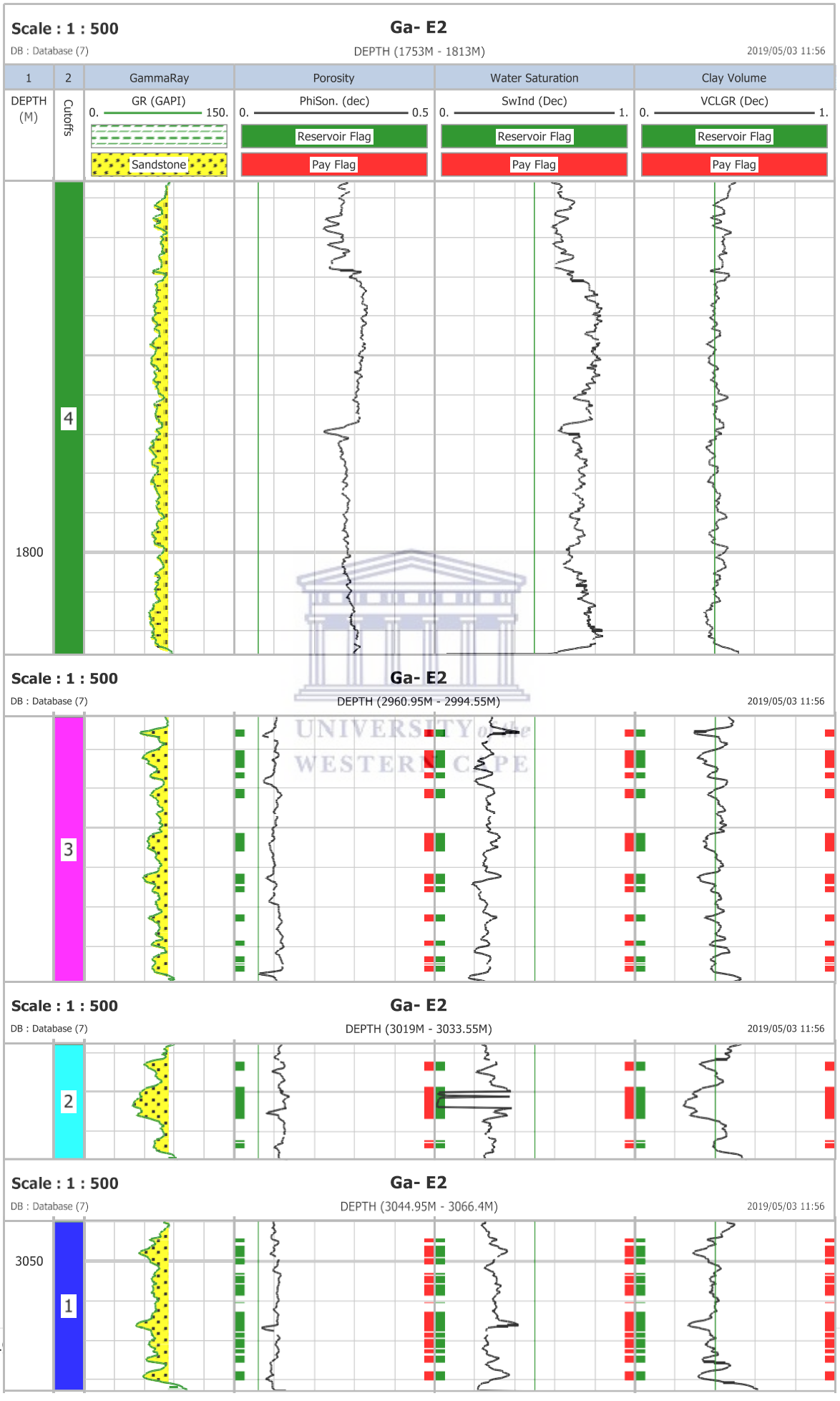

Appendix E: Core sample and thin section

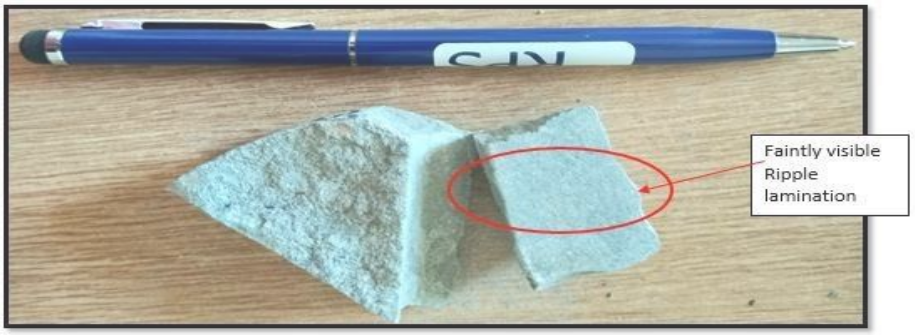

Appendix E1: Core sample 1 of shaly sandstone representing facies B retrieved at 2218 m.

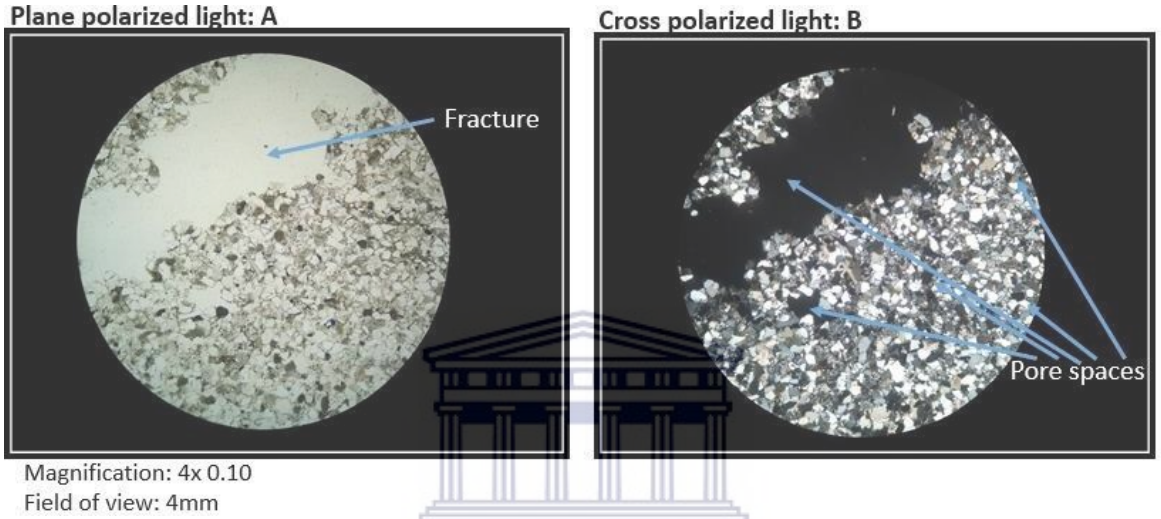

Appendix E2: Photomicrograph of sample 1 at 2180 m under magnification of 4x 0.10 where porosity is clearly delineated by the fracture (as seen in both A and B) and other interstitial spaces which are more clearly identified under cross polarized light in B.

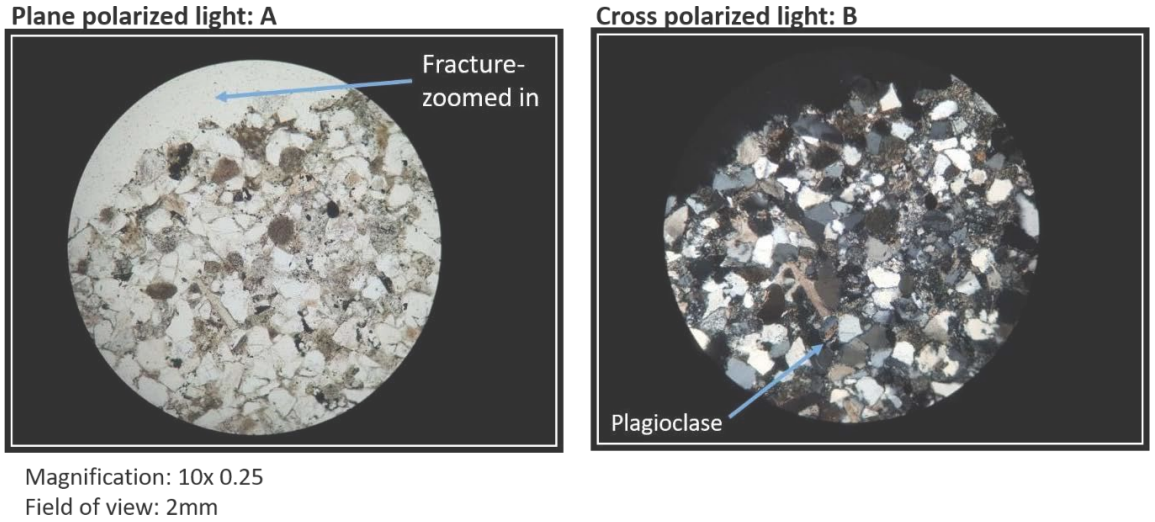

Appendix E3: Photomicrograph of sample 1 at 2180 m under magnification of 10x 0.25 showing sub-rounded to sub- angular grains in plane and cross polarized light with the fracture zoomed in along with distinctive feldspars.

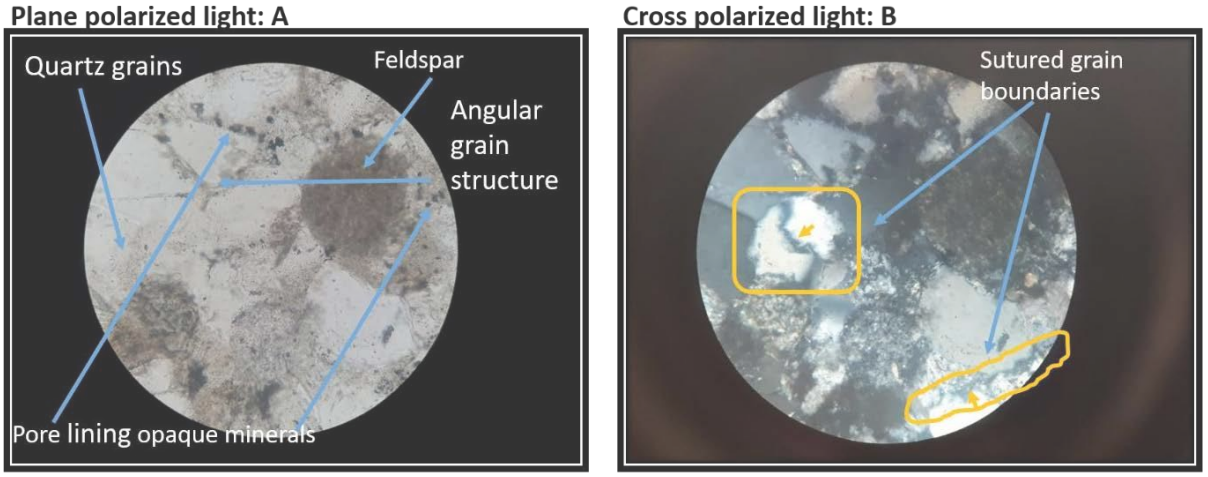

Magnification 40x 0.65
Field of view: 0.6 mm

Appendix E4: Photomicrograph of sample 1 at depth 2180 m under magnification of 40x 0.65 showing structural features i.e. angularity of grains in A, sutured grain boundaries in B and a close up of quartz and pore lining opaque minerals in A.

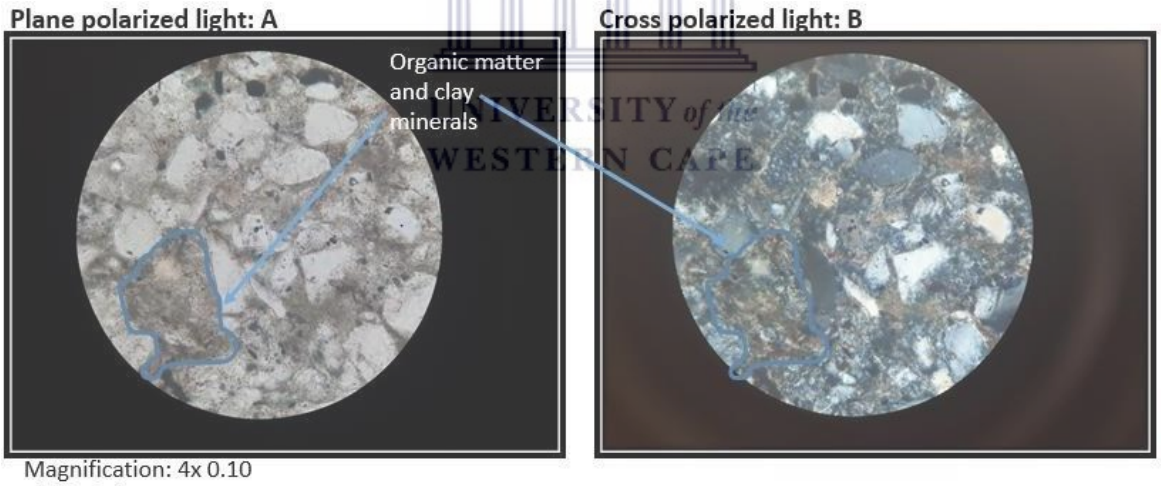

Magnification: 4x 0.10
Field of view: 2mm

Appendix E5: Photomicrograph of sample 3 at 2329 m under magnification of 4x 0.10 showing organic matter and clay minerals between the sub angular grains in both A and B.

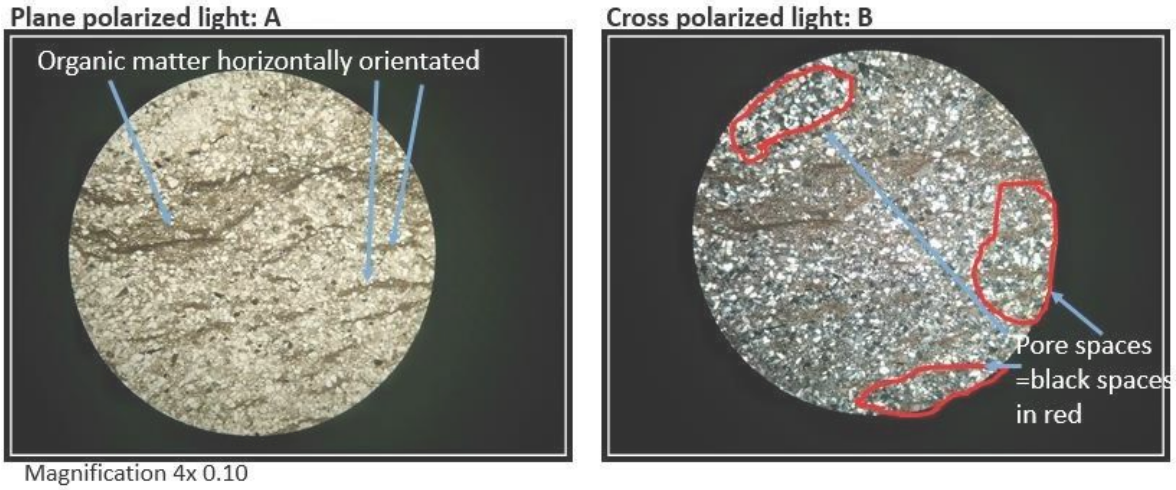

Appendix E6: Photomicrograph of sample 4 at 2344.07 m under magnification of 4x 0.10 showing horizontal orientation of organic matter in A and pore spaces in B

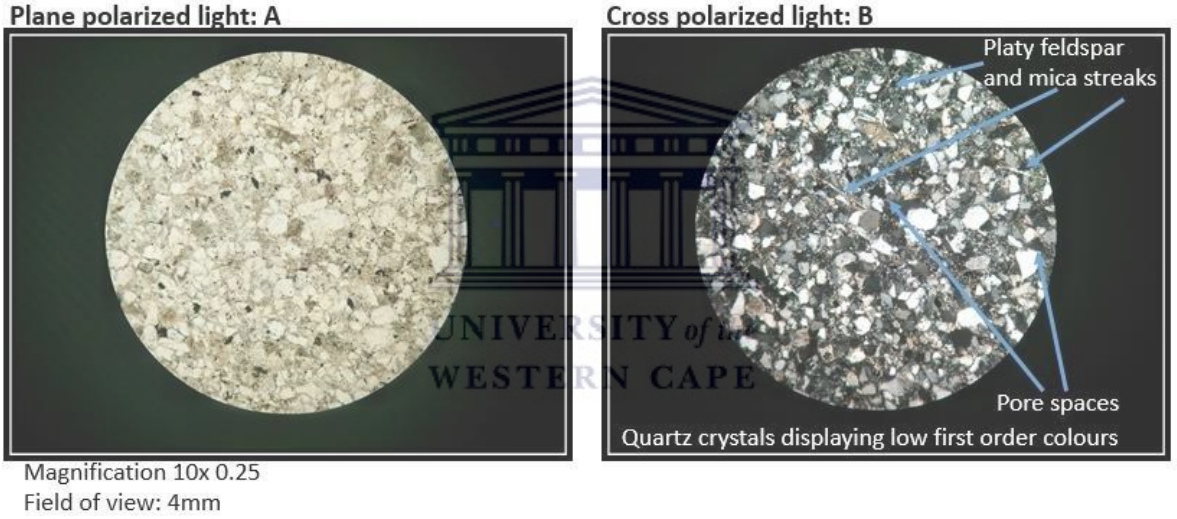

Appendix E7: Photomicrograph of sample 5 at 3135 m under magnification of 10x 0.25 showing misleading appearance of well sorting in both A and B. Platy feldspar and mica streaks are more clearly shown in B.

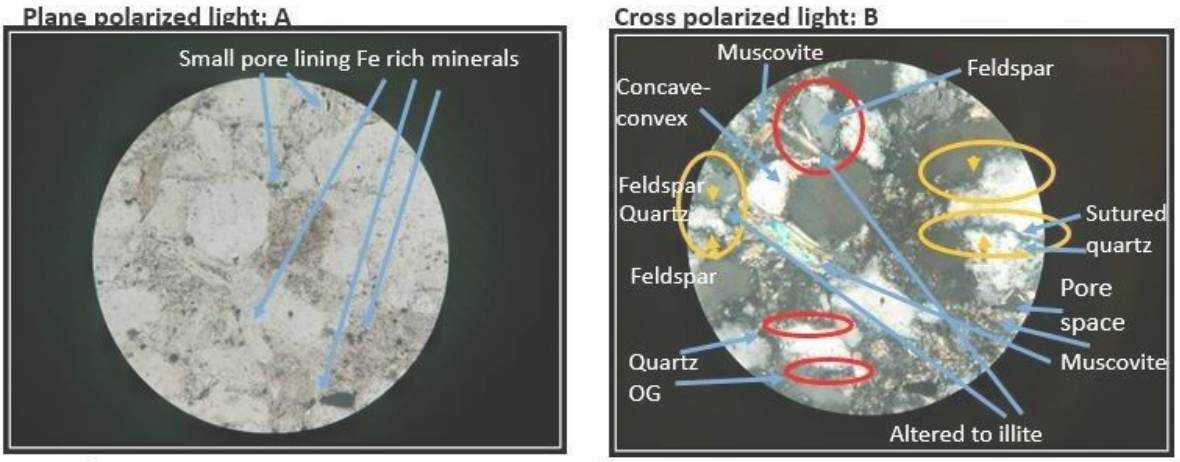

Appendix E8: Photomicrograph of sample 5 at 3135 m under magnification of 40x 0.65 showing pore lining iron rich minerals in A. Muscovite, quartz and feldspar are identified in B along with structural features such as concave- convex boundary and sutured grains. Quartz overgrowth and alteration of minerals to illite is also identified in B.

Plane polarized light: A

Cross polarized light: B

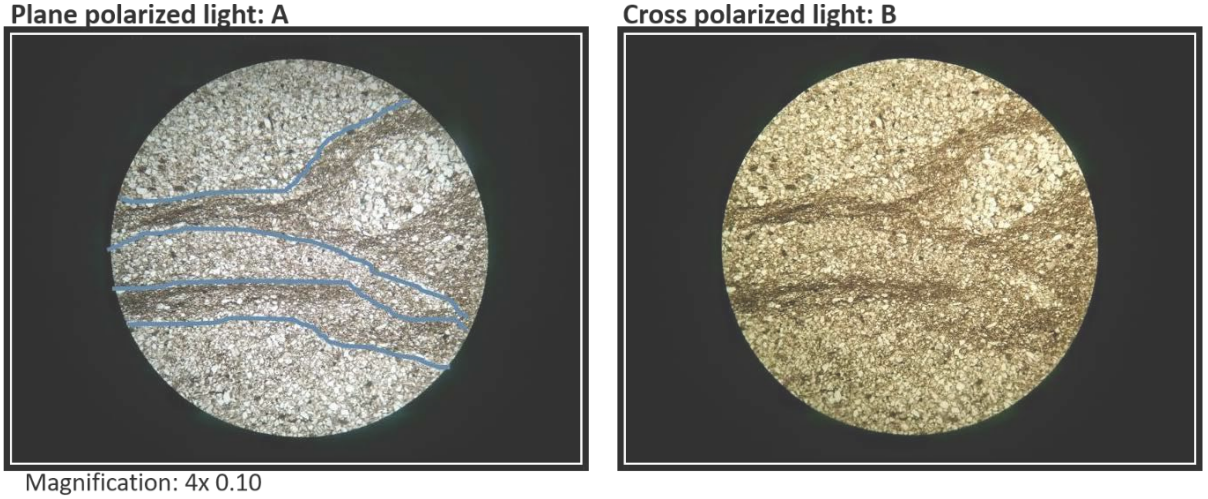

Magnification: 4x 0.10
Field of view: 4mm

Appendix E9: Photomicrograph of sample 8 at 3017 m under magnification of 4x 0.10 showing clay matrix and organic orientation outlined by the blue markers in A.

Plane polarized light: A

Cross polarized light: B

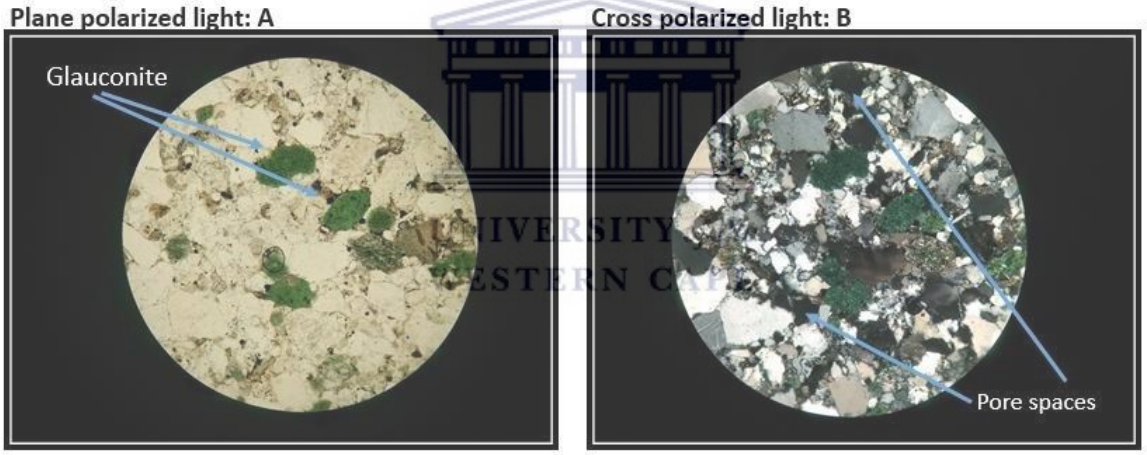

Magnification: 10x 0.25
Field of view: 2mm

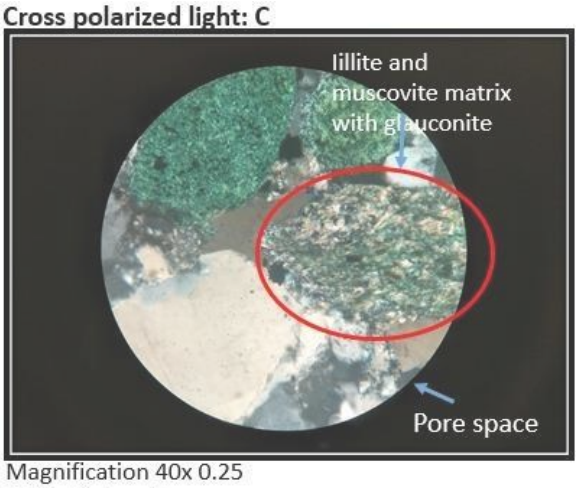

Appendix E10: Photomicrograph of sample 9 at 3021.25 m under magnification of 10x 0.25 showing green glauconite grains in A and pore spaces in B. Photomicrograph of C showing Illite and muscovite matrix with glauconite, as well as porosity.

Appendix E11: Core sample 10 of shaly sandstone representing facies C retrieved at 3088 m.

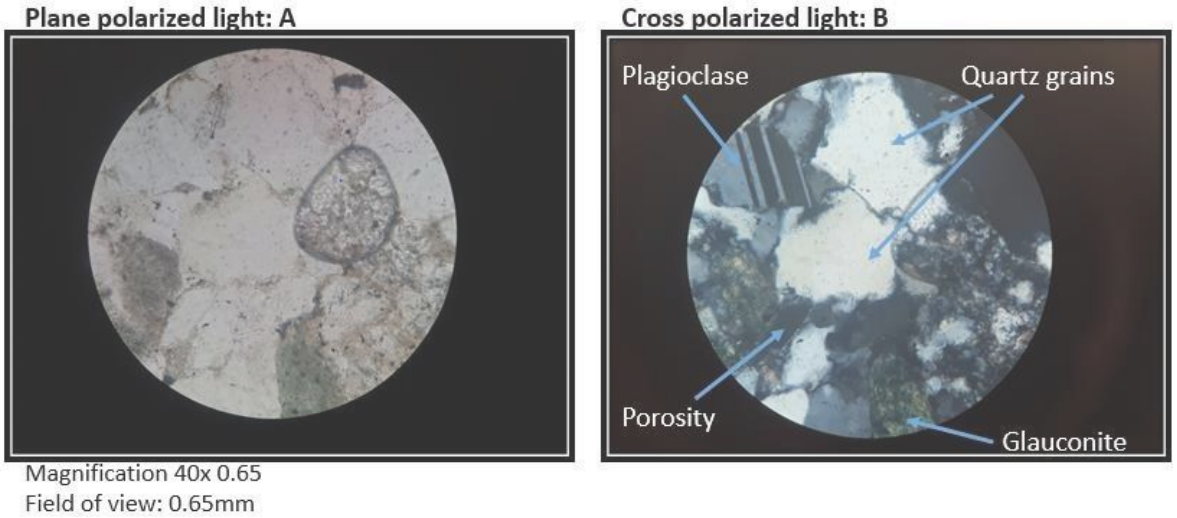

Appendix E12: Photomicrograph of sample 10 at 3088 m under magnification of 40x 0.65 showing plagioglase, glauconite and quartz grains along with porosity in B.

Appendix F: XRD

Sample 2

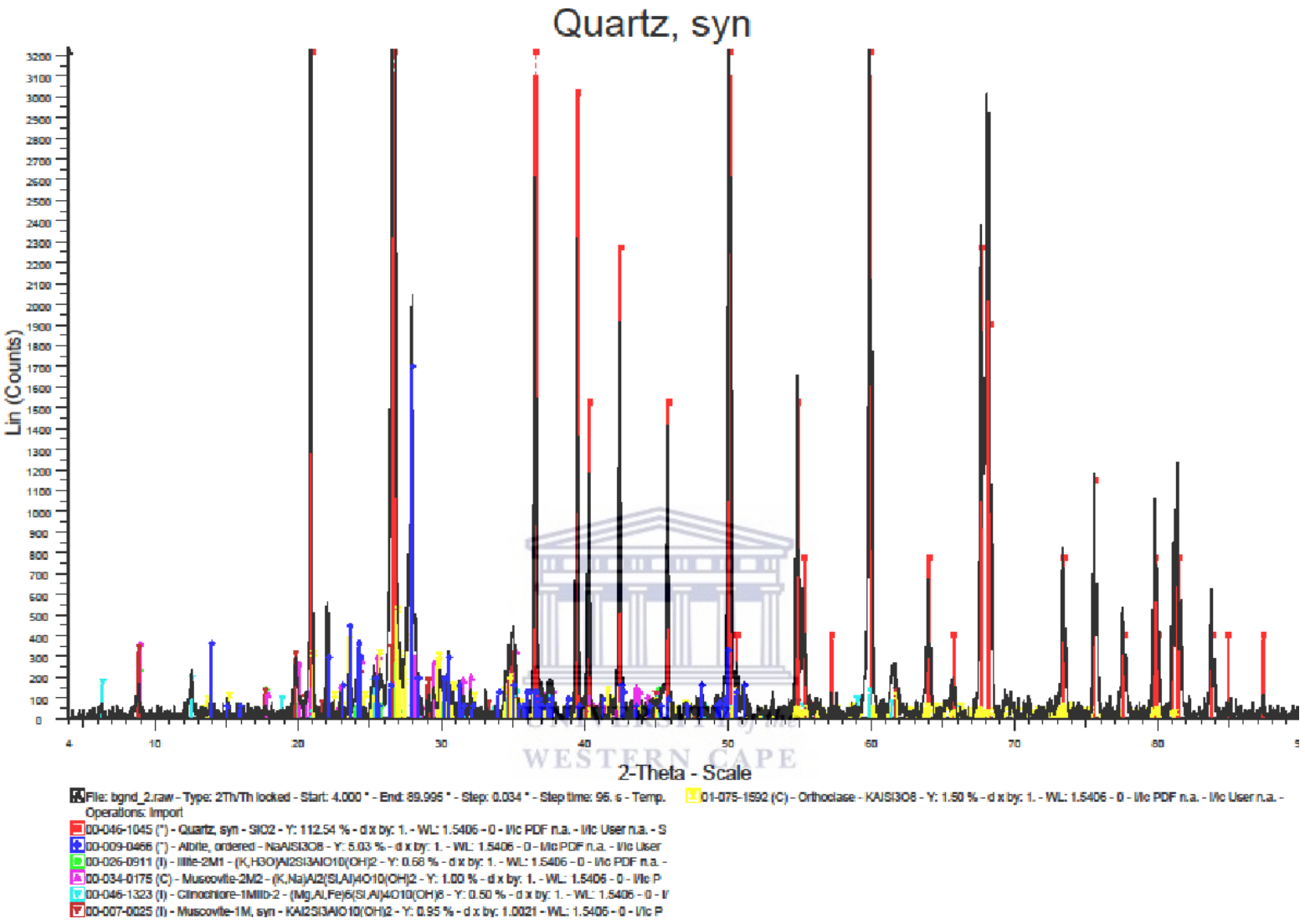

Figure 8.3: XRD qualitative plot for sample 2 at 2218 m.

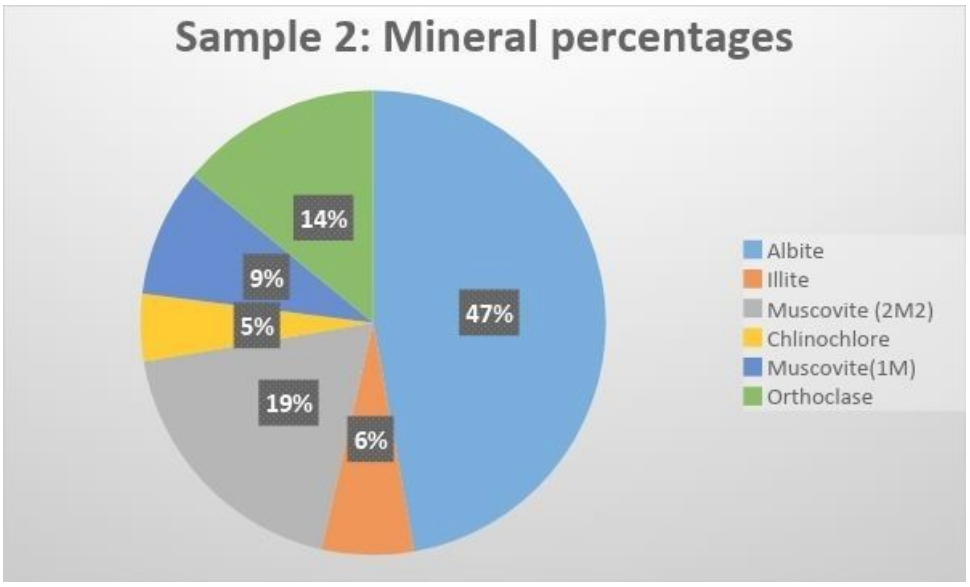

Figure 7.4: Pie chart of mineral aggregates of sample 2 at 2218 m.

Sample 3

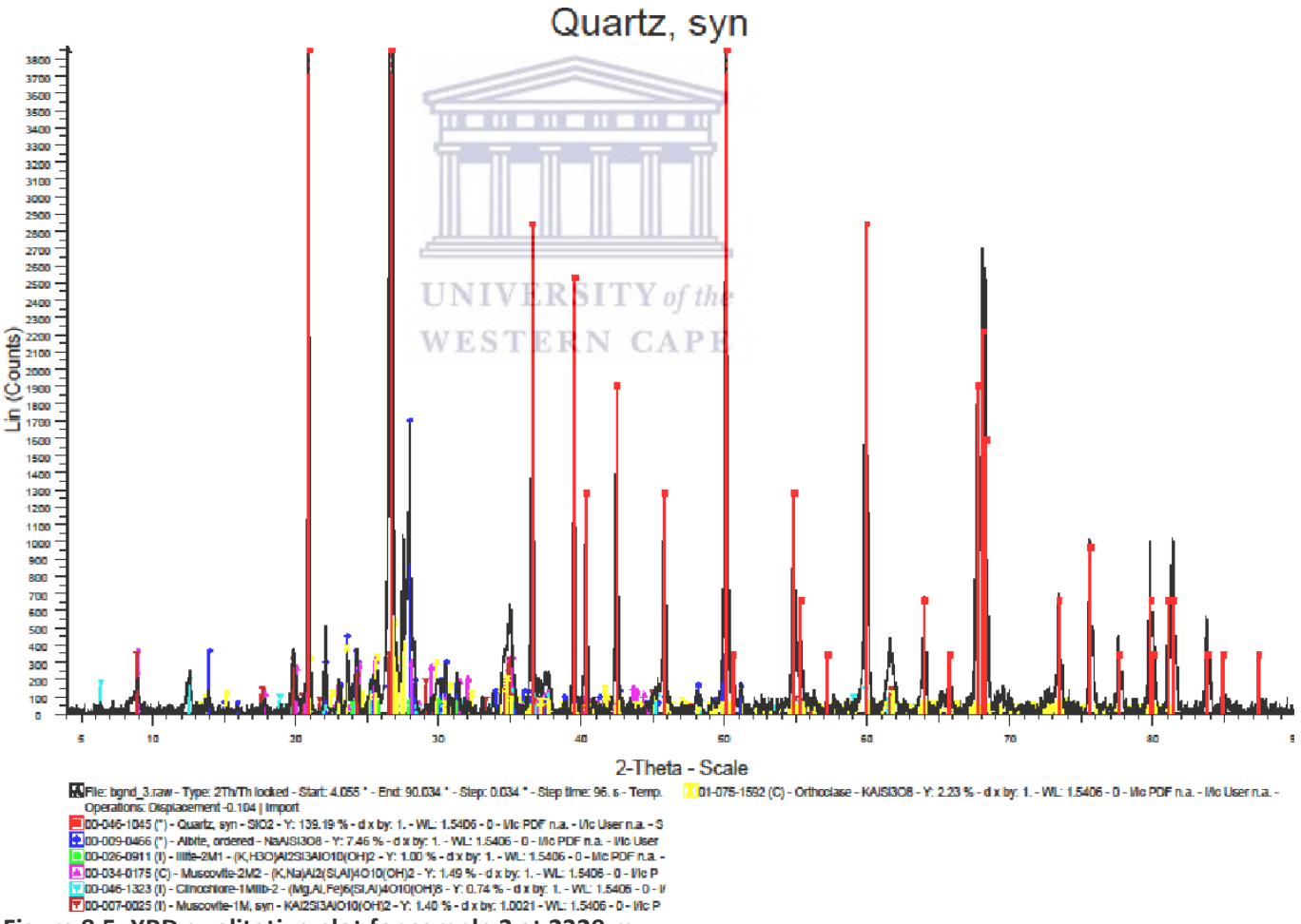

Figure 8.5: XRD qualitative plot for sample 3 at 2329 m.

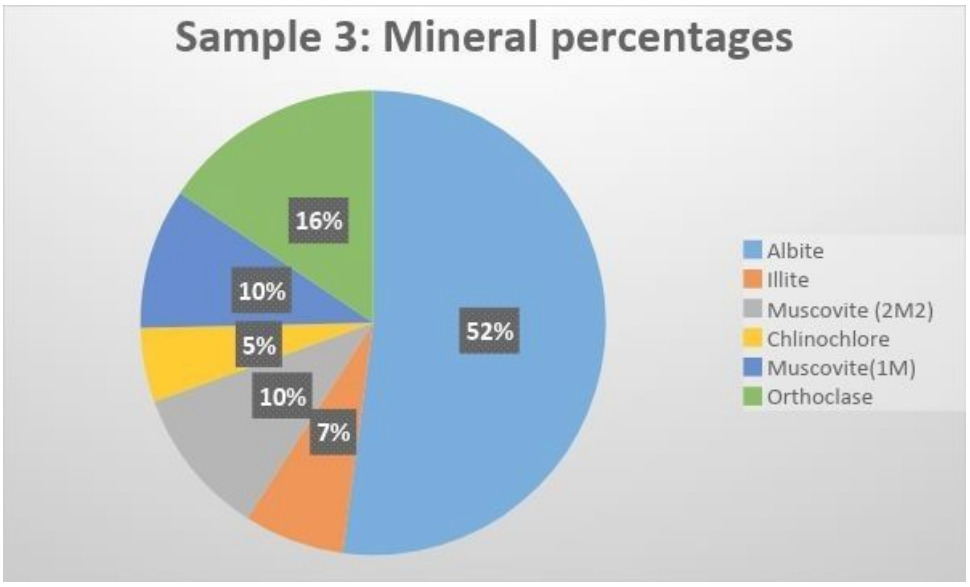

Figure 8.6: Pie chart of mineral aggregates of sample 3 at 2329 m.

Sample 4

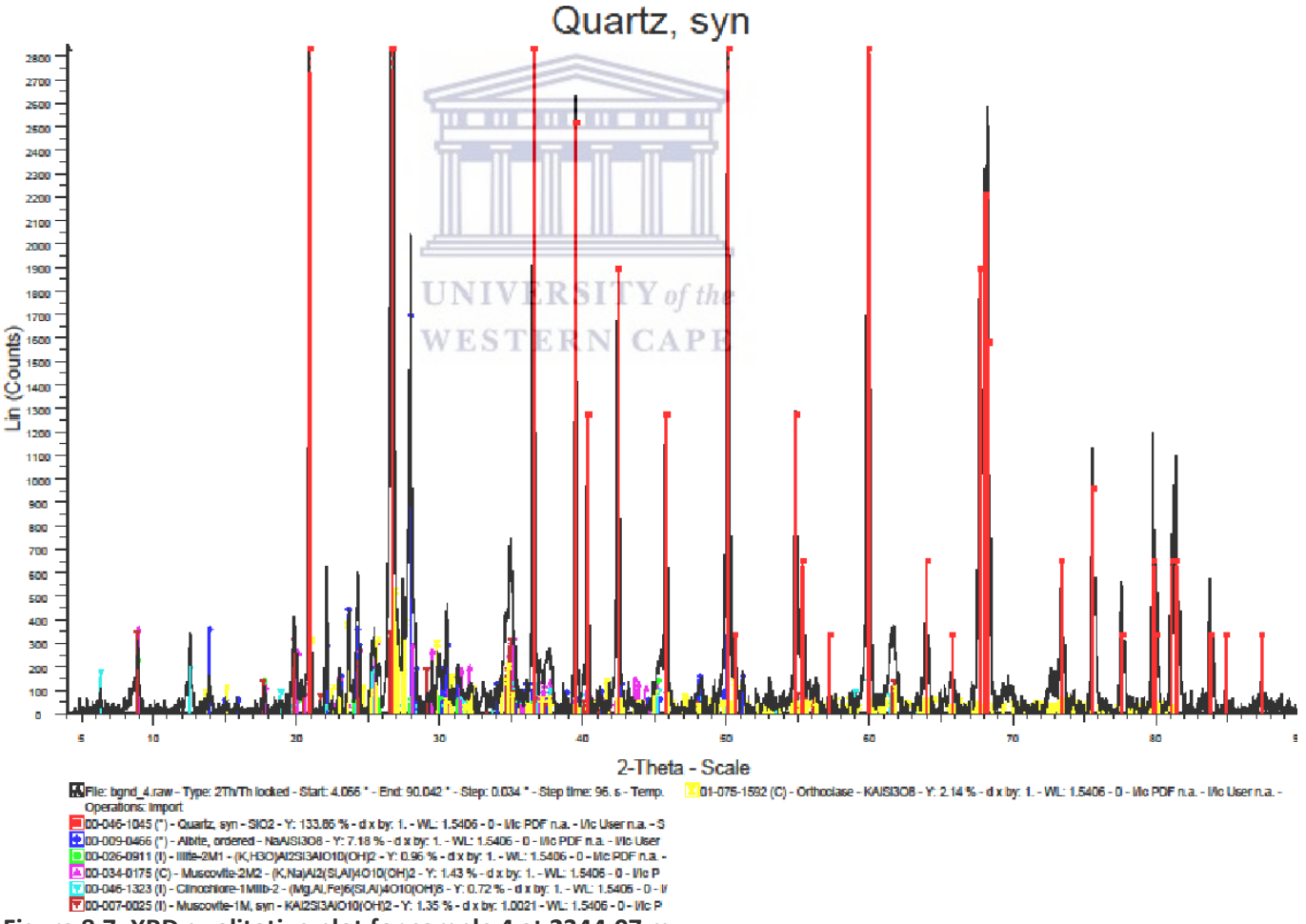

Figure 8.7: XRD qualitative plot for sample 4 at 2344.07 m.

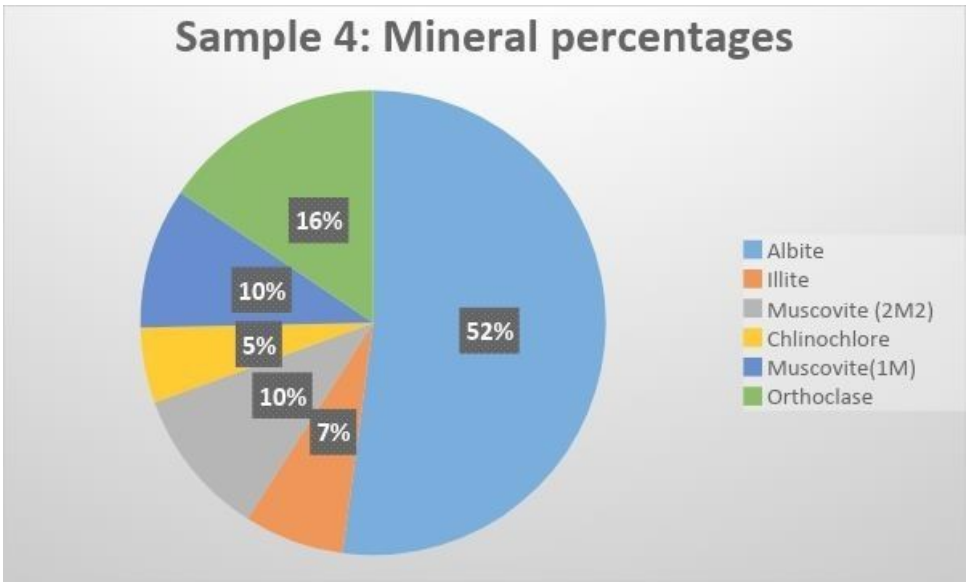

Figure 8.8: Pie chart of mineral aggregates of sample 4 at 2344.07 m.

Sample 5

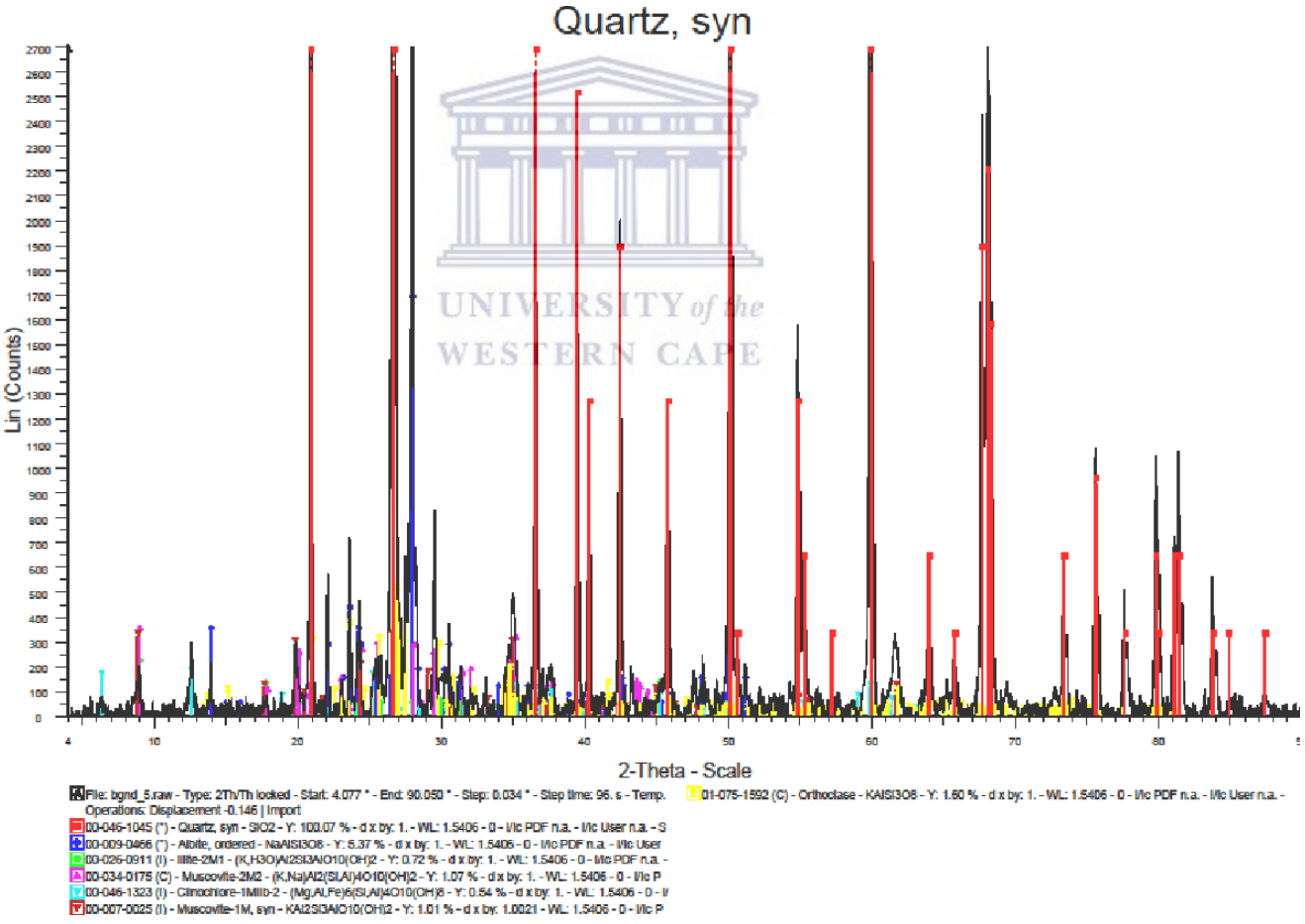

Figure 8.9: XRD qualitative plot for sample 5 at 3135 m.

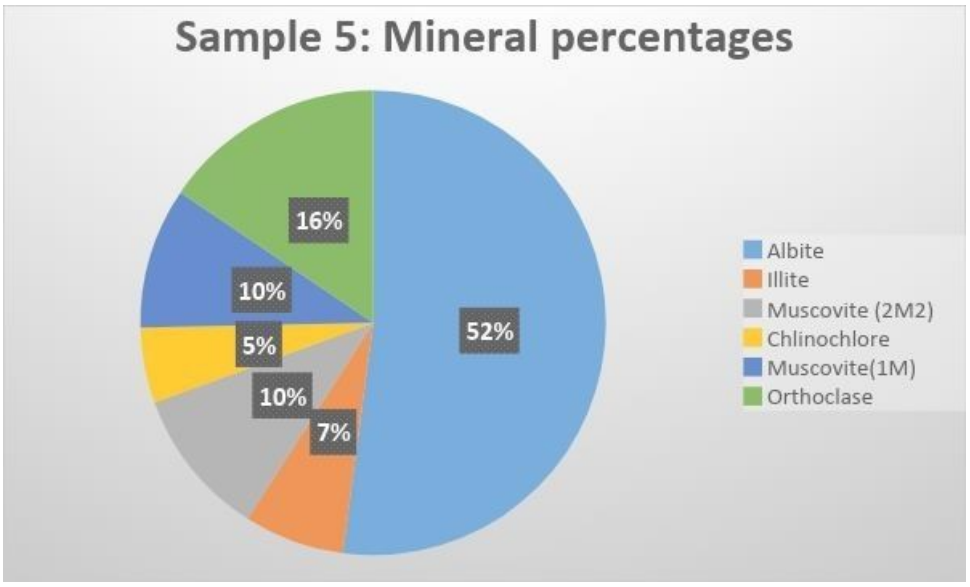

Figure 8.10: Pie chart of mineral aggregates of sample 5 at 3135 m.

Sample 7

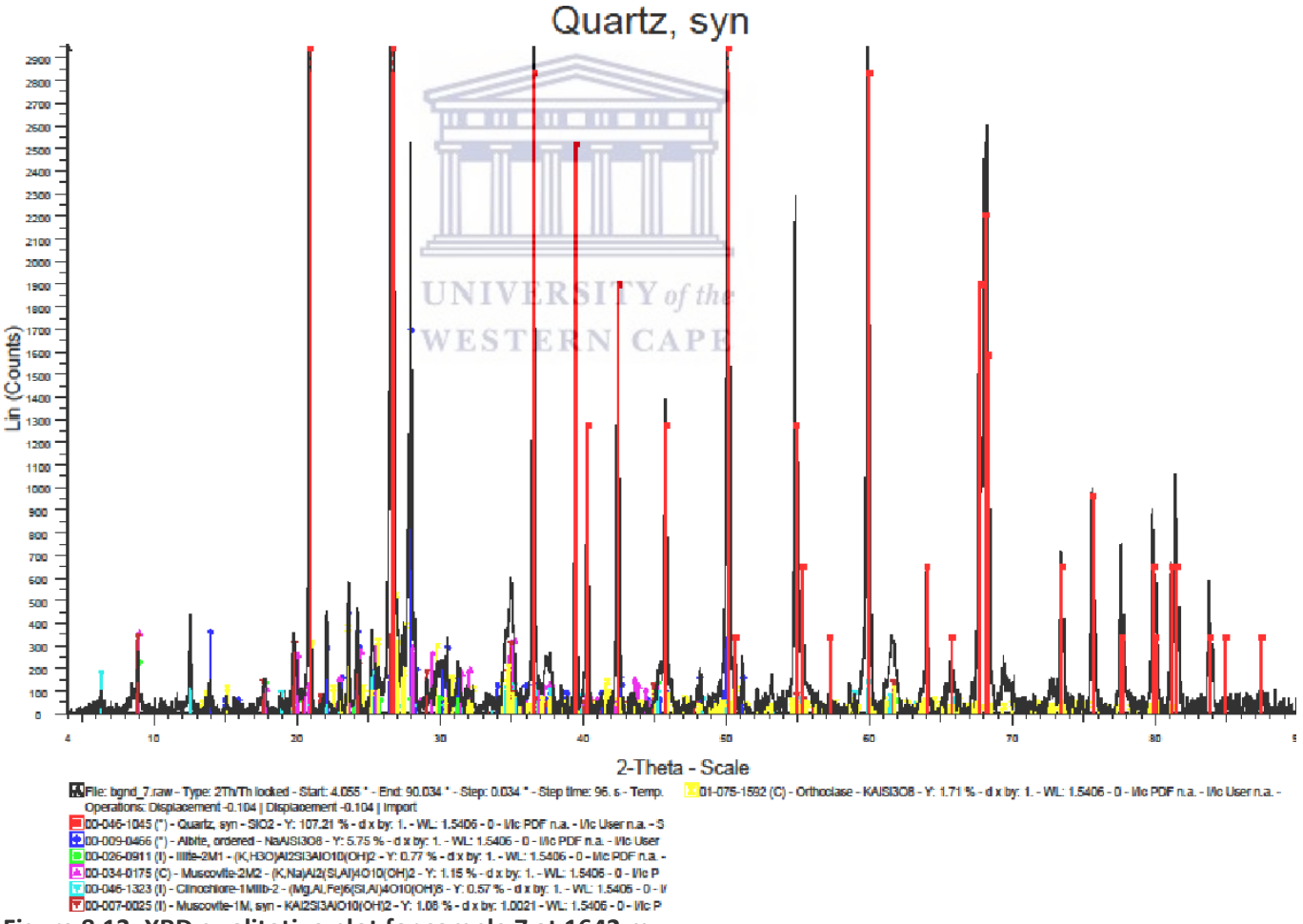

Figure 8.13: XRD qualitative plot for sample 7 at 1642 m.

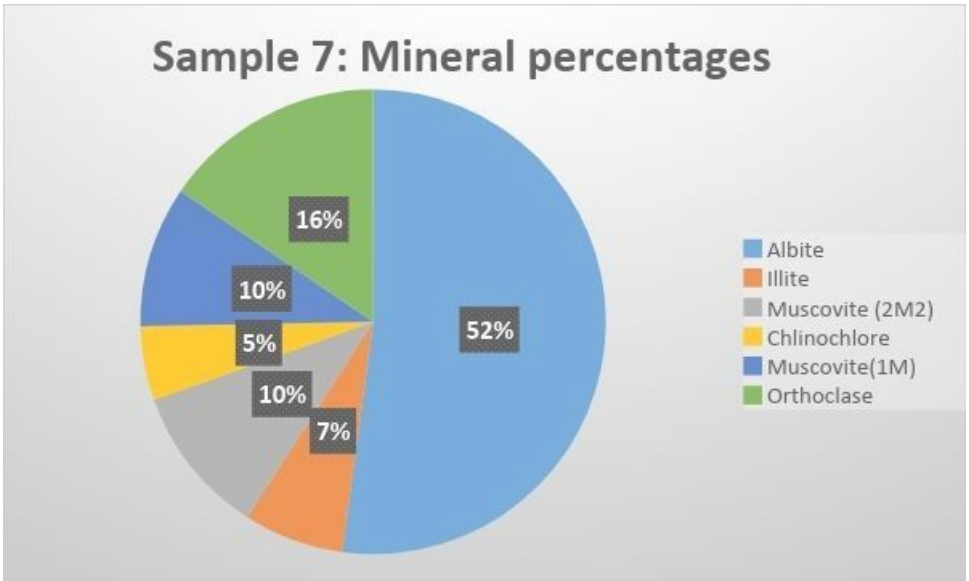

Figure 8.14: Pie chart of mineral aggregates of sample 7 at 1642 m.

Sample 8

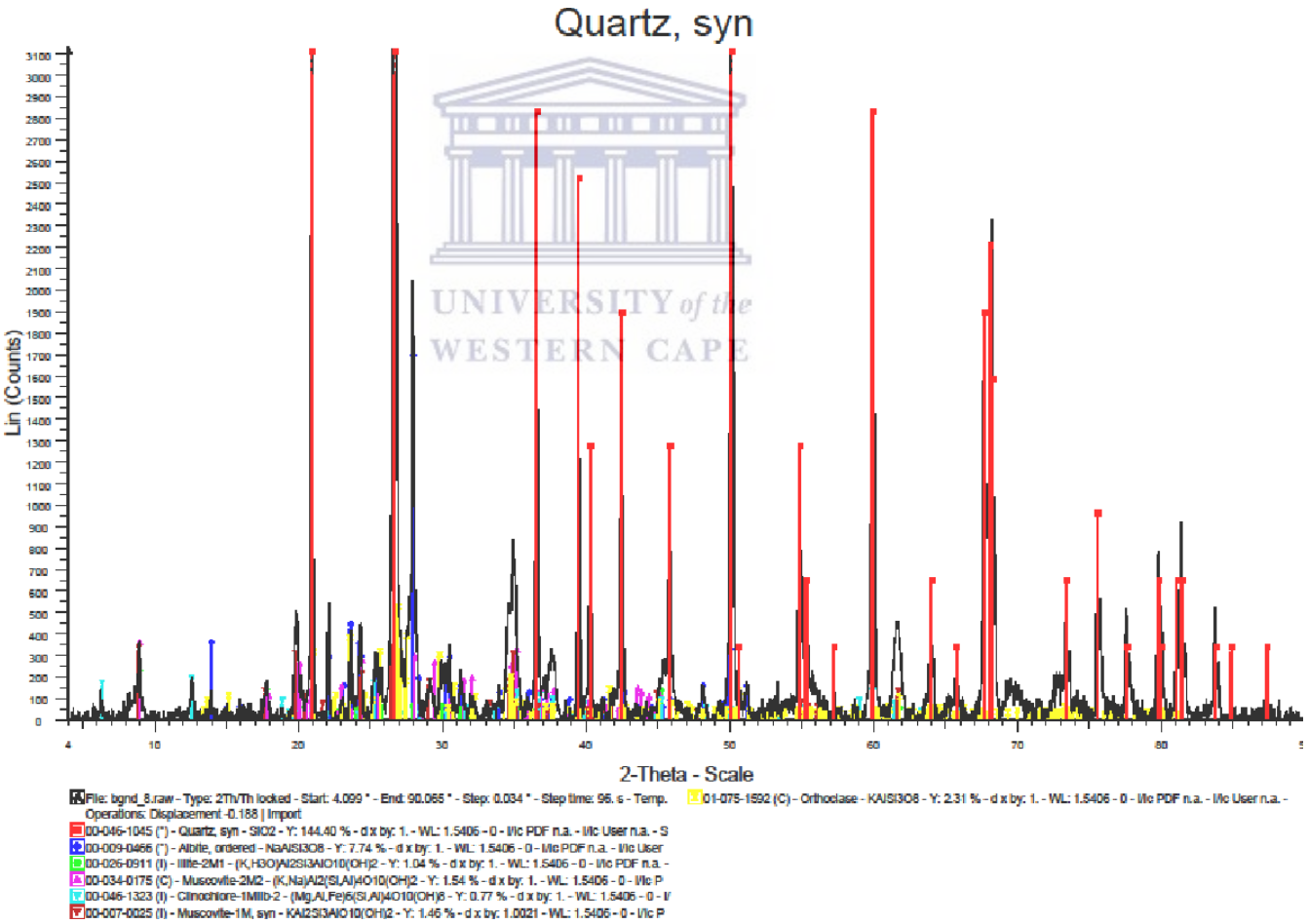

Figure 8.15: XRD qualitative plot for sample 8 at 3017 m.

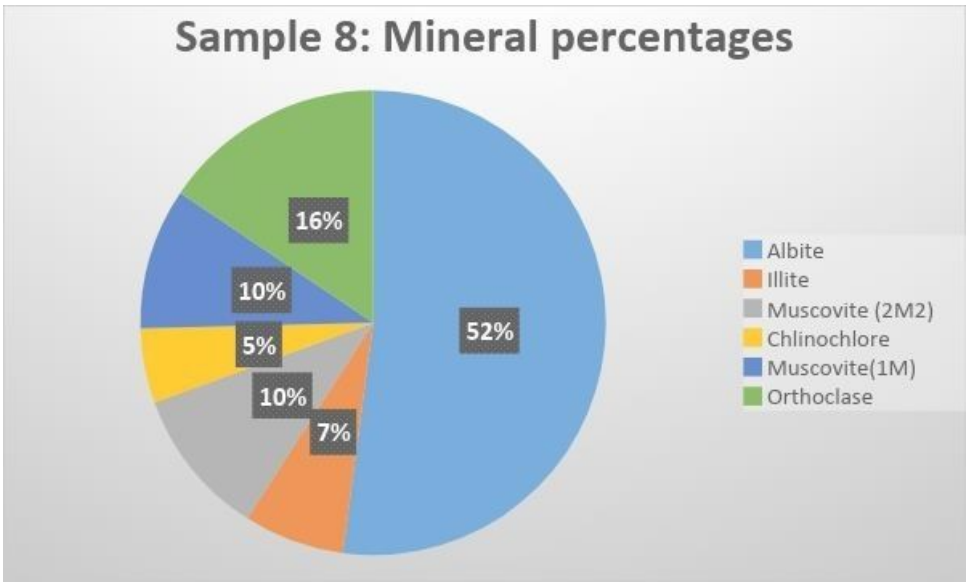

Figure 8.16: Pie chart of mineral aggregates of sample 8 at 3017 m.

Sample 9

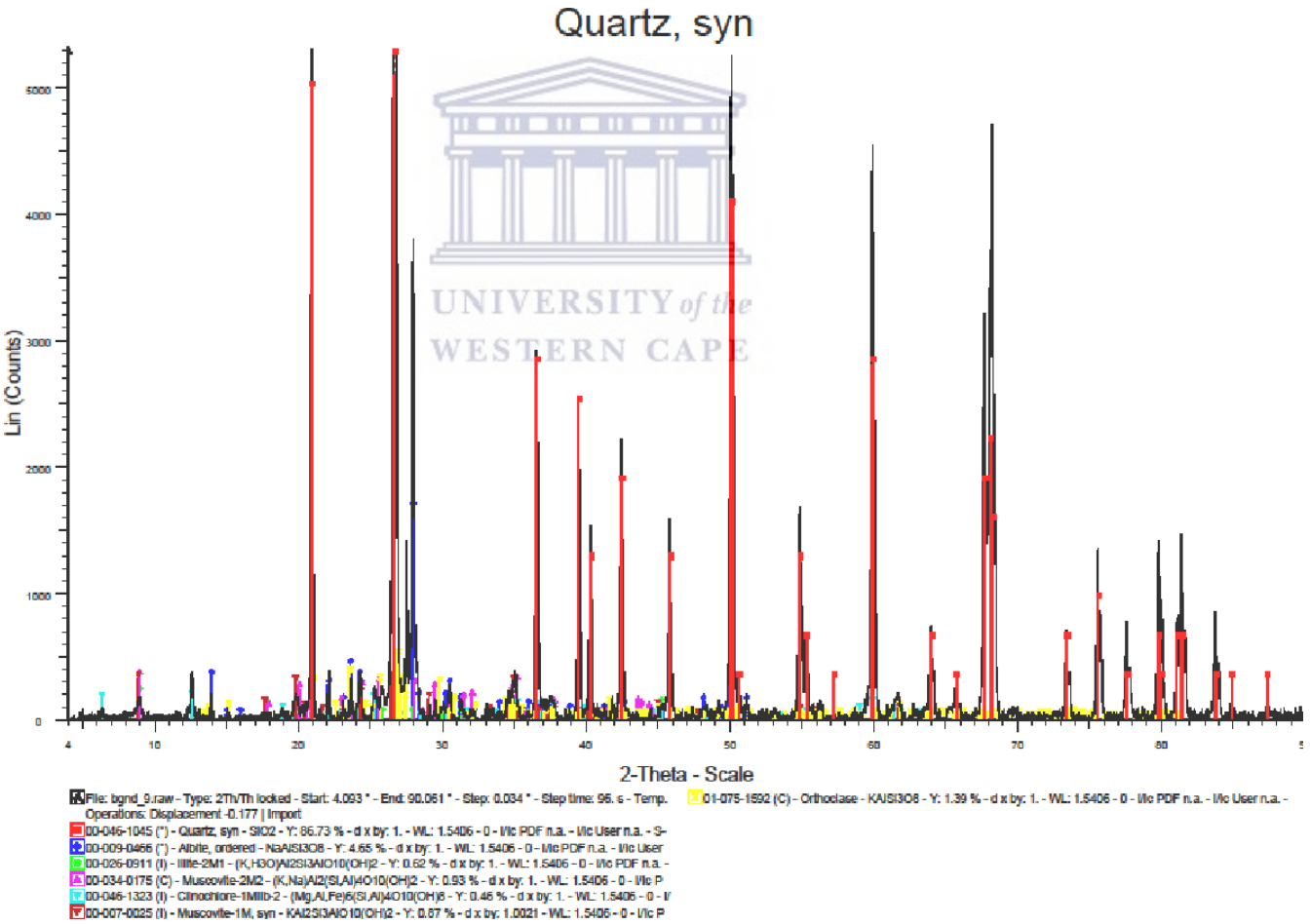

Figure 8.17: XRD qualitative plot for sample 9 at 3021.25 m.

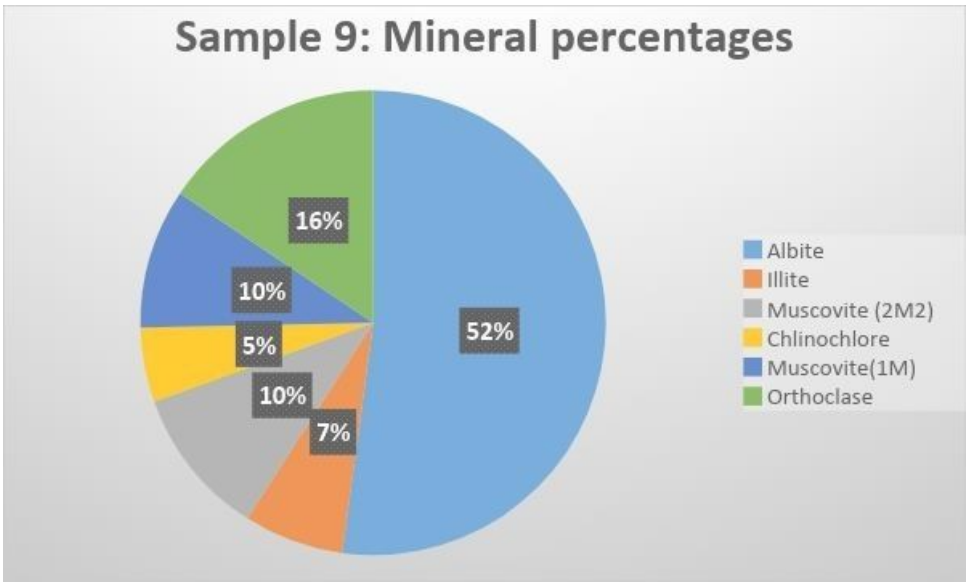

Figure 8.18: Pie chart of mineral aggregates of sample 9 at 3021.25 m.

Sample 10

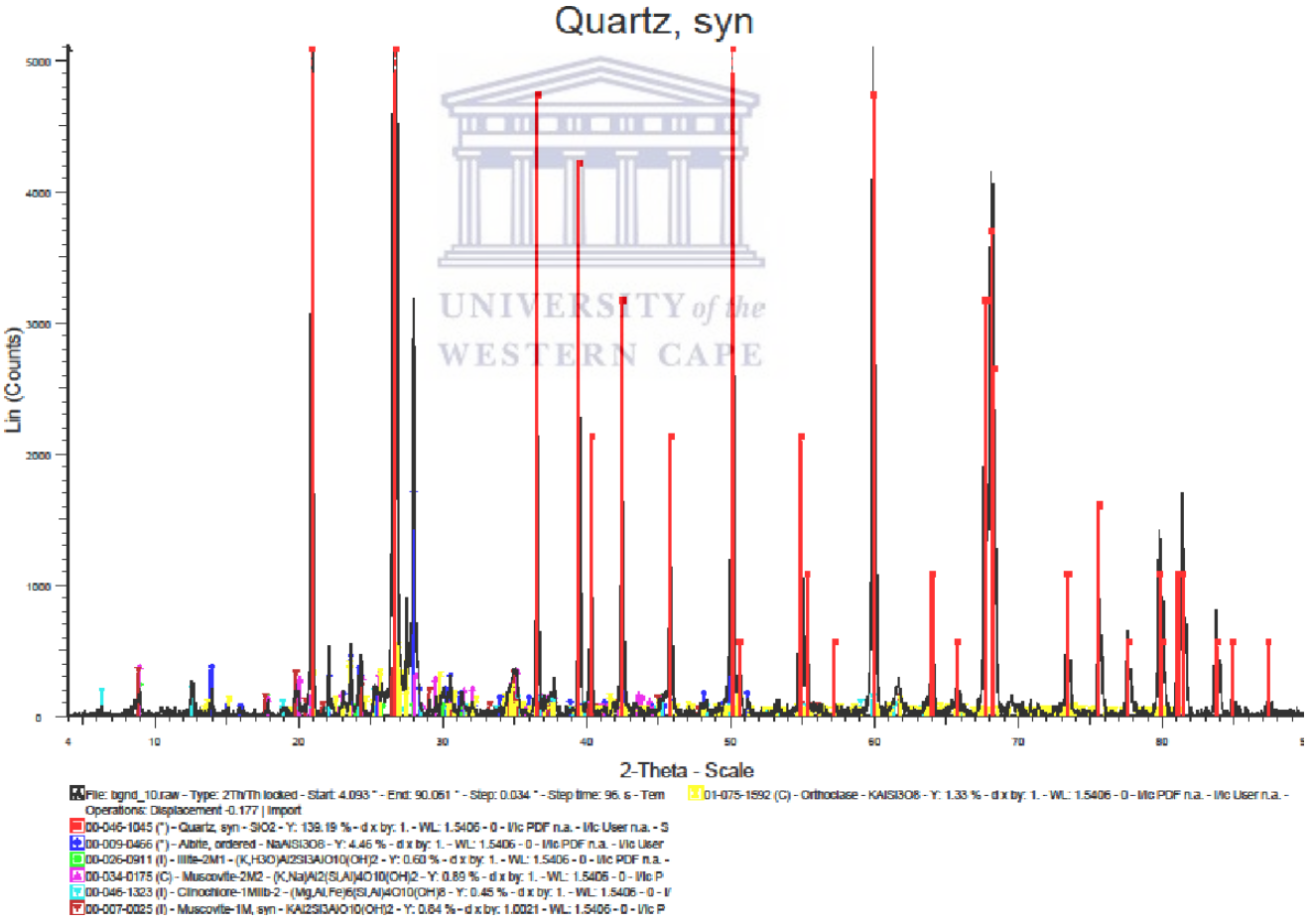

Figure 8.19: XRD qualitative plot for sample 10 at 3088 m.

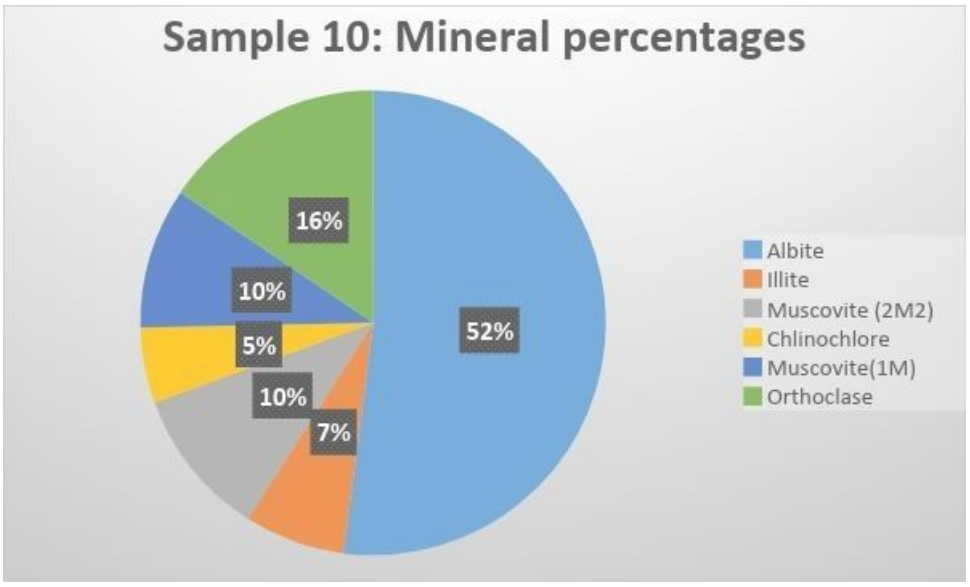

Figure 8.20: Pie chart of mineral aggregates of sample 10 at 3088m.

Appendix G: SEM

Appendix G: SEM

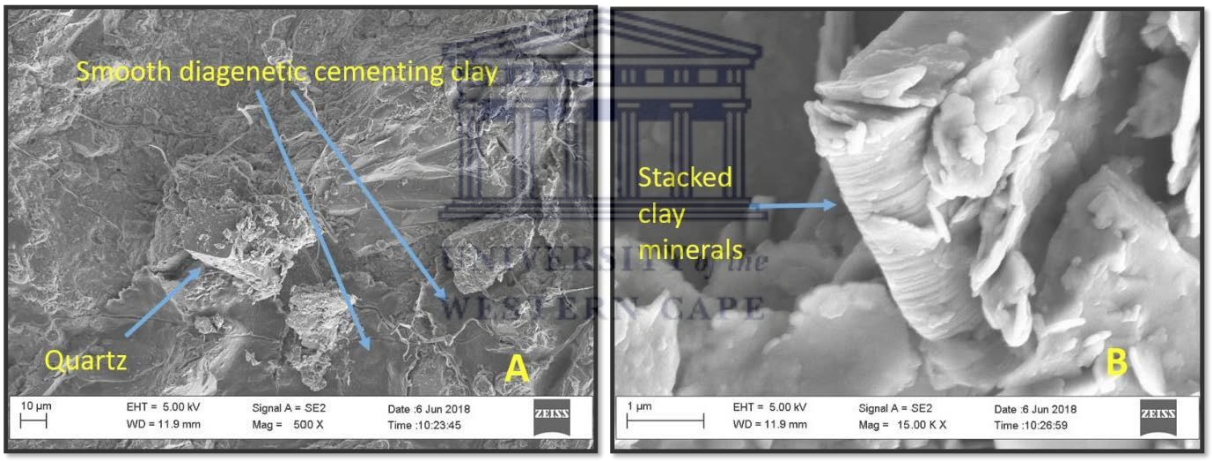

Appendix G1.1: Sample 1 at 2180 m showing smooth diagenetic cementing clay on a larger underlying substrate in A. Sample 1.2 at 2180 m showing stacked clay minerals in B.

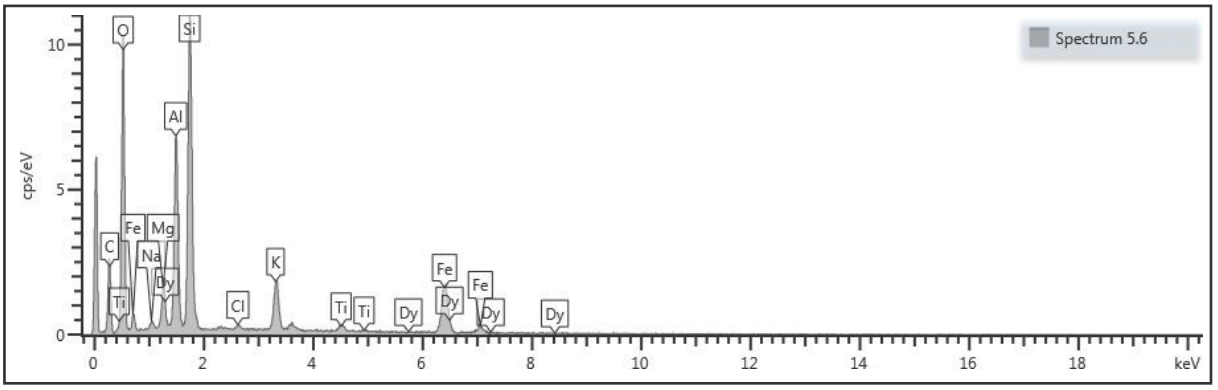

Appendix G1.2: EDS Graph (cps/Ev vs keV) for sample 1

Element	Atomic %
C	39.23
O	41.53
Na	0.36
Mg	1.28
Al	4.95
Si	7.84
Cl	0.11
K	1.38
Ti	0.24
Fe	2.95
Dy	0.12
Total:	100.00

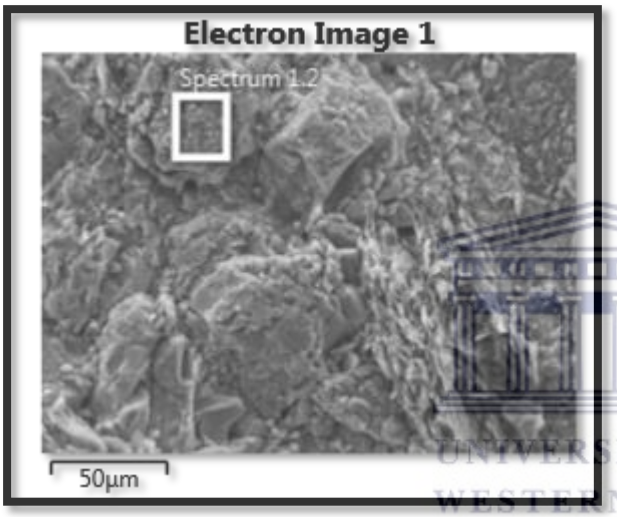

Appendix G1.3: Electron image with chemical constituents for sample 1

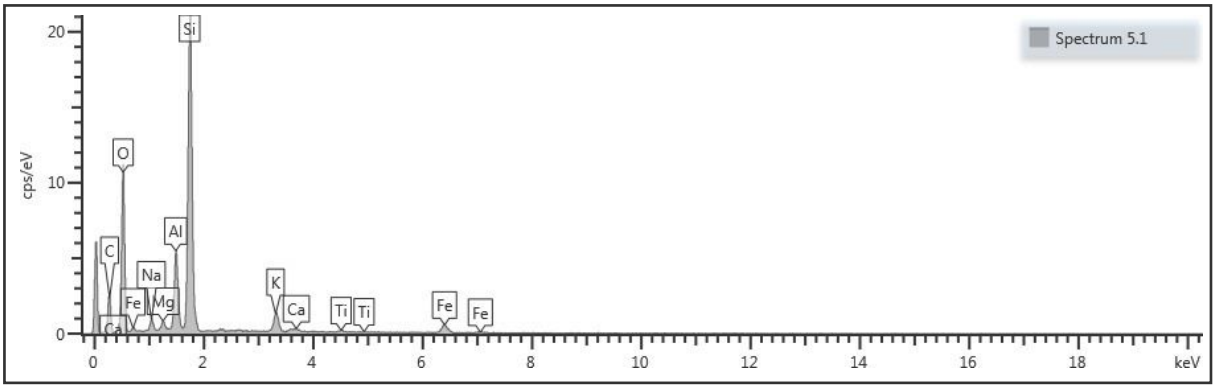

Appendix G1.4: EDS Graph (cps/Ev vs keV) for sample 1

Element	Atomic %
C	38.91
O	42.49

Na	0.79
Mg	0.42
Al	3.08
Si	12.34
K	0.91
Ca	0.12
Ti	0.10
Fe	0.84
Total:	100.00

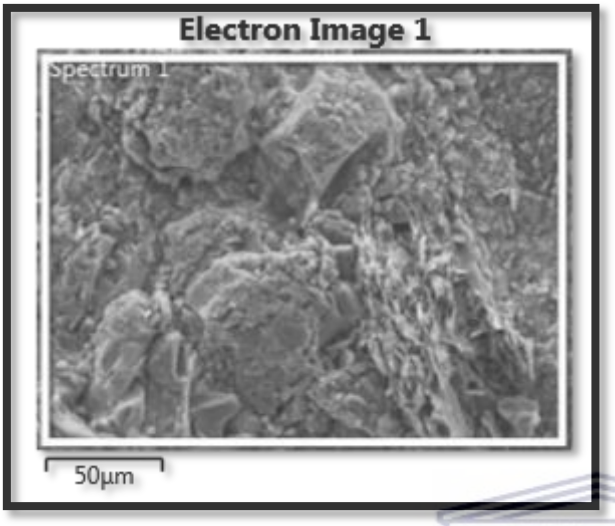

Appendix G1.5: Electron image with chemical constituents for sample 1

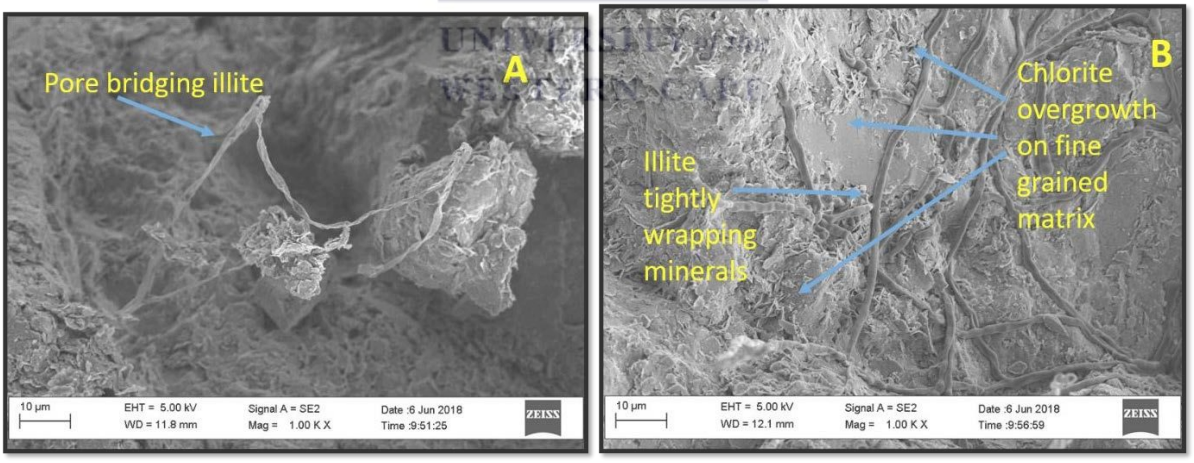

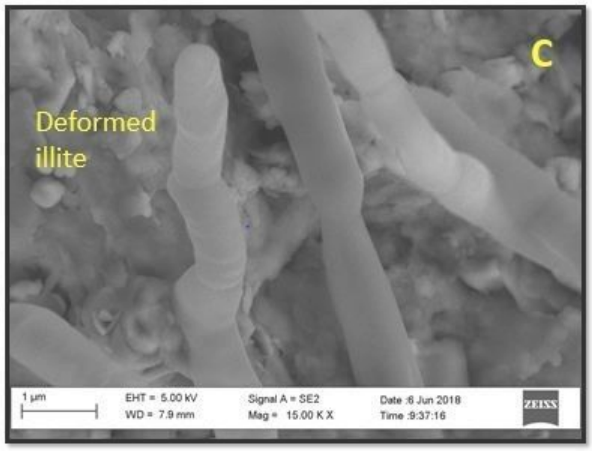

Appendix G2.1: Sample 2 at 2218 m showing pore bridging illite in A, chlorite on fine grained matrix and illite tightly wrapping minerals in B, and deformed illite in C.

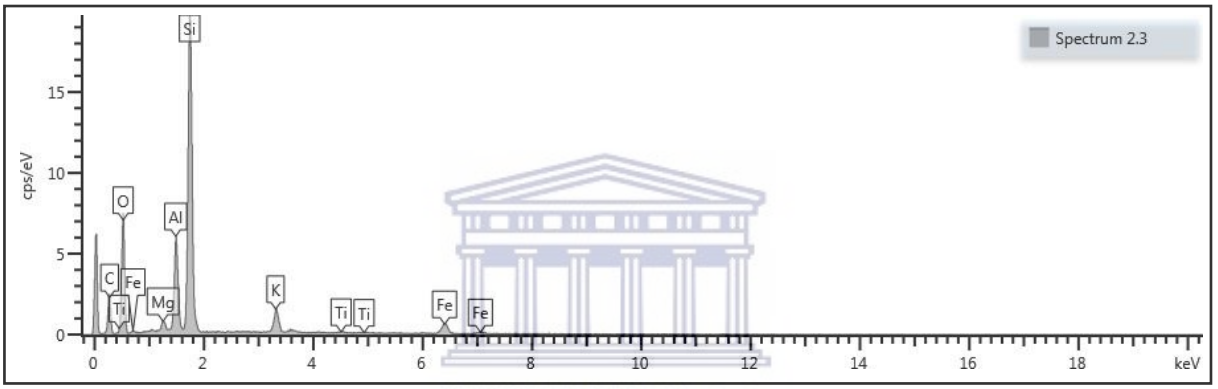

Appendix G2.2: EDS Graph (cps/Ev vs keV) for sample 2

Element	Atomic %
C	43.57
O	36.34
Mg	0.51
Al	3.80
Si	13.37
K	1.17
Ti	0.08
Fe	1.16
Total:	100.00

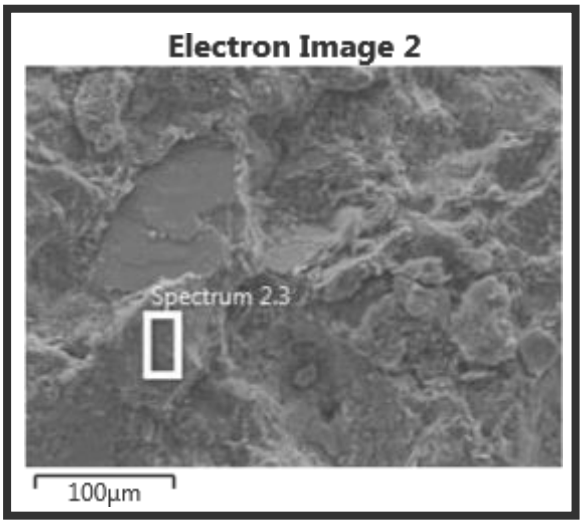

Appendix G2.3: Electron image with chemical constituents for sample 2

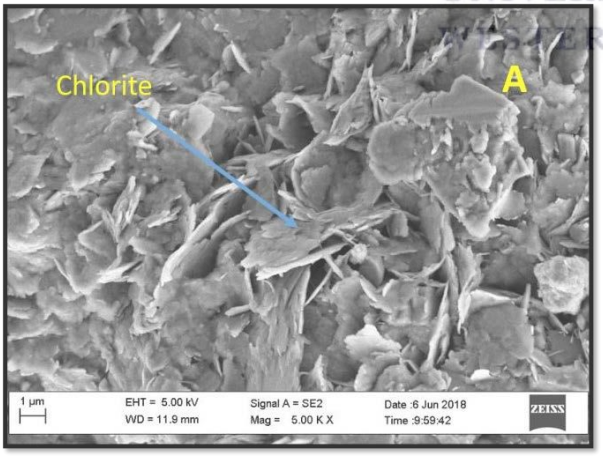

Appendix G3.1: Sample 2.2 at 2218 m showing larger perspective of chlorite grain orientation in A and a close up of the face to edge geometry of the chlorite flakes are displayed in B.

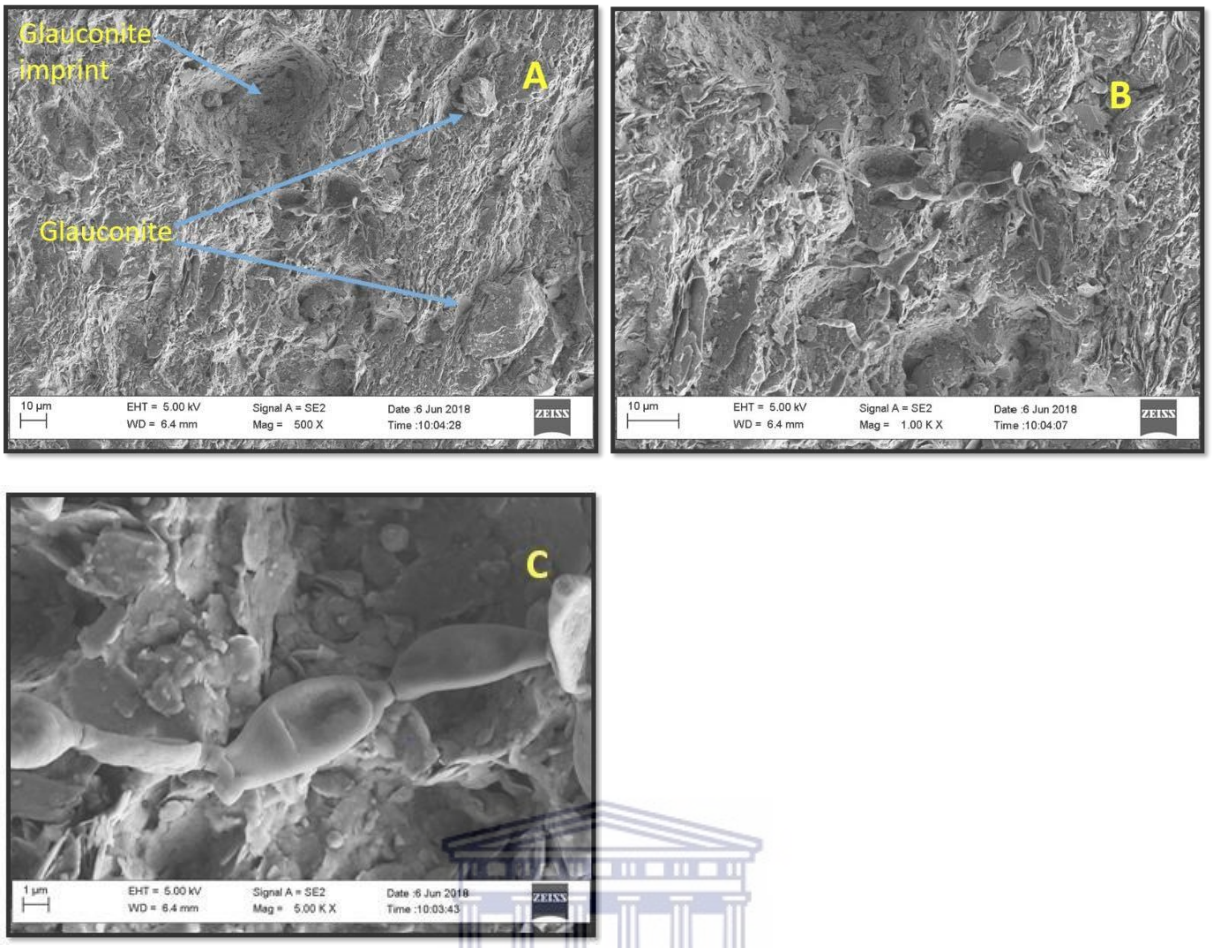

Appendix G3.2: Sample 3.1 at 2329 m showing glauconite imprint in both A and B as well as glauconite pallets in A. C shows a close- up or organic matter.

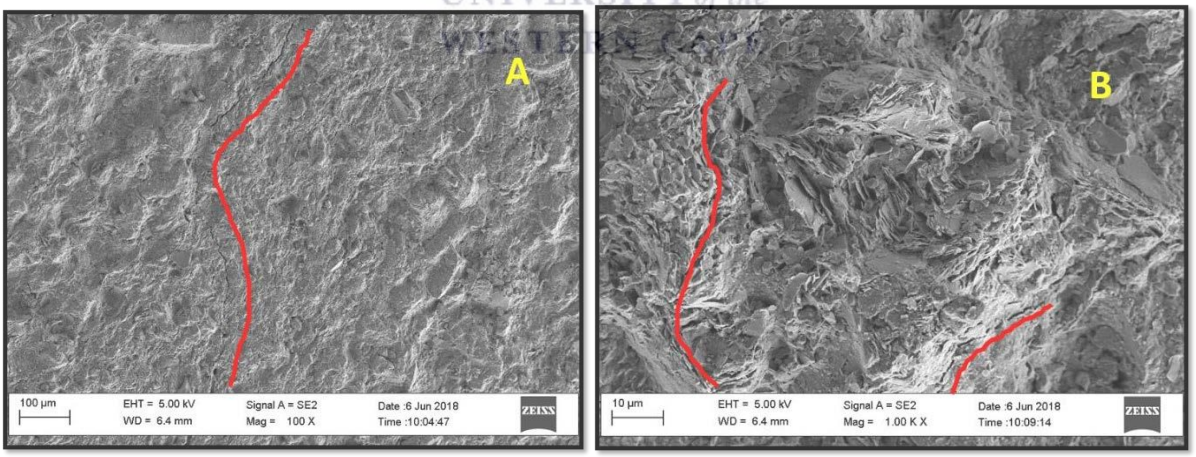

Appendix 3.3: Sample 3 at 2329 m displays the planes of weakness in both a and B.

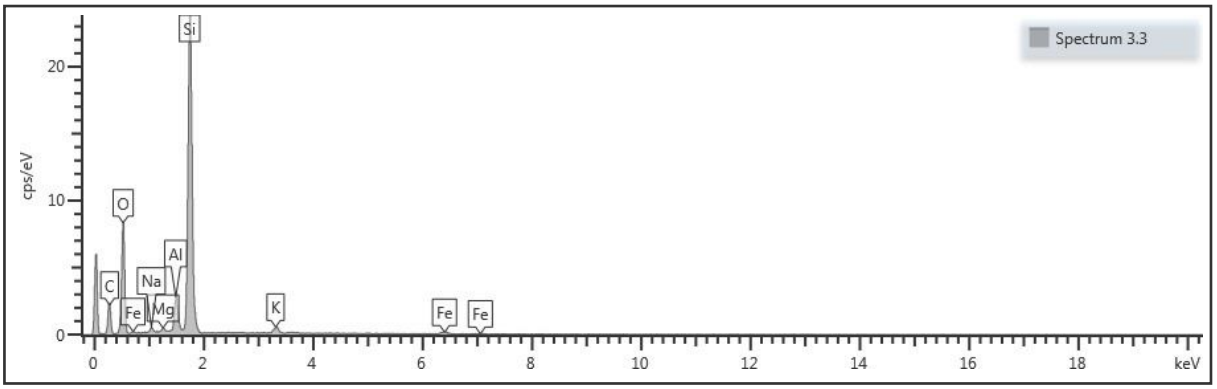

Appendix 3.4: EDS Graph (cps/Ev vs keV) for sample 3

Element	Atomic %
C	42.85
O	39.32
Na	0.41
Mg	0.20
Al	1.58
Si	14.96
K	0.38
Fe	0.30
Total:	100.00

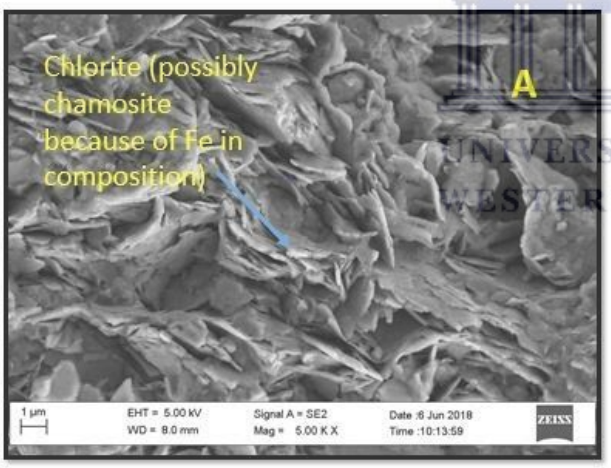

Appendix G4.1: Sample 4 at 2344.07 m displays Chlorite flakes closely packed are shown in A.

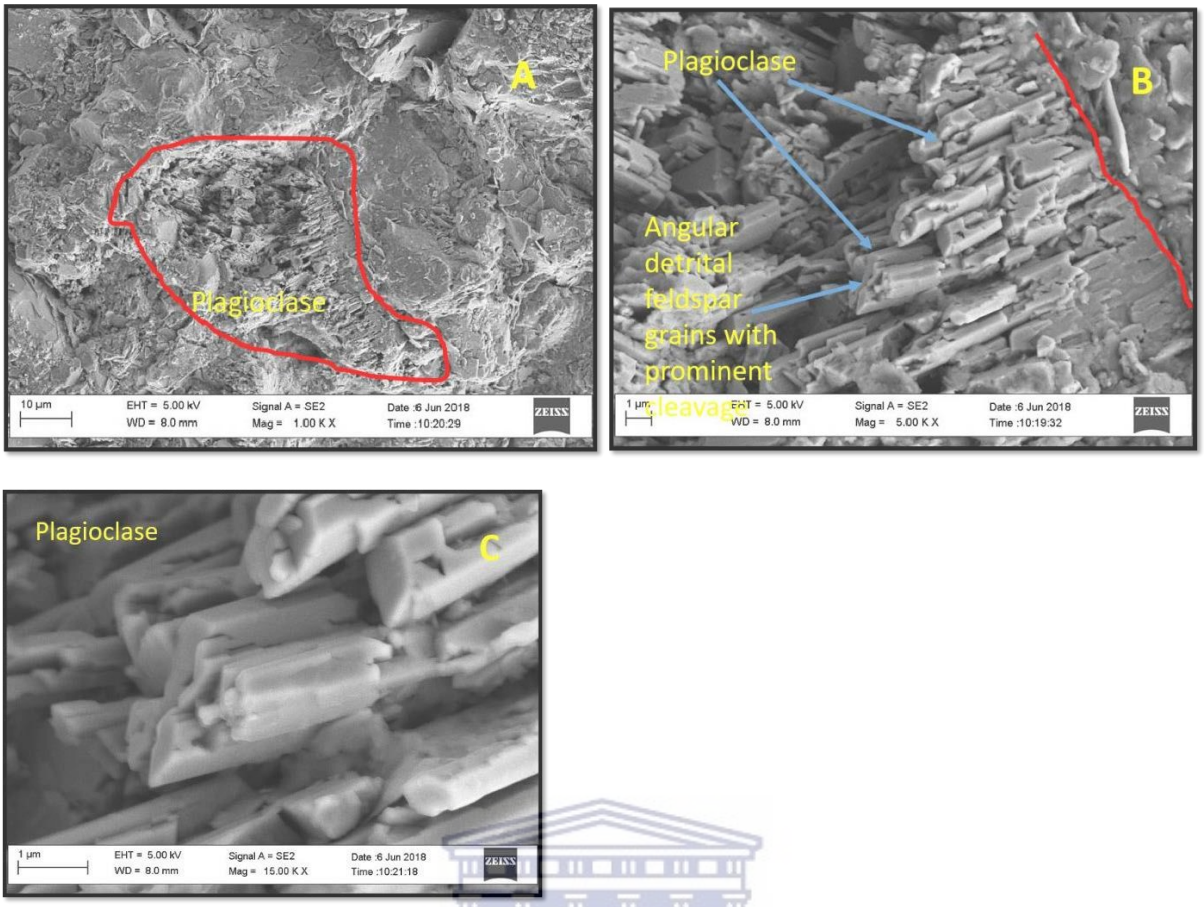

Appendix G4.2: Sample 4 at 2344.07 m displays ground matrix surrounding a centered group of plagioclase minerals in A. The angular detrital plagioclase grains are shown to be protruding towards the opposite side of the matrix demarcated by the red marker. Close up of the structural arrangement of the plagioclase is displayed in C.

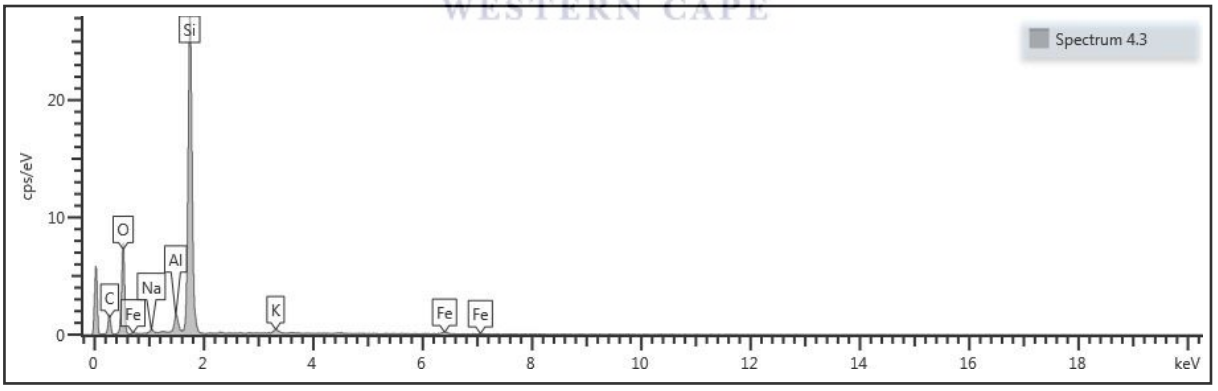

Appendix G4.3: EDS Graph (cps/Ev vs keV) for sample 4

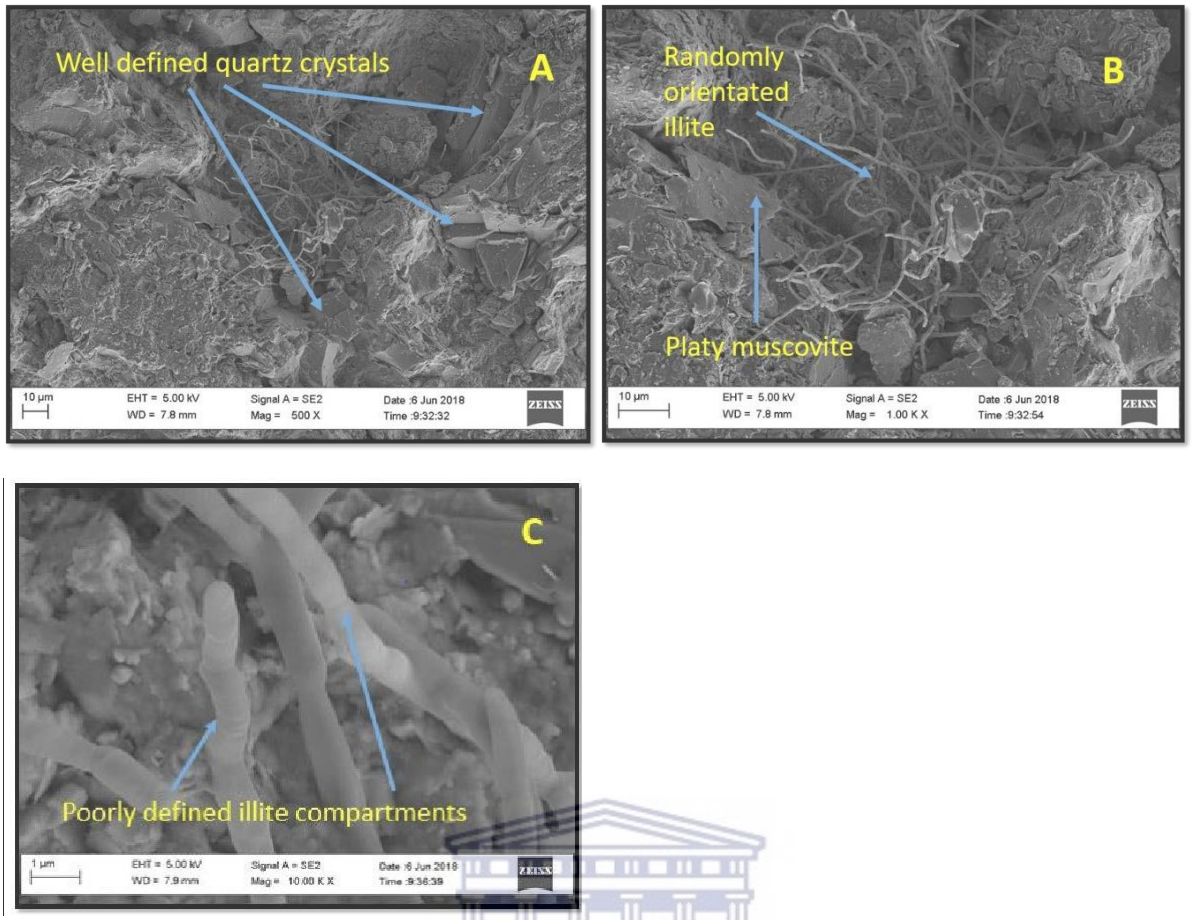

Appendix G5.1: Sample 5 at 3135 m showing well defined quartz crystals in A, randomly orientated illite with platy muscovite in B. A close up of the poorly defined illite compartments is shown in C.

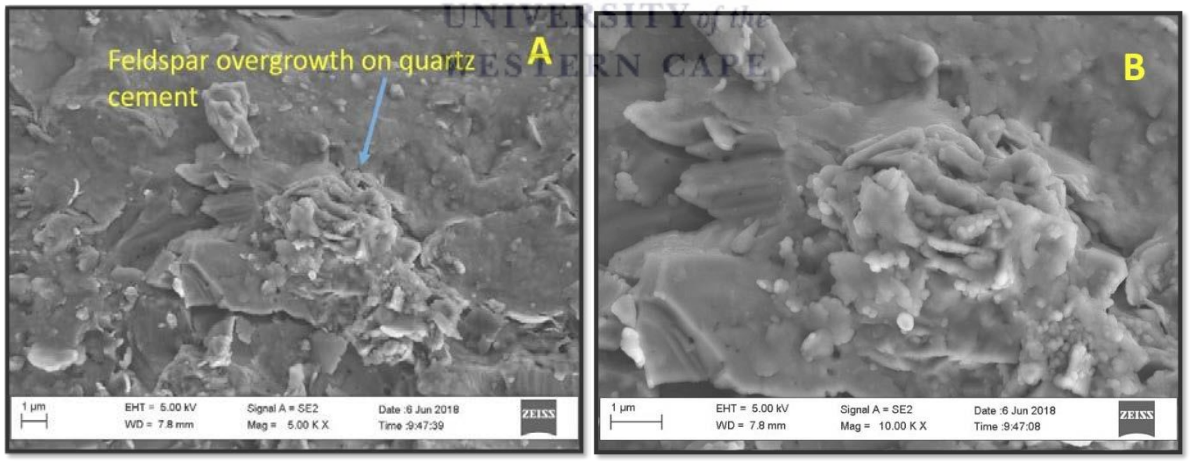

Appendix G5.2: Sample 5.3 at 3135 m showing feldspar overgrowth on quartz cement in A, a close up of the heaped up overgrowth is displayed in B.

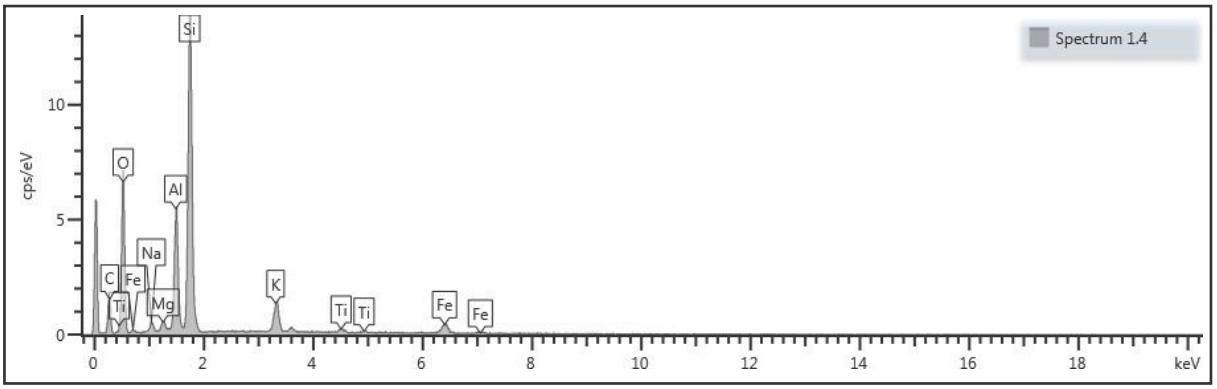

Appendix G5.3: EDS Graph (cps/Ev vs keV) for sample 5

Element	Atomic %
C	37.96
O	41.24
Na	0.65
Mg	0.44
Al	4.68
Si	12.42
K	1.43
Ti	0.23
Fe	0.95
Total:	100.00

Appendix G5.4

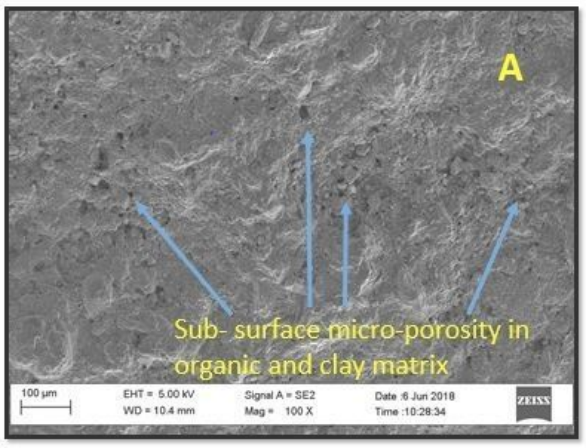

Appendix G6.1: Sample 6 at 1422 m showing sub- surface micro-porosity in organic and clay matrix in A.

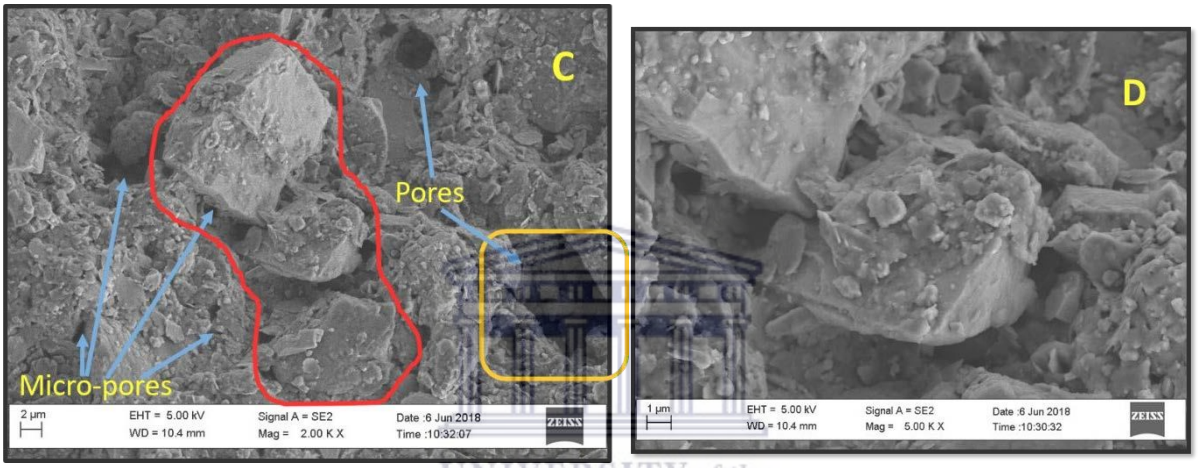

Appendix G6.2: Sample 6 at 1422 m showing micro- pores and well defined quartz grains with overgrowth demarcated by the red marker in C with a close up of some of these grains in D.

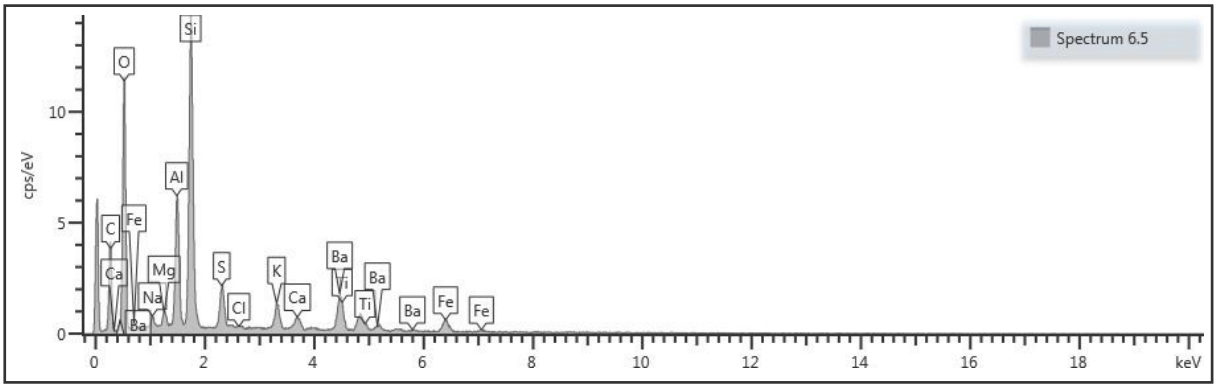

Appendix G6.3: EDS Graph (cps/Ev vs keV) for sample 6

Element	Atomic %
C	45.09
O	38.58
Na	0.43
Mg	0.48

Al	3.48
Si	7.60
S	1.12
Cl	0.06
K	0.69
Ca	0.38
Ti	0.18
Fe	0.75
Ba	1.17
Total:	100.00

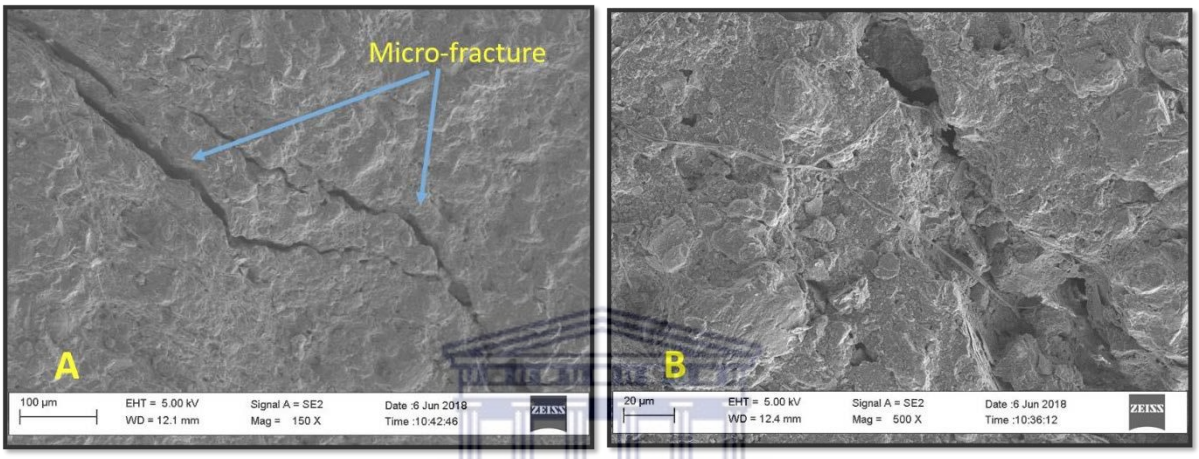

Appendix G7.1: Sample 7 at 1642 m showing micro- fracturing in A and B with some micro-pores in B.

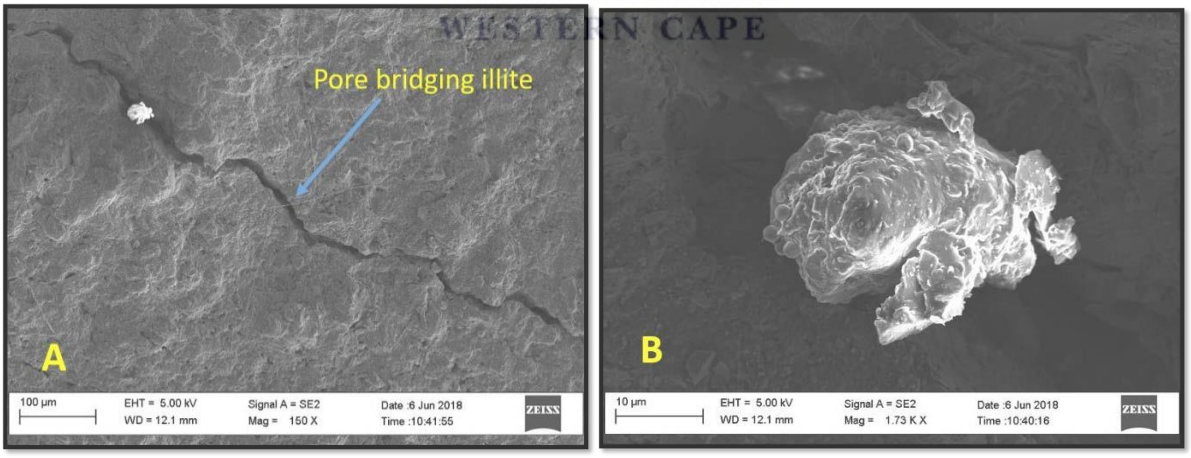

Appendix G7.2: Sample 7 at 1642 m displaying pore bridging illite and glauconite grain in A. A close-up of the glauconite grain in B shows its flaky texture constituting the grain.

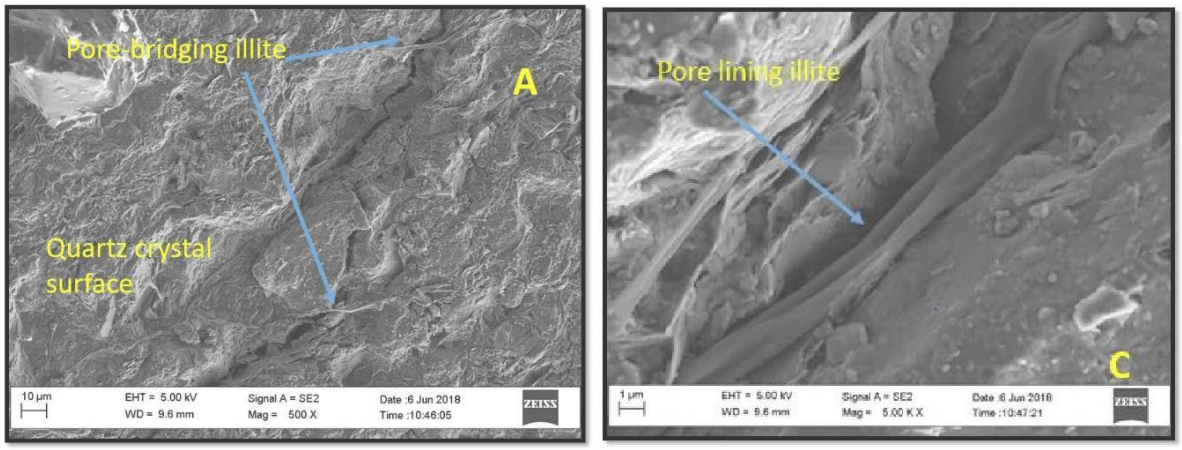

Appendix G8.1: Sample 8 at 3017 m showing pore bridging illite and silicate rich crystal surface in A. Pore infiltrating illite tightly fitted in micro- fracture is shown in C.

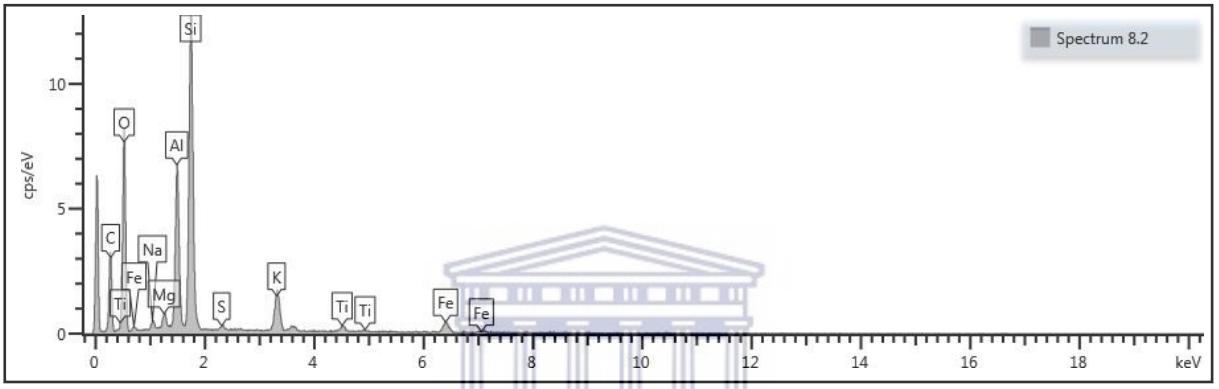

Appendix G8.2: EDS Graph (cps/Ev vs keV) for sample 8

Element	Atomic %
C	46.17
O	37.96
Na	0.40
Mg	0.48
Al	4.29
Si	8.35
S	0.13
K	1.26
Ti	0.23
Fe	0.73
Total:	100.00

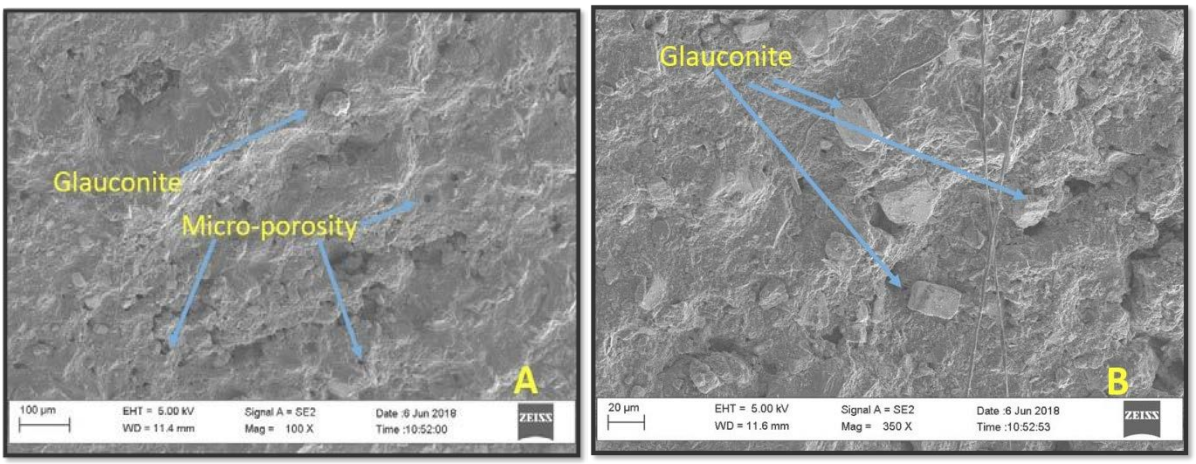

Appendix G9.1: Sample 9 at 3021.25 m display glauconite grains and micro- porosity in A and B.

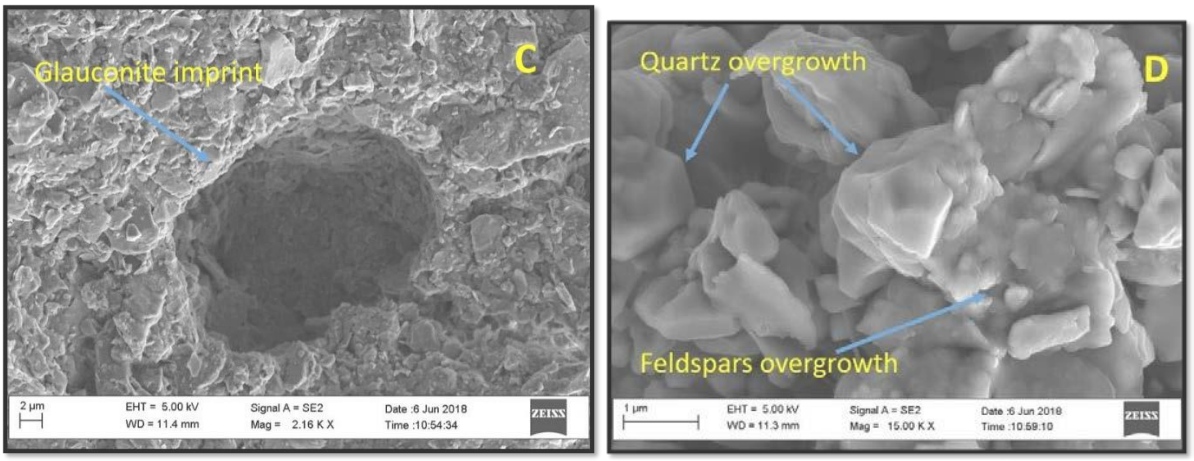

Appendix G9.2: Sample 9 at 3021.25 m show Glauconite imprint is shown in C. Quartz overgrowth and feldspar overgrowth is shown in D.

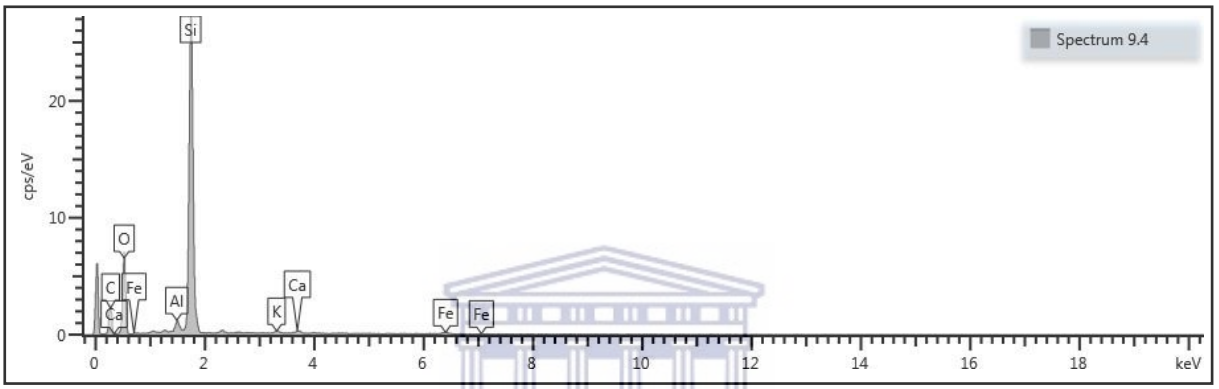

Appendix G9.3: EDS Graph (cps/Ev vs keV) for sample 9

Element	Atomic %
C	47.83
O	34.58
Al	0.52
Si	16.47
K	0.16
Ca	0.20
Fe	0.24
Total:	100.00

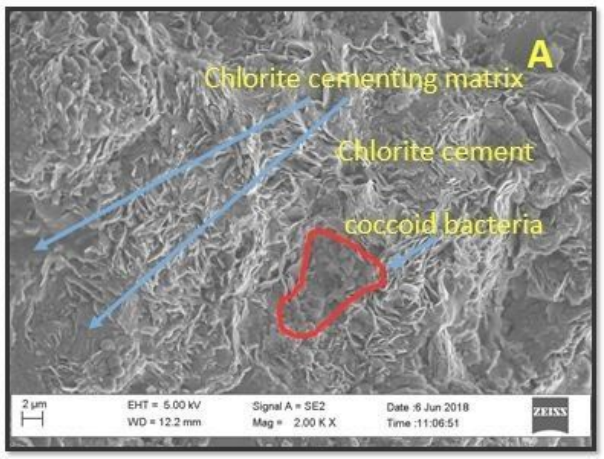

Appendix G10.1: Sample 10 at 3088 m displaying a largely chlorite cementing matrix alongside coccoid bacteria in A. A close up of the flaky chlorite and coccoid bacteria is shown in B.

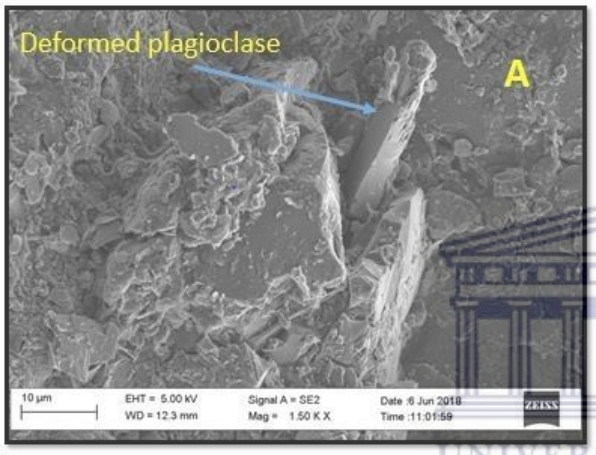

Appendix G10.2: Sample 10 at 3088 m shows protruding deformed plagioclase.

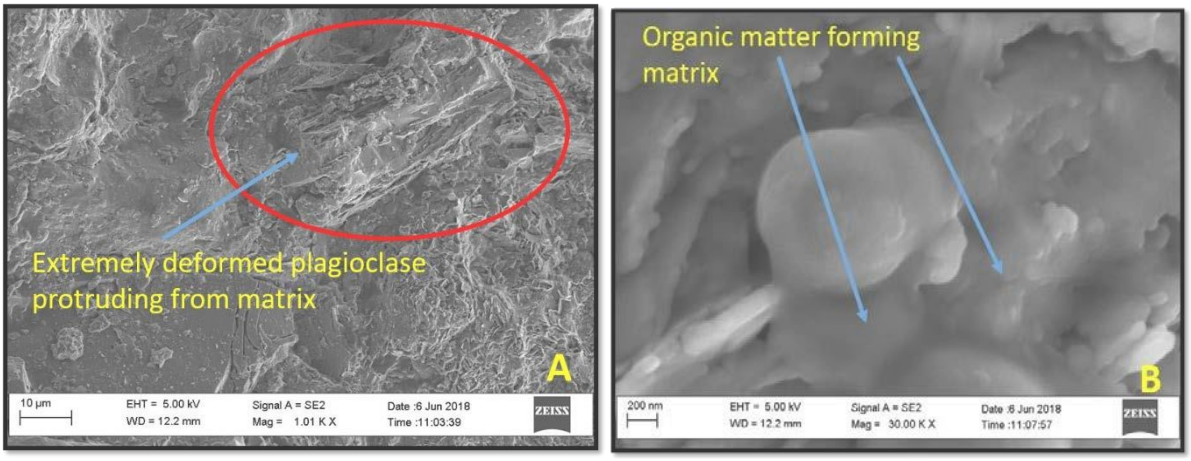

Appendix G10.3: Sample 10 at 3088 m shows extremely deformed plagioclase partially protruding from ground matrix is shown in A. Organic matter forming part of ground matrix is shown in B.

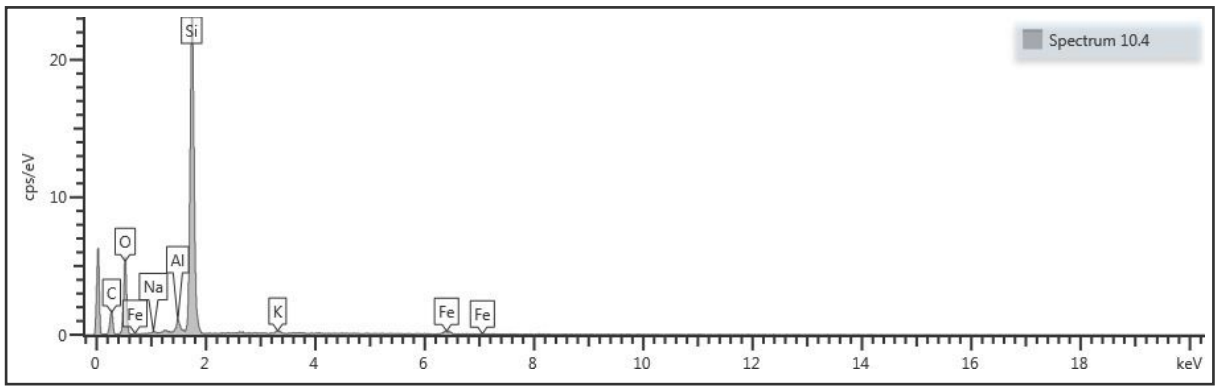

Appendix G10.4: EDS Graph (cps/Ev vs keV) for sample 10

Element	Atomic %
C	45.45
O	34.98
Na	0.15
Al	0.65
Si	18.07
K	0.21
Fe	0.49
Total:	100.00